UNIVERSITÀ DEGLI STUDI DI NAPOLI ‘‘FEDERICO II’’

SCUOLA POLITECNICA E DELLE SCIENZE DI BASE

Department of Chemical, Materials and

Production Engineering

Ph.D. program in

INDUSTRIAL PRODUCT AND PROCESS ENGINEERING

XXXII CYCLE

ENHANCED SEAWATER SCRUBBING FOR FLUE-GAS CLEANING

Advisor board

Prof. Amedeo Lancia

Prof. Francesco Di Natale

PhD. Alessandro Erto

Doctoral Candidate

Domenico Flagiello

Ph.D. Program Coordinator

Prof. Giuseppe Mensitieri

ABSTRACT

This thesis work is focused on the development of new seawater-based scrubbing process for flue-gas cleaning, to be applied to both land-based industrial and power generation plants and to maritime shipping. Seawater scrubbing is receiving a growing attention mostly thanks to the diffusion of marine scrubbers for desulphurization of IFO fueled Marine Diesel Engines exhaust. The process is a viable option also for coastal infrastructures where seawater is abundant and it is funded on the exploitation of seawater alkalinity, which provides a valid and cost-effective sorbent for SO_2. Seawater scrubbing can be improved by using caustic soda or other less common additives. Among them, oxidative reactants such as sodium chlorite ($NaClO_2$), hydrogen peroxide (H_2O_2), ferrous-EDTA (Fe(II)-EDTA), sodium persulfate ($Na_2S_2O_8$) or potassium ferrate (K_2FeO_4) have been suggested.

This work adopts experimental and modelling methodologies to investigate the seawater scrubbing with caustic soda and sodium chlorite addition for the treatment of model flue gases as those coming from real marine diesel engines and coal/oil combustion plants.

The work provides an analysis of SO_2 solubility in the different water-based absorbing solutions and the estimation of the absorption efficiency of SO_2 in packed and spray columns. The experiments are ruled out to define the optimal operating conditions for industrial and marine applications and to interpret how chemical reactions improve the mass transfer rate. The experimental campaign is supported by a dedicated modelling analysis accounting for equilibria, mass transfer and pressure drops in a unique framework, which is a valuable tool for the design of large scales applications.

As a real case application, a comparison between spray and packed towers for a realistic marine engines is carried out, demonstrating that the packed tower can be a valid and cost effective solution, thanks to the far lower size and weight, which overcome the additional cost of packing.

Finally, the effects of seawater-based scrubbing on the quality of the exhaust scrubbing solution are analyzed, for the possible capture of other gas pollutants. To this aim, a critical analysis of the properties of scrubber wash water in terms of heavy metals and organics is carried out. Test on real marine diesel engines shows that the emissions of heavy metals and organic compounds are in line with the current EU regulations on wash water discharge in natural water bodies and mostly of the analytes comply with the 2016/39/EU amendment of the Water Framework Directive.

Finally, in order to further extend the field of investigation, the effect on other gaseous pollutants such as NO_x of sodium chlorite seawater scrubbing is analyzed. Experimental evidences shows that sodium chlorite solutions provides a valuable removal of NO_x compounds, opening to the possibility of a joint de-SO_x/de-NO_x process that is particularly advantageous for marine applications. In particular, the capture of NO_x was promoted by the presence of SO_2 in the exhausted gas and a complete removal can be achieved without any competitive effect. This was due to particular oxidation mechanisms occurring under acidic conditions arising during the absorption process.

Key words:

Exhaust Gas Cleaning System (EGCS); Flue Gas Desulphurization (FGD); Seawater Scrubbing (SWS); Wet Oxidation Scrubbing (WOS); Wet Scrubbers; De-SO_x units; De-NO_x units

Ph.D. Candidate:

Domenico Flagiello, PhD program in Industrial Product and Process Engineering, XXXII cycle

Tutors:

Prof. Amedeo Lancia;

Prof. Francesco Di Natale;

Ph.D. Alessandro Erto

Ph.D. Program Coordinator:

Prof. Giuseppe Mensitieri

The Ph.D. thesis has been revised by:

- Alessandro Paglianti, Professor at University of Bologna "ALMA MATER STUDIORUM", Italy - *Dipartimento di Ingegneria Civile, Chimica, Ambientale e dei Materiali*;

- Dino Musmarra, Professor at University of Campania "Luigi Vanvitelli", Italy - *Dipartimento di Ingegneria Civile, Design, Edilizia e Ambiente*;

- Kent Salo, Senior Lecturer at Chalmers University of Technology, Göteborg, Sweden - *Department of Mechanics and Maritime Sciences*.

SUMMARY

List of Symbols

a	Functional dependency for Graetz liquid number, [-]
$a_d(t)$	Time-dependent specific surface area of droplet, [$m^2 \cdot m^{-3}$]
$a_{d,j}$	Droplet surface involved in the mass transfer, [m^2]
a_d°	Minimum specific area of a spherical droplet undergoing shape oscillations, [$m^2 \cdot m^{-3}$]
a_e	Effective wet surface area of packing, [$m^2 \cdot m^{-3}$]
A_{eq}	Constant parameter for K_{eq} evaluation, [$(mol \cdot mol^{-1})^d$]
A_H	Constant parameter for K_H evaluation, [atm]
a_n	Nominal surface of packing, [$m^2 \cdot m^{-3}$]
b	Functional dependency for Kapitza number, [-]
B_1, B_2	Friction constants, [-]
B_{eq}	Constant parameter for K_{eq} evaluation, [K]
B_H	Constant parameter for K_H evaluation, [K]
Bo	Bond number, [-]
B_p	Base width of a packing corrugation, [m]
c	Coefficient of proportionality for liquid-side mass transfer, [-]
C°_{CO}	CO gas inlet concentration, [% vol.]
$C^\circ_{CO_2}$	CO_2 gas inlet concentration, [ppm_v]
$C^\circ_{NO_{x(g)}}$	NO_x gas inlet concentration, [ppm_v]
$C^\circ_{SO_{2(g)}}$	SO_2 gas inlet concentration, [ppm_v]
C_1, C_2, C_3	Stichlmair constants, [-]
$C_{A,b}$	Liquid concentration of component A in the bulk, [$kmol \cdot m^{-3}$]
$C_{A,i}$	Liquid concentration of component A at the interface, [$kmol \cdot m^{-3}$]
$C_{B,b}$	Liquid concentrations of component B in the bulk liquid, [$kmol \cdot m^{-3}$]
$C_{CO_{(g)}}$	CO gas outlet concentration, [% vol.]
$C_{CO_{2(g)}}$	CO_2 gas outlet concentration, [ppm_v]
C_D	Total drag coefficient, [-]
C_{eq}	Constant parameter for K_{eq} evaluation, [K^{-1}]
C_E^{SRP}	Correction factor for liquid-side mass transfer, [-]
C_G^{BP}	Coefficient of proportionality for gas-side mass transfer, [-]
C_G^{BRF}	Coefficient of proportionality for gas-side mass transfer, [-]
C_G^{BS}	Coefficient of proportionality for gas-side mass transfer, [-]
C_G^{Delft}	Coefficient of proportionality for gas-side mass transfer, [-]

C_G^{SRP}	Coefficient of proportionality for gas-side mass transfer, [-]
C_H	Constant parameter for K_H evaluation, [K^{-1}]
C_L^{BS}	Coefficient of proportionality for liquid-side mass transfer, [-]
C_M	Mass concentration of metals in the fuel, [$mg \cdot kg^{-1}$]
$C_{M,max}$	Maximum concentration for each heavy metal, [$mg \cdot kg^{-1}$]
$C_{M,obs}$	Metals content observed in the wash water samples, [$mg \cdot kg^{-1}$]
C_{NaClO_2}	Liquid concentration of $NaClO_2$, [mol·L]
C_{NaOH}	Liquid concentration of NaOH, [mol·L]
$C_{NO_{x(g)}}$	NO_x gas outlet concentration, [ppm_v]
$C_{p,d}^{SRP}$	Coefficient of proportionality for pressure drop in dry conditions, [-]
$C_{P,l}^{Delft}$	Coefficient of proportionality for pressure drop, [-]
$C_{P,lp}^{Delft}$	Coefficient of proportionality for pressure drop at loading point, [-]
$C_{p,w}^{SRP}$	Coefficient of proportionality for pressure drop in wet conditions, [-]
C_P^{BS}	Coefficient of proportionality for pressure drop, [-]
C_{react}	Concentration of the reagent in liquid phase, [$kmol \cdot m^{-3}$]
$C_{SO_{2(g)}}$	SO_2 gas outlet concentration, [ppm_v]
d	Characteristic dimension of the liquid film, [m]
D	Scrubber diameter, [m]
$d_{b/s}$	Operating dosage $HCO_3^-/SO_{2(g)}$, [$mol \cdot mol^{-1}$]
$d_{c/n}$	Operating dosage $ClO_2^-/NO_{x(g)}$, [$mol \cdot mol^{-1}$]
$d_{c/s}$	Operating dosage $ClO_2^-/SO_{2(g)}$, [$mol \cdot mol^{-1}$]
D_d	Diameter for a spherical droplet, [m]
$D_{d,cr}$	Critical diameter for a spherical droplet, [m]
$D_{d,cut}$	Minimum droplet size, [m]
D_{eq}	Constant parameter for K_{eq} evaluation, [K^{-1}]
d_{eq}	Equivalent diameter, [m]
D_G	Gas diffusivity in gas phase, [$m^2 \cdot s^{-1}$]
D_H	Constant parameter for K_H evaluation, [K^{-1}]
d_h	Hydraulic diameter, [m]
d_{hG}	Hydraulic diameter relating to gas phase, [m]
$D_{L,A}$	Diffusivity of gas component *A* in the liquid phase, [$m^2 \cdot s^{-1}$]
$D_{L,B}$	Diffusivity of gas component *B* in the liquid phase, [$m^2 \cdot s^{-1}$]
E_∞	Enhancement factor for an instantaneous reaction in liquid phase, [-]
E_a	Activation energy, [$kJ \cdot mol^{-1}$]

E_L	Enhancement factor for the reaction in the liquid phase, [-]
Eo	Eötvös number, [-]
FC	Fuel consumption, [$L \cdot h^{-1}$]
F_{eff}	Efficiency pumping factor, [-]
F_{eq}	Equilibrium function that represents the solubility of the gaseous solute in the liquid phase, [-]
f_G	Gas friction factor, [-]
F_G	Gas load factor, [$Pa^{0.5}$]
$F_{G,des}$	Gas load factor values referred to the design conditions, [$Pa^{0.5}$]
$F_{G,flood}$	Gas load factor values referred to the flooding point, [$Pa^{0.5}$]
$F_{G,lp}$	Gas load factor at loading point, [$Pa^{0.5}$]
F_L	Liquid load factor, [$m \cdot h^{-1}$]
F_{LG}	Flow parameter, [-]
F_{Load}	Enhancement factor for pressure drops, above the loading point, [-]
f_M	Friction factor deriving from wall-gas and liquid-gas contact, [-]
Fr_L	Froude liquid number, [-]
F_{SE}^{SRP}	Surface enhancement factor of packing, [-]
F_t	Correction factor for total liquid hold-up due to effective wetted area, [-]
g	Acceleration of gravity, [$m \cdot s^{-2}$]
G	Volumetric gas flow rate, [$m^3 \cdot h^{-1}$]
G_{eng}	Total exhaust gas flow rate produced by the engine, [$m^3 \cdot h^{-1}$]
G_m	Molar gas flow rate, [$mol \cdot s^{-1}$]
G_{mass}/S	Mass gas flow rate per unit of section in the column, [$kg \cdot m^{-2} \cdot s^{-1}$]
Gr_L	Graetz number, [-]
h	Impact distance droplet-wall, [m]
Ha	Hatta number, [-]
h_L	Liquid volumetric hold-up, [$m^3 \cdot m^{-3}$]
$h_{L,d}$	Dynamic liquid hold-up, [$m^3 \cdot m^{-3}$]
$h_{L,s}$	Real column hold-up, [$m^3 \cdot m^{-3}$]
H_p	Peak height of packing corrugation, [m]
h_{pe}	Height of a single packing module, [m]
H_R	Relative humidity, [water mass/dry air mass]
HTU_G	Height of Transfer Unit for the gas phase, [m]
HTU_{OG}	Height of Transfer Unit related to the gas phase, [m]

$I_{G,pe}$	Length of gas flow channel in a packing element, [m]
Ka_L	Kapitza number, [-]
K_d	Direct reaction rate constant, $[(kmol \cdot m^{-3})^{1-r} \cdot s^{-1}]$
K_{eq}	Le Châtelier's constant, $[(mol \cdot mol^{-1})^{p-r}$ or $(kmol \cdot m^{-3})^{p-r}]$
K_{eq}°	Chemical equilibrium reaction constant evaluated at T° = 298.15 K, $[(mol \cdot mol^{-1})^{p-r}$ or $(kmol \cdot m^{-3})^{p-r}]$
$k_{G,A}$	Gas-side mass transfer coefficient of component *A*, $[kmol \cdot m^{-3} \cdot atm^{-1} \cdot s^{-1}]$
K_H	Henry's constant, [atm]
K_H°	Henry constant evaluated at T° = 298.15 K, [atm]
K_{H_A}	Henry constant of the component *A*, $[atm \cdot m^3 \cdot kmol^{-1}]$
K_i	Inverse reaction rate constant, $[(kmol \cdot m^{-3})^{1-p} \cdot s^{-1}]$
$k_{L,A}$	Liquid-side mass transfer coefficient of component *A*, $[s^{-1}]$
$k_{o,d}$	Direct frequency factor, $[(kmol \cdot m^{-3})^{1-r} \cdot s^{-1}]$
$k_{o,i}$	Inverse frequency factor, $[(kmol \cdot m^{-3})^{1-p} \cdot s^{-1}]$
K_{OG}	Overall mass transfer coefficient related to the gas phase, $[mol \cdot m^{-2} \cdot s^{1}]$
$K_{OL}a_e(z)$	Overall mass transfer coefficient related to the liquid phase in a differential volume *Sdz* of the column, $[mol \cdot m^{-3} \cdot s^{-1}]$
K_p	Equilibrium constants expressed in terms of gas partial pressures when the reaction occurs in the gaseous phase, $[(atm)^{p-r}]$
k_x	Liquid-side mass transfer coefficient per unit surface, $[mol \cdot m^{-2} \cdot s^{-1}]$
$k_{x,j}$	Liquid -side mass transfer coefficients for a single *j-th* droplet, $[mol \cdot m^{-2} \cdot s^{-1}]$
$k_{x,SO_2}a_e$	Liquid-side mass transfer coefficient of SO_2 per unit volume, $[mol \cdot m^{-3} \cdot s^{-1}]$
$k_xa_e(z)$	Liquid-side mass transfer coefficients for all the droplets in a differential volume *Sdz* of the column, $[mol \cdot m^{-3} \cdot s^{-1}]$
k_y	Gas-side mass transfer coefficient per unit surface, $[mol \cdot m^{-2} \cdot s^{-1}]$
$k_{y,j}$	Gas -side mass transfer coefficients for a single *j-th* droplet, $[mol \cdot m^{-2} \cdot s^{-1}]$
$k_{y,lam}$	Gas-side mass transfer coefficient for laminar regime, $[mol \cdot m^{-2} \cdot s^{-1}]$
$k_{y,SO_2}a_e$	Gas-side mass transfer coefficient of SO_2 per unit volume, $[mol \cdot m^{-3} \cdot s^{-1}]$
$k_{y,turb}$	Gas-side mass transfer coefficient for turbulent regime, $[mol \cdot m^{-2} \cdot s^{-1}]$
$k_ya_e(z)$	Gas-side mass transfer coefficients for all the droplets in a differential volume *Sdz* of the column, $[mol \cdot m^{-3} \cdot s^{-1}]$
L	Volumetric liquid flow rate, $[L \cdot h^{-1}]$
L_{eq}	Equivalent length of the channel, [m]

L/G	Liquid-gas volumetric ratio or mass ratio, [$L \cdot m^{-3}$]or [$kg \cdot kg^{-1}$]
$L_m(z)$	Effective liquid flowing along the scrubber, [$mol \cdot s^{-1}$]
L_m/G_m	Liquid-gas molar ratio, [$L \cdot m^{-3}$]
L_{mass}/S	Mass liquid flow rate per unit of section in the column, [$kg \cdot m^{-2} \cdot s^{-1}$]
LVF	Liquid volume fraction, [$m^3 \cdot m^{-3}$]
M	Morton number, [-]
m	Reaction order of component *A*, [-]
M_L	Mass liquid flow rate, [$kg \cdot s^{-1}$]
m_p	Droplet mass, [kg]
M_S	Absorbing batch solution, [g]
MW_S	Molecular weight of the absorbing solution, [$g \cdot mol^{-1}$]
n	Reaction order of component *B*, [-]
N_A	Absorption rate of the component *A* from gas to liquid, [$kmol \cdot m^{-3} \cdot s^{-1}$]
N_c	Number of bends in a unit height of packing, [-]
N_n	Number of nozzles installed, [-]
NTU_{OG}	Number of Transfer Units related to the gas phase, [-]
p	Reaction order on the product-side, [-]
$P_{A,AV}$	Logarithmic mean between $P_{A,in}$ and $P_{A,out}$, [atm]
$P_{A,b}$	Partial pressures of gas component *A* in the bulk, [atm]
$P_{A,i}$	Partial pressures of gas component *A* at the interface, [atm]
$P_{A,in}$	Partial pressure of *A* in the gas stream before absorption, [atm]
$P_{A,out}$	Partial pressure of *A* in the gas stream after absorption, [atm]
pH	pH value of the aqueous solution, [-]
$Power_p$	Pump power, [kW]
P_p	Pumping pressure, [Pa]
P_s	Perimeter per unit cross-sectional area of packing, [$m \cdot m^{-2}$]
$Q_{G,m}$	Molar gas flow rate in the bubble column in feed-batch mode, [$mol \cdot s^{-1}$]
$Q_{G,v}$	Volumetric gas flow rate in the bubble column in feed-batch mode, [$L \cdot h^{-1}$]
r	Reaction order on the reagent-side, [-]
R	Universal gas constant ($8.31 \cdot 10^{-3}$ $kJ \cdot mol^{-1} \cdot K^{-1}$), [$kJ \cdot mol^{-1} \cdot K^{-1}$]
R^2	Determination coefficient, [-]
r_A	Reaction rate of a generic *A* species, [$kmol \cdot m^{-3} \cdot s^{-1}$]
Re	Reynolds number, [-]
Re_G	Reynolds gas number, [-]

S	Column section, [m^2]
SDM	Sauter mean diameter, [m]
S_G	Perimeter of the single packing channel crossed by the gas phase in wet condition, [m]
Sh_L	Sherwood liquid number, [-]
S_i	Length of the interfacial chord of packing, [m]
S_p	Slant height of a packing corrugation, [m]
SP	Stop distance, [m]
T	Absolute temperature, [K]
t^*	Saturation time in the bubble column tests, [s]
t_c	Contact time, [s]
T_G	Flue-gas temperature, [°C]
T_L	Liquid temperature, [°C]
U	Slip velocity, [$m \cdot s^{-1}$]
u_{Gs}	Superficial gas velocity, [$m \cdot s^{-1}$]
u_j	Nozzle injection velocity, [$m \cdot s^{-1}$]
U_j	Velocity of the sprayed droplets, [$m \cdot s^{-1}$]
u_{Ls}	Superficial gas and liquid velocity, [$m \cdot s^{-1}$]
v_e	Eddy velocity, [$m \cdot s^{-1}$]
V_p	Packing volume, [m^3]
We_L	Weber liquid number, [-]
x	Mole fraction of the solute in the liquid phase, [$mol \cdot mol^{-1}$]
x^*	Mole fraction of solute in the liquid phase that is in equilibrium with the solute in the gas phase, [$mol \cdot mol^{-1}$]
x_A	Mole fraction of gas solute *A* in liquid phase, [$mol \cdot mol^{-1}$]
$x_{A,i}$	Interfacial mole fraction of generic solute *A* in liquid phase, [$mol \cdot mol^{-1}$]
$x_{eq,A}$	Mole fraction of gas solute *A* in the liquid phase, [$mol \cdot mol^{-1}$]
x_i	Interfacial mole fraction of solute in liquid phase, [$mol \cdot mol^{-1}$]
$x_S(t)$	Amount of SO_2 captured per liquid mole unit over time, [$\mu mol \cdot mol^{-1}$]
x_S^*	Mole fraction of total sulphur dissolved in the liquid phase that is in equilibrium with the SO_2 in the gas phase, [$mol \cdot mol^{-1}$]
y	Gas mole fraction of generic gas solute along the column, [$mol \cdot mol^{-1}$]
y^*	Gas mole fraction of gas solute at equilibrium with liquid phase, [$mol \cdot mol^{-1}$]
y_1	Gas mole fraction at outlet of the column, [$mol \cdot mol^{-1}$]
y_2	Gas mole fraction at inlet of the column, [$mol \cdot mol^{-1}$]

y_A	Mole fraction of generic solute *A* in gas phase, [mol·mol^{-1}]
$y_{A,i}$	Interfacial mole fraction of generic solute *A* in gas phase, [-]
$y_{eq,A}$	Mole fraction of gas solute A at equilibrium with liquid phase, [-]
y_i	Interfacial mole fraction in gas phase, [-]
Z	Effective contact height of the column, [m]
Z_c	Total height of the column, [m]

Greek Symbols

$(\partial y/\partial x)_i$	Slope of the equilibrium function (F_{eq}) at the interfacial conditions (x_i,y_i) of each scrubber section, [-]
$(1+\varepsilon)$	Ratio of the maximum to minimum drop surface area, [-]
α	Exponential parameter for pressure drops, [-]
α	Adjustment parameter for liquid-side mass transfer, [-]
γ_a	Activity coefficient, [-]
δ_f	Liquid film thickness, [m]
δ_p	Packing thickness, [mm]
ΔD_d	Cumulative volumetric droplet size distribution, [m]
ΔG_r°	Standard Gibbs free energy of reaction, [kJ·mol^{-1}]
ΔH_s	Enthalpy of gas dissolution, [kJ·mol^{-1}]
ΔP	Pressure drops, [Pa]
ΔP_A	Driving force for absorption (difference between the partial pressure of A in the bulk and at the interface), [atm]
$\Delta P_d/Z$	Gas pressure drops per meter of packing in dry conditions, [Pa·m^{-1}]
ΔP_L	Liquid pressure for atomization, [Pa]
ΔP_{tot}	Total pressure drops, [mbar]
$\Delta P_w/Z$	Gas pressure drops per meter of packing in wet conditions, [Pa·m^{-1}]
ε_p	Void fraction of the packing, [-]
ζ_{DC}	Interaction coefficient relative to direction change losses, [-]
ζ_{GG}	Gas-gas interaction coefficient, [-]
ζ_{GL}	Overall gas-liquid interaction coefficient, [-]
η_{SO_2}	SO_2 removal efficiency, [-]
η_{NO_x}	NO_x removal efficiency, [-]
θ_c	Corrugation packing angle or inclination angle, [°]
θ_s	Spray angle, [°]

λ	Stripping factor, [-]
λ_{air}	Mean free path of air, [m]
λHTU_L	Height of Transfer Unit for the liquid phase, [m]
μ_G	Gas mass viscosity, [$kg \cdot m^{-1} \cdot s^{-1}$]
μ_L	Liquid mass viscosity, [$kg \cdot m^{-1} \cdot s^{-1}$]
ξ_{GL}	Gas-liquid friction factor, [-]
ΠC^p	Product of the concentrations of the chemical species of the products with a total reaction order *p* on the product-side given by the sum of the stoichiometric coefficients of the reaction products, [$(mol \cdot mol^{-1})^p$ or $(kmol \cdot m^{-3})^p$]
ΠC^r	Product of the concentrations of the chemical species of the products with a total reaction order *r* on the reagent-side given by the sum of the stoichiometric coefficients of the reaction products, [$(mol \cdot mol^{-1})^r$ or $(kmol \cdot m^{-3})^r$]
$\Pi \gamma_a^p$	Product of the activity coefficients of the chemical species of the products with a total reaction order *p* on the product side given by the sum of the stoichiometric coefficients of the reaction products, [-]
$\Pi \gamma_a^r$	Product of the activity coefficients of the chemical species of the products with a total reaction order *r* on the product-side given by the sum of the stoichiometric coefficients of the reaction products, [-]
σ_c	Liquid surface tension of packing material, [$N \cdot m^{-1}$]
σ_L	Liquid surface tension, [$N \cdot m^{-1}$]
$\Sigma \Delta G^\circ_{f,p}$	Sum of standard Gibbs free energy of formation for the products of the chemical reactions, [$kJ \cdot mol^{-1}$]
$\Sigma \Delta G^\circ_{f,r}$	Sum of standard Gibbs free energy of formation for the reagents of the chemical reactions, [$kJ \cdot mol^{-1}$]
τ_i	Shear stress at the gas-liquid interface, [$N \cdot m^{-2}$]
τ_{osc}	Oscillation time scale, [s]
τ_{wG}	Shear stress on channel wall relative to the gas phase flowing in the channel, [$N \cdot m^{-2}$]
Υ	Geometric parameters, [-]
υ_A	Stoichiometric coefficients of component *A* (gas absorbed), [-]
υ_B	Stoichiometric coefficients of component *B* (reagent), [-]
φ	Fraction of the triangular flow packing channels occupied by liquid, [-]
Φ	Physical and transport parameters of liquid and gas, [-]
$\phi(z)$	Droplet volume fraction for each axial position *z*, [-]
ϕ_f	Fugacity coefficient, [-]

Ω_p	Fraction of packing surface area occupied by holes, [-]
ρ_{air}	Mass air density, [kg·m^{-3}]
ρ_{bulk}	Bulk density of packing material, [kg·m^{-3}]
ρ_F	MGO fuel density, [kg·L^{-1}]
ρ_G	Gas mass density, [kg·m^{-3}]
ρ_L	Liquid mass density, [kg·m^{-3}]
ρ_x	Molar liquid density, [mol·m^{-3}]
ρ_y	Molar gas density, [mol·m^{-3}]

List of Figures

Figure IV.23. *Comparison between the concentrations of the heavy metals and organic species that varied more than 5 times respect to the Kattegat seawater in the Samples 1,2 and 3*

Figure IV.24. *Comparison between the concentrations of the heavy metals in the three wash water samples with the available regulations: EU-EQS, DA-EQS, STR-EQS, EPA-NRWQC, IT-DL and DE-DL*

Figure IV.25. *Comparison between the concentrations of the organics and PAHs in the three wash water samples with the available regulations: EU-EQS and EPA-NRWQC*

Figure IV.26. *Experimental and modelling SO_2 solubility (A-C) and experimental pH values of the saturated solution (D-F) as a function of total sulphur absorbed (x_S) obtained in three different scrubbing solutions, each at different initial pH. Figures A and D refer to the natural solution pH = 8.20 - 8.55; Figures B and E refers to solutions acidified at pH 6; Figures C and F refers to solutions acidified at pH 3*

Figure IV.27. *Modelling profile of the solution pH as a function of total absorbed sulphur for SW, SWC0.1 and SWC0.2, as calculated by ASPEN PLUS® in the Flash block. Figure A is related to non-altered initial pH of scrubbing solutions; Figure B is related to initial pH value of scrubbing solutions equal to 6; Figure C is related to initial pH value of scrubbing solutions equal to 3*

Figure IV.28. *Experimental results of SO_2 removal efficiency for a simulated flue-gas (32 $m^3 \cdot h^{-1}$) contained 500, 1000 and 2000 ppm_v of SO_2 at 1 atm and 60 °C, for different liquid-gas ratio (from 1.25 to 4.06 $L \cdot m^{-3}$) and using three different scrubbing solutions (SW, SWC0.1 and SWC0.2) at 25 °C with their natural initial pH and after acidification until 6 and 3. The removal efficiencies were a function of the ratio between the total dosage of the alkalinity in SW solution expressed as HCO_3^- moles and the SO_2 moles in the feed gas (A) or the ratio between the dosage of ClO_2^- moles in both SWC solutions and the SO_2 moles in the feed gas (B)*

Figure IV.29. *Experimental and modelling results of SO_2 removal efficiency (A) and wash water pH solutions (B) for a simulated flue-gas (32 $m^3 \cdot h^{-1}$) contained 500, 1000 and 2000 ppm_v of SO_2 at 1 atm and 60 °C, for different liquid-gas ratio (from 1.25 to 4.06 $L \cdot m^{-3}$) and using three different scrubbing solutions (SW, SWC0.1 and SWC0.2) at 25 °C with their natural initial pH and after acidification until 6 and 3*

Figure IV.30. *ASPEN PLUS® modelling profiles of SO_2 mole fraction in the gas stream from the bottom (0 m) to the top of the column (0.892 m) and bicarbonates, chlorites and pH trend in the liquid stream from the top to the bottom, for the two SWC solutions at non-altered pH (8.33 and 8.55). Simulation data for four case studies (A-D) were reported above*

Figure IV.31. *Experimental results of total NO_x removal efficiency (A) and wash water pH solutions (B) for a simulated flue-gas (32 $m^3 \cdot h^{-1}$) containing 1030 ppm_v of NO_x at 1 atm and 25 °C, for different liquid-gas ratio (from 1.25 to 4.06 $L \cdot m^{-3}$) and using five different scrubbing solutions at 25 °C: seawater at pH 8.2 (SW); four seawater solutions containing from 0.25 to 1% w/w of $NaClO_2$ at pH from 8.56 to 9.4*

Figure IV.32. *Experimental results of total NO_x removal efficiency at 40 °C (A) and 60 °C (B) for a simulated flue-gas (32 $m^3 \cdot h^{-1}$) containing 1030 ppm_v of NO_x at 1 atm, for different liquid-gas ratio*

(from 1.25 to 4.06 L·m^{-3}) and using five different scrubbing solutions at 25 °C: seawater at pH 8.2 (SW); four seawater solutions containing from 0.25 to 1% w/w of $NaClO_2$ at pH from 8.56 to 9.4

Figure IV.33. *Experimental results of NO_x removal efficiency for a simulated flue-gas (32 m^3·h^{-1}) containing 1030 ppm_v of NO_x at 1 atm, for different liquid-gas ratio (from 1.25 to 4.06 L·m^{-3}) and using four different scrubbing solutions (SWC0.25, SCWC0.5,SWC0.75 and SWC1.0) at 25 °C with their non-altered initial pH. The removal efficiencies were a function of the ratio between the dosage of ClO_2^- moles in the SWC solutions and the NO_x moles in the feed gas. The results were shown parametrically with the temperature of gas fed (25, 40 and 60 °C)*

Figure IV.34. *Experimental results of total NO_x removal efficiency (A) and wash water pH solutions (B) for a simulated flue-gas (32 m^3·h^{-1}) containing 1030 ppm_v of NO_x at 1 atm, for different liquid-gas ratio (from 1.25 to 4.06 L·m^{-3}) and using the seawater solution with $NaClO_2$ at 1% w/w (SWC1.0) at 25 °C and different initial pH: 9.4, 6 and 3*

Figure IV.35. *Experimental results of total NO_x removal efficiency at 40 °C (A) and 60 °C (B) for a simulated flue-gas (32 m^3·h^{-1}) containing 1030 ppm_v of NO_x at 1 atm, for different liquid-gas ratio (from 1.25 to 4.06 L·m^{-3}) and using the seawater solution with $NaClO_2$ at 1% w/w (SWC1.0) at 25°C and different initial pH: 9.4, 6 and 3*

Figure IV.36. *Experimental results of NO_x removal efficiency for a simulated flue-gas (32 m^3·h^{-1}) containing 1030 ppm_v of NO_x at 1 atm and 60 °C, for different liquid-gas ratio (from 1.25 to 4.06 L·m^{-3}) and using seawater solution with 1% w/w of $NaClO_2$ (SWC1.0) at 25 °C with their natural initial pH and after acidification until 6 and 3. The removal efficiencies were a function of the ratio between the dosage of ClO_2^- moles in the SWC1.0 solution and the NO_x moles in the feed gas. The results were shown parametrically with the initial pH of SWC1.0 solution (9.4, 6 and 3)*

Figure IV.37. *Experimental results of SO_2 removal efficiency (A) and wash water pH solutions (B) in a simulated flue-gas (32 m^3·h^{-1}) containing SO_2 = 500 ppm_v and NO_x = 1030 ppm_v at 1 atm and 25 °C, for different liquid-gas ratio (from 1.25 to 4.06 L·m^{-3}) and using five different scrubbing solutions at 25 °C: seawater at pH 8.2 (SW); four seawater solutions containing from 0.25 to 1% w/w of $NaClO_2$ at pH from 8.56 to 9.4*

Figure IV.38. *Experimental results of total NO_x removal in a simulated flue-gas (32 m^3·h^{-1}) containing only 1030 ppm_v of NO_x (A) and total NO_x removal in a simulated flue-gas (32 m^3·h^{-1}) containing SO_2 = 500 ppm_v and NO_x = 1030 ppm_v (B). The experiments were performed at 1 atm and 25 °C, for different liquid-gas ratio (from 1.25 to 4.06 L·m^{-3}) and using five different scrubbing solutions at 25 °C: seawater at pH 8.2 (SW); four seawater solutions containing from 0.25 to 1% w/w of $NaClO_2$ at pH from 8.56 to 9.4*

Figure IV.39. *Experimental results of total NO_x removal in a simultaneous absorption at 40 °C (A) and total NO_x removal in in a simultaneous absorption at 60 °C (B). The experiments were performed with a simulated flue-gas (32 m^3/h) containing SO_2 = 500 ppm_v and NO_x = 1030 ppm_v at 1 atm, for different liquid-gas ratio (from 1.25 to 4.06 L·m^{-3}) and using five different scrubbing solutions at 25 °C: seawater at pH 8.2 (SW); four seawater solutions containing from 0.25 to 1% w/w of $NaClO_2$ at pH from 8.56 to 9.4*

Figure IV.40. *Experimental results of total NO_x removal efficiency (A) and wash water pH solutions*

(B) in a simulated flue-gas (32 $m^3 \cdot h^{-1}$) containing SO_2 = 500 ppm_v and NO_x = 1030 ppm_v at 1 atm and 25 °C, for different liquid-gas ratio (from 1.25 to 4.06 $L \cdot m^{-3}$) and using seawater solution with $NaClO_2$ at 1% w/w (SWC1.0) at 25 °C and different initial pH: 9.4, 6 and 3

Figure IV.41. *Experimental results of total NO_x removal in a simultaneous absorption at 40 °C (A) and total NO_x removal in in a simultaneous absorption at 60 °C (B). The experiments were performed with a simulated flue-gas (32 m^3/h) containing SO_2 = 500 ppm_v and NO_x = 1030 ppm_v 1 atm, for different liquid-gas ratio (from 1.25 to 4.06 $L \cdot m^{-3}$) and using seawater solution with $NaClO_2$ at 1% w/w (SWC1.0) at 25 °C and different initial pH: 9.4, 6 and 3*

List of Tables

I. INTRODUCTION

The removal of sulphur dioxide from combustion flue gases is a major historical problem of Chemical Engineering since its early beginning [1]–[3]. Early concepts of Flue Gas Desulphurization (FGD) process appear to have germinated in 1850 in England, and the application to large-scale power plants can be dated in the 1920s in England too ([1], [3]–[5]**)**. The first FGD plant entered in operation at the Battersea Station in London in 1931 (**Figure I.1**). In 1935, a second one went into service at the Swansea Power Station, while a third one was installed in 1938 at the Fulham Power Station. All the three installations were abandoned during the World War II.

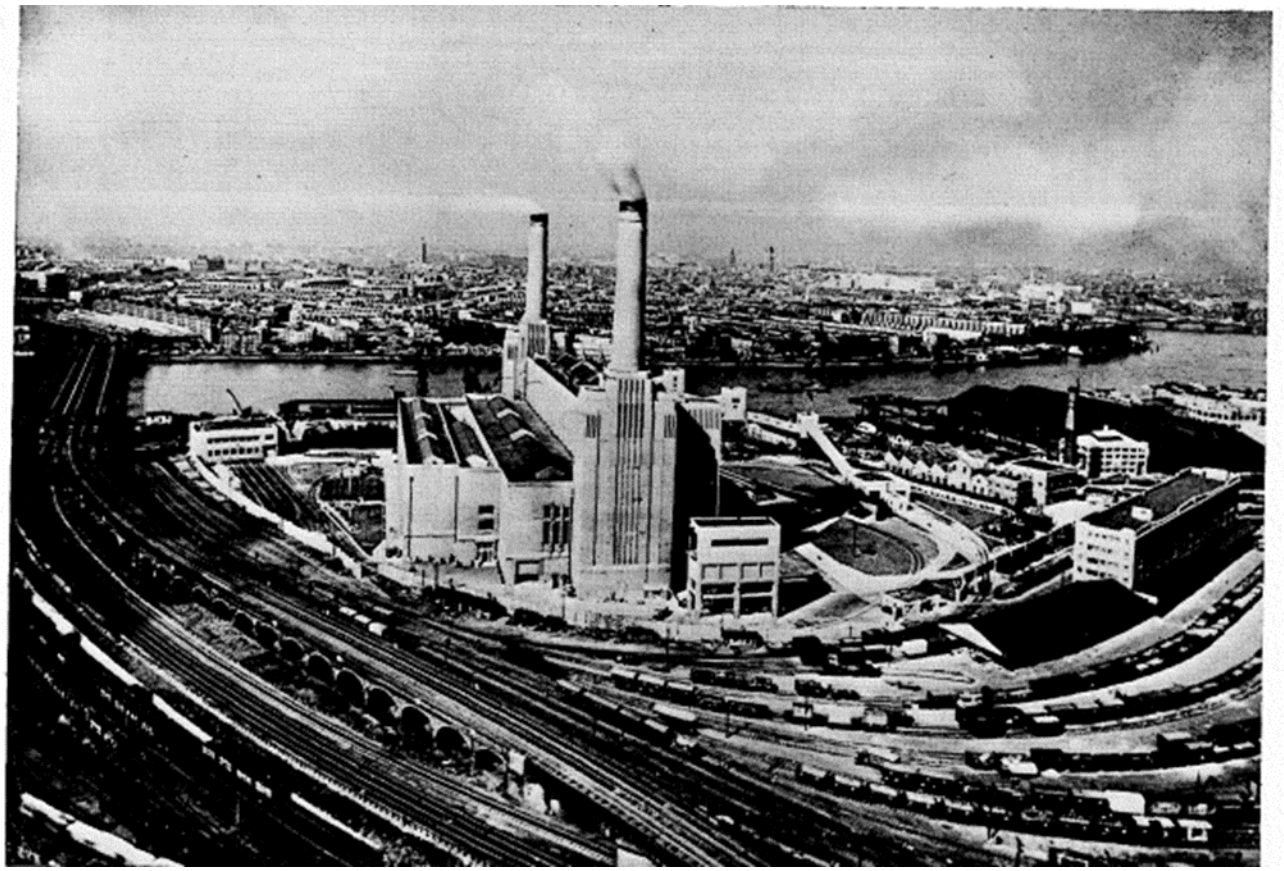

Figure I.1. *Battersea Power Station, mid 1930's* [1]. *(Photo courtesy of Central Electricity Generating Board)*

Sulphur is a common contaminant of coal and heavy oils; it is present in some wastes and in biomasses and is abundant in minerals. Therefore, its emissions in the atmosphere derive mostly from the use of coal in power plants, heavy oils in maritime shipping, biomasses in domestic and commercial heating and in smelting processes (**Figure I.2**). Mostly, sulphur is emitted in the atmosphere as sulphur dioxide, sulphur trioxide, sulphuric acid and sulphate solid particles.

Figure I.2 shows that most of the energy consumed worldwide still comes from the combustion of coal and oil.

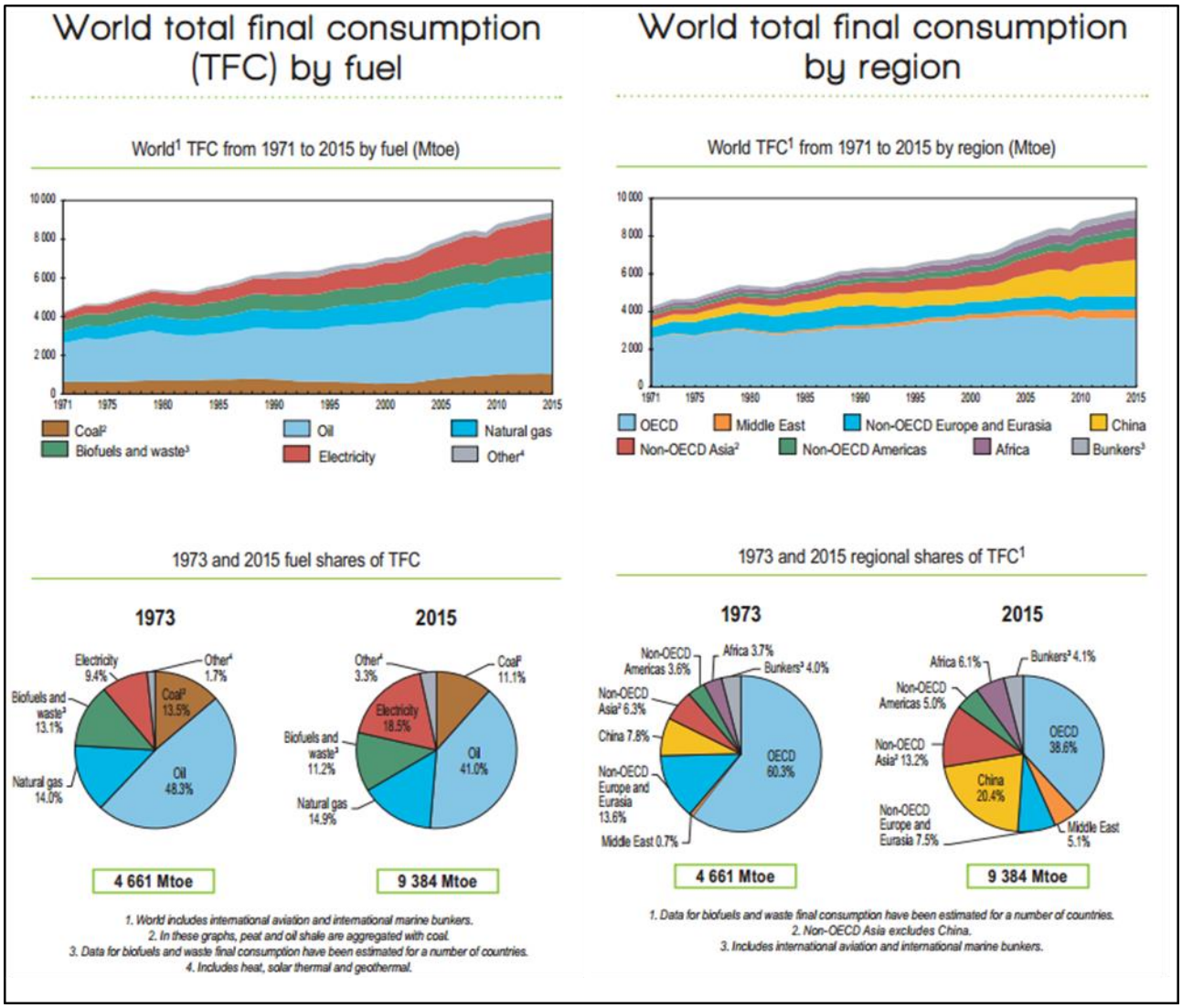

Figure I.2. *Total fuel consumption by energy sources and user regions from 1973 to 2015: IEA analysis based on IIASA data*

The specific consumption of these two energy sources is shown in **Figure I.3**; data were retrieved from a recent study of the International Energy Agency (IEA).

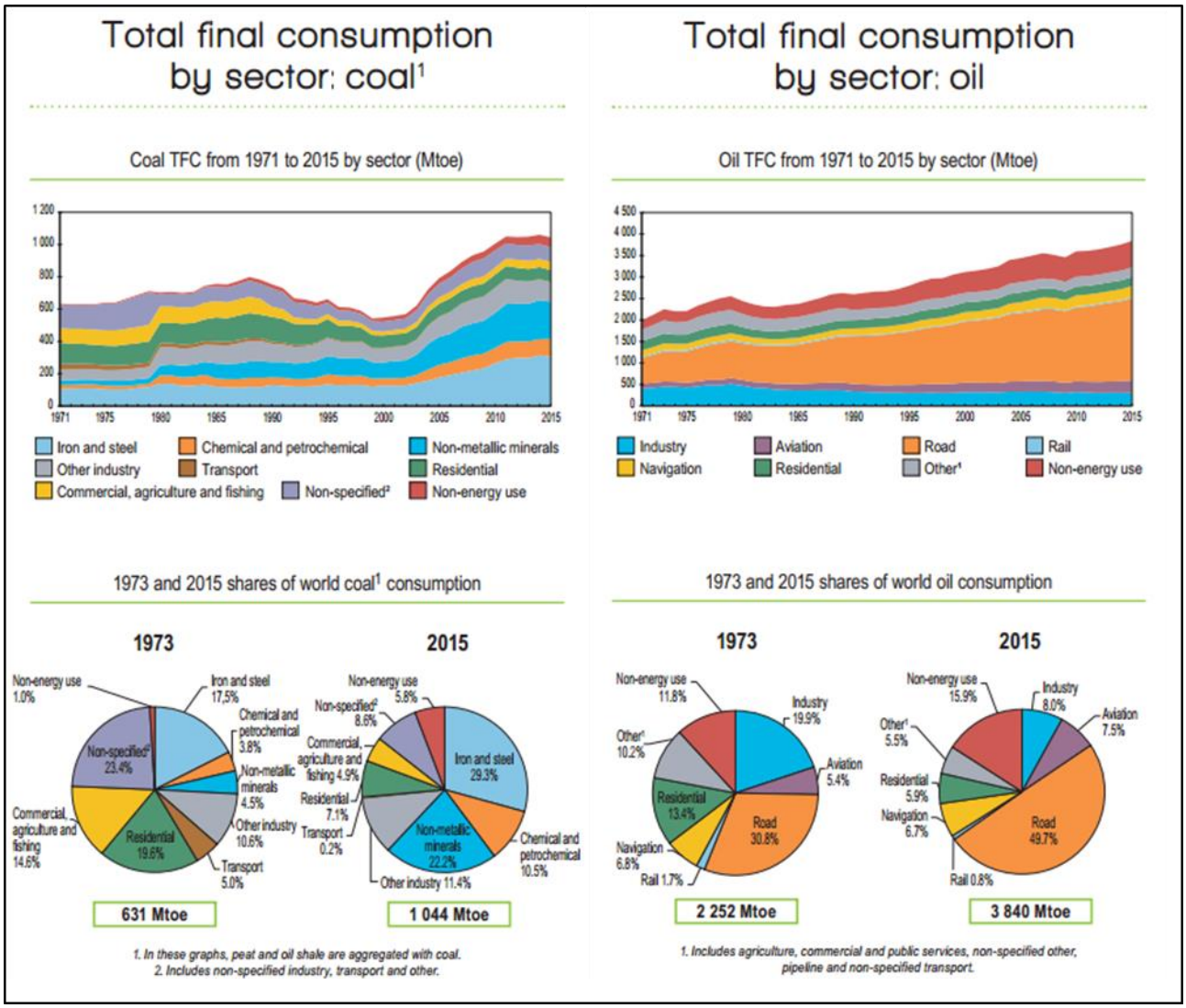

Figure I.3. *Total fuel consumption of coal and oil from 1973 to 2015 with the relevant fields of application: IEA analysis based on IIASA data*

The **Figure I.4** shows the geographical distribution by fuel associated to the energy production activities in the states of the European Union.

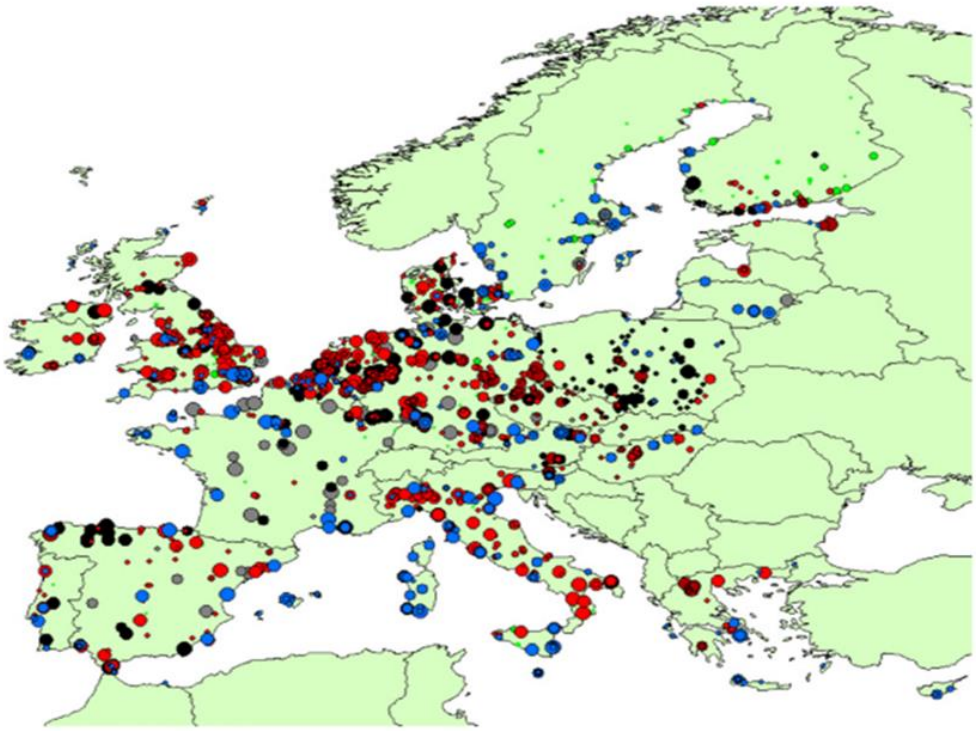

Figure I.4. *Geographical distribution by fuel of operating thermal plants in EU-25. Red color denotes gas-fueled plants, black color denotes coal, brown color denotes lignite, blue denotes oil, yellow denotes nuclear, green denotes biomass/waste plants* [6]

In the most developed and rich countries, the first regulations on sulphur emissions date back to the '70s of the last century and the technologies for gas purification are available since the beginning of the same century. **Figure I.5** shows the trend of global sulphur dioxide emissions from 1850s to 2000s, in particular for primary source and end-use sector.

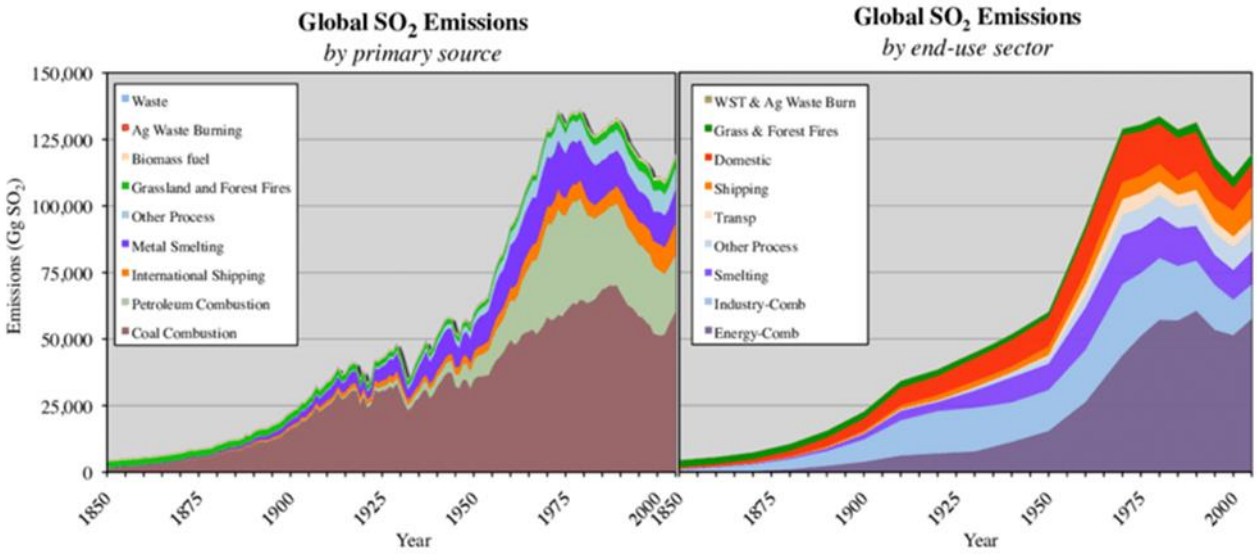

Figure I.5. *Global SO_2 emission from 1850 to 2000 by primary source and by end-use sector* [7]

Figure I.5 shows that global emissions of SO_2 increased rapidly from the early 1900s associated with the development of industrial activities and then decreased around the 1980s after the introduction of stricter regulations for environmental and human health protection in force since 1970s, which significantly contributed to the reduction of the emissions, in spite of the increase in energy consumption.

Nevertheless, the road to a total desulphurization has been completed only in a limited number of processes. Nowadays, the sulphur fraction in distillates fuels has been reduced to ppm and the removal of SO_2 at the incineration plants of municipal solid waste is an essential step always present in the flue-gas depurative train, which assures very low SO_2 outlet concentration. On the contrary, the emissions from coal and heavy fuel combustion in power plants, transport, smelting and industrial productions are still high (see **Figure I.6**).

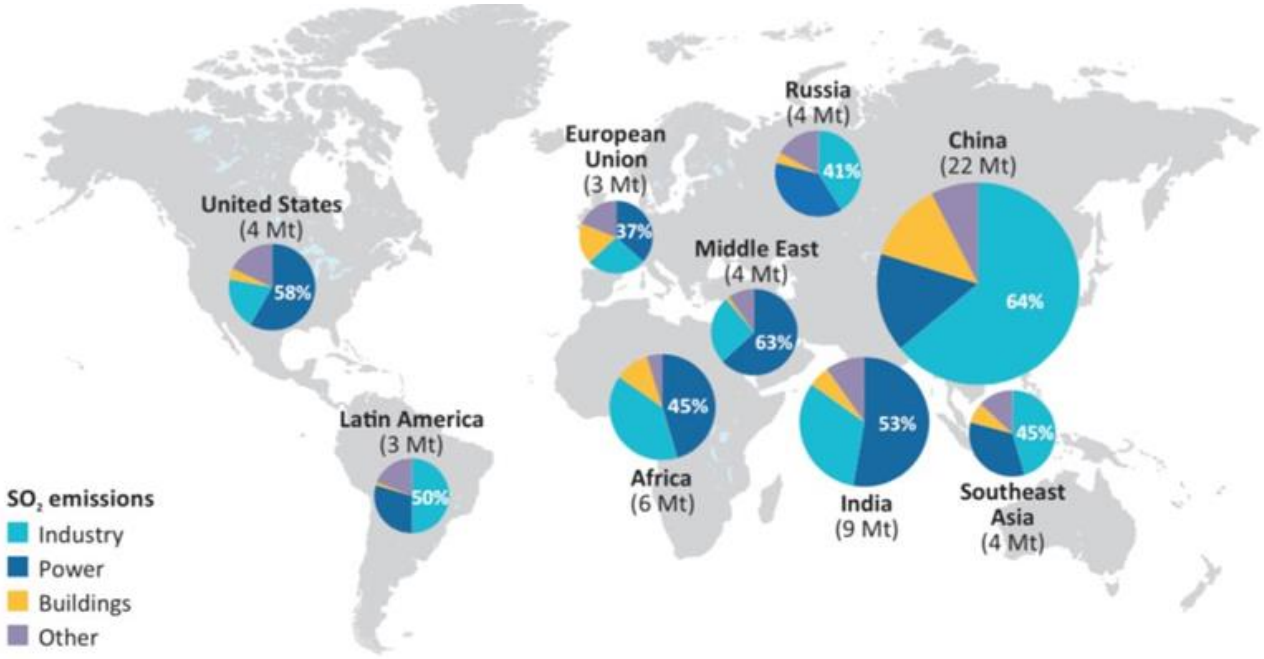

Figure I.6. *Energy-related SO_2 emissions by region and sector in 2015. Source: IEA analysis based on IIASA data*

Table I.1 shows the sulphur-content in coal by coalfields of the major producing countries, while the sulphur-content in the main fuel oils used for combustion processes are reported in **Table I.2**.

Table I.1. *Sulphur-content in coal by coalfields of the major producing countries, used for combustion processes* [8]

Coal	**sulphur-content % w/w**
Australia, Queensland basin	0.2 - 1.3 (air dried)
Canada, Western	0.2 - 1.2
China, Shanxi	0.4 - 6.0

Columbia, Cerrejon	0.4 - 0.9 (air dried)
Germany, Rurh	0.7 - 0.8
India, Raniganj and Jharia	0.5 - 0.8 (air dried)
Indonesia, Kalimantan	0.1 - 0.9
Poland, Upper Silesian basin	0.8 - 1.8
Russia, Kuznetsk basin	0.3 - 0.8
South Africa, Witbank and Highveld	0.3 - 2.4 (air dried)
UK, East Pennine	0.8 - 2.4
USA, Illinois basin	0.2 - 7.7

Table I.2. *Sulphur-content in the main fuel oils used for combustion processes* [9], [10]

Fuel Oils	**Sulphur-content % w/w**
HFO (Heavy Fuel Oil) - A bunker fuel, pure or nearly pure residual oil, roughly equivalent to No.6 fuel oil	> 3.5%
IFO (Intermediate Fuel Oil) - A blend of gasoil and heavy fuel oil, with less gasoil than marine Diesel oil	< 3.5%
LS 380 (Low-Sulphur fuel) - Intermediate fuel oil with a maximum viscosity of 380 cP	< 1.0%
LS 180 (Low-Sulphur fuel) - Intermediate fuel oil with a maximum viscosity of 180 cP	< 1.0%

The directive 2010/75/UE enacted by the European Parliament and the Council for large power generation plants, which establishes the best available techniques (BAT) for emissions control (integrated pollution prevention and control) is in force since August 2017. **Table I.3** shows the regulatory limits for SO_2 emissions for new or existing installations in which coal, lignite and solid or liquid fuels are burnt.

Table I.3. *Maximum SO_2 emission levels indicated by the Directive 2010/75/UE valid for new or existing installations that use coal, lignite and solid or liquid fuels*

Nominal Power [MWth]	**SO_2 emission limits [mg·Nm^{-3}] by coal or lignite**		**SO_2 emission limits [mg·Nm^{-3}] by solid or liquid fuels**	
	New installation	*Existing installation*	*New installation*	*Existing installation*
50 - 100	150 - 200	170 - 400	200	350
100 - 300	80 - 150	135 - 220	100	200
> 300	20 - 75	50 - 220	75	150

From January 2021, the new UE guidelines (2010/75/UE) will significantly reduce the maximum allowed SO_2 emissions for large coal-fired power plants, which will be set from an average value of 200 to 150 mg·m^{-3} [11], [12]. Similarly, for USA and China, which are the major countries that use power generation plants, the SO_2 emission limits are 136 and 35 mg·m^{-3}, respectively [11]. For other

emerging countries, the new emission limits related to coal-fired power generation stations that burn coal are: Australia: 200 mg·Nm^{-3}; India: 100 mg·Nm^{-3}; Japan: 200 mg·Nm^{-3}; South Africa: 500 mg·Nm^{-3}; Indonesia: 750 mg·Nm^{-3} [11], [13].

In order to further reduce sulphur emissions from its territory, the European Union ratified the 2016/2284/UE Regulation, which defines new and more severe reduction targets for SO_2 emissions in its countries. This new directive amends the directive 2003/35/UE and repeals the 2001/81/UE. It forces to reduce the anthropogenic atmospheric emissions of SO_2 for the Member States, progressively until 2029 and for the subsequent years. **Figure I.7** shows the target of SO_2 emission reductions (as percentages) for EU countries in the period between 2020 - 2029 and starting from 2030.

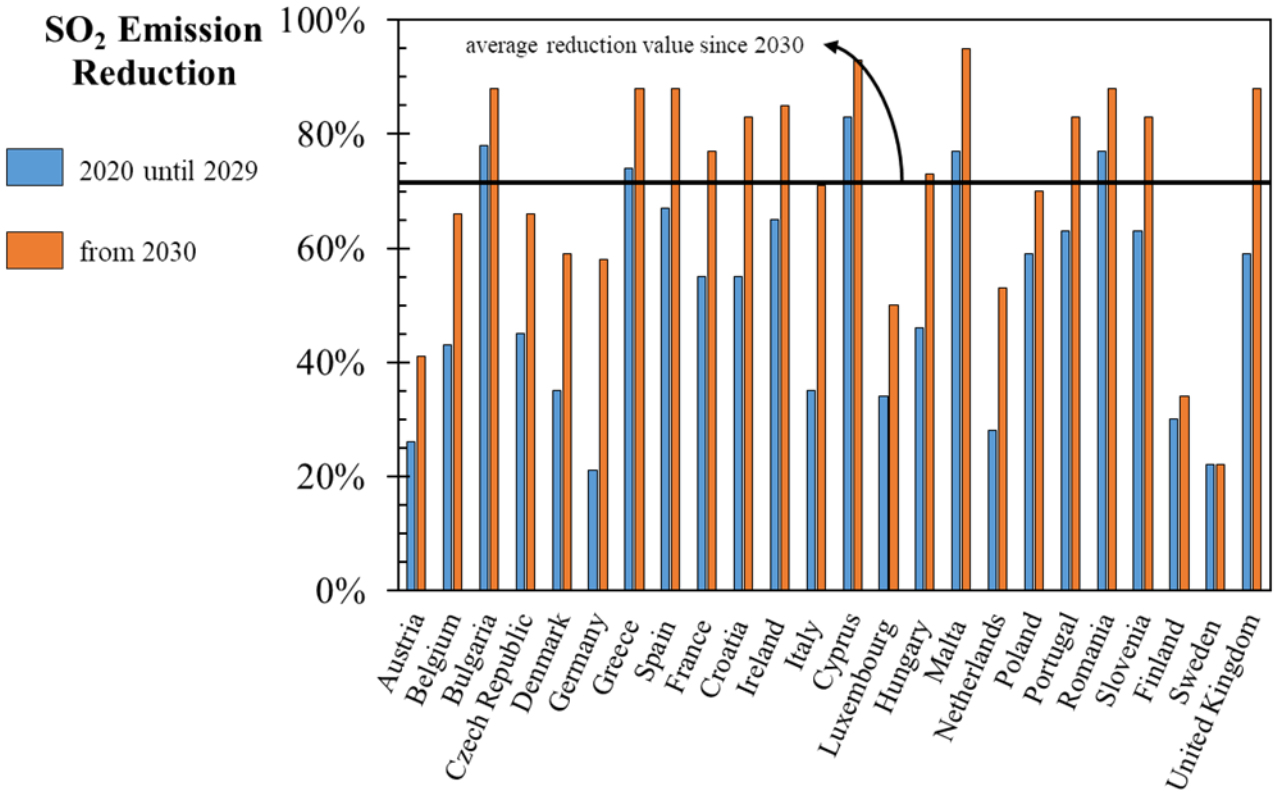

Figure I.7. *SO_2 emission reductions until 2029 and starting from 2030 as established by new directive 2016/2284/UE*

Most of the European countries are forced to reduce by more than 70% of their actual emissions starting from 2030.

The major routes to reduce sulphur emissions are fuel purification and flue-gas after-treatments, named Flue Gas Desulphurization (FGD) processes ([1], [3], [4], [14]–[16]). Currently, dry, wet and gas-gas technologies are available ([1], [3]–[5]), with variable market shares in the different countries of the globe.

After their first industrial applications in 1920s, large-scale FGD units did not re-appear in commercial operation until the 1970s, and most of the active plants operated in the United States and Japan [1], [4]. As of June 1973, there were 42 FGD units in operation, ranging in size from 5 to 250 megawatts (MW): 36 in Japan and 6 in the United States.

Until about the 2000s, there were 678 FGD units operating worldwide (in 27 countries), corresponding to a total energy production of about 229 GW. About 45% of that FGD capacity was allocated in the United States, 24% in Germany, 11% in Japan and 20% in the other countries. Approximately 79% of the units, representing about 199 GW of capacity, were using lime or limestone wet scrubbing, while about 18% (or 25 GW) utilized spray-dry scrubbers or dry sorbent injection systems ([1], [4], [5]**)**.

Dry processes were developed by Donath in 1915 for SO_2 removal from furnace gases [1]. In this process, dry lime is injected directly into the bed of the furnace; SO_2 adsorption from the gas takes place on the surface of the lime, where SO_2 subsequently reacts. This process was implemented on a large scale in the 1960s but it was not very successful due to low capture efficiencies and high sorbent costs [1], [5].

Scrubbers based on wet processes have actually the highest removal efficiency and are those commonly preferred to treat gases with high sulphur contents [1], [5]. **Figure I.8** show the typical configurations adopted for the wet and dry scrubbers:

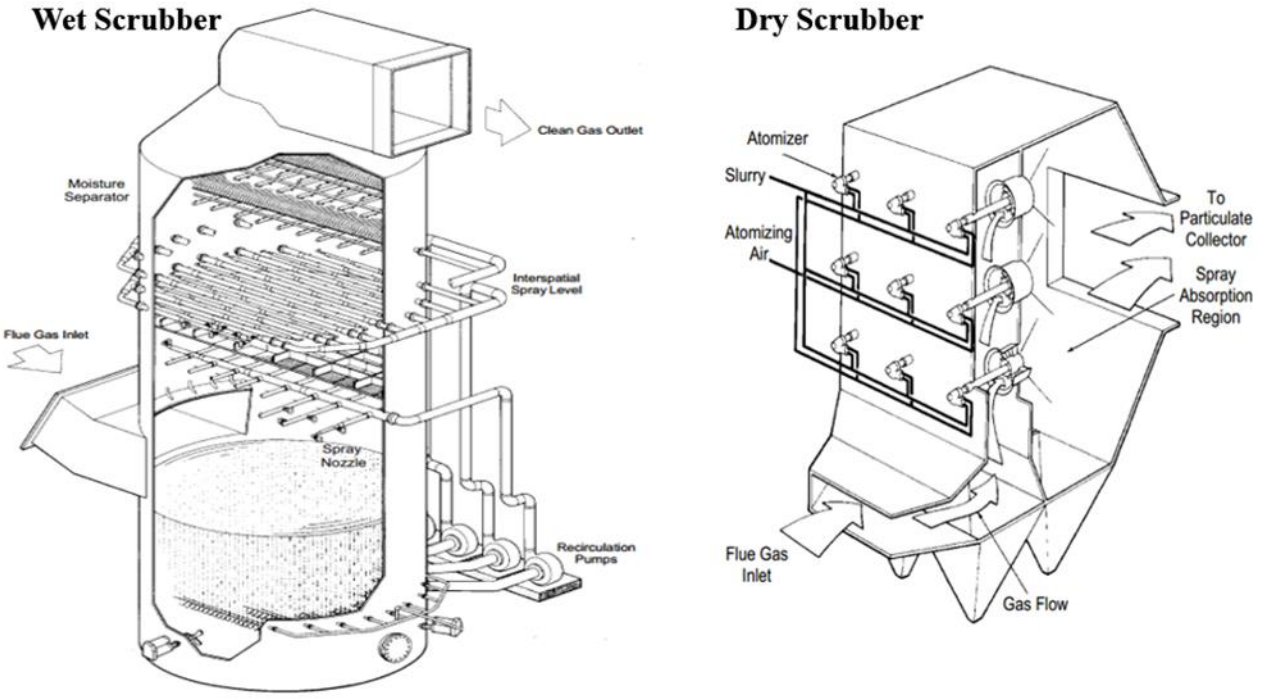

Figure I.8. *Typical constructive schemes for wet and dry scrubbers* [4]

Water-based FGD processes derives from the natural capacity of freshwater to remove acid gases thanks to its alkalinity. In fact, the solubility of SO_2 in pure, distilled water depends on the physical gas-liquid equilibrium between gaseous and water dissolved SO_2, *i.e.* H_2SO_3 and its chemical dissolution species. One of the first studies was performed by **Johnstone and Leppla** [17], which examined the solubility of SO_2 in water at various partial pressures and temperatures. They also studied the solubility of SO_2 in dilute sulfuric acid solutions, simulating the influence of sulfuric acid build-up in recycled water scrubbers on the SO_2 absorption efficiency.

During SO_2 absorption, water progressively acidifies as a slight dissociation of H_2SO_3 in HSO_3^- and SO_3^{2-} occurs. The Henry-law constant for SO_2 dissolution in distilled water at 20 °C is: 1.46 $mol \cdot kg^{-1} \cdot bar^{-1}$.

The carbonate/bicarbonate content of natural waters emphasizes the chemical absorption of SO_2, through the following reactions:

$$SO_{2(g)} + H_2O \rightleftharpoons H_2SO_{3(aq)} \quad (1)$$

$$H_2SO_{3(aq)} + CO_3^{2-} \rightleftharpoons HSO_3^- + HCO_3^- \quad (2)$$

$$HSO_3^- + CO_3^{2-} \rightleftharpoons SO_3^{2-} + HCO_3^- \quad (3)$$

$$H_2SO_{3(aq)} + HCO_3^- \rightleftharpoons HSO_3^- + H_2CO_{3(aq)} \quad (4)$$

$$HSO_3^- + HCO_3^- \rightleftharpoons SO_3^{2-} + H_2CO_{3(aq)} \quad (5)$$

$$H_2CO_{3(aq)} \rightleftharpoons CO_{2(g)} + H_2O \quad (6)$$

This larger dissociation of H_2SO_3 occurring under alkaline conditions gives rise to a significant improvement of SO_2 solubility in water: SO_2 dissolves integrally in water as long as there are enough HCO_3^- and CO_3^{2-} ions to complete the reactions. A molar ratio of 1:2 between SO_2 and alkaline species, intended as carbonates or bicarbonates, is necessary for SO_2 to be absorbed before H_2SO_3 is formed and the Henry law correlation is established.

Due to the high variability of natural water alkalinity [18] and to the significant amount of required freshwater, supplementary chemicals are commonly added to water to reduce its consumption. This also allows reducing the absorbing liquid flow rate and keeping the hydrodynamics of absorption column within optimal operating ranges. The class of chemicals that are commonly adopted includes the following compounds: sodium hydroxide, ammonia, lime, limestone, magnesium oxide, sodium carbonate/bicarbonate or sodium sulphite **(**[1], [5], [19]**)**. The main reactions occurring in the presence of an alkali can be represented by **Eq. (1)** and the following **Eqs. (7)-(8)**:

$$H_2SO_{3(aq)} + OH^- \rightleftharpoons HSO_3^- + H_2O \quad (7)$$

$$HSO_3^- + OH^- \rightleftharpoons SO_3^{2-} + H_2O \quad (8)$$

In coastal areas, seawater can be used as FGD absorption liquid for land-based plants. Seawater is largely adopted also in maritime scrubbers to comply with the regulations imposed in open water and coastal areas on the equivalent sulphur content in the fuel (IMO, MARPOL Annex VI - Regulation 14, [20], [21]). Since 1st January 2015, the International Maritime Organization (IMO) established that the equivalent sulphur emissions must be lower than 0.1% in weight in some coastal regions named "Sulphur Emission Control Areas" (SECAs), while a value lower than 3.5% w/w in open seas (GLOBAL areas) was prescribed until 31st December 2019. The 0.1% sulphur limit also applies for all the European ports. From 1st January 2020, sulphur emissions for open seas must be equivalent to a sulphur content in fuel lower than 0.5% in weight worldwide. **Figure I.9** shows the IMO Marpol limitations for SO_2 emissions in the SECA areas (including European ports), for the oceangoing vessel, in China and in California, also reporting information about the restrictions existing on the use of marine scrubbers.

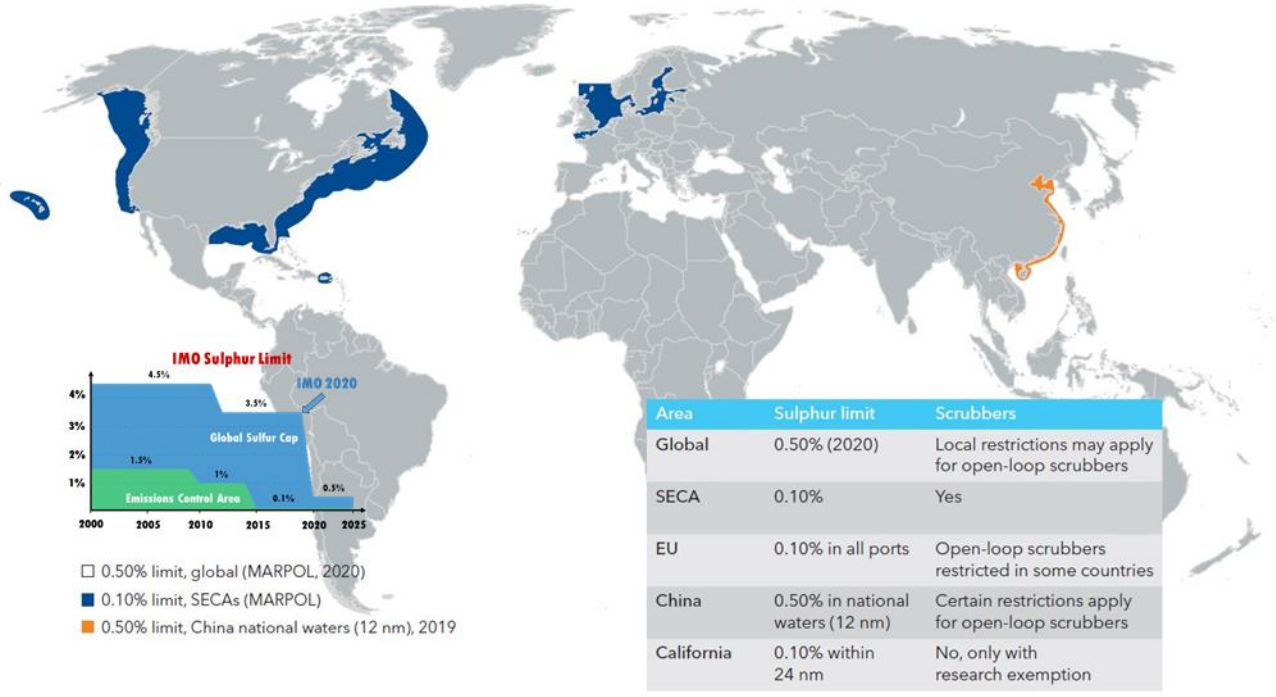

Area	Sulphur limit	Scrubbers
Global	0.50% (2020)	Local restrictions may apply for open-loop scrubbers
SECA	0.10%	Yes
EU	0.10% in all ports	Open-loop scrubbers restricted in some countries
China	0.50% in national waters (12 nm)	Certain restrictions apply for open-loop scrubbers
California	0.10% within 24 nm	No, only with research exemption

Figure I.9. *Summary scheme of the SO_2 emission limits (IMO MARPOL VI - Regulation 14) for maritime transport*

While current SECAs include USA and Canada coasts, Baltic and North Sea, the proposed potential future SECAs include Mediterranean and Norway Sea, Australian and China coasts (**Figure I.10**).

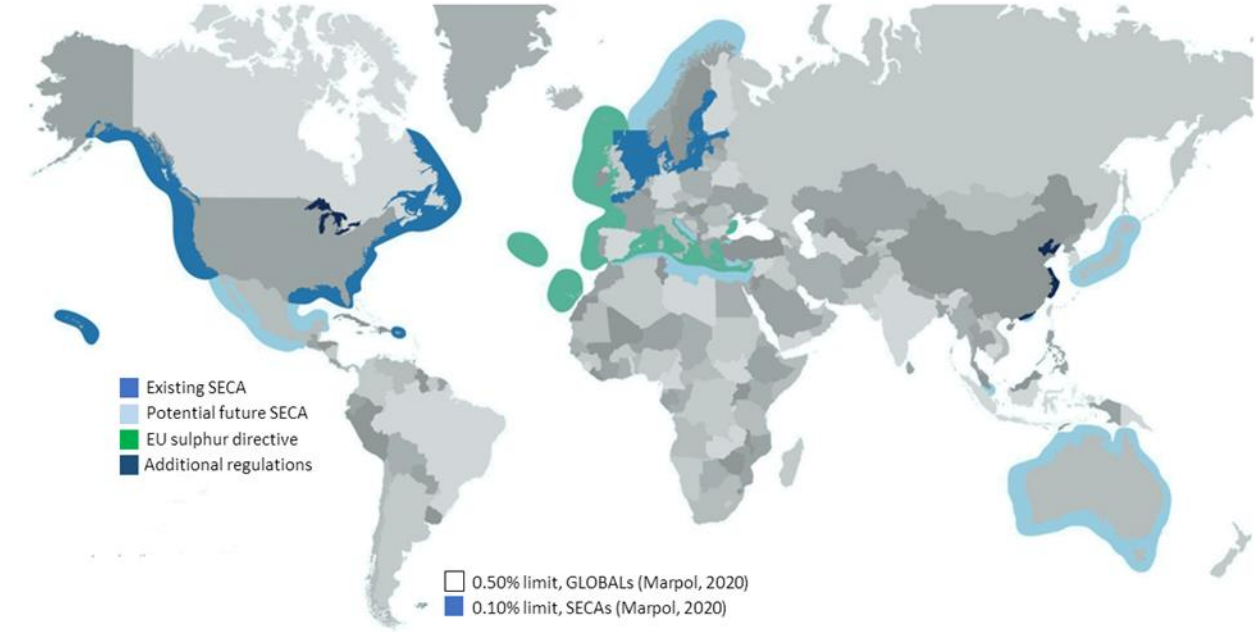

Figure I.10. *Existing and potential future SECAs*

Table I.4 shows the main heavy oils used for maritime transport and their sulphur-content.

Table I.4. *Sulphur-content in the main fuel oils used for maritime transport* [9], [10]

Fuel Oils	**Sulphur-content % w/w**
HFO (Heavy Fuel Oil) - A bunker fuel, pure or nearly pure residual oil, roughly equivalent to No.6 fuel oil	> 3.5%
FFO (Furnace Fuel Oil) - A bunker fuel, pure or nearly pure residual oil, roughly equivalent to No.5 or 6 fuel oil	> 3.5%
NSFO (Navy Special Fuel Oil) - A bunker fuel, pure or nearly pure residual oil, roughly equivalent to No.5 or 6 fuel oil	> 3.5%
IFO (Intermediate Fuel Oil) - A blend of gasoil and heavy fuel oil, with less gasoil than marine Diesel oil	< 3.5%
MDO (Marine Diesel Oil) - A blend of heavy gasoil that may contain very small amounts of black refinery feed stocks, but has a low viscosity up to 12 cP so it need not be heated for use in internal combustion engines	from 1 to 3.5%
LS 380 (Low-Sulphur fuel) - Intermediate fuel oil with a maximum viscosity of 380 cP	< 1.0%
LS 180 (Low-Sulphur fuel) - Intermediate fuel oil with a maximum viscosity of 180 cP	< 1.0%
MGO (Marine Gas Oil) - Roughly equivalent to No. 2 fuel oil, made from distillate only	< 1.0%
LSMGO (Low-Sulphur Marine Gas Oil) - The fuel is to be used in EU Ports and Anchorages	< 0.1%
ULSMGO (Ultra-Low-Sulphur Marine Gas Oil) - Referred to as Ultra-Low-Sulphur Diesel (0.0015% S) in the US and Auto Gas Oil (0.001% S) in the EU. Maximum sulphur allowable in US territories and territorial waters (inland, marine, and automotive) and in the EU for inland use	< 0.001%

The Heavy Fuel Oil (HFO) is the traditional marine fuel, with high sulphur content, that can be used only outside SECA areas. After 2020, the HFO was replaced by a ultra-low sulphur fuel oil (ULSFO),

which contains 0.5% sulphur, and must be adopted outside SECAs [22]. For inside SECAs navigation, the MGO fuel, which is more expensive but cleaner (*i.e.* with less than 0.1% sulphur) must be used ([20], [21], [23]–[26]**)**. Fuels price constantly fluctuate due to market forces and the variability of the cost of crude oil [22]. About 80% of the total bunker fuel relates to heavy fuel oil. Heavy fuel oil (HFO) mainly consists of residual refinery streams from the distillation or cracking units in the refineries [26]. Intermediate fuel oil (IFO) 380 is a mix of 98% of residual oil and 2% of distillate oil, while IFO 180 is a mix of 88% of residual oil and 12% of distillate oil [26]. Other bunker fuels different than the HFO are the marine Diesel oil (MDO), which mainly consists of distillate oil, and the marine gas oil (MGO), which is a pure distillate oil and has the lowest sulphur content [26]. **Notteboom** [26] reveals that the price difference between IFO 380 and MGO (0.1% sulphur) fluctuated strongly in time (30% to 250% price difference in the period 1990 - 2009). The price difference between low sulphur fuel (LS 380) and MDO fluctuated between 40% and 190% (in the period 1990 - 2009), with a long-term average of 87%. In other words, the specified MDO is on average 87% more expensive than LS 380. Overall, the cost of marine distillate fuels is about twice what residual fuels costs due to increasing demand and the cost of the desulphurization process.

In general, two approaches are proposed by **Gu and Wallace** [22] to save on cleaner fuel consumption: the SECA evasion approach ,which consists in adopting a longer navigation in order to get out of the control of the SECAs or the fuel-switching approach, which requires only slight modifications on the ship, and thus very limited initial investments, but the price of MGO to be adopted is much higher than that of HFO, and of its future replacement ULSFO, which leads to a dramatic increase in the operational costs of a vessel. However, the low sulphur fuel, besides being more expensive, are usually not compatible with the lubrication system used with heavy fuel oil. Recently, fuel blends of marine gas oil and heavy fuel oil that comply with the 0.1% sulphur content, but avoid the need of new lubrication systems, are available on the market as so-called SECA fuels.

An alternative approach to match the SO_x emission regulations is the use of Exhaust Gas Cleaning System (EGCS). To this aim, FGD marine scrubbers can be installed onboard in order to clean the exhausted gases from SO_x, and therefore, to allow to keep using the cheap HFO inside and outside SECAs. In the last years, a significant investment in the use of marine scrubbers in the European SECA has been made, as an economically attractive alternative to the use of expensive, low-sulphur fuel [27]. It is expected that economic factors will determine whether further investments in scrubbers will be made in light of the global limit of 0.5% sulphur in the fuel and new limitations on SO_2 emissions in flue gases, which came into effect in 2020. Furthermore, **Gu and Wallace** [22] suggested a mathematical model that allows comparing the difference in the costs associated to fuel-switching or EGCS *i.e.* seawater scrubbers adoption.

The use of seawater as scrubbing liquid is related to the natural abundance of dissolved alkaline species in seawater, which shift the chemical equilibria towards a greater dissociation of H_2SO_3 (see **Eqs. (1)-(6)**). Generally, the total sulphur contained in the natural seawaters is in a 4:1 ratio between SO_3^{2-} and HSO_3^-, while the total alkalinity is in a 3:1 ratio between HCO_3^- and CO_3^{2-}.
The percentages of sulphurous acid in its dissociated forms and the abundance of alkaline species as a function of pH are reported in **Figure I.11**.

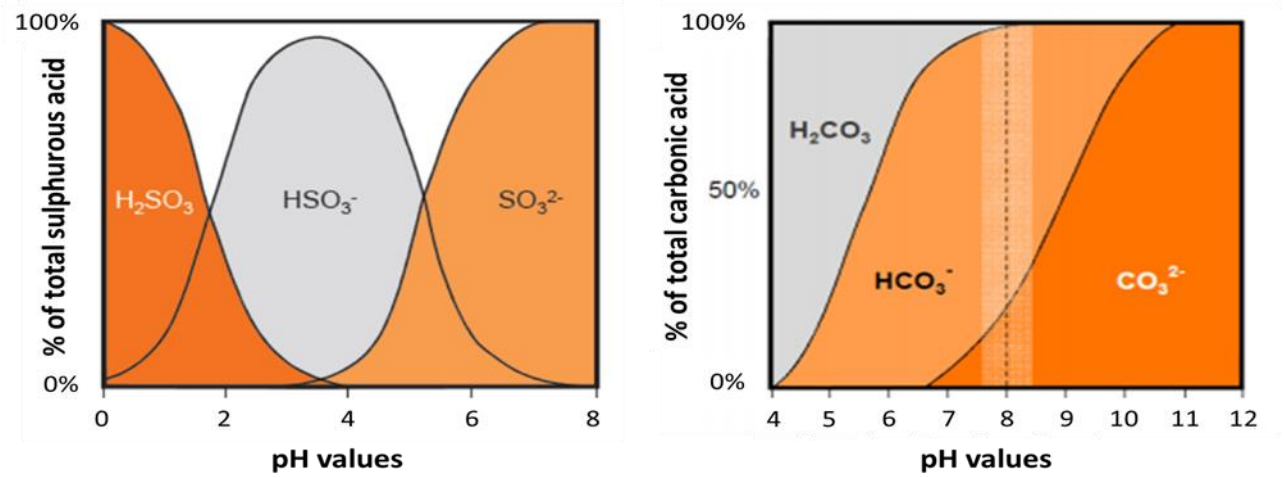

Figure I.11. *Percentage of total sulphurous acid and relative abundance of carbonic acid, bicarbonate ion and carbonate ion in seawater as a function of pH* [28]

In the Mediterranean Sea and in the Oceans, the alkalinity of water is quite high: 2300 - 2400 $\mu mol \cdot L^{-1}$, allowing an appreciable chemical absorption of sulphur dioxide. On contrary, Baltic sea and north Pacific have a lower alkalinity. **Figure I.12** shows the alkalinity distribution from a world map with relative values for areas and ports.

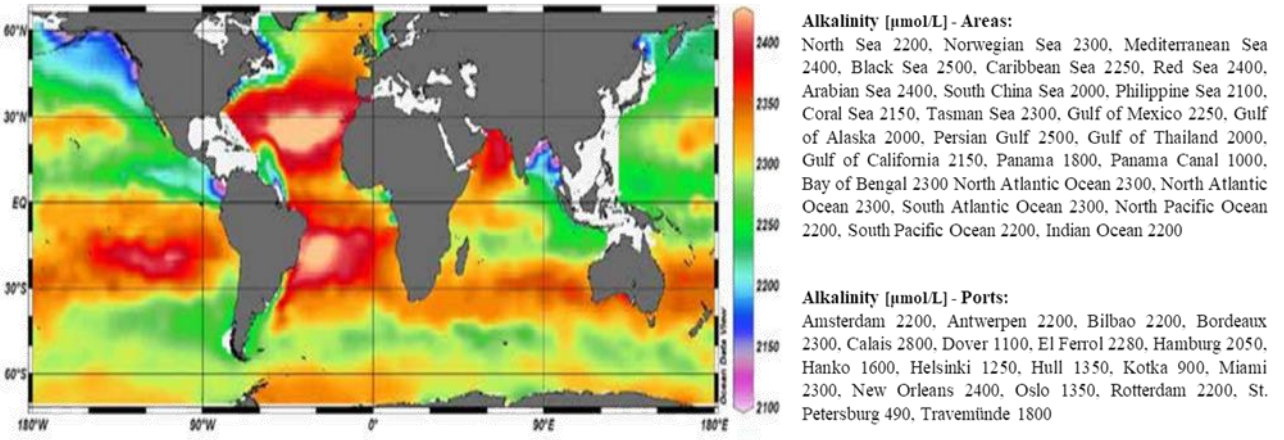

Figure I.12. *Surface alkalinity of open seas worldwide* [29]

Besides, seawater is free of charge and is the largest form of water available on the Earth (97.5% of the total existing amount), but also far less useful for humans than the precious freshwater.

Seawater is more corrosive than freshwater and can cause risks to FGD vessel, nozzles, pumps, pipes, valves etc., thus requiring more expensive materials for the equipment construction. Manufacturers adopt nickel-based alloys, titanium or non-metallic materials such as epoxy and composites for corrosion prevention. Besides, due to the higher saline content, ranging between 33 - 37 $g \cdot L^{-1}$ (see **Figure I.13**), a specific attention has to be given to the possible precipitation of hydroxides when basic chemicals, such as NaOH, are added to seawater.

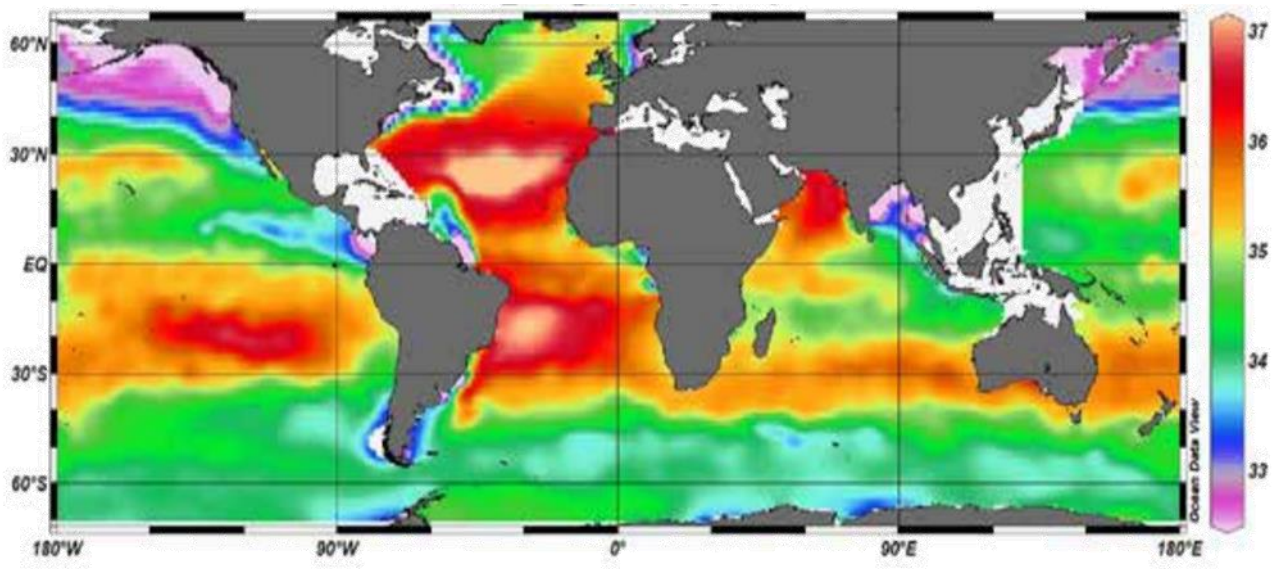

Figure I.13. *Surface salinity of open seas worldwide* [29]

Although alkalinity and salinity show a similar distribution, there is not a defined connection between the buffering capacity of water and its salinity.

Until today, the low cost of freshwater in many countries makes the scrubbers operated with freshwater with the addition of chemicals more effective than the seawater scrubbers when the alkalinity levels are very low and, in some cases, even less expensive.

However, freshwater is a precious resource (represents only 2.5% of the total existing water) and its scarcity is recognized as a critical societal challenge for the next years [30]: a protection of clean water resources is indeed one of the 17 United Nation sustainable goals.

In this scenario, the use of seawater can have the double effect of reducing the consumption of freshwater and of chemicals, while keeping constants the performances of wet FGD units. Seawater also has an additional advantage: thanks to the high saline content, there is a high tendency to convert sulfites to the harmless sulphates, a result that is usually achieved only by oxidation processes in conventional freshwater-based FGD processes, *e.g.* the lime-gypsum one.

den Boer and Hoen [27] provided an economic assessment on a case-study of a product tanker MS Nord Buttarly, reported in **Table I.5**, where the use of freshwater (FSW) with chemicals and seawater (SWS) scrubbers are compared.

Table I.5. *Results case study product tanker MS Nord Buttarly* [27]

	Seawater Scrubber (SWS)		**Freshwater Scrubber (FWS)**	
Additional costs for MGO fuel use	1.662	k€	1.662	k€
Scrubber costs				
Annual investment costs	1.482	k€	1.854	k€
Caustic soda consumption costs			153	k€
Additional fuel costs	69	k€	46	k€
Slurry disposal costs	11	k€	11	k€
Maintenance costs	22	k€	22	k€
Total scrubber costs	**1.586**	**k€**	**2.087**	**k€**

This case study points out that the use of a freshwater scrubber is 500 k€ more expensive than a seawater scrubber on annual basis, because of higher investment costs and caustic soda consumption. This explains the limited number of freshwater scrubbers installed on board ships.

Although the number of seawater scrubbers in marine field is increasing year by year (**Figure I.14**), mostly thanks to the growth of the maritime market, the number of scientific papers on seawater scrubbing is limited.

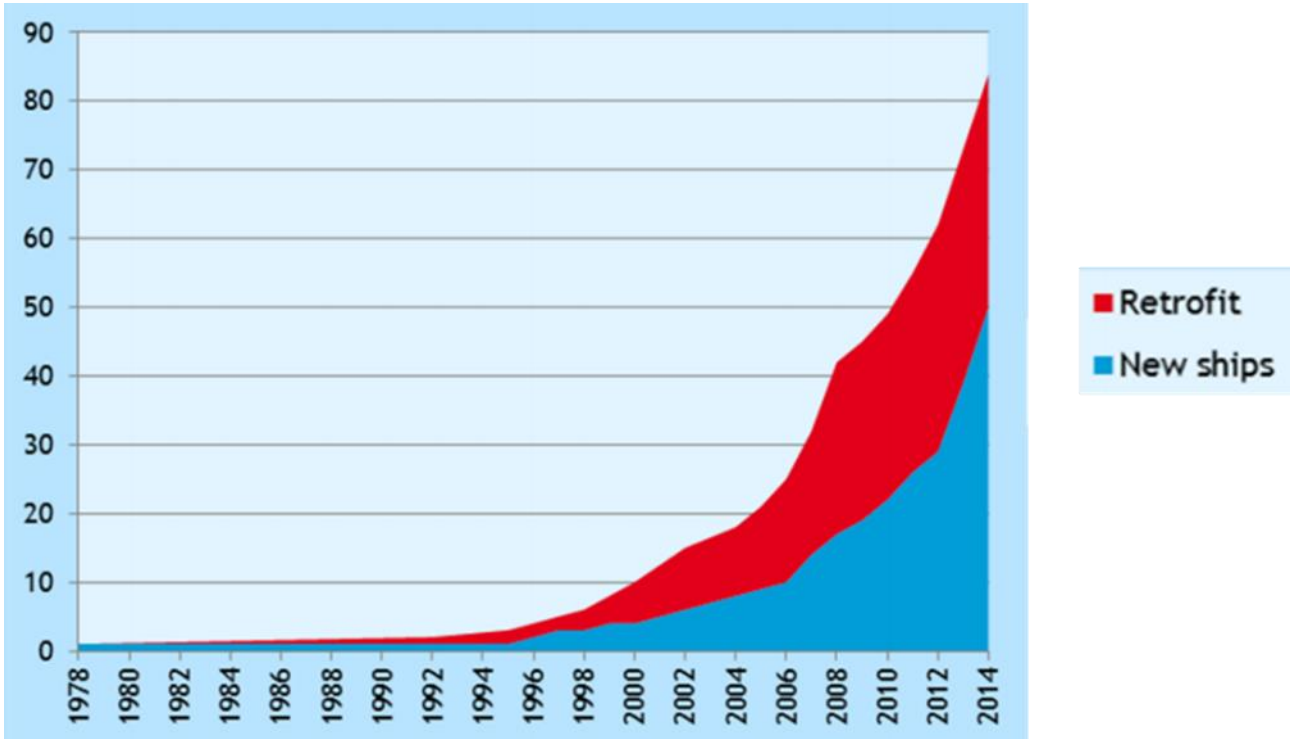

Figure I.14. *Development of the world fleet with seawater scrubbers installed* [27]

The Exhaust Gas Cleaning Systems Association (EGCSA) estimated that there are by 2015 about 300 (member and non-member) exhaust cleaning gas systems installed or on order, and Carnival Corporation made a significant investment on EGCS waiting for the new SECA targets for 2015 [27]. In 2014, the number of installations and orders was 122, showing the sharp increase of interest by the maritime industry for scrubbers prior to the coming into effect of the 0.1% sulphur cap in January 2015. Scrubbers are most widely installed on Roll-On/Roll-Off (Ro-Ro) ships, offshore service ships, cruise/passenger ships and gas carriers, see **Figure I.15**.

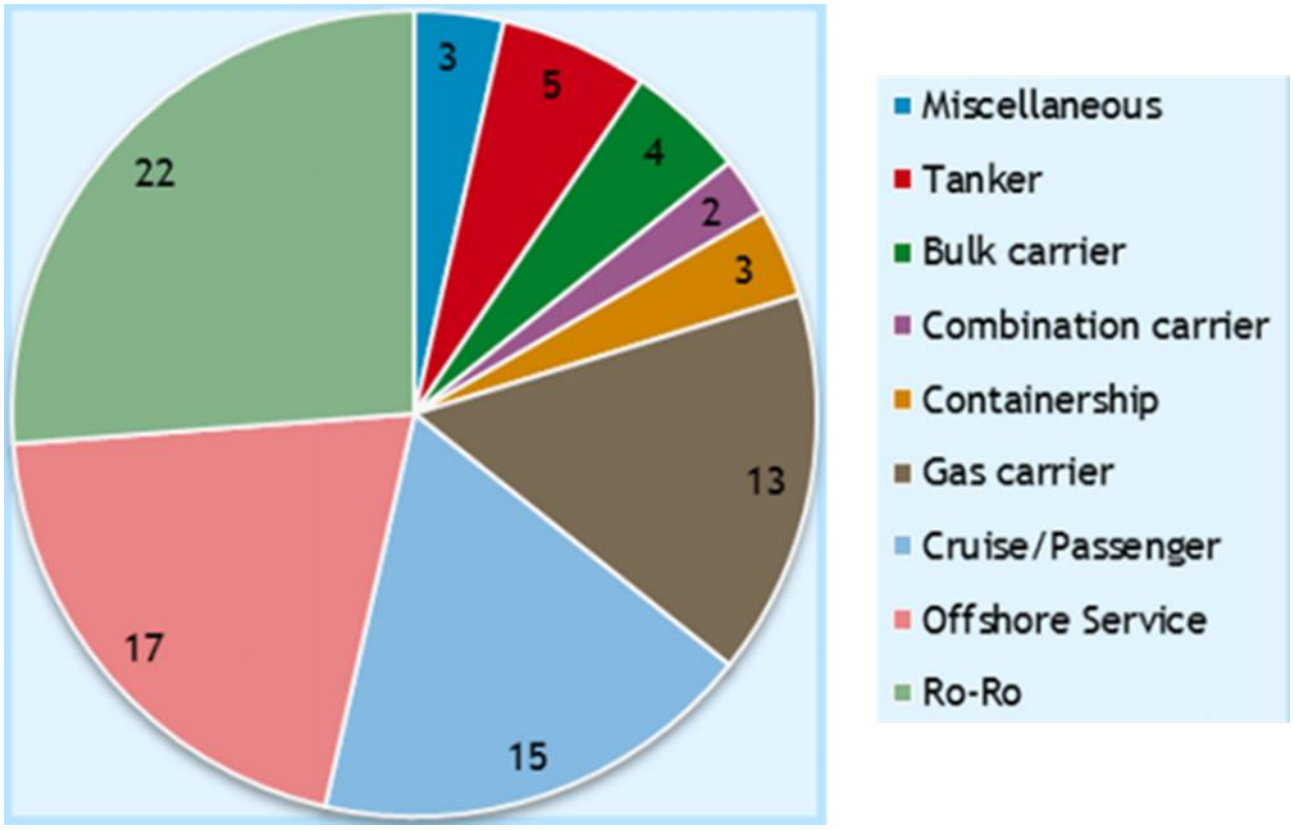

Figure I.15. *Distribution of exhaust gas scrubbers over ship types* [27]

Especially Ro-Ro ships and offshore service ships typically operate in the SECAs and relatively large numbers of scrubbers fitted onto Ro-Ro ships can be explained by the fierce competition with truck transport [27].

Hybrid scrubbers and open loop scrubbers were the most widely installed on ships [27]. In the year 2014, 24 hybrid, 23 open loop and 8 closed loop scrubbers were installed on ships, while the number of installed dry scrubbers amounted only 2 and the unknown were 27 [27].

In general, several different exhaust gas cleaning technologies can be adopted for marine desulphurization of the exhaust gas, based either on dry or wet scrubbing (wet-scrubbers can be

operated in two different modes, closed-loop or open-loop [20]). An overview on the different scrubber technologies currently available are listed in **Table I.6**.

Table I.6. *Overview on the different scrubber technologies currently available as EGCS for use on-board ship* [20]

Type of Scrubbers	Description
Dry-Scrubbers	Dry-scrubbers make use of granulates of calcium hydroxide for the de-sulphurization of the exhaust gases. However, the main class of ECGS adopted on-board ships is wet scrubbers, which can reduce the emissions of SO_x to the atmosphere by washing the exhausts with a liquid, often represented by seawater. Wet scrubbers can be operated in two different modes, closed-loop or open-loop [20].
Wet-Scrubbers	**Open-loop mode**: the simplest types of scrubber are open-loop type, in which seawater is usually used as scrubbing liquid due to its natural alkalinity [20]. If alkalinity is too low, open-loop scrubbers cannot be used or need to be amended with sodium hydroxide or other chemicals to increase the buffering capacity [31]. Scrubbing liquid effluent has to be processed (using multicyclones or cyclonic separators, [27], [32]), essentially by removing sludge and oil and then the washwater is diluted on-board with fresh seawater until it meets the established limits for pH, turbidity, PAH, and nitrates, before before being discharged back into the sea (typically at a discharge rate of 45 $m^3 \cdot Wh^{-1}$ at pH ~ 3, [33]). The amount of generated sludge by open-scrubbers is approximately 0.1 to 0.4 $kg \cdot Wh^{-1}$, depending on the amount of water mixed with the particulates [27]. Generally, the sludge produced by the treatment contains high levels of sulphur, THC, PAH, PCBs, vanadium, nickel and copper [27]. A cruise ship with approximately 2700 passengers operating in open-loop mode can produces around 7 m^3 of sludge per week [31]. Scrubber sludge must be stored on board in a separate tank and must be delivered ashore to appropriate collection systems in ports [31].
	Closed-loop mode: scrubbers re-cycle most of the scrubbing liquid (initially represented fresh water) and alkalinity is kept almost constant by continuously adding NaOH, with an average flow rate of approximately 20 $m^3 \cdot MWh^{-1}$. Once scrubbed, the wash water is treated to remove the scrubbing products and pumped back into the system. A minor fraction of the wash water, the so called "bleed-off" (0.1 - 0.3 $m^3 \cdot MWh^{-1}$) is discharged and an equal flow rate in integrated in the loop, in order to keep the total flow rate as constant. Closed loop systems can also operate for short periods without any discharge. Some closed loop scrubbers with a limited discharge rate can also use seawater for scrubbing: the discharge rate is then set by the need to avoid precipitation of calcium sulfate as the sulfate concentration of the seawater increases during operation [31]
	Hybrid mode: most of the scrubbers present on the market are hybrid-scrubbers, which can be flexible and operate in both "open loop" and "closed loop" mode [33]. When running in closed loop, the water is re-circulated and buffered with caustic soda and a minor part (approximately 0.1 to 0.3 m^3 $M \cdot Wh^{-1}$) is discharged as bleed-off [33]. In comparison, an average sized RoRo vessel equipped with a 12 MW engine running at maximum load would produce 13000 m^3 of washwater on a daily basis from an open-loop scrubber [33]. Despite the increasing use of scrubbers, far lees is known about the potential impact of the discharged wash water on the marine environment [34]. The use of open loop scrubbers implies that exhaust substances usually deposited on the sea surface are more intensively transferred to the marine environment in a limited space and time, generating temporary higher concentrations of pollutants, eutrophying and acidifying substances.

In just three years from 2015, the number of scrubber installations has rapidly increased and a survey conducted by the exhaust gas cleaning system association (EGCSA) showed that, as of May 2018, the number of ships with scrubbers installed or about to be installed was as high as 983, about 88% more than the 2015 forecast [34]. The increasing number of installed scrubbers seems to be due to

the belief that from a cost-benefit analysis about the incidence of to the GLOBAL sulphur cap of 0.5% by the year 2020 the dominant response would be the use of scrubbers.

A futuristic projection of the vessel traffic densities for total fleet over the next 30 years, it was proposed by **Eyring et al.** [35] and reported in **Figure I.16**. The authors compared the calculated 2050 vessel traffic predicted with the actual data in 2000.

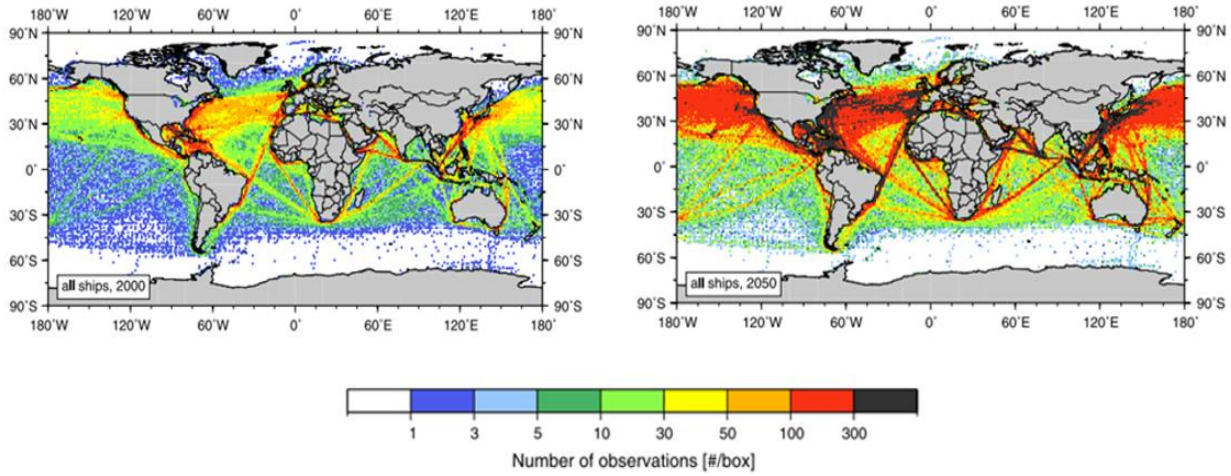

Figure I.16. *Vessel traffic densities for different ship types of the total fleet in 2000 (left plot) and 2050 (right plot)*

These data suggest that a significant increase in the total global fleet in the next 30 years could also correspond to new and strong investments in the marine scrubbers market.

Whatever is the type of scrubber adopted, the use of seawater in scrubbers still requires large amount of liquid-to-gas ratios to achieve sufficient FGD efficiency, also for the high salinity of ocean waters. This increases the scrubber height and its footprint as well as the cost associated to pumps, piping and auxiliary wash water treatment units.

Commercial marine scrubbers available so far mainly consist of conventional spray towers fed with pure seawater or seawater enhanced with NaOH [36]. These units are often bulky and characterized by heavy constructions, which lead to a fuel penalty for ships in the range 2 - 4% [24]. Furthermore, it is important considering that when the fuel meets the new quality standards, as in ocean water so far, the scrubber can be switched-off. Hence, although by-pass piping is suggested for these dry-operations, space limitations do not allow the adoption of the by-pass and a hot, oily, gas is passed directly through the scrubber. Therefore, in the first and second generation scrubbers adopted so far, the risk of packing corrosion due to the exposure to acid seawater and oil deposition led to prefer simpler spray scrubber to the packed ones. To the next generation scrubbers, higher performances are requested to comply with the more restrictive regulations imposed by the IMO for SECAs and to reduce weight and size requirements. These considerations lead to propose new approaches for

marine scrubbers, such as those based on the use of electrified sprays [37]–[40] and to reconsider structured packings [41]–[46], assuming that the improvements in onboard space management of the new systems allow the addition of by-pass lines.

To improve seawater scrubbers, chemicals can be added; however, the risk of salt precipitation reduces the amount of basic substances that can be added to seawater and discourage the use of lime or limestone. For this reason, sodium hydroxide and magnesium oxides are commonly used in maritime scrubbers, in spite of their higher costs (around 0.2 - 0.4 k€ per ton).

Practical implications of marine scrubber use on board ship mainly are related to the logistic of the consumables, foremost caustic soda (NaOH). The typical consumption of caustic soda as a function of initial sulphur content in the fuel is reported in **Table I.7**.

Table I.7. *NaOH additive consumption required to reach corresponding reductions in sulphur in atmospheric emissions to comply SECA target (0.1% w/w S equivalent) with respect to the sulphur content in the fuel* [2]

% sulphur removed	NaOH consumption (litres of 50% solution per MWh)
2.9	11
2.4	8
1.4	4
0.9	1

As an alternative, oxidants can be added to the seawater to improve SO_2 absorption by oxidating sulfites (SO_3^{2-}) to sulfates (SO_4^{2-}), hence allowing to increase the amount of SO_2 absorbed and transformed into sulfites. Several oxidants have been proposed in the literature, such as: hydrogen peroxide (H_2O_2) ([47], [48], [57], [49]–[56]); ferrous EDTA (Fe(II)-EDTA) [58]–[61]; sodium chlorite ($NaClO_2$) ([36], [62], [71]–[74], [63]–[70]), sodium persulfate ($Na_2S_2O_8$) ([55], [56], [75]) or potassium ferrate (K_2FeO_4) [76], [77].

Among them, sodium chlorite has the advantage of easier storage and handling and a higher stability compared to the hydrogen peroxide and ferrous EDTA, and a better oxidative ability compared to the sodium persulfate and potassium ferrate. The main reaction in the wet oxidation process of SO_2 using sodium chlorite is given below:

$$2SO_{2(g)} + NaClO_2 + 2H_2O \rightleftharpoons 2H_2SO_{4(aq)} + NaCl_{(aq)} \quad (9)$$

Sodium chlorite has an additional advantage: it can be exploited also in acidic conditions that even improve its oxidative ability, so that the absorption of SO_2 can be carried out in conditions under which salts precipitation do not occur. This also avoid the problems related to the scaling of packings

as well as the possible clogging of nozzles, which would occur for excessive content of basic compounds.

At the best of our knowledge, there are no available study on the use of sodium chlorite in seawater as sorbent for SO_2. Very few equilibrium studies of SO_2 absorption in pure seawater solutions [78], [79] and in solutions containing NaOH are available in the literature, while they are almost absent for $NaClO_2$ solutions. Similarly, experimental data about the absorption rate with chemical reaction for sodium chlorite solutions are poorly available at date.

This lack of information hinders the use of seawater enhanced with sodium chlorite in FGD processes, in spite of the great potentialities of this process.

This Ph.D. thesis aims to study the desulphurization of combustion flue gases, both simulated and real, by seawater-based solutions containing either sodium hydroxide (NaOH) or sodium chlorite ($NaClO_2$). The work is predominantly based on the experimental findings that were achieved through the design, construction and operation of lab-scale units aimed to address equilibrium and dynamic absorption data in different gas-liquid contactor. Equilibrium tests were carried out in a feed-batch bubble column with controlled hydrodynamics.

Dynamic tests were performed in a packed-bed column equipped with a structured packing (Mellapak 250.X), which assured high reproducibility of column hydrodynamics and mass transfer performances during the three years experimental campaign. These FGD experiments allowed evaluating the design and scale up criteria for scrubbing processes based on seawater-based solutions enhanced with $NaClO_2$.

Further experimental tests were performed in pilot scale plants. A first set of experiments was carried out on a spray column in order to test SO_2 absorption from model flue gases, using seawater with controlled spray properties and chemical composition. A second set of experiments was performed on a complex spray scrubber used to remove SO_2 from the exhaust gases of a real heavy-duty marine Diesel engine, in cooperation with the Chalmers University of Technology at Göteborg (SE).

Finally, a comparison between spray and packed towers for the seawater scrubbing process was performed and the effect of the FGD process on other gas pollutants (*e.g.* NO_x) and wash waters (in terms of heavy metals and organics content) was estimated.

Experiments were analyzed by using dedicated mathematical models available in the pertinent literature for an accurate description of phase equilibria with chemical reactions, mass transfer and pressure drops in spray and structured packing towers. A commercial software for chemical process design (ASPEN PLUS®) and a specific MATLAB® program were used to describe the packed and the spray column performances, respectively.

The thesis is divided into three main sections:

- Section 1 – Analysis of the State-of-the-Art on FGD processes with seawater and seawater enhanced with $NaClO_2$, also including the mass transfer and pressure drop models for spray and packed towers;
- Section 2 – Detailed description of the experimental campaign and the modelling approach adopted in the thesis work;
- Section 3 – Description and discussion of the experimental results and their interpretation.

The Thesis work is based on a number of scientific papers published and submitted during the Ph.D. course and therein reported:

1. Flagiello, D., Di Natale, F., Erto, A., Lancia, A. (2017). Marine diesel engine flue gas desulphurization by seawater scrubbing in a structured packing absorption column. *Proceedings of the 40th ASICI*, Rome.
2. Flagiello, D., Erto, A., Lancia, A., Di Natale, F. (2018). Experimental and modelling analysis of seawater scrubbers for sulphur dioxide removal from flue-gas. *Fuel*, 214, 254-263.
3. Flagiello, D., Di Natale, F., Carotenuto, C., Erto, A., Lancia, A. (2018). Seawater Desulphurization of Simulated Flue Gas in Spray and Packed Columns: an Experimental and Modelling Comparison. *Chemical Engineering Transaction*, 69.
4. Flagiello, D., Parisi, A., Lancia, A., Carotenuto, C., Erto, A., Di Natale, F. (2019). Seawater desulphurization scrubbing in spray and packed columns for a 4.35 MW marine diesel engine. *Chemical Engineering Research and Design*, 148, 56-67.
5. Flagiello, D., Lancia, A., Erto, A., Di Natale, F. (2019). Desulphurization of combustion flue-gases by Wet Oxidation Scrubbing (WOS). *Proceedings of the 42th ASICI*, Ravenna.
6. Flagiello, D., Di Natale, F., Lancia, A., Erto, A. (2020). Characterization of mass transfer coefficients and pressure drops for packed towers with Mellapak 250.X. Under review on *Chemical Engineering Research and Design*.
7. Flagiello, D., Di Natale, F., Lancia, A., Erto, A. (2020). Wet oxidation scrubbing (WOS) for flue-gas desulphurization using sodium chlorite seawater solutions. Under review on *Fuel*.
8. Flagiello, D., Parisi, A., Lancia, A., Di Natale F. (2020). Microsoft Excel Solver tool for Mass Transfer evaluation in Packed-bed columns. Under review on *Chemical Engineering Research and Design*.

II. THEORETICAL FRAMEWORK

II.1. SO_2 and NO_x absorption by water and seawater solutions

Sulphur dioxide is quite soluble in water at temperature and pressure (almost atmospheric) commonly adopted for absorption process. The reaction network of SO_2 solubilization in water starts with the dissolution of gaseous SO_2 in water, according to the following equilibrium:

$$SO_{2(g)} \rightleftharpoons SO_{2(aq)} \tag{10}$$

After the dissolution, sulphur dioxide is hydrolyzed by water thus producing sulfites and bisulfites ([17], [42], [78]–[81]).

$$SO_{2(aq)} + 2H_2O \rightleftharpoons H_3O^+ + HSO_3^- \tag{11}$$

$$HSO_3^- + H_2O \rightleftharpoons H_3O^+ + SO_3^{2-} \tag{12}$$

It is worth noting that the SO_2 solubility can be further increased by both physical contributions, ruled by Henry's law, and chemical contribution, ruled by possible chemical reactions in the liquid phase. In fact, sulphur dioxide is strongly acid; therefore, its chemical absorption is enhanced in alkaline solutions. For instance, sodium hydroxide is often used because it releases OH^- ions in the solution changing the ionic product of water, promoting its dissociation and the subsequent neutralization of H_3O^+ ions, deriving from both the SO_2 hydrolysis reactions, and the simultaneous deprotonation of HSO_3^- ([42], [78]–[80]).

$$2H_2O \rightleftharpoons H_3O^+ + OH^- \tag{13}$$

The absorption of sulphur dioxide from a polluted gas stream (SO_2 in air) could also follow a different pathway, starting with an oxidation reaction that produce $SO_{3(g)}$:

$$2SO_{2(g)} + O_2 \rightleftharpoons SO_{3(g)} \tag{14}$$

and its subsequent absorption in water, being $SO_{3(g)}$ more soluble than $SO_{2(g)}$. The solubilization of $SO_{3(g)}$ in water leads to the formation of a concentrated sulfuric acid solution as shown in the following reactive network:

$$SO_{3(g)} \rightleftharpoons SO_{3(aq)} \tag{15}$$

$$SO_{3(aq)} + H_2O \rightleftharpoons H_2SO_{4(aq)} \tag{16}$$

However, the reaction of SO_2 with oxygen in gaseous phase has a very slow kinetics, although it is thermodynamically favored at low temperature by its exothermic nature, and it usually occurs only in the presence of a catalyst. For this reason, the conversion to $SO_{3(g)}$ and the sulfuric acid production

are usually negligible. Therefore, the mechanism of SO_2 absorption can be ascribed to the sole dissolution of $SO_{2(g)}$ in water.

The absorption of $SO_{2(g)}$ in seawater solutions is increased with respect to distilled water thanks its natural alkalinity, expressed as carbonates (CO_3^{2-}) and bicarbonates (HCO_3^-). The consequent increase in basicity determines the neutralization of H_3O^+ ions, hence increasing the solubility of $SO_{2(g)}$, while $CO_{2(g)}$ is developed by their equilibrium in water. $CO_{2(g)}$ originates from the equilibrium with $CO_{2(aq)}$ which can give rise to a partial stripping from the absorbing liquid:

$$HCO_3^- + H_2O \rightleftharpoons H_3O^+ + CO_3^{2-} \quad (17)$$

$$CO_{2(aq)} + 2H_2O \rightleftharpoons H_3O^+ + HCO_3^- \quad (18)$$

$$CO_{2(g)} \rightleftharpoons CO_{2(aq)} \quad (19)$$

Several dissolved ions, commonly present in seawater, can modify the chemical equilibria of $SO_{2(aq)}$ by different interactions. In particular, the presence of sulfates (SO_4^{2-}), nitrates (NO_3^-) and, in particular, chlorides (Cl^-) in the absorbing liquid determines a further increase in solubility, which enhances the SO_2 absorption ([42], [78], [79]**)**. Nitrites (NO_2^-) Fluorides (F^-) and bromides (Br^-) are normally present in trace into seawater and do not exert significant effects on the equilibria ([42], [78], [79]).

Similarly, the NO_x chemical absorption from a gaseous stream (air and NO_x) in water is characterized by a complex network of reactions, involving both the gas and the liquid phases. Compared to SO_2, more components such as NO, NO_2, N_2O_3, N_2O_4, HNO_2 and HNO_3 are present in both gas and liquid phases, and their interactions make this process much complicated. Indeed, there are many parallel and series reactions concurrently with absorption and desorption of the species in solution (**Figure II.1**).

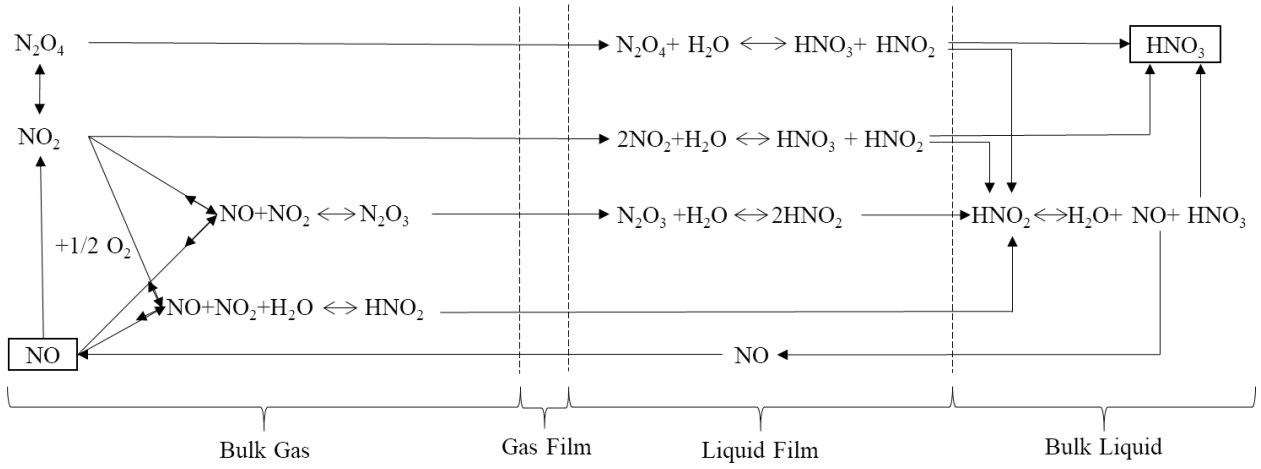

Figure II.1. *Reactive scheme for NO_x absorption in water* [82]

The reactions network shown in **Figure II.1** considers the two-film theory and is used for describing the NO_x absorption in water, ending up in HNO_3 formation. When the HNO_3 concentration in the liquid phase is low, *i.e.* less than 30% w/w, the controlling reaction is the oxidation of nitrogen monoxide, while the other reactions in the gas phase are instantaneous and produce other intermediates.

The solubility in water of the reaction products increases along with their molecular weight and the mass transfer resistance in gaseous phase may be neglected. In this case, the absorption efficiency is almost determined by $NO_{(g)}$ oxidation in the gas phase [83]. Nevertheless, for higher HNO_3 concentrations in the liquid phase, *i.e.* more than 60% w/w, the $HNO_{3(g)}$ vapor pressure becomes significant and thus it is more likely that other reactions in the gas film occur, including the direct reaction between $NO_{(g)}$ and $HNO_{3(g)}$ to form nitrogen dioxide and water [83]**.** The reactions network in the gas phase leads to the formation of many components with a higher solubility, thanks to their higher molecular weight. The $NO_{(g)}$ chemical absorption is mainly related to nitrogen dioxide formation, which is about an order of magnitude more soluble than nitrogen monoxide, and $N_2O_{4(g)}$ and $N_2O_{3(g)}$ formation, both much more soluble in water [82], [83]**.** The presence of these compounds promotes the $HNO_{2(aq)}$ and $HNO_{3(aq)}$ formation and influences the equilibria in the gas phase. These acids dissolve completely in water thanks to their high solubility. Due to its scarce solubility in water or into more alkaline solutions as seawater, $NO_{(g)}$ can desorbs and thus can be oxidized again to $NO_{2(g)}$ in the gaseous phase. The nitrogen dioxide is partly absorbed, producing $HNO_{2(g)}$ and $HNO_{3(g)}$, and partly reacts forming the two intermediates, $N_2O_{3(g)}$ and $N_2O_{4(g)}$, reiterating the reactive loop above described.

To complete the SO_2 and NO_x absorption system, it is necessary to recover the data regarding the physical gas-liquid and chemical reaction equilibria. The Henry's constant K_H [atm] is associated with physical gas-liquid equilibria, while the equilibrium or Le Châtelier's constant K_{eq} [$(mol \cdot mol^{-1})^{p-r}$ or $(kmol \cdot m^{-3})^{p-r}$] (where p is sum of the stoichiometric coefficients of products, and r is the sum of stoichiometric coefficients of reagents) is associated with the chemical reaction equilibria. They are used in the following equations:

$$y_A = K_{H_A} x_A \tag{20}$$

$$K_{eq} = \frac{\Pi C^p}{\Pi C^r} \tag{21}$$

Where: y_A and x_A [$mol \cdot mol^{-1}$] are the mole fraction of generic gas solute A respectively in gas and liquid phase; ΠC^p [$(mol \cdot mol^{-1})^p$ or $(kmol \cdot m^{-3})^p$] is the product of the concentrations of the chemical species of the products with a total reaction order p on the product-side given by the sum of the

stoichiometric coefficients of the reaction products; ΠC^r [(mol·mol^{-1})^r or (kmol·m^{-3})^r] is the product of the concentrations of the chemical species of the products with a total reaction order r on the reagent-side given by the sum of the stoichiometric coefficients of the reaction products.

It should be noted that the equilibrium constants can also be expressed in terms of gas partial pressures [atm] when the reaction occurs in the gaseous phase and K_{eq} is replaced with K_p [(atm)$^{p-r}$].

After a screening of the pertinent literature, a gas solubility and a chemical equilibrium constants dataset were selected. Both these datasets are partially reported in the Dechema Database available in ASPEN PLUS®. For the other data not listed in the software database, the enthalpies of gas dissolution (ΔH_s , [kJ·mol^{-1}]) and standard Gibbs free energies of reaction (ΔG_r°, [kJ·mol^{-1}]) were determined from **Perry** [9] and **R. Sander** [84] data, allowing to complete the dataset. The standard values of Gibbs free energy of reaction (ΔG_r°) were calculated according to Hess's law using data provided by **Perry** [9].

$$\Delta G_r^o = \sum \Delta G_{f,p}^o - \sum \Delta G_{f,r}^o \tag{22}$$

Where the $\Sigma \Delta G^\circ_{f,r}$ and $\Sigma \Delta G^\circ_{f,p}$ are the sum of standard Gibbs formation [kJ·mol^{-1}], for the reagents and the products of the chemical reactions, respectively.

The equilibrium constants can be generally described by the van't Hoff equation, which expresses their temperature dependence (*e.g.* [85]).

$$K_H = A_H + \frac{B_H}{T} \tag{23}$$

$$K_{eq} = A_{eq} + \frac{B_{eq}}{T} \tag{24}$$

Where: A_H [atm] and B_H [K] are constant parameters for K_H evaluation; A_{eq} [(mol·mol^{-1})$^{p-r}$] and B_{eq} [K] are constant parameters for K_{eq} evaluation; T [K] is the absolute temperature. It is worth underlining that when K_H and K_{eq} are reported as functions of these parameters, it is important to include a sufficient number of significant digits for B_H and B_{eq} values, because the constants depend exponentially on them. Alternatively, an expression based on the constants at the reference temperature T° = 298.15 K can be written:

$$K_H(T) = K_H^\circ \cdot e^{\frac{-\Delta H_s}{R}\left(\frac{1}{T}-\frac{1}{T^\circ}\right)} \tag{25}$$

$$K_{eq}(T) = K_{eq}^\circ \cdot e^{\frac{-\Delta G_r^o}{R}\left(\frac{1}{T}-\frac{1}{T^\circ}\right)} \tag{26}$$

in which R is the universal gas constant ($8.31 \cdot 10^{-3}$ kJ·mol^{-1}·K^{-1}); K_H° and K_{eq}° are the Henry and chemical equilibrium reaction constants, respectively, both evaluated at T° = 298.15 K; and $\Delta H_s/R$ and $\Delta G_r^\circ/R$ correspond to $-B_H$ and $-B_{eq}$, respectively.

This expression of van't Hoff equation is valid only in a limited temperature range, in which ΔH_s and ΔG_r° do not significantly change with temperature. In order to cover a larger temperature range, in which ΔH_s and ΔG_r° cannot be considered as constant, different empirical methods can be used. Frequently, the dependence of these parameters on temperature is expressed as the sum of several terms. Hence, the analytical derivative is simply the sum of the derivatives of the individual terms. For example, **Wilhelm et al.** [86] and **Luckas et al.** [87] used these expressions for Henry constants (K_H) and chemical equilibrium constants (K_{eq}):

$$Ln(K_H) = A_H + \frac{B_H}{T} + C_H \cdot Ln(T) + D_H T \tag{27}$$

$$Ln(K_{eq}) = A_{eq} + \frac{B_{eq}}{T} + C_{eq} \cdot Ln(T) + D_{eq} T \tag{28}$$

where C_H [K^{-1}] and D_H [K^{-1}] are further constant parameters for K_H evaluation; C_{eq} [K^{-1}] and D_{eq} [K^{-1}] are further constant parameters for K_{eq} evaluation.

Tables II.1–2 show a summary of physical gas-liquid equilibrium parameters and chemical equilibrium reactions parameters for SO_2 and NO_x absorption in water and the dissociation reactions of carbonate, sulfate, nitrate, chloride, fluoride and bromide usually present in seawater.

Table II.1. *Physical gas-liquid equilibrium parameters (**Eq. (27)**) and the enthalpy of gas dissolution values of the components involved in SO_2 and NO_x absorption in water or seawater*

Eq.	Physical gas-liquid Equilibria	ΔH_s	Constant Parameters				Ref.
		kJ·mol^{-1}	A_H atm	B_H K	C_H K^{-1}	D_H K^{-1}	
(15)	$SO_{2(g)} \rightleftharpoons SO_{2(aq)}$	-24.1	72.45	-5578	-8.76	0	[86]
(19)	$CO_{2(g)} \rightleftharpoons CO_{2(aq)}$	-19.9	159.20	-8477	-21.96	$5.78 \cdot 10^{-3}$	[86]
(29)	$NO_{(g)} \rightleftharpoons NO_{(aq)}$	-13.3	385.40	-14034	-60.78	$6.02 \cdot 10^{-3}$	[88]
(30)	$NO_{2(g)} \rightleftharpoons NO_{2(aq)}$	-23.1	16.92	-2776	0	0	[89]
(31)	$N_2O_{(g)} \rightleftharpoons N_2O_{(aq)}$	-22.4	16.60	-2600	0	0	[90]
(32)	$N_2O_{3(g)} \rightleftharpoons N_2O_{3(aq)}$	-23.1	13.99	-2776	0	0	[89]
(33)	$N_2O_{4(g)} \rightleftharpoons N_2O_{4(aq)}$	-29.1	-8.21	3500	0	0	[91]
(34)	$H_2SO_{4(g)} \rightleftharpoons H_2SO_{4(aq)}$	-73.9	16.85	-8900	0	0	[88]
(35)	$HNO_{2(g)} \rightleftharpoons HNO_{2(aq)}$	-39.9	16.56	-4900	0	0	[90]

(36)	$HNO_{3(g)} \rightleftharpoons HNO_{3(aq)}$	-72.3	20.94	-8700	0	0	[90]
(37)	$HCl_{(g)} \rightleftharpoons HCl_{(aq)}$	-49.9	-47.54	1215	8.37	$9.60 \cdot 10^{-3}$	[88]
(38)	$HF_{(g)} \rightleftharpoons HF_{(aq)}$	-10.1	-47.54	1215	0	0	[92]
(39)	$HBr_{(g)} \rightleftharpoons HBr_{(aq)}$	-3.1	32.62	-1572	-4.59	0	[88]

Table II.2. *Chemical equilibrium reactions parameters (**Eq. (28)**) and standard Gibbs free energies values of the reactions involved in SO_2 and NO_x absorption in water or seawater*

Eq.	**Chemical reaction Equilibria**	ΔG_r° $kJ \cdot mol^{-1}$	**Constant Parameters**				**Ref.**
			A_{eq} $(mol \cdot mol^{-1})^{p-r}$	B_{eq} K	C_{eq} K^{-1}	D_{eq} K^{-1}	
(13)	$2H_2O \rightleftharpoons H_3O^+ + OH^-$	79.9	132.89	-40.24	-9.60	0	[87]
(11)	$SO_{2(aq)} + 2H_2O \rightleftharpoons H_3O^+ + HSO_3^-$	10.1	-5.97	637.40	0	0.01	[87]
(12)	$HSO_3^- + 2H_2O \rightleftharpoons H_3O^+ + SO_3^{2-}$	41.2	-25.30	-1333	0	0	[87]
(40)	$H_2SO_{4(aq)} + H_2O \rightleftharpoons H_3O^+ + HSO_4^-$	-80.2	-12.15	9643	0	0	[87]
(41)	$HSO_4^- + H_2O \rightleftharpoons H_3O^+ + SO_4^{2-}$	11.4	-18.62	2953	0	0	[87]
(18)	$CO_{2(aq)} + 2H_2O \rightleftharpoons H_3O^+ + HCO_3^-$	36.4	231.46	-12092	-36.78	0	[87]
(17)	$HCO_3^- + H_2O \rightleftharpoons H_3O^+ + CO_3^{2-}$	58.9	216.05	-12432	-35.48	0	[87]
(42)	$2NO_{(g)} + O_2 \rightleftharpoons 2NO_{2(g)}$	-70.6	-3.19	8491	0	0	Eq. (26)
(43)	$2NO_{2(g)} \rightleftharpoons N_2O_{4(g)}$	-4.7	-3.19	571	0	0	Eq. (26)
(44)	$NO_{(g)} + NO_{2(g)} \rightleftharpoons N_2O_{3(g)}$	1.5	-3.19	-187	0	0	Eq. (26)
(45)	$NO_{(g)} + NO_{2(g)} + H_2O_{(g)} \rightleftharpoons 2HNO_{2(g)}$	6.9	-3.19	-838	0	0	Eq. (26)
(46)	$2NO_{2(g)} + H_2O_{(g)} \rightleftharpoons HNO_{2(g)} + HNO_{3(g)}$	9.3	-3.19	-1123	0	0	Eq. (26)
(47)	$3NO_{2(g)} + H_2O_{(g)} \rightleftharpoons NO_{(g)} + 2HNO_{3(g)}$	11.7	-3.19	-1409	0	0	Eq. (26)
(48)	$NO_{2(g)} + HNO_{2(g)} \rightleftharpoons NO_{(g)} + HNO_{3(g)}$	2.37	0	-285	0	0	Eq. (26)
(49)	$2NO_{2(aq)} + H_2O \rightleftharpoons HNO_{2(aq)} + HNO_{3(aq)}$	14.1	7.17	-1701	0	0	Eq. (26)
(50)	$NO_{(aq)} + NO_{2(aq)} + H_2O \rightleftharpoons 2HNO_{2(aq)}$	6.8	9.84	-823	0	0	Eq. (26)
(51)	$3NO_{2(aq)} + H_2O \rightleftharpoons NO_{(aq)} + 2HNO_{3(aq)}$	21.4	4.50	-2579	0	0	Eq. (26)
(52)	$N_2O_{4(aq)} + H_2O \rightleftharpoons HNO_{2(aq)} + HNO_{3(aq)}$	18.9	-4.50	-2273	0	0	Eq. (26)
(53)	$N_2O_{3(aq)} + H_2O \rightleftharpoons 2HNO_{2(aq)}$	5.3	-3.36	-636	0	0	Eq. (26)
(54)	$3HNO_{2(aq)} \rightleftharpoons HNO_{3(aq)} + 2NO_{(aq)} + H_2O$	0.4	-12.51	-54.24	0	0	Eq. (26)
(55)	$HNO_{2(aq)} + H_2O \rightleftharpoons H_3O^+ + NO_2^-$	13.9	-4.01	-1681	0	0	Eq. (26)
(56)	$HNO_{3(aq)} + H_2O \rightleftharpoons H_3O^+ + NO_3^-$	-34.5	-4.01	4156	0	0	Eq. (26)
(57)	$HCl_{(aq)} + H_2O \rightleftharpoons H_3O^+ + Cl^-$	-25.7	-4.01	3094	0	0	[87]

(58)	$HF_{(aq)} + H_2O \rightleftharpoons H_3O^+ + F^-$	18.1	-4.02	-2169	0	0	Eq. (26)
(59)	$HBr_{(aq)} + H_2O \rightleftharpoons H_3O^+ + Br^-$	-85.2	-20.90	10246	0	0	[87]

Table II.2 shows all the chemical reactions for all the possible species directly involved in SO_2 and NO_x absorption, *i.e.* the species containing the following elements: S, C, N, Cl, H, O, F, Br. The presence $NO_{(g)}$ and $NO_{2(g)}$ does not significantly affect the capture of sulphur dioxide because their solubility is negligible compared to SO_2 (about three and two orders of magnitude below, respectively). On the contrary, the presence of $SO_{2(g)}$ in the gas stream to be absorbed could influence the solubility of $NO_{x(g)}$, in particular for $NO_{2(g)}$.

To better describe the chemical equilibria in the case of non-dilute aqueous solutions, predictive models for the calculation of the fugacity (ϕ_f) and the activity coefficients (γ_a) must be considered. If the operating pressure of absorption is about 1 atm, the fugacity coefficient for gas phase components was set equal to unity ($\phi_f = 1$). The equilibrium of SO_2 and NO_x in water and seawater has been the subject of several papers, which pointed out the most relevant ionic species and proposed useful methods for the calculation of the activity coefficients, and of electric charge balance equation ([42], [78], [79]**)**. Most scientific papers, the Electrolyte Non-Random Two Liquid [93], Pitzer [94] and Bromley-Pitzer [95] correlations were generally adopted for the determination of the activity coefficients.

For absorption in non-dilute aqueous solutions, the **Eq. (21)** is re-proposed in a new form considering the corrections due to the activities in the liquid phase:

$$K_{eq} = \frac{\Pi C^p}{\Pi C^r} \cdot \frac{\Pi \gamma_a^p}{\Pi \gamma_a^r} \tag{60}$$

in which $\Pi\gamma_a{}^p$ is the product of the activity coefficients of the chemical species of the products with a total reaction order *p* on the product side given by the sum of the stoichiometric coefficients of the reaction products, while $\Pi\gamma_a{}^r$ is the product of the activity coefficients of the chemical species of the products with a total reaction order *r* on the product-side given by the sum of the stoichiometric coefficients of the reaction products.

The data related to the reaction rates of SO_2 and NO_x absorption in water or seawater, as retrieved from the pertinent literature, were also reported. In general, the reaction rates, of a generic *A* species, can be expressed as a power law of the concentration and the rate constants depend on temperature, according to an Arrhenius-like dependence:

$$r_A = k_{o,d} \cdot e^{-\frac{E_a}{RT}} \Pi C^r - k_{o,i} \cdot e^{-\frac{E_a}{RT}} \Pi C^p \tag{61}$$

where: r_A [kmol·m^{-3}·s^{-1}] is the reaction rate; $k_{o,d}$ [(kmol·m^{-3})$^{1-r}$·s^{-1}] is the direct frequency factor; $k_{o,i}$ [(kmol·m^{-3})$^{1-p}$·s^{-1}] is the inverse frequency factor; E_a [kJ·mol^{-1}] is the activation energy related to the specific reaction; R is the universal gas constant (8.31·10^{-3} kJ·mol^{-1}·K^{-1}); T [K] is the absolute temperature; ΠC^r [(kmol·m^{-3})^r] is the product of the concentrations of the chemical species of the products with a total reaction order r on the product-side given by the sum of the stoichiometric coefficients of the reaction products; ΠC^p [(kmol·m^{-3})^p] is the product of the concentrations of the chemical species of the products with a total reaction order p on the product side given by the sum of the stoichiometric coefficients of the reaction products. The inverse reaction rate constant (K_i, [(kmol·m^{-3})$^{1-p}$·s^{-1}]) can be calculated as the ratio between the direct reaction rate constant (K_d, [(kmol·m^{-3})$^{1-r}$·s^{-1}]) and the equilibrium constant (K_{eq}).

$$K_i(T) = \frac{K_d(T)}{K_{eq}(T)} = \frac{k_{o,d} \cdot e^{-\frac{E_a}{RT}}}{A_{eq} \cdot e^{-\frac{\Delta G_r^\circ}{RT}}} = k_{o,i} \cdot e^{-\frac{E_a}{RT}} \tag{62}$$

Differently, the absorption of SO_2 in water or seawater, for which the reactions are mainly instantaneous, can be described by chemical equilibrium correlations. On the contrary, the network of NO_x absorption is completely controlled by kinetic reactions in the gas and liquid phase (previously proposed in **Table II.2**). The main step is the oxidation of nitrogen oxide to nitrogen dioxide; in fact, this reaction triggers the formation of much more soluble compounds (N_2O_3, N_2O_4, HNO_2 and HNO_3) in water. The $NO_{(g)}$ oxidation in the presence of oxygen is favored at high pressure and low temperature; it can be considered irreversible at temperature lower than 350 °C. Its kinetic behavior is unusual if compared to all the other exothermic reactions occurring in gas phase (*i.e.* $SO_{2(g)}$ oxidation in $SO_{3(g)}$). According to [96], this kinetics is defined as anti-Arrhenius since the reaction rate increases by decreasing the temperature, hence the activation energy is negative. Nevertheless, it should be specified that the conversion of this reaction is low at low $NO_{(g)}$ concentrations, like in the process of NO_x removal from flue-gas from coal-fired or diesel engines. The chemical absorption of NO_x in water is particularly influenced by the kinetic of $NO_{(g)}$ oxidation since the presence of $NO_{2(g)}$ can lead to the formation of nitrogen tetroxide, which is the main compound that catalyzes the consequent dissolution of the various nitrogenous compounds to form HNO_2 and, mostly, HNO_3 [96], [97]. A thorough study of the relevant literature allowed to develop a rigorous kinetic reaction model for NO_x absorption in water. The **Table II.3** shows the kinetic parameters of the reactions involved in the absorption of SO_2 and NO_x in water or seawater.

Table II.3. *Reaction kinetic equation parameters for SO_2 and NO_x absorption in water or seawater. When the activation energy E_a is not available, the direct frequency factor $k_{o,d}$ is equivalent to the direct reaction rate constant K_d evaluated at 25 °C*

Eq.	Direct reaction rates			Inverse reaction rates			Ref.
	$k_{o,d}$ $(kmol \cdot m^{-3})^{1-r} \cdot s^{-1}$	E_a $kJ \cdot mol^{-1}$	ΠC^r $(kmol \cdot m^{-3})^r$	$k_{o,d}$ $(kmol \cdot m^{-3})^{1-p} \cdot s^{-1}$	E_a $kJ \cdot mol^{-1}$	ΠC^p $(kmol \cdot m^{-3})^p$	
(11)	$1 \cdot 10^2$	2.49	$[SO_2]$	$9 \cdot 10^6$	19.93	$[HSO_3^-] \cdot [H_3O^+]$	[80]
(18)	$1.05 \cdot 10^8$	57.78	$[CO_2]$	$3 \cdot 10^{13}$	52.33	$[HCO_3^-] \cdot [H_3O^+]$	[98]
(49)	$2.41 \cdot 10^2$	-4.40	$[NO]^2 \cdot [O_2]$	$9.66 \cdot 10^{11}$	186.05	$[NO_2]^2$	[99]
(49)	$1.27 \cdot 10^7$		$[NO_2]^2$	$8.51 \cdot 10^{14}$	57.07	$[N_2O_4]$	[97]
(49)	$4.75 \cdot 10^{12}$		$[NO] \cdot [NO_2]$	$3.25 \cdot 10^{18}$	39.65	$[N_2O_3]$	[100]
(49)	$1.10 \cdot 10^5$	4.13	$[NO_2]^2 \cdot [H_2O]$	$1.07 \cdot 10^4$	4.13	$[HNO_2] \cdot [HNO_3]$	[101]
(49)	$5.41 \cdot 10^6$		$[NO] \cdot [NO_2]$	*The inverse reaction rate is negligible*			[102]
(49)	$4.69 \cdot 10^7$		$[NO_2]^2$	*The inverse reaction rate is negligible*			[103]
(52)	$1.69 \cdot 10^4$		$[N_2O_3]$	*The inverse reaction rate is negligible*			[104]
(52)	$2.21 \cdot 10^{16}$	79.14	$[N_2O_4]$	*The inverse reaction rate is negligible*			[105]
(54)	$2.23 \cdot 10^4$	93.76	$[HNO_2]^4 \cdot [NO]^{-2}$	*The inverse reaction rate is negligible*			[105]

II.2. SO_2 and NO_x absorption by wet oxidation in $NaClO_2$ aqueous solutions

As described in the previous paragraph, $NO_{(g)}$ is almost insoluble in water and it accounts for more than 90% of NO_x in a typical flue-gas. In order to achieve a high removal efficiency, NO can be converted to NO_2 by using strong oxidants, such as sodium chlorite ($NaClO_2$). Indeed, sodium chlorite dissolves in water and forms ClO_2^-, which is an effective reactant for the simultaneous absorption and oxidation of NO_x and SO_2. Furthermore, $NaClO_2$ can be readily utilized as an aqueous solution due to its good solubility in water (390 gL at 17 °C, as retrieved by **International Chemical Safety Card 1045 s.d.**). In a wet scrubber, NO and SO_2 gases are spontaneously absorbed by aqueous $NaClO_2$ solution and oxidized to generate different ions such as NO_2^-, NO_3^-, SO_3^{2-}, HSO_3^-, SO_4^{2-}. On the contrary, ClO_2^- is mainly reduced to ClO^- and Cl^-.

Sodium chlorite has a good oxidizing ability at high pH while it is an excellent oxidizer when the pH is very low ([66], [67], [69], [72]). Chlorite ions is mainly consumed to oxidize NO into NO_2 and most of the nitrogen oxides are absorbed via hydrolysis of N_2O_3 and N_2O_4 which require high pH according to the reactions presented in **Table II.2**. Therefore, the pH of the solution should be low enough to assure that chlorite has a high oxidizing power, but high enough to allow the absorption

via hydrolysis of N_2O_3 and N_2O_4. Hence, pH is a crucial parameter to oxidize NO into NO_2 and to absorb NO_2 thereafter. Differently, the presence of chlorite increases the removal efficiency of SO_2, regardless the pH, even under acidic conditions that usually are not suitable for acid gas absorption. In fact, low pH values have a strong impact on the formation of other strong oxidizers such as $ClO_{2(g)}$ and $Cl_{2(g)}$. This effect is due to its higher solubility in water with respect to NO and NO_2 (at 25 °C, about 650 and 50 times more, respectively) and its fast oxidation reaction with the oxidant agents. In the literature**,** $ClO_{2(g)}$ and $Cl_{2(g)}$ are proven to be remarkably efficient oxidants as well as absorbent, in a wide pH range (*i.e.* from 3.5 to 8), differently from sodium chlorite, and thus they can improve the NO_x and SO_2 removal efficiencies ([66], [69], [70], [72], [106], [107]). Recent reports [72] suggest that the oxidation reaction pathways can be divided into two different reactive schemes, depending on whether the reaction occurs under acidic conditions or not.

The mechanism of $SO_{2(g)}$ absorption in water includes the liquid-gas phase equilibrium and the hydrolysis reactions in water (**Eqs. (10)-(12)**). When sodium chlorite is present, it dissociates in water into ClO_2^- and the SO_2 solubility increases, thanks to the occurrence of oxidation reactions between HSO_3^- and SO_3^{2-} with chlorite ions [72], [107], with so-called "*Basic Oxidation Mechanism"* (BOM) when the pH > 6:

$$HSO_3^- + ClO_2^- + H_2O \rightleftharpoons H_3O^+ + SO_4^{2-} + ClO^- \quad (63)$$

$$HSO_3^- + ClO^- + H_2O \rightleftharpoons H_3O^+ + SO_4^{2-} + Cl^- \quad (64)$$

$$SO_3^{2-} + ClO_2^- \rightleftharpoons SO_4^{2-} + ClO^- \quad (65)$$

$$SO_3^{2-} + ClO^- \rightleftharpoons SO_4^{2-} + Cl^- \quad (66)$$

Chlorite and hypochlorite ions (ClO_2^- and ClO^-) are in equilibrium with their associated acids according to the equations:

$$HClO_{2(aq)} + H_2O \rightleftharpoons H_3O^+ + ClO_2^- \quad (67)$$

$$HClO_{(aq)} + H_2O \rightleftharpoons H_3O^+ + ClO^- \quad (68)$$

The physical gas-liquid equilibrium equations of these acids are reported below:

$$HClO_{2(g)} \rightleftharpoons HClO_{2(aq)} \quad (69)$$

$$HClO_{(g)} \rightleftharpoons HClO_{(aq)} \quad (70)$$

Meanwhile, the dissociation reactions of sulfuric and hydrochloric acid (H_2SO_4 and HCl) coupled with the physical gas-liquid equilibria were reported in **Table II.2**.

The overall reaction of SO_2 with $NaClO_2$ solutions could be obtained from the previous equations, as proposed by different authors ([67]–[70], [108]):

$$2SO_{2(aq)} + ClO_2^- + 6H_2O \rightleftharpoons 4H_3O^+ + 2SO_4^{2-} + Cl^- \quad (71)$$

The mechanism of NO_x absorption in $NaClO_2$ solutions could be studied considering only the oxidation reaction pathways with chlorite ([67]–[70], [108]) due to the poor solubility of NO and NO_2 in water and the very slow hydrolysis reactions [107], [109] (see **Table II.2**). The oxidation reactions for NO_x absorption at pH > 6 (*Basic Oxidation Mechanism*, BOM) are reported below:

$$NO_{(aq)} + ClO_2^- \rightleftharpoons NO_{2(aq)} + ClO^- \quad (72)$$

$$NO_{(aq)} + ClO^- \rightleftharpoons NO_{2(aq)} + Cl^- \quad (73)$$

The overall oxidation reaction of NO to NO_2 in liquid phase is reported in following:

$$2NO_{(aq)} + ClO_2^- \rightleftharpoons 2NO_{2(aq)} + Cl^- \quad (74)$$

Nitrogen dioxide is much more soluble than NO (about 12 times) and, once formed by the oxidation reactions with chlorite, it can hydrolyze in water:

$$2NO_{2(aq)} + 3H_2O \rightleftharpoons 2H_3O^+ + NO_2^- + NO_3^- \quad (75)$$

Nitrites can be further oxidized to nitrates in the presence of chlorite ions:

$$NO_2^- + 0.5ClO_2^- \rightleftharpoons NO_3^- + 0.5Cl^- \quad (76)$$

The dissociation reactions of nitrous and nitric acid (HNO_2 and HNO_3) coupled with the physical gas-liquid equilibria were also reported in **Table II.2**.

The overall oxidation reaction of NO_2 to NO_3^- could be obtained from the sum of hydrolysis (**Eq. (75)**) and oxidation reactions (**Eq. (76)**):

$$4NO_{2(aq)} + ClO_2^- + 6H_2O \rightleftharpoons 4H_3O^+ + 4NO_3^- + Cl^- \quad (77)$$

In the literature, many authors ([67]–[70], [72], [107], [108]) consider a combination of the **Eqs. (74)** and **(77)** as a global NO_x oxidation reaction, which leads to the complete oxidation of NO to NO_2 and, after, to nitrates formation:

$$4NO_{(aq)} + 3ClO_2^- + 6H_2O \rightleftharpoons 4H_3O^+ + 4NO_3^- + 3Cl^- \quad (78)$$

Summing up, gaseous SO_2 and NO_x are spontaneously absorbed and oxidized by ClO_2^- ions to HNO_3 and H_2SO_4, respectively, given that the Gibbs free energies of the reactions reported in the **Eqs. (71) ,(74)** and **(77)** have negative values at room temperature and atmospheric pressure. **Zhao et al.** [71] and **Kaczur** [109] reported the standard redox potentials of the species involved in the reactions described above: ClO_3^-/Cl^- (1.45 V), ClO_2^-/ClO^- (1.64 V), ClO_2^-/Cl^- (1.57 V), ClO^-/Cl^- (0.89 V), NO_2/NO (1.07 V), SO_4^{2-}/SO_3^- (0.93 V), NO_3^-/NO (0.96 V), NO_3^-/NO_2^- (0.94 V). These values confirmed that the redox potentials of ClO_2^-/Cl^- and ClO_2^-/ClO^- are higher than the others and,

therefore, it is possible to assume that the previously reported reactions involving chlorite correctly describe the oxidation process. In addition, the studies of **Chien et al.** [65] showed that all the sulphur and nitrogen present as SO_2 and NO_x into flue-gas were completely converted to their maximum oxidation state, such as sulfates and nitrates. These results confirmed the hypotheses on the overall oxidation reactions (**Eqs. (71),(74)** and **(77)**) in the place of the entire oxidation mechanism equations. In acidic $NaClO_2$ solution, ClO_2^- ions are spontaneously converted to $ClO_{2(aq)}$ and $Cl_{2(aq)}$ in the presence of H_3O^+ ions, as follows ([72], [106], [108]–[110]):

$$5ClO_2^- + 4H_3O^+ \rightleftharpoons 4ClO_{2(aq)} + Cl^- + 6H_2O \quad (79)$$

$$ClO_2^- + 4H_3O^+ + 3Cl^- \rightleftharpoons 2Cl_{2(aq)} + 6H_2O \quad (80)$$

The overall reactions of SO_2 absorption in $NaClO_2$ solution under acidic conditions (*Acidic Oxidation Mechanism*, AOM, when the pH < 6) are shown below ([62], [66], [69], [71], [72], [108], [111]–[113]):

$$5SO_{2(aq)} + 2ClO_{2(aq)} + 18H_2O \rightleftharpoons 12H_3O^+ + 5SO_4^{2-} + 2Cl^- \quad (81)$$

$$SO_{2(aq)} + Cl_{2(aq)} + 6H_2O \rightleftharpoons 4H_3O^+ + SO_4^{2-} + 2Cl^- \quad (82)$$

An alternative reaction network, however equivalent to the previous reactions, involves the products of SO_2 hydrolysis in water (*i.e.* HSO_3^- and SO_3^{2-}) $NaClO_2$ solution under acidic conditions are shown below.

$$5HSO_3^- + 5SO_3^{2-} + 4ClO_{2(aq)} + 11H_2O \rightleftharpoons 9H_3O^+ + 10SO_4^{2-} + 4Cl^- \quad (83)$$

$$HSO_3^- + SO_3^{2-} + 2Cl_{2(aq)} + 7H_2O \rightleftharpoons 5H_3O^+ + 2SO_4^{2-} + Cl^- \quad (84)$$

NO is believed to oxidize to NO_2, which in turn is oxidized and absorbed as nitrates, thanks to the *Acidic Oxidation Mechanism*, AOM at pH < 6, ([66], [67], [69]–[72], [108], [113]–[115]):

$$5NO_{(aq)} + 2ClO_{2(aq)} + 3H_2O \rightleftharpoons 5NO_{2(aq)} + 2H_3O^+ + 2Cl^- \quad (85)$$

$$NO_{(aq)} + Cl_{2(aq)} + 3H_2O \rightleftharpoons NO_{2(aq)} + 2H_3O^+ + 2Cl^- \quad (86)$$

$$5NO_{2(aq)} + ClO_{2(aq)} + 9H_2O \rightleftharpoons 6H_3O^+ + 5NO_3^- + Cl^- \quad (87)$$

$$2NO_{2(aq)} + 3Cl_{2(aq)} + 12H_2O \rightleftharpoons 8H_3O^+ + 2NO_3^- + 6Cl^- \quad (88)$$

Part of the chlorine and chlorine dioxide is neutralized due to hydrolysis reactions in water [116]:

$$2ClO_{2(aq)} + 3H_2O \rightleftharpoons 2H_3O^+ + ClO_2^- + ClO_3^- \quad (89)$$

$$Cl_{2(aq)} + 3H_2O \rightleftharpoons 2H_3O^+ + ClO^- + Cl^- \quad (90)$$

The dissociation of chloric acid ($HClO_3$) and the physical gas-liquid equilibrium complete the absorption network in liquid phase:

$$HClO_{3(aq)} + H_2O \rightleftharpoons H_3O^+ + ClO_3^- \quad (91)$$

$$HClO_{3(g)} \rightleftharpoons HClO_{3(aq)} \quad (92)$$

In conclusion, NO_x and SO_2 removal using sodium chlorite in acidic solution involves a complex combination of reactions (all spontaneous with negative standard Gibbs free energy) and, due to the overlapping of different mechanisms ascribable to different active compounds, the NO_x and SO_2 removal efficiency of the system is enhanced. It is underlined that in general the acid gases absorption would be disfavored in an acid environment while, in this case, the pollutant removals are favored thanks to the formation of further oxidizers, *i.e.* ClO_2 and Cl_2.

Another important implication is related to the increase of NO_x absorption due to the effect of the simultaneous presence of SO_2 in the flue-gas: in fact, the absorption of SO_2 favors a rapid acidification of the solution, which in turn determines the formation of chlorine dioxide and chlorine ([70], [72], [106], [107], [110], [112], [114], [115], [117]). The standard redox potentials of ClO_2^-/Cl^- (1.59 V), ClO_2/Cl^- (1.51 V), Cl_2/Cl^- (1.35 V), retrieved by **Kaczur** [109]**,** confirmed that the value related to ClO_2 and ClO_2^- are very similar and also greater than the value of Cl_2. It is possible considering both the oxidation pathways (basic with chlorite and acidic with chlorine dioxide) as active reaction mechanisms under acidic conditions. When the $NaClO_2$ solution is acidified, the color of solution becomes light yellow (moderately acid pH) until to greenish (strongly acid pH) that are associated with the formation of ClO_2 associated to a pungent odor, due to its stripping [72], [106].

$$ClO_{2(g)} \rightleftharpoons ClO_{2(aq)} \quad (93)$$

$$Cl_{2(g)} \rightleftharpoons Cl_{2(aq)} \quad (94)$$

In fact, chlorine dioxide has a very low perceptive odor level at 1 - 2 ppm_v. The same odor can be perceived when NO_x is absorbed in the presence of SO_2, which causes a quick acidification of the solution and the develop of chlorine gas.

Generally, the oxidation with chlorine is not accounted since the formation of chlorine from chlorite decomposition is considered as negligible. In fact, during the experimental tests carried out by **Park et al.** [72], the UV-vis absorptions of the ClO_2^-, Cl_2 and ClO_2 species in $NaClO_2$ solution were monitored at different pH levels, prior to the reaction with NO and SO_2, as presented in **Figure II.2.**

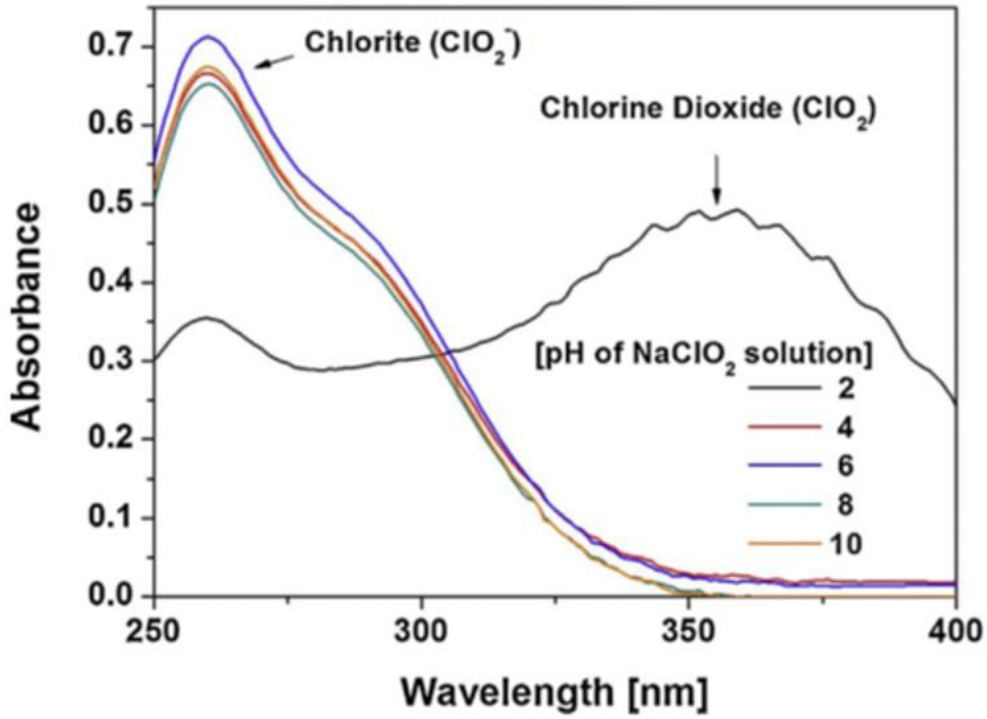

Figure II.2. *UV-vis absorption spectrum related to Cl^-, ClO_2^-, ClO^-, Cl_2 and ClO_2 in sodium chlorite solutions for different pH values* [72]

The absorption wavelengths of Cl^-, ClO_2^-, ClO^-, Cl_2 and ClO_2 are centered at 190, 259, 293, 330, and 358 nm, respectively [65], [109]. Based on the experimental data, a relatively high concentration of chlorite was present in the pH range of 4 - 10, whereas no meaningful absorption peaks for Cl_2 and ClO_2 were detectable in this pH range. It can thus be deduced that most of the NO and SO_2 can be absorbed and oxidized by ClO_2^- ions in the pH range of 4 - 10.

On the other hand, at pH = 2.0, the intensity of the absorption peak of chlorine dioxide markedly increased due to the occurrence of the reactions presented in the **Eqs. (79)** and **(80)** in the presence of H_3O^+ ions, under strongly acidic conditions. Chlorine (Cl_2) was not readily detected in the UV-vis absorption spectra because it only exists in the gas phase and it can be considered as a secondary pollutant under strongly acidic conditions of $NaClO_2$ solution.

The studies of **Park et al.** [72] were recently confirmed by **Hao et al.** [111]. They showed that that the formation of chlorine dioxide could be observed even at pH values higher than 2: these studies confirmed that the acidic conditions are responsible for the chlorine dioxide formation. **Hao et al.** [111] also measured the absorbance of ClO_2 at different pH and temperatures, confirming a significant and somewhat complex influence of these parameters on the amount of ClO_2 produced.

Figure II.3 shows the absorbance tests of chlorine dioxide by varying the pH and temperature of the analyzed solution (100 mL and 2% of $NaClO_2$).

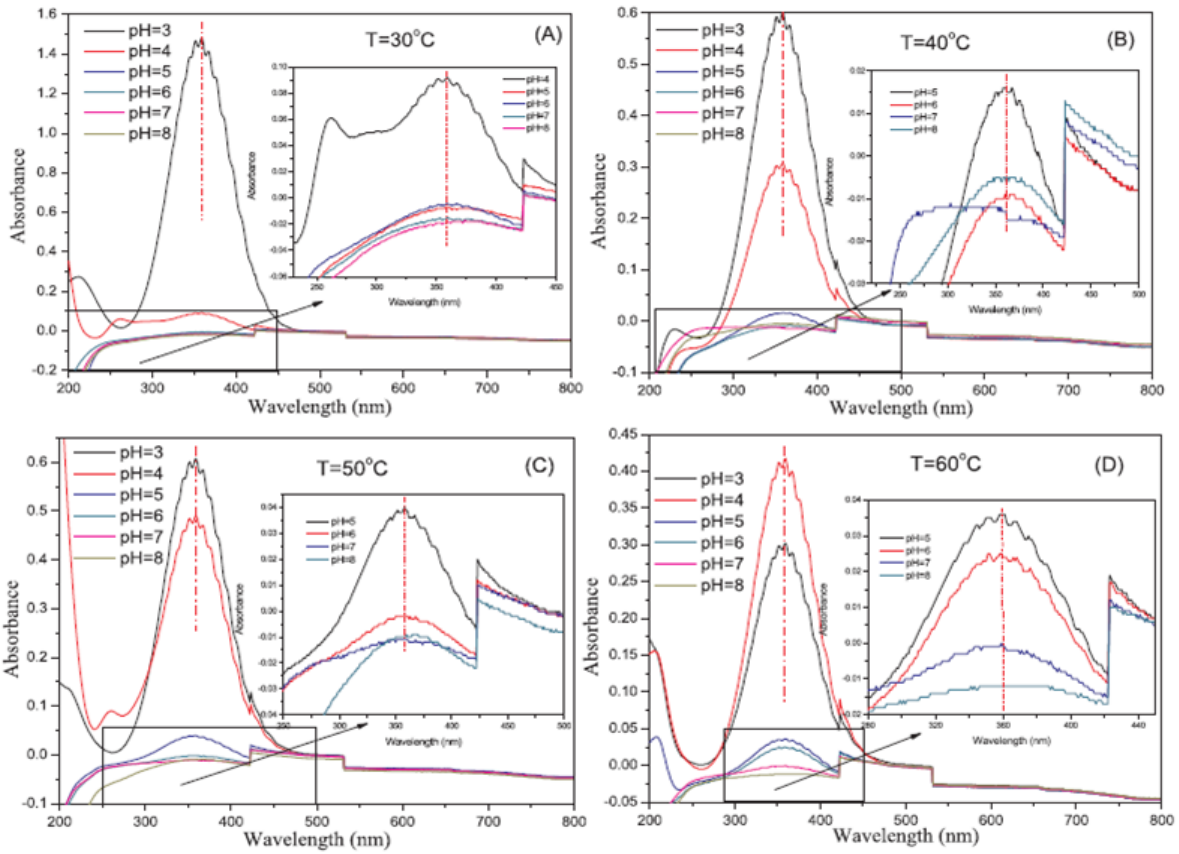

Figure II.3. *UV-Vis spectrum related to ClO_2 for different pH and temperature values. A solution pH = 3,4,5,6,7,8 and temperatures of 30 °C (A), 40 °C (B), 50 °C (C) and 60 °C (D) are considered. The total concentration of $NaClO_2$ is 2% in a 100 mL solution* [111]

Figure II.3 showed that a decrease in pH leads to an increase in the rate of chlorine dioxide generation by the decomposition reaction of chlorite (**Eq. (79)**) under acidic conditions. On the contrary, when the initial solution pH is kept constant, it can be observed that the temperature has a double effect: on the one hand it promotes an increase in the decomposition rate of ClO_2^- with formation of chlorine dioxide, on the other hand it favors the transfer of $ClO_{2(aq)}$ to the gaseous phase, due to the reduction of the solubility related to the increase in the temperature, with consequent reduction of the absorbance peak of this chemical species even under acidic pH conditions. This effect is amplified in the temperature range 50 - 60 °C and for pH values 3, 4 and 5. The results in **Figure II.3** confirmed that chlorine dioxide desorption in gaseous phase could reduce the oxidizing powerful in aqueous solution, but at the same time activates a *Gaseous Oxidation Mechanism* (GOM).

Figure II.4 shows the absorbance peaks of chlorine dioxide at 50 °C and pH = 3 after the addition of different ion contents in 100 mL of $NaClO_2$ solution at 2% [111].

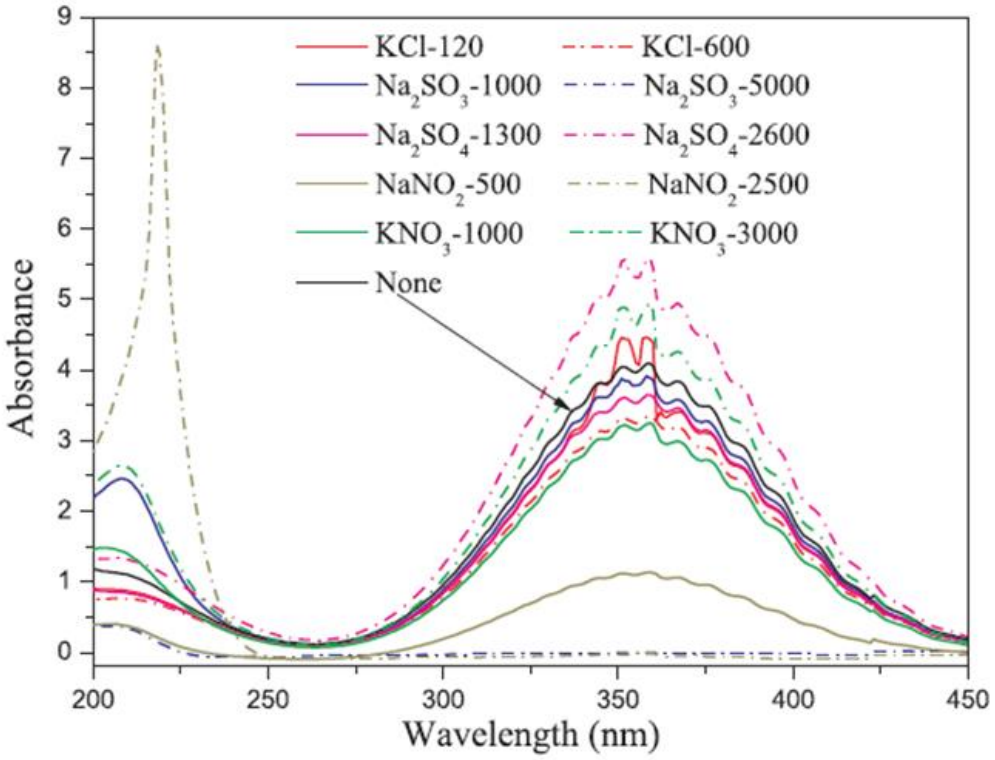

Figure II.4. *UV-Vis spectrum related to ClO_2 after addition of different ionic contents. Concentration of sodium chlorite in solution: 2%, volume of the solution: 100 mL, temperature and the pH: 50 °C and 3.0, respectively* [111]

Hao et al. [111] also showed that high concentrations of sulfates (SO_4^{2-}) and nitrates (NO_3^-) determined an increase in the peak of the ClO_2 absorbance (**Figure II.4**): this effect can be ascribed to the high electrolytic strength and to the capacity that such ions have to modify the activity coefficients in aqueous solution. On the contrary, high concentrations of sulfites (SO_3^{2-}) and nitrites (NO_2^-) inhibit the formation of ClO_2, except at low concentrations of sulfite which had no significant effect (**Figure II.4**). Differently, the chlorides (Cl^-) did not have a significant effect on the formation of dioxide even though **Deshwal et al.** [114] showed that when chloride content increased in solution, chlorine formation was favored. **Mo et al.** [118] showed that the conversion of sodium chlorite in chlorine dioxide in the presence of hydrochloric acid, and therefore of chlorides in acid conditions, was favored.

Regarding to molecular chlorine, it was not detected by absorption spectra because the Cl_2 generated in the liquid phase is directly transferred to the gas phase, interacting with SO_2 and NO_x.

Although a major part of the oxidizers is used for the oxidation of NO_x to nitrate and SO_2 to sulfate, a non-negligible fraction might escape away causing a secondary pollution. Usually, $ClO_{2(g)}$ and $Cl_{2(g)}$ concentrations in the outlet gas are negligible at pH values equal or greater than 3.0, probably due to the high solubility of these gases in aqueous solution [114] and also because a quick reactive

mechanism (*Gaseous Oxidation Mechanism*, GOM) between $ClO_{2(g)}$ and $Cl_{2(g)}$ and other pollutants in the gaseous stream could also occur [108], [119]. Therefore, the reactive mechanisms occurring in aqueous solution (**Eqs. (81)-(88)**) must be considered also for the gas phase (GOM):

$$5SO_{2(g)} + 2ClO_{2(g)} + 6H_2O_{(g)} \rightleftharpoons 5H_2SO_{4(g)} + 2HCl_{(g)} \quad (95)$$

$$SO_{2(g)} + Cl_{2(g)} + 2H_2O_{(g)} \rightleftharpoons H_2SO_{4(g)} + 2HCl_{(g)} \quad (96)$$

$$5NO_{(g)} + 2ClO_{2(g)} + H_2O_{(g)} \rightleftharpoons 5NO_{2(g)} + 2HCl_{(g)} \quad (97)$$

$$NO_{(g)} + Cl_{2(g)} + H_2O_{(g)} \rightleftharpoons NO_{2(g)} + 2HCl_{(g)} \quad (98)$$

$$5NO_{2(g)} + ClO_{2(g)} + 3H_2O_{(g)} \rightleftharpoons 5HNO_{3(g)} + HCl_{(g)} \quad (99)$$

$$2NO_{2(g)} + 3Cl_{2(g)} + 4H_2O_{(g)} \rightleftharpoons 2HNO_{3(g)} + 6HCl_{(g)} \quad (100)$$

The presence of secondary pollutants such as chlorine and chlorine dioxide in the flue-gas after the wet-oxidation scrubbing was verified by **Tang et al.** [119]**.** They performed some experiments with a double bubble column: in the first, oxidation occours with consequent absorption of $SO_{2(g)}$ and $NO_{x(g)}$ using a 0.1% w/w $NaClO_2$ solution, while in the second the $ClO_{2(g)}$ and $Cl_{2(g)}$ were absorbed with a 5% wt/wt NaOH concentrate solution. The oxidation column was fed with a simulated flue-gas at 2 $L \cdot min^{-1}$ containing SO_2 = 1015 ppm_v, NO = 510 ppm_v, O_2 = 7.20% vol. and N_2 as gas balance. The absorption column was fed with a part of the gas coming from the oxidation section (0.5 $L \cdot min^{-1}$). The oxidation and absorption solution were both 1.0 L at 50 °C. The experimental analyses aimed at verifying the presence of Cl^- and ClO_2^- in solution that could be attributed to the former presence of $Cl_{2(g)}$ and $ClO_{2(g)}$ in the gas. In fact, in alkaline conditions, Cl_2 is rapidly hydrolyzed to Cl^- and ClO^- (following **Eq. (90)**), while ClO_2 is converted to ClO_2^- and ClO_3^- (following **Eq. (89)**). The concentration of $Cl_{2(g)}$ was approximately constant for the whole experiment (0.14 - 0.17 ppm_v), and much less than that of $ClO_{2(g)}$ (maximum value equal to 6.65 ppm_v). This result confirmed that the major chlorine-based component contained in the gaseous stream emitted from the oxidation column was mainly $ClO_{2(g)}$. In addition, the initial oxidation liquid was colourless and transparent, then gradually turned into yellow light, and finally greenish as long as all of chlorine-containing ions were transferred in the absorption solution, *i.e.* chlorides in greater quantities, unreacted chlorites and a certain amount of chlorates (deriving from the hydrolysis of $ClO_{2(aq)}$).

Tables II.4–5 resume the physical gas-liquid equilibrium parameters and chemical equilibrium parameters involved in SO_2 and NO_x absorption when a sodium chlorite aqueous solution is used as absorbing solution.

On the other hand, **Table II.6** shows the parameters of the chemical equilibria in the gas phase that occur between $SO_{2(g)}$ and $NO_{x(g)}$ with $Cl_{2(g)}$ and $ClO_{2(g)}$.

Table II.4. *Physical gas-liquid equilibrium parameters (**Eq. (27)**)and enthalpy of gas dissolution values of the components involved in SO_2 and NO_x absorption in sodium chlorite aqueous solutions*

Eq.	Physical gas-liquid Equilibria	ΔH_s $kJ \cdot mol^{-1}$	Constant Parameters				Ref.
			A_H atm	B_H K	C_H K^{-1}	D_H K^{-1}	
(70)	$HClO_{(g)} \rightleftharpoons HClO_{(aq)}$	-49.1	-22.27	5900	0	0	[84]
(67)	$HClO_{2(g)} \rightleftharpoons HClO_{2(aq)}$	-49.1	-22.27	5900	0	0	[84]
(92)	$HClO_{3(g)} \rightleftharpoons HClO_{3(aq)}$	-49.1	-22.27	5900	0	0	[84]
(93)	$ClO_{2(g)} \rightleftharpoons ClO_{2(aq)}$	-29.1	-56.73	-143	10.75	0	[88]
(94)	$Cl_{2(g)} \rightleftharpoons Cl_{2(aq)}$	-16.6	-108.38	2428	19.19	$8.92 \cdot 10^{-4}$	[86]

Table II.5. *Chemical equilibrium parameters (**Eq. (28)**) and standard Gibbs free energies values of the reactions involved in SO_2 and NO_x absorption in sodium chlorite aqueous solutions*

Eq.	Chemical reaction Equilibria	ΔG_r° $kJ \cdot mol^{-1}$	Constant Parameters				Ref.
			A_{eq} $(mol \cdot mol^{-1})^{p-r}$	B_{eq} K	C_{eq} K^{-1}	D_{eq} K^{-1}	
(63)	$HSO_3^- + ClO_2^- + H_2O \rightleftharpoons H_3O^+ + SO_4^{2-} + ClO^-$	-270.8	-4.02	32569	0	0	Eq. (26)
(64)	$HSO_3^- + ClO^- + H_2O \rightleftharpoons H_3O^+ + SO_4^{2-} + Cl^-$	-311.2	-4.02	37432	0	0	Eq. (26)
(65)	$SO_3^{2-} + ClO_2^- \rightleftharpoons SO_4^{2-} + ClO^-$	-312.1	0	37528	0	0	Eq. (26)
(66)	$SO_3^{2-} + ClO^- \rightleftharpoons SO_4^{2-} + Cl^-$	-352.4	0	42390	0	0	Eq. (26)
(71)	$5SO_{2(aq)} + ClO_2^- + 6H_2O \rightleftharpoons 4H_3O^+ + 2SO_4^{2-} + Cl^-$	-623.6	-16.06	75004	0	0	Eq. (26)
(74)	$2NO_{(aq)} + ClO_2^- \rightleftharpoons 2NO_{2(aq)} + Cl^-$	-270.3	8.92	32514	0	0	Eq. (26)
(77)	$4NO_{2(aq)} + ClO_2^- + 6H_2O \rightleftharpoons 4H_3O^+ + 4NO_3^- + Cl^-$	-352.3	-1.72	42379	0	0	Eq. (26)
(78)	$4NO_{(aq)} + 3ClO_2^- + 6H_2O \rightleftharpoons 4H_3O^+ + 4NO_3^- + 3Cl^-$	-790.4	8.95	95065	0	0	Eq. (26)
(79)	$5ClO_2^- + 4H_3O^+ \rightleftharpoons 4ClO_{2(aq)} + Cl^- + 6H_2O$	-211.1	16.07	25387	0	0	Eq. (26)
(80)	$ClO_2^- + 4H_3O^+ + 3Cl^- \rightleftharpoons 2Cl_{2(aq)} + 6H_2O$	-50.5	24.10	10090	0	0	Eq. (26)
(101)	$5HSO_3^- + 2ClO_{2(aq)} + 8H_2O \rightleftharpoons 7H_3O^+ + 5SO_4^{2-} + 2Cl^-$	-2905	-641.80	349415	0	0	Eq. (26)
(102)	$HSO_3^- + Cl_{2(aq)} + 4H_2O \rightleftharpoons 3H_3O^+ + SO_4^{2-} + 2Cl^-$	-372	-16.07	44741	0	0	Eq. (26)
(103)	$5SO_3^{2-} + 2ClO_{2(aq)} + 3H_2O \rightleftharpoons 2H_3O^+ + 5SO_4^{2-} + 2Cl^-$	-1555	4.02	187104	0	0	Eq. (26)
(104)	$SO_3^{2-} + Cl_{2(aq)} + 3H_2O \rightleftharpoons 2H_3O^+ + SO_4^{2-} + 2Cl^-$	-53.1	0	6394	0	0	Eq. (26)
(81)	$5SO_{2(aq)} + 2ClO_{2(aq)} + 18H_2O \rightleftharpoons 12H_3O^+ + 5SO_4^{2-} + 2Cl^-$	-1410	-48.21	169646	0	0	Eq. (26)

(82)	$SO_{2(aq)} + Cl_{2(aq)} + 6H_2O \rightleftharpoons 4H_3O^+ + SO_4^{2-} + 2Cl^-$	-353.3	-16.07	42494	0	0	Eq. (26)
(85)	$5NO_{(aq)} + 2ClO_{2(aq)} + 3H_2O \rightleftharpoons 2H_3O^+ + 5NO_{2(aq)} + 2Cl^-$	-489.4	5.31	58859	0	0	Eq. (26)
(86)	$NO_{(aq)} + Cl_{2(aq)} + 3H_2O \rightleftharpoons 2H_3O^+ + NO_{2(aq)} + 2Cl^-$	-114.9	-9.38	13822	0	0	Eq. (26)
(87)	$5NO_{2(aq)} + ClO_{2(aq)} + 9H_2O \rightleftharpoons 6H_3O^+ + 5NO_3^- + Cl^-$	-251.6	-22.24	30258	0	0	Eq. (26)
(88)	$2NO_{2(aq)} + 3Cl_{2(aq)} + 12H_2O \rightleftharpoons 8H_3O^+ + 2NO_3^- + 6Cl^-$	-197.1	-37.02	23694	0	0	Eq. (26)
(89)	$2ClO_{2(aq)} + 3H_2O \rightleftharpoons 2H_3O^+ + ClO_2^- + ClO_3^-$	6.18	-8.03	-743	0	0	Eq. (26)
(90)	$Cl_{2(aq)} + 3H_2O \rightleftharpoons 2H_3O^+ + ClO^- + Cl^-$	62.2	-12.05	-7476	0	0	Eq. (26)
(68)	$HClO_{(aq)} + H_2O \rightleftharpoons H_3O^+ + ClO^-$	13.3	-16.15	-1603	0	0	[87]
(67)	$HClO_{2(aq)} + H_2O \rightleftharpoons H_3O^+ + ClO_2^-$	11.3	-4.01	-1359	0	0	Eq. (26)
(91)	$HClO_{3(aq)} + H_2O \rightleftharpoons H_3O^+ + ClO_3^-$	14.2	-4.01	-1708	0	0	Eq. (26)

Table II.6. *Chemical equilibrium parameters (**Eq. (28)**) and standard Gibbs free energies values of the reactions involved in SO_2 and NO_x absorption system in sodium chlorite aqueous solutions*

Eq.	**Chemical reaction Equilibria**	ΔG_r° $kJ \cdot mol^{-1}$	**Constant Parameters** A_{eq} $(mol \cdot mol^{-1})^{p-r}$	B_{eq} K	C_{eq} K^{-1}	D_{eq} K^{-1}	**Ref.**
(95)	$5SO_{2(g)} + 2ClO_{2(g)} + 6H_2O_{(g)} \rightleftharpoons 5H_2SO_{4(g)} + 2HCl_{(g)}$	-826.54	-19.17	99410	0	0	Eq. (26)
(96)	$SO_{2(g)} + Cl_{2(g)} + 2H_2O_{(g)} \rightleftharpoons H_2SO_{4(g)} + 2HCl_{(g)}$	-86.73	-6.39	10431	0	0	Eq. (26)
(97)	$5NO_{(g)} + 2ClO_{2(g)} + H_2O_{(g)} \rightleftharpoons 5NO_{2(g)} + 2HCl_{(g)}$	-379.52	-3.19	45646	0	0	Eq. (26)
(98)	$NO_{(g)} + Cl_{2(g)} + H_2O_{(g)} \rightleftharpoons NO_{2(g)} + 2HCl_{(g)}$	2.67	0	-321	0	0	Eq. (26)
(99)	$5NO_{2(g)} + ClO_{2(g)} + 3H_2O_{(g)} \rightleftharpoons 5HNO_{3(g)} + HCl_{(g)}$	-160.47	-9.58	19300	0	0	Eq. (26)
(100)	$2NO_{2(g)} + 3Cl_{2(g)} + 4H_2O_{(g)} \rightleftharpoons 2HNO_{3(g)} + 6HCl_{(g)}$	90.34	-3.19	-10865	0	0	Eq. (26)

It is remarked that for the SO_2 and NO_x absorption system, the equations set of physical gas-liquid and chemical reaction equilibria shown in **Tables II.4–6** must be coupled with those reported in **Tables II.1–2**.

In the 1970s, the kinetics of NO_x and SO_2 absorption in $NaClO_2$ aqueous solutions was studied by **Teramoto et al.** [120] and **Sada et al. (**[62], [121], [122]**)**. They performed a series of NO absorption kinetics studies at different NO and $NaClO_2$ initial concentrations, initial pH values of absorbent solution and using a semi-batch agitated vessel with a flat gas-liquid interface. In the 90's, **Brogren et al.** [110] and **Hsu et al.** [63] performed similar tests using a packed column and a stirred tank, respectively.

The mass transfer of the component *A* from gas to liquid can be expressed by the absorption rate (N_A, [kmol·m^{-3}·s^{-1}]) according to the two-film model [123]–[125] showed in **Figure II.5**:

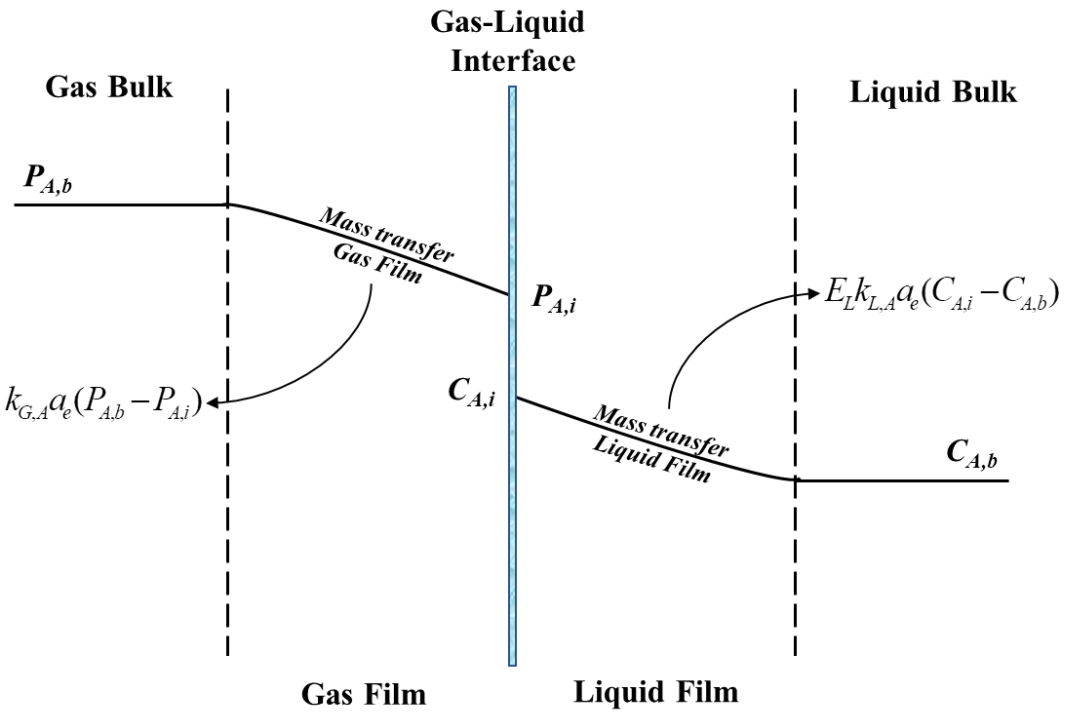

Figure II.5. *Scheme of the two-film theory for the absorption of component A from the gaseous to the liquid phase*

The equation that describe the absorption rate (N_A) considering the mass transfer contribution in the gas and liquid phase is reported below:

$$N_A = k_{G,A} a_e (P_{A,b} - P_{A,i}) = E_L k_{L,A} a_e (C_{A,i} - C_{A,b}) \quad (105)$$

where $k_{G,A}$ [kmol·m^{-3}·atm^{-1}·s^{-1}] is the gas-side mass transfer coefficient of component *A*; $k_{L,A}$ [s^{-1}] is the liquid-side mass transfer coefficient of component *A*; a_e [m^2·m^{-3}] is the effective surface area for mass transfer; $P_{A,b}$ and $P_{A,i}$ are the partial pressures [atm] of gas component *A*, in the bulk and at interface, respectively; $C_{A,b}$ and $C_{A,i}$ are the liquid concentrations [kmol·m^{-3}] of component *A*, in the bulk and at interface, respectively; E_L is the enhancement factor for the reaction in the liquid phase. The enhancement factor represents a useful indication of the limiting step of the process; it is defined as the ratio between the actual mass transfer rate in the liquid phase in the presence of chemical reactions and the corresponding mass transfer rate due to diffusion and convective phenomena. Therefore, its value is equal to 1 for physical absorption [125], [126]. The mass transfer rate in a liquid-gas separation process is increased in the presence of one or more chemical reactions in aqueous phase. Two main cases can be cited [52]: if the chemical reaction is instantaneous, the process is governed by the mass transfer rate, while in the case of a non-instantaneous chemical

reaction it is controlled by the kinetics of the reaction. Many textbooks [125], [126] have focused on the gas-liquid mass transfer with chemical reaction in liquid phase and have classified the reaction regimes into fast, moderate or slow, also distinguishing when the reagent in liquid phase is in excess or not.

The enhancement factor (E_L) can be expressed according to the Hatta number (*Ha*). Hatta number is defined as the maximum possible reaction rate of component *A* in the film related to the maximum transfer rate of the same component *A*.

The numerical solution is usually presented in the graphical form given by **Zarzycki and Chacuk** [125]. This graph correlates the enhancement factor (E_L) with the Hatta number (*Ha*), parametric in the enhancement factor for an instantaneous reaction (E_∞), which is defined as:

$$E_\infty = 1 + \frac{\nu_A}{\nu_B}\frac{k_{L,B}C_{B,b}}{k_{L,A}C_{A,i}} = 1 + \frac{\nu_A}{\nu_B}\sqrt{\frac{D_{L,B}}{D_{L,A}}}\frac{C_{B,b}}{C_{A,i}} \tag{106}$$

in which, υ_A and υ_B are the stoichiometric coefficients of component *A* (gas absorbed) and component *B* (reagent), $D_{L,A}$ [$m^2 \cdot s^{-1}$] and $D_{L,B}$ [$m^2 \cdot s^{-1}$] are the diffusivity of component *A* and *B* in the liquid, $C_{A,i}$ [$kmol \cdot m^{-3}$] e $C_{B,b}$ [$kmol \cdot m^{-3}$] are the liquid concentrations of component *A* at interface and component *B* in the bulk liquid.

The approximate analytical solution for E_L was first proposed by **Zarzycki and Chacuk** [125] and can be expressed by the following equation:

$$E_L = \frac{\sqrt{\dfrac{Ha(E_\infty - E_L)}{(E_\infty - 1)}}}{tgh\sqrt{\dfrac{Ha(E_\infty - E_L)}{(E_\infty - 1)}}} \tag{107}$$

The maximum error of the enhancement factor calculated from this equation and obtained from a numerical solution is less than 3%. Unfortunately, **Eq. (107)** is implicit in E_L and the solution had to be calculated by an iterative method. To avoid this inconvenience, several equations were proposed for calculating the enhancement factor E_L in an explicit form. One of such equations, which is simple and precise (maximum error is less than 5%), was proposed by **Zarzycki and Chacuk** [125].

$$\left(E_L - 1\right)^{-1.35} = (E_\infty - 1)^{-1.35} - \left(\frac{\sqrt{Ha}}{tgh\sqrt{Ha}} - 1\right)^{-1.35} \tag{108}$$

Many authors ([62], [63], [110], [121], [122]) have confirmed that the reaction rates related to chlorite oxidation fall within the fast regime because $Ha > 3$ and the chemical reaction occurs in the liquid

film. In a fast reaction regime ($Ha > 3$), $E = Ha$ ([62], [63], [110], [121]–[123], [125], [126]) and the Hatta number is equal to:

$$Ha = \frac{\sqrt{D_{L,A} K C_{A,i}}}{k_{L,A}^2} \tag{109}$$

Where K [s^{-1}] is rate constant of the reaction.

This expression is valid when the reagent B in liquid bulk ($C_{B,b}$) is stoichiometrically in excess with respect to the concentration of the component A ($C_{A,i}$) in liquid phase. If not, the concentration of the reagent in the bulk ($C_{B,b}$) cannot be incorporated in the kinetic constant (K) and the Hatta number must be expressed as following:

$$Ha = \frac{\sqrt{D_{L,A} K C_{A,i} C_{B,b}}}{k_{L,A}^2} \tag{110}$$

Under these kinetic regime conditions, the absorption rate can be expressed as:

$$N_A = \Delta P_A \left(\frac{1}{k_{G,A} a_e} + \frac{k_{L,A} K_{H_A}}{a_e \sqrt{\frac{2}{m+1} D_{L,A} K C_{A,i}^{m+1} C_{B,b}^n}} \right)^{-1} \tag{111}$$

in which, ΔP_A [atm] is driving force for absorption (difference between the partial pressure of A in the bulk and at the interface), K_{H_A} [atm·m^3·$kmol^{-1}$] is the Henry constant of the component A, m is the reaction order of component A and n is the reaction order of reagent B.

According to **Lancia et al.** [127] if the gas-liquid contact is well mixed, $\Delta P_A = (P_{A,b} - K_{HA} C_{A,i})$ can be evaluated by substituting $P_{A,b}$ with $P_{A,AV}$ (representative of average gas-phase composition, which is the logarithmic mean between $P_{A,in}$ and $P_{A,out}$) and $C_{A,i}$ with the $C_{A,b}$ concentration.

$$\Delta P_A = P_{A,AV} - C_{A,b} \tag{112}$$

$$P_{A,AV} = \frac{P_{A,in} - P_{A,out}}{Ln\left(\frac{P_{A,in}}{P_{A,out}} \right)} \tag{113}$$

Where $P_{A,in}$ [atm] is the partial pressure of A in the gas stream before absorption, while $P_{A,out}$ [atm] is the partial pressure of A in the gas stream after absorption.

According to the two-film model, for a fast reaction, the gas component A is exhausted before it spreads into the liquid phase; thus, the concentration of A in the bulk liquid phase is 0 [127]. Therefore, the equation can be further simplified as following:

$$N_A = \left(P_{A,AV}\right)\left(\frac{1}{k_{G,A}a_e} + \frac{k_{L,A}K_{H_A}}{a_e\sqrt{\frac{2}{m+1}D_{L,A}KC_{A,i}^{m+1}C_{B,b}^{n}}}\right)^{-1} \quad (114)$$

Using this expression for absorption rate, **Sada et al.** ([62], [121], [122]), **Brogen et al.** [110] and **Hsu et al.** [63] evaluated the kinetic constant of reaction (K_d) for NO (A) with $NaClO_2$ (B) in **Eq. (78)** and in the presence of sodium hydroxide (NaOH). The reaction order of NO = *m* and $NaClO_2$ = *n* can be found through the slope of lines in log-log plots of $C_{A,i}$ and $C_{B,b}$ versus N_A, respectively.

A summary of the above mentioned studies on NO absorption rate in $NaClO_2$/NaOH solutions, at different pH and temperature values, is listed in **Table II.7**.

Table II.7. *Relevant kinetic studies of NO absorption with $NaClO_2$ solutions* [65]

Eq.	$C^{\circ}_{NO_x}$ ppm_v	C_{NaClO_2} $mol\cdot L^{-1}$	C_{NaOH} $mol\cdot L^{-1}$	***pH*** -	***T*** ° C	***(m)*** -	***(n)*** -	K_d $(kmol\cdot m^{-3})^{1-r}\cdot s^{-1}$	**Ref.**
(78)	8000 - 150000	0.1 - 1.5	0.05 - 0.5	-	25	25	25	$3.80\cdot10^{12}\,e^{(-3.73[NaOH])}$	[62]
(78)	5000 - 75000	0.29 - 1.64	0.015	-	25	25	25	$2.10\cdot10^{12}$	[120]
(78)	1500 - 150000	0.25 - 2.0	0.2 - 1.5	-	25	25	25	$7.32\cdot10^{8}$	[121]
(78)	290	0.1 - 1.0	-	8	20	20	20	$1.55\cdot10^{6}$	[110]
(78)	290	0.1 - 1.0	-	9	20	20	20	$1.40\cdot10^{6}$	[110]
(78)	290	0.1 - 1.0	-	10	20	20	20	$3.80\cdot10^{5}$	[110]
(78)	290	0.1 - 1.0	-	11	20	20	20	$1.22\cdot10^{4}$	[110]
(78)	200 - 1000	0.05 - 1.0	-	9.2 - 9.9	30	30	30	$6.55\cdot10^{8}$	[63]

In more recent studies, **Chien et al.** [65] have investigated the NO reaction kinetics in $NaClO_2$ solution in the presence of SO_2, working at low NO and SO_2 concentrations, *i.e.* 100 - 800 ppm_v and 0 - 1500 ppm_v, respectively. These gases were diluted with oxygen at a 9% vol/vol concentration, balance nitrogen.The $NaClO_2$ concentrations in the initial solution ranged between 0.001 - 0.05 M and the solution pH was adjusted with HCl and NaOH to reach values between 4 and 10. The temperature range was 26 - 65 °C and the pressure 1 atm.

The experimental set-up was a spraying column where the simulated flue-gas flowed continuosly, and the scrubbing solution was also sprayed continuosly without recirculation.

The range of rate constants of NO measured, when SO_2 was not present in the gas flue, were between $1.32\cdot10^{7}$ and $1.21\cdot10^{8}$ $(mol\cdot L^{-1})^{-3}\cdot s^{-1}$.

According to **Chien et al.** [65], the absorption rate increases with NO and $NaClO_2$ concentrations while the influence of gas-liquid contact time and temperature on the absortpion rate is not significant under the investigated range of operating parameters. In fact, although the solubility of NO decreases by increasing the temperature, the reaction rate increases. These two opposite effects compensate

each other and determine a negligible effect of the operating temperature. Moreover, the absorption rate increases as the initial pH value decreases while the rate constant increases as the initial pH value decreases from 10 to 7. This may be due to the oxidative power of $NaClO_2$ that increases as the pH decreases ([72], [106], [109], [110], [115]). Nevertheless, the rate constant slightly increases and reaches a plateau as the pH value decreases from 7 to 4, probably because the solubility of NO decreases by increasing the ionic strength. For **Eq. (78)**, the reaction order of NO (*m*) is 2 and this value is consistent with the results of **Sada et al.** ([62], [121], [122]), **Brogen et al.** [110] and **Hsu et al.** [63]. The reaction order of $NaClO_2$ (*n*) is 2 and this value is higher than the value retrieved by **Sada et al.** ([62], [121], [122]), **Brogen et al.** [110] and **Hsu et al.** [63], and may have resulted from the pH values of $NaClO_2$ solutions, which are different from those adopted in the other researches. Furthermore, the reaction rate constant usually varies with temperature according to the Arrhenius equation; the average activation energy resulted to 53.97 $kJ \cdot mol^{-1}$ and the frequency factor (k_o) equal to $6.93 \cdot 10^{16}$ $(mol \cdot L^{-1})^{-3} \cdot s^{-1}$.

Chien et al. [65] investigated also the reaction kinetics of the simultaneous absorption of SO_2 and NO (with experimental conditions described above). First, they studied the effect of NO concentration on its absorption rate at constant SO_2 concentration (at 1000 ppm_v). The experimental results showed that NO absortpion rate increases with NO concentration, but the SO_2 absorption rate is not affected by NO concentration. A possible explanation is that the solubility of SO_2 is much higher than that of NO, and also the competition with NO for the reaction with $NaClO_2$ was favored towards the oxidation of SO_2. Conversely, at constant NO concentration (320 ppmv), SO_2 absorption rate increases with SO_2 concentration because SO_2 absorption is a gas-phase controlled process, but simultaneously the NO absorption rate slightly decreases, likely for competion effect in the oxidation reactions. Similar results were reported by **Sada et al.** [62]. Besides, SO_2 solubility into $NaClO_2$ solution is much higher than the corresponding of NO, thus determining a higher SO_2 reaction rate. For the same reason, the NO absorption rate in the presence of SO_2 is lower when compared with the value retrieved for NO single-compound removal from the simulated flue-gas ([66], [69], [72], [112], [128]).

During the experiments, **Chien et al.** [65] observed that the decrease of pH deriving from SO_2 absorption leads to the formation of chlorine dioxide and chlorine that oxidize NO and SO_2, although it is difficult to quantify the ClO_2 gas produced. However, the color of the aqueous solution became yellow-green with pungent odor due to ClO_2 formation, this effect also observed by **Adewuyi et al.** [113] experiments. In particular, ClO_2 is produced during the absorption process but only in the simultaneous removal of SO_2 and NO experiments. Therefore, ClO_2 could be formed also in the presence of NO alone, but the pH value of $NaClO_2$ solution used for absorption experiments might

be not low enough to form the ClO_2. However, in the aforementioned research there are not information about kinetics of desulphurization with a $NaClO_2$ solution and thus further studies on kinetics of SO_2 and NO simultaneous removal are reported in the following.

Zhao et al. [71] conducted some experimental runs on the simultaneous absorption of NO and SO_2 in a bubble reactor, which greatly decreases mass transfer resistance and accelerates the reaction rates. The tests were performed keeping the initial concentration of NO at 500 $mg \cdot m^{-3}$ and by varying the SO_2 initial concentration in the range 550 - 3079 $mg \cdot m^{-3}$ and, subsequently, keeping SO_2 at 2000 $mg \cdot m^{-3}$ and varying NO initial concentration from 280 to 1550 $mg \cdot m^{-3}$.

The concentration of $NaClO_2$ was 0.005 mol/L and the corresponding initial pH was 5. The experimental results showed that the reaction is divided into two zones over time, namely the fast and slow reaction zones. This could be due to the formation of ClO_2 and Cl_2 from $NaClO_2$ in acid solution. Initially, they react with SO_2 and NO in the fast reaction zone; thereafter, the reaction rates decrease due to consumption of these coumpounds by oxidation reaction with SO_2 and NO and the concentrations of the two pollutants approximately decline linearly with time in the slow reaction zone, which corresponds to the typical zero order reaction.

The removal efficiency of SO_2 increases with the initial concentration of SO_2 during a certain time. It may be speculated that the gas-liquid mass transfer is enhanced when the partial pressure of SO_2 increases. For the reaction reported in **Eq. (71)**, when the temperature was set at 50 °C, the frequency factor (k_o) was 1.22 $(mol \cdot L^{-1})^{-0.4} \cdot s^{-1}$, the activation energy (E_a) is 66.25 $kJ \cdot mol^{-1}$ and the reaction order was 1.4 in the quick reaction zone.

As for SO_2, the removal efficiency of NO increased with the initial concentration of NO for a certain time. Also in this case, it may be assumed that the gas-liquid mass transfer is enhanced when the NO partial pressure increases. For the reaction reported in **Eq. (78)**, when the temperature was set at 50 °C, the k_o was $3.15 \cdot 10^3$ $(mol \cdot L^{-1})^{-1} \cdot s^{-1}$, the E_a is 42.50 $kJ \cdot mol^{-1}$ and the reaction order was 2 in the quick reaction zone.

The experimental results showed that the maximum efficiencies of desulphurization and denitrification were 100% and over 95%, respectively. Furthermore, other tests were carried out by varying the temperature in the range 40 - 70°C and keeping the SO_2 and NO initial concentration at 2000 $mg \cdot m^{-3}$ and 500 $mg \cdot m^{-3}$, respectively. An increase in the temperature favored the reaction rates for the simultaneous desulphurization and denitrification. However, for temperature higher than 50 °C, the reaction rate slightly decreased being the reactions of desulphurization and denitrification both exothermic, as reported in the previous thermodynamic analysis (**Table II.5)**. In addition, $NaClO_2$ more easily decompose when the temperature increases. Hence, there is an optimal

temperature for the reaction rates of the simultaneous desulphurization and denitrification by $NaClO_2$ solution, which, based on the experimental results, was found to be 50 °C.

Park et al. [72] have studied the effect of the simultaneous absorption in a spray column simulated and the flue-gas and liquid sprayed flowed in continuos. In their work, the effects of SO_2 and NO concentration, $NaClO_2$ concentration, pH value at 25 °C on both the absorption rates were investigated. The tests were perfomed by varying the initial concentration of SO_2 from 200 up to 500 $mg \cdot m^{-3}$ and a total gas flow rate equal to 1.0 $Nm^3 \cdot min^{-1}$. The molar concentration of $NaClO_2$ was varied from 0.2 to 0.5 $mol \cdot L^{-1}$ at a 6 $L \cdot h^{-1}$ constant solution flow rate. The initial pH of $NaClO_2$ solution was varied from 2 to 10 by using HCl solution. The wet-oxidation reactor had a variable length, with consequent different gas-liquid time contact values (from 0.25 up to 1.25 s). The experimental results showed that NO removal slightly increased by increasing the liquid-gas contact, while SO_2 was almost completely absorbed also at the lowest contact time (0.25 s). This effect was due to the greater solubility of SO_2 and probably to a faster reaction rate. Also the solution pH had a considerable effect on NO absorption, which increased dramatically until about 100% when pH is lower, probably due to the formation of further oxidizers, such as chlorine and chlorine dioxide.

Park et al. [72] evaluated also the rate constant of SO_2 reaction with ClO_2^- at 25 °C (**Eq. (71)**) which was 5.57 $(kmol \cdot m^{-3})^{-1} \cdot s^{-1}$ and the reaction orders resulted to be 0.22 and 0.88 for SO_2 and $NaClO_2$, respectively. Similarly, for NO (**Eq. (78)**) was estimated a 64.84 $(kmol \cdot m^{-3})^{-1} \cdot s^{-1}$ reaction rate and 0.64 and 0.69 as reaction orders for NO and $NaClO_2$, respectively.

For completeness, the kinetic reaction model of chlorite decomposition to chlorine dioxide in acid solution should be accounted for. When the solution is acidified, chlorite yields mainly chlorine dioxide. Moreover, the decomposition of chlorite in acid solution may produce chlorate and chloride at low concentration [72]**.** The rate of decomposition is greatly influenced by the experimental conditions, especially by pH and presence of chloride [106].

Taylor et al. [129] and **White et al.** [130] conducted specific studies about the presence of chlorine dioxide in $NaClO_2$ solution at pH value less than 5. According to **Sada et al.** [62], the molar ratio between the consumed chlorite and produced chlorine dioxide is equal to 0.5, (**Eq. (79)**). Recent studies ([66], [113], [117], [130]) proposed that chlorite decomposition is catalyzed by the chlorides, which are invariably present either as impurities or as decomposition products. In the studies of **Deshwal et al.** [106], the decomposition of sodium chlorite under acidic conditions was studied in a continuous stirred vessel at different temperatures (15 - 35 °C), working with a pH maintained below 2 by continuous addition of acid and chlorite. For the **Eq. (79)**, the frequency factor (k_o) was $8.98 \cdot 10^6$, E_a was equal to 37.75 $kJ \cdot mol^{-1}$ and reaction orders of ClO_2^- and H_3O^+ were both equal to 1.0.

Mo et al. [118] provided other data about the decomposition rate of chlorite in acidic solutions. The experiments were performed using only HCl as the catalyst of the reaction of ClO_2 formation. They estimated a k_o equal to $2.28 \cdot 10^4$, an E_a = 37.90 kJ·mol^{-1} and a reaction order of 1.0 and 1.39 for $NaClO_2$ and HCl, respectively.

The reaction kinetic parameters for oxidation reactions of SO_2 and NO with sodium chlorite and acidic dissociation of ClO_2^- are reported in **Table II.8**.

Table II.8. *Reaction kinetics parameters for the oxidation of SO_2 and NO in $NaClO_2$ aqueous solutions and ClO_2^- acidic dissociation. When the activation energy E_a is not available, the direct frequency factor $k_{o,d}$ is equivalent to the direct reaction rate constant K_d evaluated at 25 °C*

Eq.	Direct reaction rates			Ref.
	$k_{o,d}$ (kmol·m^{-3})$^{1-r}$·s^{-1}	E_a kJ·mol^{-1}	ΠC^r (kmol·m^{-3})^r	
(71)	1.22	66.25	$[SO_2]^{1.4}$	Zhao et al. [71]
(71)	5.57		$[SO_2]^{0.22} \cdot [NaClO_2]^{0.88}$	Park et al. [72]
(78)	$3.15 \cdot 10^3$	42.50	$[NO]^2$	Zhao et al. [71]
(78)	$6.93 \cdot 10^{16}$	53.97	$[NO]^2 \cdot [NaClO_2]^2$	Chien et al. [65]
(78)	64.84		$[NO]^{0.64} \cdot [NaClO_2]^{0.69}$	Park et al. [72]
(79)	$8.98 \cdot 10^6$	37.75	$[ClO_2^-] \cdot [H_3O^+]$	Deshwal et al. [106]
(79)	$2.28 \cdot 10^4$	37.90	$[NaClO_2] \cdot [HCl]^{1.39}$	Mo et al. [118]

There are not much data available in the literature for the reactive mechanism in the gas involving $ClO_{2(g)}$ and $Cl_{2(g)}$. Only some research published by **Li et al.** [131]**; Leu et al.** [132]**; Weinhart et al.** [133] described a radical kinetic model for the oxidation of $NO_{(g)}$ with $ClO_{2(g)}$ but valid for different pressure conditions (much lower than 1 atm). However, the reaction kinetic model in **Table II.7** considers the overall reactions involving the oxidation of SO_2 and NO_x, and probably takes into account both the oxidations in aqueous and gaseous phase for $ClO_{2(g)}$ and $Cl_{2(g)}$ presence.

II.3. Mass transfer models for packed and spray towers

II.3.1. Packed-bed towers

In the last 40 years, the introduction of structured packing has changed the conventional design of equipment for chemical processes, in particular for distillation and gas absorption units. Structured packings assure low pressure drops and high mass transfer rates thanks to a high turbulence in the gas and liquid phases (**Bravo et al.** [134]**; Brunazzi and Paglianti** [135]**; Rocha et al.** [136]**; Olujić et al.** [137]) that move with abrupt change of directions in the open channels of the packing. The surface

(often perforated for liquid dripping) is corrugated to increase the liquid-gas contact **(Olujić et al.** [137]**; Olujić et al.** [138]**; Brunazzi et al.** [139]).

In the literature, the increase in the mass transfer efficiencies is commonly ascribed to the packing angle (generally 45° or 60°) and, consequently, to the inclination of the gas channels inside the packing ([137], [140], [141]). It has also been verified that the mass transfer improves in the presence of corrugations or holes along the packing surface [142] and depends on the construction materials [141].

The mass transfer models require the knowledge of several geometric and construction parameters of a general structured packing, which are reported in **Figure II.6**.

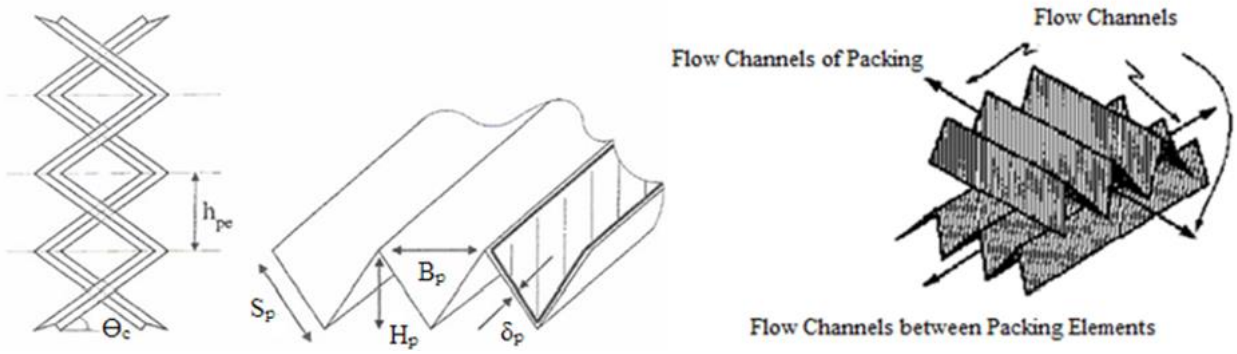

Figure II.6. *The geometric and construction parameters of a general structured packing*

The parameter δ_p [mm] is the packing thickness; B_p [m] is the base width of a packing corrugation; S_p [m] is the slant height of a packing corrugation; H_p [m] is the peak height of a packing corrugation; and θ_c [°] is the corrugation packing angle or inclination angle.

The predictive models presented in the following are based on different theories of mass transfer for structured and random packings developed by several authors in the last thirty years and provided the liquid-side (k_x) and gas-side (k_y) mass transfer coefficient per unit surface [$mol \cdot m^{-2} \cdot s^{-1}$] and effective wet surface area (a_e) expressed as [$m^2 \cdot m^{-3}$].

In **Table II.9** the predictive models for randomized and structured packings were reported:

Table II.9. *Predictive models of mass transfer for randomized and structured packed towers*

Packing type	Predictive Models
Random	Billet and Schultes [143]
Structured	Bravo et al. [134], [144]; Billet and Schultes [143]; Brunazzi and Paglianti [135]; Olujić et al. [142]

Whenever possible, the models were presented explicating all the model parameters and using a uniform symbolism. However, in some cases, the models include specific formulas and numerical procedures to calculate their parameters (for example the liquid hold-up or the liquid film thickness), for which, for the sake of simplicity, we refer directly to the original papers.

II.3.1.1. The Bravo et al. (*BRF*) model

In 1985, **Bravo, Rocha and Fair** [134] developed one of the first models for estimating the mass transfer coefficients for packed-bed columns, using Sulzer BX-type structured packings. The model allows determining the gas mass transfer coefficient (k_y) as:

$$k_y = C_G^{BRF}\left(\left[\frac{u_{Gs}}{\varepsilon_p \sin\theta_c} + \frac{3}{2}\frac{\rho_L u_{Ls}}{P_s}\left(\frac{1}{3}\frac{gP_s\rho_L^2}{\mu_L\rho_L u_{Ls}}\right)^{1/3}\right]\frac{\rho_G d_{eq}}{\mu_G}\right)^{0.8}\left(\frac{\mu_G}{D_G\rho_G}\right)^{1/3}\left(\frac{D_G}{d_{eq}}\right)\rho_y \tag{115}$$

in which: C_G^{BRF} is a proportionality factor put equal to 0.0338; ρ_y [mol·m^{-3}] is the molar gas density; D_G [m^2·s^{-1}] is the gas diffusivity in gas phase; g is the acceleration of gravity in m·s^{-2}; u_{Gs} and u_{Ls} are the superficial gas and liquid velocity in m·s^{-1}; ρ_G and ρ_L are the gas and liquid mass density in kg·m^{-3}; μ_G and μ_L are the gas and liquid mass viscosity in kg·m^{-1}·s^{-1}. The characteristic geometric parameters were the equivalent diameter (d_{eq}) and the perimeter per unit cross-sectional area (P_s). These parameters can be calculated knowing the packing dimension parameters, such as B_p, S_p and H_p. Generally, the characteristic packing dimension are provided by the vendor or can be find in the relevant literature.

For the evaluation of the mass transfer coefficient in the liquid film (k_x), the model adopted the penetration theory and provided the following expression:

$$k_x = C_L^{BRF}\sqrt{\frac{\frac{3}{2}\frac{\rho_L u_{Ls}}{P_s}\left(\frac{1}{3}\frac{gP_s\rho_L^2}{\mu_L\rho_L u_{Ls}}\right)^{1/3} D_L}{\pi d_{eq}}}\rho_x \tag{116}$$

where D_L is the gas diffusivity in liquid phase expressed in m^2·s^{-1} and ρ_x [mol·m^{-3}] is the molar liquid density. In this work, C_L^{BRF} is a calibration parameter that was posed equal to 2 in the original model of **Bravo et al.** [134]**.**

Regarding to the effective mass transfer surface area (a_e), the authors assumed the wet surface equal to the nominal surface (a_n), due to the particular corrugation and capillarity of the packing studied.

$$\frac{a_e}{a_n} = 1 \tag{117}$$

II.3.1.2. The *SRP* model

In a subsequent model, **Bravo Rocha and Fair** [144] used a new set of equations for the mass transfer coefficients and the surface area. In particular, this new model, called "Separations Research Program", *SRP*, included two additional factors to predict the effective surface area, following the first studies provided by **Shi and Mersmann** [145]. The first is a surface enhancement factor (F_{SE}^{SRP}), which varies with the packing-type, and the second is a correction factor for total hold-up due to effective wetted area (F_t).

The correction parameter F_t can be calculated as proposed by **Bravo et al.** [144] and **Rocha et al.** [136]. The values of the surface enhancement factor (F_{SE}^{SRP}) are reported in **Rocha et al.** [136], [146] for some of the existing packings. Hence, the a_e is calculated as:

$$\frac{a_e}{a_n} = F_{SE}^{SRP} F_t \tag{118}$$

The *SRP* model for k_y is:

$$k_y = C_G^{SRP}\left(\left(\frac{u_{Gs}}{\varepsilon_p\left(1-h_L\right)\sin\theta_c}+\frac{u_{Ls}}{\varepsilon_p h_L \sin\theta_c}\right)\frac{\rho_G S_p}{\mu_G}\right)^{0.8}\left(\frac{\mu_G}{D_G\rho_G}\right)^{1/3}\left(\frac{D_G}{S_p}\right)\rho_y \tag{119}$$

where C_G^{SRP} is a proportional factor estimated by **Bravo et al.** [144] as 0.054. The characteristic dimension is represented by the slant dimension of the corrugation, S_p. In this revisited model, the effective gas and liquid velocities have a different formulation with respect to *BRF* model because take into account also the liquid hold-up. The liquid hold-up (h_L) could be evaluated by the knowledge of the pressure drop in wet conditions and its complete formulation is reported in **Bravo et al.** [144] and **Rocha et al.** [136]. The liquid mass transfer coefficient is calculated according to the penetration theory, adding a correction factor:

$$k_x = 2\sqrt{\frac{\frac{u_{Ls}}{\varepsilon_p h_L \sin\theta_c}D_L}{\pi S_p C_E^{SRP}}}\rho_x \tag{120}$$

The C_E^{SRP} correction factor, defined as the surface renewal of the packing, accounts for the changes in the liquid rate that, in turn, may affect the average liquid residence time. **Murrieta** [147] estimated a value of C_E^{SRP} equal to 0.9.

II.3.1.3. The Billet and Schultes (*BS*) model

Billet and Schultes [143] studied the mass transfer phenomena in packed columns for absorption and distillation processes. This model can be used for any columns with fluids in counter-current, and for both structured and random packings. The authors developed their model applying the penetration theory to both gas and liquid phases. The liquid mass transfer coefficient is defined as:

$$k_x = C_L^{BS}\sqrt{\frac{D_L}{d_h}}\left(\frac{g\rho_L}{\mu_L}\right)^{1/6}\left(\frac{u_{Ls}}{a_n}\right)^{1/3}\rho_x \tag{121}$$

where d_h is the characteristic length of the packing (hydraulic diameter, [m]) and C_L^{BS} is the calibration parameter applied to the liquid phase. The characteristic packing dimension (d_h) is equal to four times the ratio between the void fraction (ε_p) and the nominal packing surface (a_n).

The mass transfer coefficient in the gas phase is calculated as:

$$k_y = C_G^{BS} D_G\left(\frac{u_{Gs}\rho_G}{a_n\mu_G}\right)^{3/4}\left(\frac{\mu_G}{D_G\rho_G}\right)^{1/3}\left(\frac{1}{\sqrt{\varepsilon_p - h_L}}\right)\sqrt{\frac{a_n}{d_h}}\rho_y \tag{122}$$

where C_G^{BS} is the calibration parameters for the gas phase.

The authors clearly stated that the calibration parameters, C_L^{BS} and C_G^{BS}, depend on the packing-type and the operating conditions of the process **Billet and Schultes** [143], [148], therefore dedicated experimental tests are needed for their determination. However, **Billet and Schultes** [143], [148] calculated their values for several random and structured packings. In the *BS* model the liquid hold-up (h_L) is a function of nominal surface area, liquid velocity and its properties (its formulation is reported in **Billet and Schultes** [143]).

The model is completed by the value of the effective wet surface area, expressed as:

$$\frac{a_e}{a_n} = \frac{1.5}{\sqrt{d_h a_n}}\left(\frac{u_{Ls}d_h\rho_L}{\mu_L}\right)^{-0.2}\left(\frac{u_{Ls}^2 d_h\rho_L}{\sigma_L}\right)^{0.75}\left(\frac{u_{Ls}^2}{g d_h}\right)^{-0.45} \tag{123}$$

where σ_L is the liquid surface tension in $N\cdot m^{-1}$

II.3.1.4. The Brunazzi and Paglianti (*BP*) model

Brunazzi and Paglianti [135] developed a mass transfer model by performing absorption tests of different pollutants such as HCl and SO_2 in NaOH solutions, mainly using structured packings such as Mellapak 250.Y and BX.

In this model, the evaluation of mass transfer coefficient in the gaseous phase is equal to that of the *SRP* model ($C_G^{BP} = C_G^{SRP}$=0.054).

$$k_y = C_G^{BP}\left(\left(\frac{u_{Gs}}{\varepsilon_p\left(1-h_L\right)\sin\theta_c}+\frac{u_{Ls}}{\varepsilon_p h_L \sin\theta_c}\right)\frac{\rho_G d_h}{\mu_G}\right)^{0.8}\left(\frac{\mu_G}{D_G\rho_G}\right)^{1/3}\left(\frac{D_G}{d_h}\right)\rho_y \tag{124}$$

Brunazzi and Paglianti [135] used a geometric characteristic parameter different from the formulation of *SRP* model, but equal to that adopted by **Billet and Schultes** [143] model.

The authors argued that the liquid mass transfer coefficient depended on the packing height and the mixing factor; for this reason, they introduced two dimensionless numbers to describe the liquid phase: the Graetz (Gr_L) and the Kapitza (Ka_L) numbers, which were correlated to k_x through the following equation.

$$k_x = c\frac{Gr_L^a}{Ka_L^b}\left(\frac{D_L}{d}\right)\rho_x \tag{125}$$

where c is a coefficient of proportionality for the Sherwood liquid number (Sh_L), a is a functional dependency for Graetz liquid number and b is a functional dependency for Kapitza number. The complete formulation of the two dimensionless numbers is shown in **Brunazzi and Paglianti** [135]. The authors determined the model parameters only for Sulzer Mellapak Y-type and BX-type. For Mellapak Y in metal alloy, which is similar to X series, the parameters are: a = 0.915; b = 0.09; c = 16.43. In this model, the characteristic dimension of the liquid film (d, [m]) was taken as four times the liquid film thickness (δ_f, [m]). The liquid film thickness (δ_f) was determined as a function of liquid properties, geometric characteristics of the packing, liquid velocity (u_{Ls}) and hold-up (h_L). Further details are reported in **Brunazzi and Paglianti** [135].

Finally, the effective wet surface area (a_e) is reported below:

$$\frac{a_e}{a_n} = \frac{d_h \sin\theta_c}{4\varepsilon_p}\sqrt{\frac{g\rho_L}{3\mu_L u_{Ls}}}\left(h_L\right)^{1.5} \tag{126}$$

The authors suggested an evaluation of the liquid hold-up (h_L) based on the experimental measurements by **Suess et al**. [149] or by a numerical approach reported in **Nardini et al.** [150]:

II.3.1.5. The *Delft* model

The *Delft* model (**Olujić et al.** [142]) considers the transition phenomena from the laminar to the turbulent regime, so that the total gas mass transfer is given by a mean of the contributions ($k_{y,lam}$ and $k_{y,turb}$):

$$k_y = C_G^{Delft}\sqrt{\left(k_{y,lam}\right)^2+\left(k_{y,turb}\right)^2} \tag{127}$$

$$k_{y,lam} = 0.664\left(\frac{D_G}{d_{eq}}\right)\left(\frac{\mu_G}{D_G\rho_G}\right)^{1/3}\sqrt{\frac{d_{hG}}{l_{G,pe}}\left(\frac{u_{Gs}}{\varepsilon_p(1-h_L)\sin\theta_c}+\frac{u_{Ls}}{\varepsilon_p h_L\sin\theta_c}\right)\frac{\rho_G d_{hG}}{\mu_G}}\rho_y \tag{128}$$

$$k_{y,turb} = \frac{\left(\frac{u_{Gs}}{\varepsilon_p(1-h_L)\sin\theta_c}+\frac{u_{Ls}}{\varepsilon_p h_L\sin\theta_c}\right)\frac{\rho_G d_{hG}}{\mu_G}\left(\frac{\mu_G}{D_G\rho_G}\right)\frac{\varphi\xi_{GL}}{8}}{1+1.27\left[\left(\frac{\mu_G}{D_G\rho_G}\right)^{2/3}-1\right]\sqrt{\frac{\varphi\xi_{GL}}{8}}}\left(\frac{D_G}{d_{hG}}\right)\left[1+\left(\frac{d_{hG}}{l_{G,pe}}\right)^{2/3}\right]\rho_y \tag{129}$$

where 0.664 and 1.27 are the proportionality coefficients validated for Montz packings; $I_{G,pe}$ [m] is the length of gas flow channel in a packing element, expressed as $h_{pe}/\sin\theta_c$; φ is the fraction of the triangular flow channels occupied by liquid and is a function of the base width dimension (B_p) and the slant height dimension (S_p); d_{hG} [m] is the hydraulic diameter for the gas phase and ξ_{GL} is the gas-liquid friction factor by **Colebrook and White** [151]. The characteristic packing dimension (d_{hG}) depends on the geometrical dimensions (B_p, S_p and H_p) and the liquid film thickness (δ_f). The complete formulations of the hydraulic diameter (d_{hG}), gas-liquid friction factor (ξ_{GL}) and liquid film thickness (δ_f) are reported in **Olujić et al.** [142]. In **Eq. (127)**, C_G^{Delft} is a fictitious calibration parameter purposely included in the present work in order to extend the application of the model to M250.X experimental data.

The liquid mass transfer coefficient was calculated through the penetration theory **Bravo et al.** [134], [144] using the hydraulic diameter for the gas phase (d_{hG}) in place of the slant height dimension (S_p).

$$k_x = 2\sqrt{\frac{D_L}{\pi d_{hG}}\frac{u_{Ls}}{\varepsilon_p h_L\sin\theta_c}C_E^{Delft}}\rho_x \tag{130}$$

The correction factor (C_E^{Delft}) was set to 0.9 (as in the *SRP* model) and the liquid hold-up (h_L) was evaluated as the product between the nominal surface area (a_n) and liquid film thickness (δ_f).

For the determination of wet surface area, **Olujić et al.** [142] proposed a version of **Onda et al.** [152] equation for the effective mass transfer area suitably adapted for structured packings:

$$\frac{a_e}{a_n} = (1-\Omega_p)\left[1-e^{-1.45\left(\frac{\sigma_c}{\sigma_L}\right)^{0.75}\left(\frac{\rho_L u_{Ls}}{a_n\mu_L}\right)^{0.1}\left(\frac{a_n u_{Ls}^2}{g}\right)^{-0.05}\left(\frac{\rho_L u_{Ls}^2}{a_n\mu_L}\right)^{0.2}}\right] \tag{131}$$

in which σ_c [N·m^{-1}] is the liquid surface tension of packing material and in general Ω_p can be considered as equal to 0.10 - 0.15 for the perforated packings ([142]).

II.3.2. Spray towers

Hydrodynamic and mass transfer phenomena in a spray scrubber are certainly very complex, due a polydispersion of drops, whose dimensions strictly depend on the type of nozzle and the atomization mechanism. For a spray tower, the mass transfer study is based on a fundamental hypothesis: the gas phase is taken as ideal and schematized as a plug flow, since the liquid volume fraction (*LVF*) in the spray tower is less than 5 - 8% of the total. The hydrodynamic properties of this system must be analysed in detail. In general, the drops tend to deform when subject to external fluid fields until normal and shear stresses balance at the fluid-fluid interface. When compared with the infinite number of possible shapes for solid particles, for fluid particles at steady state these possibilities are severely limited because features such as sharp corners or protuberances are precluded by the interfacial force balance.

Drops in free rise or fall in infinite media and under the influence of gravity are generally grouped into the following three categories [153]: spherical, spheroidal (or ellipsoidal) and spherical-cap or ellipsoidal-cap (**Figure II.7**).

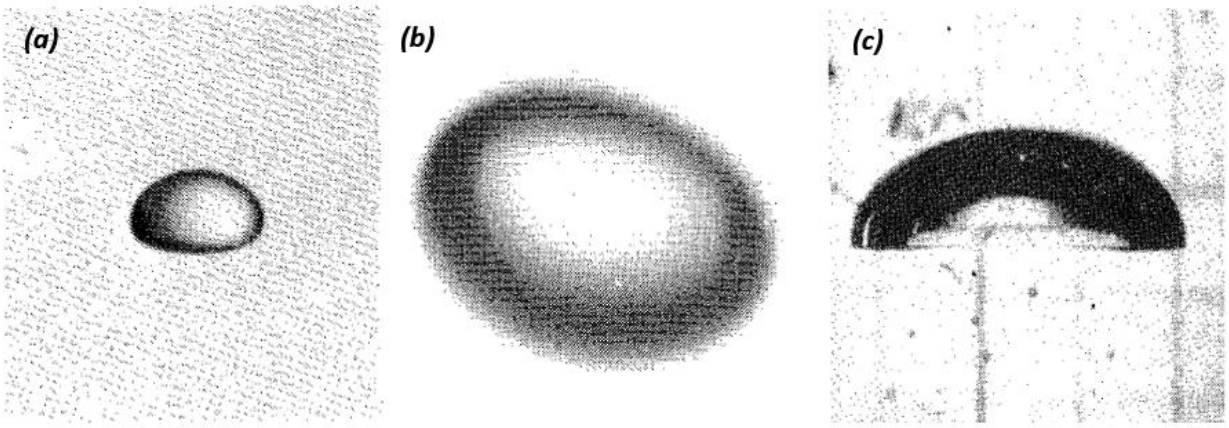

Figure II.7. *Imagines of drops in different shape regimes: (a) spherical, (b) spheroidal, (c) spherical-cap* [153]

Generally, drops can be approximated by spheres if the interfacial tension and/or viscous forces are greater than the inertia ones. In particular, fluid particles are defined as spherical if the minor to major axis ratio lies in the range 1 ± 0.1. The term spheroidal is generally used for oblate drops with a convex interface around the entire drop surface. Moreover, ellipsoidal drops commonly undergo to periodic dilations or random wobbling motions, which make their shape characterization extremely difficult. Large drops tend to adopt flat or indented bases and to lose any fore-and-aft symmetry. Such fluid particles may look very similar to segments cut from spheres or from oblate spheroids of low eccentricity; in these cases, the terms "spherical-cap" and "ellipsoidal-cap" are used. If the drop

particle has an indentation in the rear zone, it is often said to be "dimpled". Large spherical or ellipsoidal-caps may also trail thin envelopes of dispersed fluid referred to as "skirts". It is possible to prepare a generalized graphical correlation in terms of Eötvös number (*Eo*), Morton number (*M*) and Reynolds number (*Re*), known as shape map or Grace diagram [154], as reported in **Figure II.8**. Although the original data were derived for bubbles in unhindered gravitational motion through liquids, it has been observed that the shape map also applies to drops [155], [156].

The dimensionless numbers are given by the following expressions:

$$E_O = \frac{g\left|\rho_L - \rho_G\right| D_d^2}{\sigma_L} \tag{132}$$

$$M = \frac{g\mu_G^4\left|\rho_L - \rho_G\right|}{\rho_G^2\sigma_L^3} \tag{133}$$

$$Re_{G,slip} = \frac{\rho_G D_d U}{\mu_G} \tag{134}$$

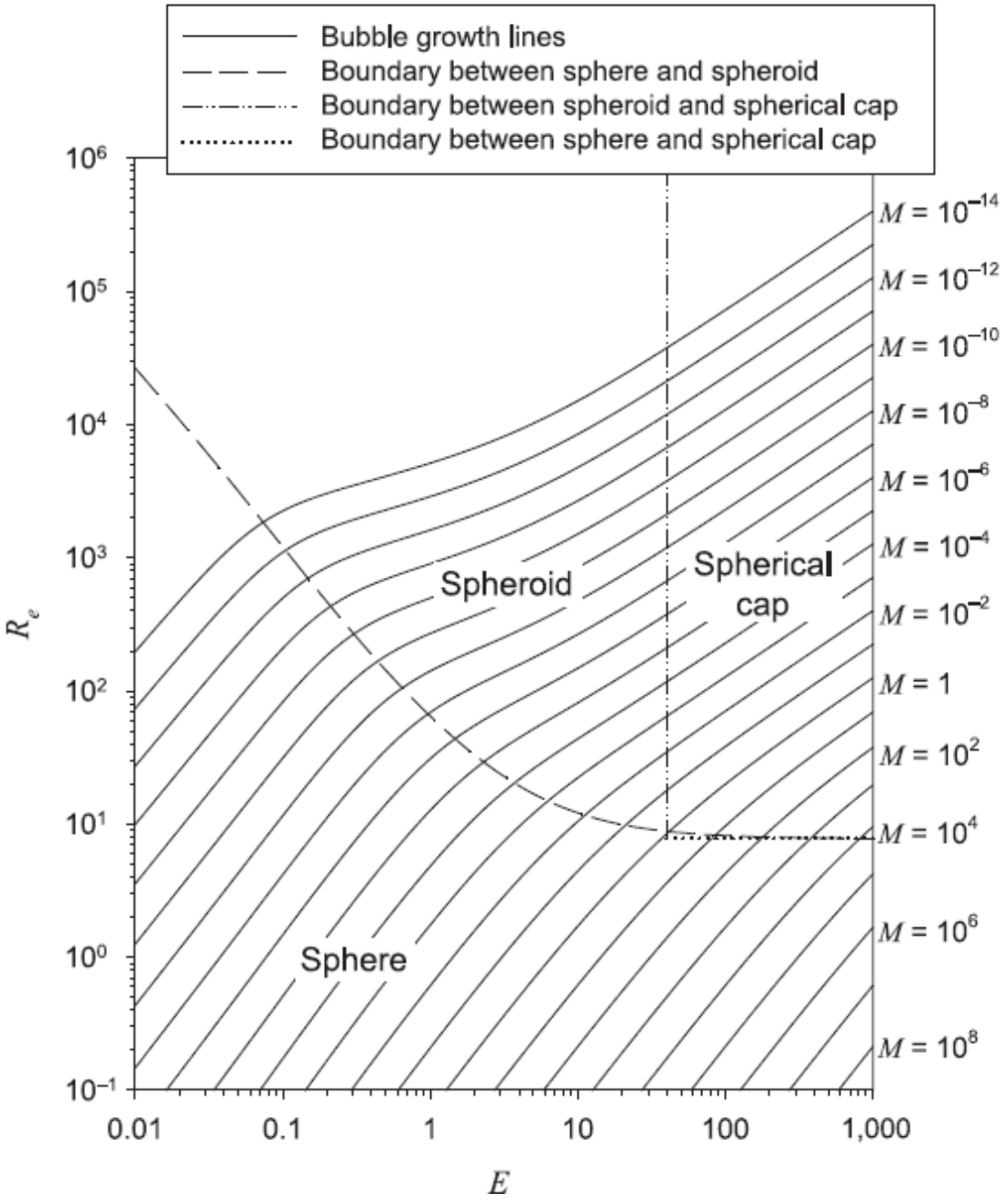

Figure II.8. *The shape map or Grace diagram for deformed droplets* [154], [155]

In **Eqs. (132)-(134)** , g [m·s^{-2}] is the gravitational acceleration; $|\rho_L$-$\rho_G|$ [kg·m^{-3}] is the absolute value of density difference between drop (ρ_L) and continuous gas phase (ρ_G); σ_L [N·m^{-1}] is the liquid surface tension; μ_G [kg·m^{-1}·s^{-1}] is the mass gas viscosity; ρ_G [kg·m^{-3}] is the mass gas density; U [m·s^{-1}] is the slip velocity, namely the terminal velocity of drop relative to the continuous gas phase; D_d [m] is the diameter for a spherical droplet, whereas it is the equivalent diameter of a spheroidal drop, defined as the diameter of a sphere with the same volume of the drop. **Figure II.8** may be used to estimate the droplet terminal velocities as well as the shape regime.

It is possible to observe that drops with different shape and terminal velocity are characterized by a different fluid-dynamic behaviour. In particular, it is possible to distinguish three different flow patterns [153], [157]–[159]: stagnant, circulating and oscillating (**Figure II.9**).

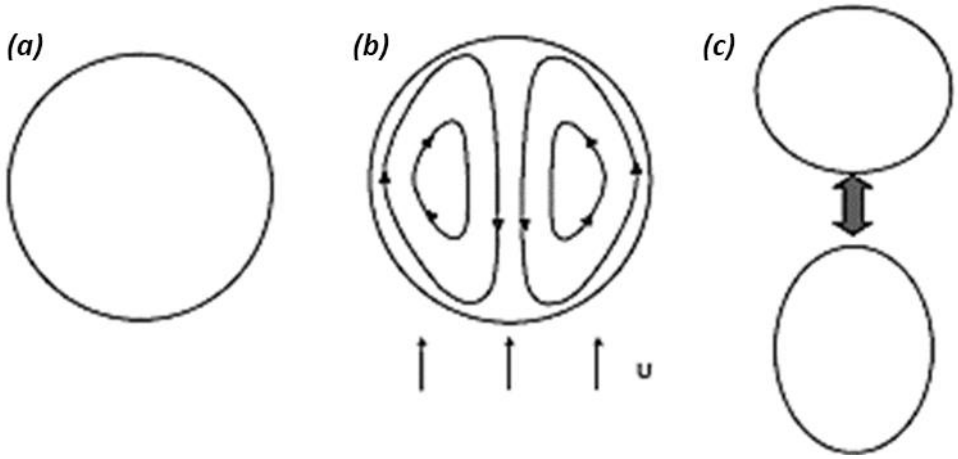

Figure II.9. *Regimes of droplet behaviour: (a) stagnant, (b) circulating, (c) oscillating* [153], [157]–[159]

A stagnant drop is spherical and rigid with no motion of the surface or in the interior; its characteristic size (D_d) is lower than 500 μm. As the characteristic dimension D_d grows, droplets tend to become circulating: circulation arises because when a droplet moves through another fluid the relative velocity results in shear forces at the interface. The liquid at the interface is swept to the rear of the droplet, and a circulation pattern can then develop. For D_d < 1000 μm circulating droplets are spherical, while larger droplets deform into ellipsoid and larger droplets deform into circulating ellipsoid. For larger droplets, oscillation begins. The transition from droplet circulation to oscillation have been thoroughly investigated by **Klee and Treybal** [160], **Grace et al.** [154] and **Skelland et al.** [161]: for air-water system, their correlations predict a critical droplet size for oscillations ($D_{d,cr}$) about equal to 1700 μm.

Theoretical predictions of the drop mass transfer coefficient will be made using one the three above mentioned droplet regimes, as outlined later.

Mass transfer in the continuous phase around drops is generally affected by a combination of molecular diffusion and natural and forced convection in the continuous gas-phase. The continuous gas phase mass transfer coefficient also depends on whether the drop is internally stagnant, circulating or oscillating. A variety of solutions for mass transfer has been obtained by using the equation of continuity for axisymmetric flow around a sphere, assuming constant physical properties [162]. In particular, the continuous gaseous phase can exhibit three different types of flow regimes as a function of the Reynolds number of gas phase:

$$Re_G = \frac{\rho_G u_{Gs} D_d}{\mu_G} \tag{135}$$

In **Eq. (135)** u_{Gs} is the superficial gas velocity, assumed as constant in the whole cross-sectional area of the scrubber (S). A steady laminar flow occurs for $Re_G < 20$, a circulating flow appears for $20 < Re_G < 400$ and unsteady fully circulating/oscillating flow appears at $Re_G > 400$. **Figure II.10** shows the typical gaseous streamlines for the different flow regimes.

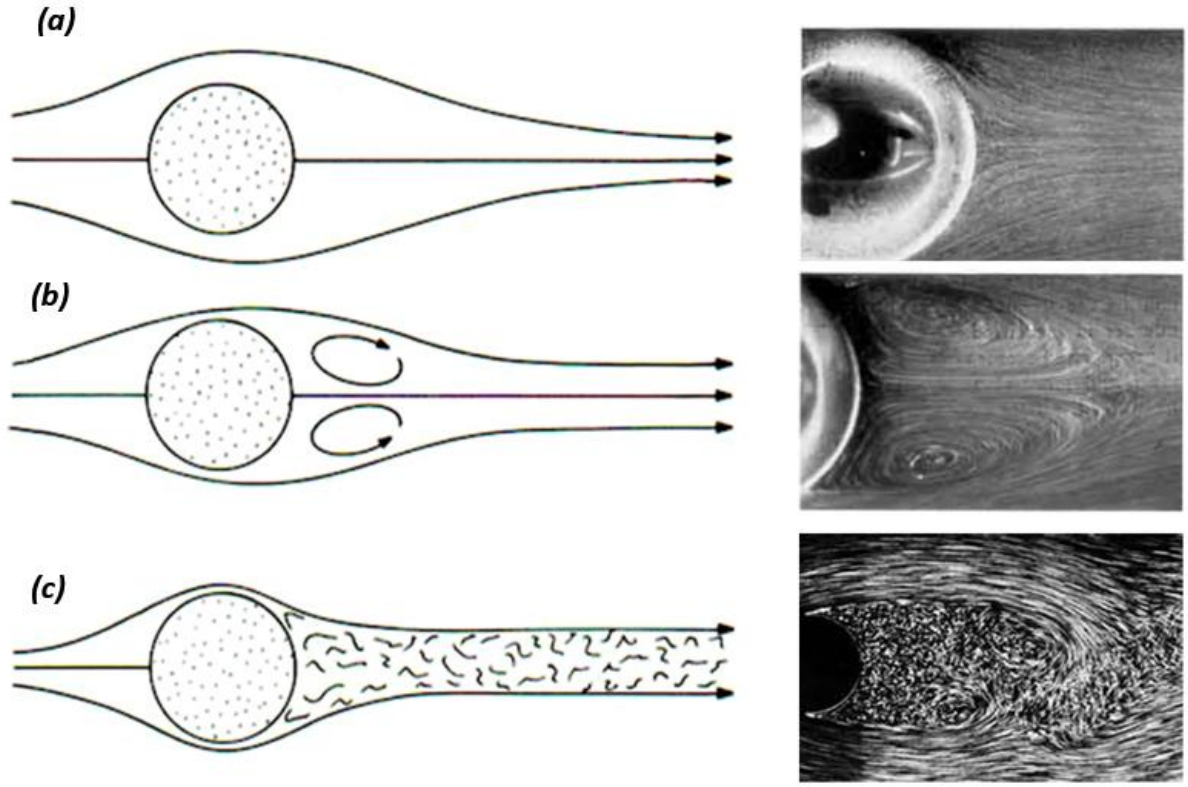

Figure II.10. *Gaseous streamlines for the different flow regimes: (a) steady laminar, (b) circulating, (c) unsteady fully circulating/oscillating flows* [162]

In the following, the main predictive models available in the pertinent literature regarding both the liquid-side and the gas-side mass transfer coefficients for a single droplet in free fall in a gaseous media are reported.

Differently from the **Section II.3.1.,** where the most adopted predictive models for packed towers were presented, the models available for spray towers have been divided according to the regimes that are established, in turn depending on the size of the single drop. In **Table II.10** the available predictive models for liquid-side (k_x) and gas-side (k_y) mass transfer coefficient per unit surface [$mol \cdot m^{-2} \cdot s^{-1}$] for a single droplet were listed, according to their reference flow patterns.

Table II.10. *Liquid-side (k_x) and gas-side (k_y) mass transfer coefficients models for a single droplet*

Liquid-side mass transfer rates models (k_x)	**Gas-side mass transfer rates models (k_y)**
Stagnant/Rigid droplets:	***Steady laminar flow:***
Danckwerts [123] - *DK* model	Friedlander [163] - *F* model
Davies [164] - *D* model	Proudman and Pearson [165] - *PP* model
Dou et al. [166] - *DPJWL* model	Brauer [167] - *B* model
	Ranz and Marshall [168] - *RM* model
	Clift et al. [153] - *C* model
Laminar circulating drops:	***Circulating flow:***
Hoh et al. [169] - *HFC* model	Lochiel and Calderbank [170] - *LC* model
Dimiccoli et al. [171] - *DDS* model	Garner and Tayeban [172] - *GT* model
Handlos and Baron [173] - *HB* model	Griffith [174] - *G* model
Laddha and Degaleesan [175] - *LD* model	Brauer [167] - *B* model
Ruckenstein [176] - *R* model	Hughmark [177] - *H* model
Skelland and Wellek [161] - *SW* model	Saboni and Alexandrova [178] - *SA* model
Saboni and Alexandrova [178] - *SA* model	
Oscillating drops:	***Unsteady fully circulating/oscillating flow:***
Handlos and Baron [173] - *HB* model	Hughmark [177] - *H* model
Rose and Kintner [179] - *RK* model	Brunson and Wellek [180] - *BW* model
Clift et al. [153] - *C* model	Yamaguchi et al. [181] - *YFK* model
Yamaguchi et al. [181] - *YFK* model	Clift et al. [153] - *C* model
Brunson and Wellek [180] - *BW* model	

The droplet surface area per unit volume [$m^2 \cdot m^{-3}$], also named as specific area (a_d), for a single spherical drop having D_d diameter, is defined as:

$$a_d = \frac{6}{D_d} \tag{136}$$

For a droplet diameter > 1000 μm, the drops tend to deform and can be considered as ellipsoidal: in this case, it is possible to evaluate the specific surface area of a single droplet, a_d, considering D_d as the equivalent diameter. Finally, droplets with diameter greater than 1700 oscillate from an oblate spheroid to a prolate one and the corresponding oscillation time scale τ_{osc} can be estimated (*vide infra*). The time-dependent specific surface area, $a_d(t)$ for oscillating droplets is calculated as [153]:

$$a_d(t) = a_d^{\circ}\left[1 + \varepsilon \sin^2\left(\frac{\pi t}{\tau_{osc}}\right)\right] \tag{137}$$

where a_d° is the minimum specific area of a spherical droplet undergoing shape oscillations.

In the following, the models listed in **Table II.10** are presented in detail, starting from those related with liquid mass transfer and sorting them based on the hypothesized flow regime.

.

II.3.2.1. Stagnant/Rigid droplets

The stagnant droplet is the simplest case, for which there is no motion of the surface nor in the interior of the droplet. As previously specified, this regime occurs for droplets with $D_d < 500\mu m$. This model was first proposed by **Higbie** [182] and subsequently modified by **Danckwerts** [123]. They proposed that the fluid at the interface could be represented as stagnant for a short time lapse (penetration time). After this time, the fluid is completely mixed, and the process begins again. In this case, the flux and the concentration profile are a function of the exposure time. For short contact times, the penetration theory may be used to predict the liquid-side mass transfer coefficient (k_x, [mol·m^{-2}·s^{-1}]) from pure diffusion:

$$k_x = 1.13 \sqrt{\frac{D_L}{\frac{\pi}{4}\left(\frac{\rho_L D_d^3}{\sigma_L}\right)^{1/2}}}\rho_x \tag{138}$$

Alternatively, **Davies** [164] turbulence model may be adopted. According to this theory, turbulent velocity fluctuations normal to the interface provide convective mass transfer. However, the surface tension restrains turbulent eddies as they approach the interface. When an eddy from the bulk approaches the interface, the surface is deformed. The surface tension exerts an opposite effect to this deformation and prevents the eddy from spreading through the interface. The resulting liquid-side mass transfer coefficient (k_x) is reported below:

$$k_x = 0.019\rho_x \left(\frac{D_d U \rho_L}{\mu_L}\right)^{1.312} \left(\frac{\mu_L^3 D_L}{\rho_L^2 D_d^3 \sigma_L}\right)^{1/2} \tag{139}$$

Dou et al. [166] proposed a model based on the two-film theory [124] for rigid drops. This model assumed that all the resistance to mass-transfer is contained in two films and not at the interface. Consequently, the interface concentrations are in equilibrium. The liquid side mass transfer coefficient (k_x) was measured by experiments and the following correlation was found:

$$k_x = 0.88\left(\sqrt{\frac{8\sigma_L}{3\pi m_p}} D_L\right)^{1/2} \rho_x \tag{140}$$

In **Eq. (140)** m_p [kg] is the droplet mass.

II.3.2.2. Laminar circulating drops

Water droplets larger than 500 μm diameter and falling at terminal velocity in air have been proven to exhibit steady internal circulation characteristics which can be correctly described using steady

circulation models [183]. In particular, a much higher absorption rates than those predicted by stagnant droplet models is expected [184].

Hoh et al. [169] extended the theory of Levich for stagnant drops to the surface of an internally well mixed drop. A correlation for the liquid side mass transfer coefficient (k_x, [mol·m^{-2}·s^{-1}]) may be written as:

$$k_x = 0.35\alpha_L^{-0.5} D_L^{0.5} v_e^{1.5} \rho_L^{-0.5} \sigma_L^{0.5} \rho_x \tag{141}$$

Typically, the value of α_L parameter may be adjusted to improve agreement with experimental data, even if a reasonable fit is obtained at $\alpha_L = 0.08$. The eddy velocity (v_e) in **Eq. (141)** must be presented in terms of measurable parameters: for this reason, a relationship between eddy velocity (v_e) and the average droplet terminal velocity (U) is required. This is provided by **Srinivasan and Aiken** [184].

Dimiccoli et al. [171] studied the kinetic and mass-transfer behaviour of spray tower absorbers. The Authors referred to **Astarita** [185] works, suggesting that drops emerging from a spray nozzle are, normally, internally well-mixed. By examining many experimental data, they have given the following correlation for k_x:

$$k_x = 0.16 \frac{D_L}{D_d} \left(\frac{\mu_L}{\rho_L D_L} \right)^{1/2} \left(\frac{U^2 \rho_L D_d}{\sigma_L} \right)^{1/2} \left(\frac{D_d U \rho_L}{\mu_L} \right)^{5/16} \rho_x \tag{142}$$

Handlos and Baron [173], **Ruckenstein** [176] and **Laddha and Degaleesan** [175] stated that the circulation arises because, when a droplet moves through another fluid, the relative velocity results in shear forces at the interface. As previously discussed, the liquid at the interface is swept to the rear of the droplet, and a circulation pattern can then develop. The circulation streamlines for a fluid sphere in Creeping flow were calculated by **Hadamard** [186]. For low Re_L flow, numerical solutions of the Navier-Stokes equation can be used to obtain the flow field inside a circulating spherical or spheroidal droplet [187], [188].

These algorithms assume that droplets have a constant shape and, therefore, are not applicable to oscillating droplets. Predictive models for liquid-side mass transfer coefficients (k_x) proposed by the abovementioned authors are listed below, respectively:

$$k_x = \frac{0.00375U}{1 + \frac{\mu_L}{\mu_G}} \rho_x \tag{143}$$

$$k_x = 2\sqrt{\frac{D_L U}{\pi D_d}} \rho_x \tag{144}$$

$$k_x = 0.023U\sqrt{\frac{\rho_L D_L}{\mu_L}}\rho_x \tag{145}$$

Skelland and Wellek [161] showed that the rate of transfer very often exceeds the value predicted by the previous relations for circulating droplets, even though no visible oscillation of these droplets could be detected. However, it may be noted that these relations were derived for conditions in which the circulation streamlines within the drop are those given by **Hadamard** [186]. In turn, these patterns are restricted to Re_L lower than 80 [189]. Therefore, an empirical correlation for larger Reynolds was required. The Authors proposed a correlation that contains the contact time , t_c, and thereby makes some allowance for the unsteady state nature of the mass transfer mechanism:

$$k_x = 31.4\left(\frac{4D_L t_c}{D_d^{\,2}}\right)^{-0.338}\left(\frac{\mu_L}{\rho_L D_L}\right)^{-0.215}\left(\frac{D_d U^2 \rho_l}{\sigma_L}\right)^{0.371}\left(\frac{D_L}{D_d}\right)\rho_x \tag{146}$$

In **Eq. (146)** the contact time (t_c, [s]) is calculated as the time from droplet detachment at the nozzle to arrival at the coalesced layer.

Saboni and Alexandrova [178] presented a simple model for the prediction of low concentration SO_2 absorption and desorption from air by falling drops. The model account for interfacial liquid friction velocity and drop size diameter as controlling parameters of the occurring phenomena. In particular, the liquid mass transfer coefficient (k_x) is given as:

$$k_x = 0.8\sqrt{\frac{D_L U}{D_d}\left(\frac{\rho_G C_D}{2\rho_L}\right)} \tag{147}$$

In **Eq. (147)**, C_D is the total drag coefficient, which can be deduced from the whose expression is proposed by **Berry and Pranger** [190]. In the work of **Saboni and Alexandrova** [178], the modelling data obtained for SO_2 absorption and desorption with a single water drop were compared to previously published experimental results and a fairly good consistence was found.

II.3.2.3. Oscillating drops

A droplet can also deform due to pressure forces around the droplet in the continuous phase. Any pressure variations that result from turbulent velocity fluctuations or wake shedding can give rise to droplet shape oscillations. These oscillations can also induce internal circulation. The streamlines for small spherical harmonic oscillations of an droplet were describes by **Lamb** [191] and discussed by **Hughes and Gilliland** [192]. Numerical simulations have been recently employed to describe large oscillations of viscous droplets with internal circulation [193]. Small water droplets falling in air are spherical and may exhibit circulation. Larger droplets deform into an ellipsoid and continue

circulating. For even larger droplets, oscillation begins when the Reynolds number reaches values approximately equal to 1000.

The time scale of oscillations may be estimated from the natural frequency for the oscillation of liquid droplets derived by **Lamb** [191]. For spherical harmonic oscillations with small amplitude, Lamb calculated the frequency for each harmonic mode.

The most important mode is the oscillation between an oblate spheroid and a prolate spheroid, and the corresponding time scale is given below:

$$\tau_{osc} = \frac{\pi}{4}\sqrt{\frac{\rho_L D_d^3}{\sigma_L}} \tag{148}$$

According to this relationship, the period for the natural mode of oscillation of a 1000 μm water droplet in air is 2.9 ms. **Schroeder and Kintner** [194] conducted experiments to observe droplet oscillation in several systems and proposed a modification to Lamb's derivation that takes into account the amplitude of the oscillation. The corresponding corrected value of oscillating time is:

$$\tau_{osc,\mathrm{mod}} = \frac{\pi}{4}\sqrt{\frac{\left(\rho_L + \frac{2}{3}\rho_G\right) D_d^3}{0.805 D_d^{0.225}\sigma_L}} \tag{149}$$

Kumar and Hartland [162] stated that the simple model of **Handlos and Baron** [173] for circulating drops (**Eq. (143)**) may be used also to predict liquid-side mass transfer coefficient (k_x) for oscillating droplets. This could reasonably be the reason for which the oscillating drops and vigorously circulating drops have often been treated under the same heading. However, in the literature some cases in which the effect of oscillation is much larger than that of circulation are also reported [172]. Furthermore, images study of oscillating drops conducted by **Rose and Kintner** [179] showed that the toroidal circulation patterns postulated by **Handlos and Baron** [173] deviate from reality. To describe mass transfer from an oscillating drop, the Authors assumed that the fluid spheroid oscillated from a nearly spherical shape to an oblate ellipsoidal one and back to a spherical shape in one period of the oscillation. All the mass transfer resistance is assumed to lie in a thin zone near the interface. The core of the drop is assumed to be well mixed: this permits a single value to represent the drop internal concentration. To predict the inside film thickness, the penetration theory was used assuming a contact time equal to the time for one oscillation cycle. This contact time was chosen as a result of the images study of the patterns of movement inside a falling oscillating drop. During each time lapse that the drop experience during a period of oscillation, the images showed that the interior of the drop was violently mixed. It was therefore assumed that the interface would be renewed during each drop oscillation cycle. Hence, the liquid mass transfer was formulated as following:

$$k_x = 0.450 D_L \frac{4}{\sqrt{\frac{\left(\rho_L + \frac{2}{3}\rho_G\right) D_d^3}{0.805 D_d^{0.225} \sigma_L}}} \rho_x \tag{150}$$

Experimental findings of mass transfer data were used to test the validity of the model (**Rose and Kintner** [179]). The average deviation for all the tested systems between calculated and measured values of k_x resulted to be approximately 15% on average.

When the shape of a drop oscillates, the surface area changes with time. Two alternative approaches have been followed to describe the way by which the area variation occurs. The surface-stretch model postulates that all the elements of the surface remain in the surface during an oscillation cycle; surface extension occurs due to stretching and thinning of the surface as the area increases. Based on additional assumptions, including of the hypothesis of oscillation from a spherical shape to oblate ellipsoidal one, **Clift et al.** [153] obtained the following equation for liquid mass transfer:

$$k_x = \frac{2}{\sqrt{\pi D_L}} \left(\frac{108.96 \sigma_L D_d^{0.225}}{\pi^2 D_d^3 \left(2\rho_G + 3\rho_L\right)} \right)^{1/4} \left(1 + \varepsilon + \frac{3}{8}\varepsilon^2\right)^{1/2} \left(\frac{D_L}{D_d}\right) \rho_x \tag{151}$$

where $(1+\varepsilon)$ is the ratio of the maximum to minimum drop surface area. Although it is difficult to predict ε, its value is close to 0.3 for many systems [153]. An alternative expression of k_x was previously obtained by **Yamaguchi et al.** [181]:

$$k_x = 1.14 \left[\frac{D_d^2 \left(\frac{108.96 \sigma_L D_d^{0.225}}{\pi^2 D_d^3 \left(2\rho_G + 3\rho_L\right)} \right)^{1/2} \rho_L}{\mu_L} \right]^{0.56} \left(\frac{\mu_L}{\rho_L D_L} \right)^{1/2} \left(\frac{D_L}{D_d} \right) \rho_x \tag{152}$$

The New-Surface-Elements model proposed by **Brunson and Wellek** [180] assumes that fresh elements are brought to the surface when the area increases, and the oldest elements are eliminated as the surface contracts. The model equation proposed for k_x is the following:

$$k_x = \frac{4}{\pi} \sqrt{\frac{D_d^2 \left(\frac{\pi}{0.452 D_d^{1.39} \sigma_L^{-0.5} \sqrt{3\rho_G + 2\rho_L}} \right)}{4 D_L}} \left(1 + \varepsilon + \frac{3}{8}\varepsilon^2\right) \left(\frac{D_L}{D_d}\right) \rho_x \tag{153}$$

II.3.2.4. Steady laminar flow

As previously discussed, when the Reynolds number for the gas phase is lower than 20, steady laminar flow occurs. The concentration in the gas continuous phase varies only in a very thin layer adjacent to the surface of the particle. According to **Friedlander** [163] the continuous-phase mass transfer coefficient is given by the following expression:

$$k_y = \left[1+\left(1+\frac{D_d U}{D_G}\right)^{1/3}\right]\left(\frac{D_G}{D_d}\right)\rho_y \tag{154}$$

Eq. (154) can be used only for $Re_G < 1$. Alternatively, for Re_G greater than 100, the **Proudman and Pearson** [165] predictive model can be adopted:

$$k_y = 0.991\left(\frac{D_d U}{D_G}\right)^{1/3}\left(1+\frac{\rho_G u_G D_d}{4\mu_G}\right)^{0.27}\left(\frac{D_G}{D_d}\right)\rho_y \tag{155}$$

Finally, for intermediate Reynolds number ($1 < Re_G < 100$), **Brauer** [167] formulated an empirical correlation on the basis of the results obtained from the numerical solutions of the diffusion equation, which follows:

$$k_y = \left\{2+\left[\frac{0.66}{1+\left(\frac{\mu_G}{\rho_G D_G}\right)}+\frac{\left(\frac{\mu_G}{\rho_G D_G}\right)}{2.4+\left(\frac{\mu_G}{\rho_G D_G}\right)}\left(\frac{0.79}{\left(\frac{\mu_G}{\rho_G D_G}\right)^{1/6}}\right)\right]\frac{\left(\frac{D_d U}{D_G}\right)^{1.7}}{1+\left(\frac{D_d U}{D_G}\right)^{1.2}}\right\}\left(\frac{D_G}{D_d}\right)\rho_y \tag{156}$$

Ranz and Marshall [168] have correlated the experimental data by direct addition of terms representing transfer by purely molecular diffusion and by force convection as:

$$k_y = \left[2+0.6\left(\frac{\rho_G u_G D_d}{\mu_G}\right)^{1/2}\left(\frac{\mu_G}{\rho_G D_G}\right)^{1/3}\right]\left(\frac{D_G}{D_d}\right)\rho_y \tag{157}$$

Clift et al. [153] proposed a revised model to better correlate the same available experimental data:

$$k_y = \left[1+0.724\left(\frac{\rho_G u_G D_d}{\mu_G}\right)^{0.48}\left(\frac{\mu_G}{\rho_G D_G}\right)^{1/3}\right]\left(\frac{D_G}{D_d}\right)\rho_y \tag{158}$$

II.3.2.5. Circulating flow

For $20 < Re_G < 400$, the gaseous flow is circulating and, consequently, the boundary-layer approximation may be assumed. **Lochiel and Calderbank** [170] developed the following theoretical equation to describe the gaseous mass transfer coefficient (k_y) around a spherical droplet:

$$k_y = 2\left(\frac{D_d U}{\pi D_G}\right)^{1/2}\left[1-\frac{2+3\frac{\mu_L}{\mu_G}}{1+\left(\frac{\mu_L\rho_L}{\mu_G\rho_G}\right)^{1/2}}\cdot\frac{1.45}{\left(\frac{\rho_G u_G D_d}{\mu_G}\right)^{1/2}}\right]^{1/2}\left(\frac{D_G}{D_d}\right)\rho_y \tag{159}$$

Kumar and Hartland [162] proposed other correlations available in literature for circulating flow around a single drop, whose gas-side mass transfer coefficient (k_y) expressions are set out below:

$$k_y = 0.6\left(\frac{D_d U}{D_G}\right)^{1/2}\left(\frac{D_G}{D_d}\right)\rho_y \tag{160}$$

$$k_y = \left\{2+1.13\left[0.16Ln\left(\frac{\rho_G u_G D_d}{\kappa^2\mu_G}\right)^{1/2}+0.35\right]^{1/2}\left(\frac{D_d U}{D_G}\right)^{1/2}\right\}\left(\frac{D_G}{D_d}\right)\rho_y \tag{161}$$

$$k_y = \left[2+0.0511\left(\frac{\rho_G u_G D_d}{\mu_G}\right)^{0.724}\left(\frac{\mu_G}{\rho_G D_G}\right)^{0.70}\right]\left(\frac{D_G}{D_d}\right)\rho_y \tag{162}$$

$$k_y = F\left[2+0.463\left(\frac{\rho_G u_G D_d}{\mu_G}\right)^{0.484}\left(\frac{\mu_G}{\rho_G D_G}\right)^{0.339}\left(\frac{D_d g^{1/3}}{D_G^{2/3}}\right)^{0.072}\right]\left(\frac{D_G}{D_d}\right)\rho_y \tag{163}$$

The **Eqs. (160)-(163)** are referred to **Garner ad Tayeban** [172], **Griffith** [174], **Brauer** [167] and **Hughmark** [177] models, respectively. In **Eq. (163)** F is a model parameter, whose value is derived by a fitting of experimental data and its expression is reported elsewhere [177]. **Saboni and Alexandrova** [178] modified the **Brauer** [167] model (**Eq.(162)**) to better describe the SO_2 absorption processes. The following revised expression for k_y was obtained:

$$k_y = \left[1.61+0.718\left(\frac{\rho_G u_G D_d}{\mu_G}\right)^{1/2}\left(\frac{\mu_G}{\rho_G D_G}\right)^{1/3}\right]\left(\frac{D_G}{D_d}\right)\rho_y \tag{164}$$

II.3.2.6. Unsteady fully circulating/oscillating flow

For Re_G > 400 the gas phase is characterized by an unsteady oscillating flow. **Hughmark** [177] derived also an equation for k_y when this gaseous flow-regime occurs:

$$k_y = \left[2 + 0.084 \left(\frac{\rho_G u_G D_d}{\mu_G} \right)^{0.484} \left(\frac{\mu_G}{\rho_G D_G} \right)^{0.339} \left(\frac{D_d g^{1/3}}{D_G^{2/3}} \right)^{0.072} \right] \left(\frac{D_G}{D_d} \right) \rho_y \tag{165}$$

Furthermore, the surface stretch model and the new surface-elements models (discussed before) should be equally applicable to the continuous phase, if the liquid dispersed-phase properties are replaced by that of the continuous gas-phase in **Eqs. (151)-(153)**.

II.4. Pressure drops models for packed and spray towers

II.4.1. Packed-bed towers

This section reports some of the most relevant predictive models to evaluate the hydrodynamic conditions of columns filled with structured packings. In particular, these equations allow predicting the pressure drops per meter of packing [Pa·m^{-1}] in both dry and wet conditions.

In **Table II.11** the predictive models for randomized and structured packings were reported:

Table II.11. *Predictive models of pressure drop for random and structured packed towers*

Packing type	Predictive Models
Random	Stichlmair et al. [195]; Billet and Schultes [148]
Structured	Stichlmair et al. [195]; Bravo et al. [144]; Billet and Schultes [148]; Brunazzi and Paglianti [196]; Olujić et al. [142]

II.4.1.1. The Stichlmair et al. (*SBR*) model

One of the first model to estimate the gas pressure drops per meter of packing in dry ($\Delta P_d/Z$) and wet conditions ($\Delta P_w/Z$) was presented by **Stichlmair et al.** [195].

$$\frac{\Delta P_d}{Z} = 0.75 f_G \left(\frac{\rho_G u_{Gs}^2}{d_{eq}} \right) \left(\frac{1-\varepsilon_p}{\varepsilon_p^{4.65}} \right) \tag{166}$$

$$\frac{\Delta P_w}{Z} = \frac{\Delta P_d}{Z}\left\{\left[\frac{1-\varepsilon_p\left(1-\frac{h_L}{\varepsilon_p}\right)}{1-\varepsilon_p}\right]^{\frac{2+j}{3}}\left(1-\frac{h_L}{\varepsilon_p}\right)^{-4.65}\right\} \tag{167}$$

Where d_{eq} [m] is the characteristic dimension (or equivalent diameter) and it is a function of void fraction (ε_p) and nominal surface area (a_n). The f_G is the gas friction factor of wall-gas contact and can be evaluated using three friction constant parameters (C_1, C_2 and C_3, called Stichlmair constants), and Reynolds gas number (Re_G). The constants depend on both geometry and material of the packings [195]. The Stichlmair parameter j in **Eq. (167)** is a model parameter that can be calculated by C_1 and C_2 (friction constants), f_G and Re_G. The formulation for f_G and Re_G are reported in **Stichlmair et al.** [195]. The liquid hold-up (h_L) is a function of the wet pressure drops and the Froude liquid number (Fr_L), and it can be calculated by an iterative method. Further details about h_L and Fr_L equations are reported in **Stichlmair et al.** [195].

II.4.1.2. The *SRP* model

The *SRP* model by **Bravo et al.** [144] for pressure drops calculation in dry and wet conditions are reported below:

$$\frac{\Delta P_d}{Z} = C_{p,d}^{SRP}\left[\left(\frac{0.177\rho_G}{S_p\varepsilon_p^2\left(\sin\theta_c\right)^2}u_{Gs}^2\right)+\left(\frac{88.774\mu_G}{S_p^2\varepsilon_p\sin\theta_c}u_{Gs}\right)\right] \tag{168}$$

$$\frac{\Delta P_w}{Z} = C_{p,w}^{SRP}\left[\frac{\Delta P_d}{Z}\left(\frac{1}{1-\left(0.614+71.35S_p\right)h_L}\right)^5\right] \tag{169}$$

The *SRP* model considers the liquid hold-up (h_L) as an important variable to describe the effect of liquid flow on pressure drops and on the effective contact surface area (a_e). The mass transfer and the hydrodynamic models were closely related; in fact, the liquid hold-up (h_L) is a function of the wet pressure drops ($\Delta P_w/Z$), and these two parameters can be calculated by an iterative method ([144] and [136]). In this case, both mass transfer and pressure drops models can be considered as a unique model (*SRP* model) for their simultaneous evaluation. $C_{p,d}^{SRP}$ and $C_{p,w}^{SRP}$ are the calibration parameters (for dry and wet conditions, respectively) that were put equal to 1 in the original model of **Bravo et al.** [144].

II.4.1.3. The Billet and Schultes (*BS*) model

Billet and Schultes [148] proposed a predictive model for dry and wet pressure drops as:

$$\frac{\Delta P_d}{Z} = C_P^{BS}\left(\frac{64}{Re_G}+\frac{1.8}{Re_G^{0.08}}\right)\left(\frac{a_n}{\varepsilon_p^3}\right)\left(\frac{F_G^2}{2}\right)\left[1+\frac{4}{a_n D}\right] \tag{170}$$

$$\frac{\Delta P_w}{Z} = C_P^{BS}\left(\frac{64}{Re_G}+\frac{1.8}{Re_G^{0.08}}\right)\left(\frac{\varepsilon_p - h_L}{\varepsilon_p}\right)^{1.5}\left(\frac{h_L}{h_{L,s}}\right)^{0.3}\left(\frac{F_G^2}{2}\right)\left[\frac{a_n}{\left(\varepsilon_p - h_L\right)^3}\right]\left[1+\left(\frac{4}{a_n D}\right)\right]e^{\frac{1.33\cdot 10^4\, Fr_L^{0.5}}{a_n^{1.5}}} \tag{171}$$

Where D [m] is the column diameter; h_L is the liquid hold-up (defined in **Billet and Schultes** [148]); $h_{L,s}$ is the real column hold-up (its formulation is reported in **Billet and Schultes** [148]); C_P^{BS} is a calibration parameter depending on the packing-type. The values of C_P^{BS} for the packings studied are reported in **Billet and Schultes** [148]. In this model the Reynolds gas number (Re_G) is a function of gas velocity and its properties, the void fraction and the wall factor parameter (further details are reported in **Billet and Schultes** [148]). The C_p^{BS} model parameter could be estimated by the fitting of experimental data in both dry and wet conditions.

II.4.1.4. The Brunazzi and Paglianti (*BP*) model

Brunazzi and Paglianti [196] developed a hydrodynamic model for Mellapak and BX packings. The total pressure drops resulted from the momentum balance of the two phases expressed as the sum of three contributions: a friction loss term (F_r) a gravitation loss term (G_r) and an acceleration loss term (A_{cc}):

$$\frac{\Delta P_d}{Z} = \left[\frac{2 f_G \rho_G u_{Gs}^2}{\left(\varepsilon_p \sin\theta_c\right)^2}\left(\frac{1}{d_h \sin\theta_c}+\frac{N_c L_{eq}}{d_h}\right)\right] \pm \left[g\rho_G\right] + \left[\frac{\rho_G u_{Gs}^2}{\varepsilon_p \sin\theta_c}\right] \tag{172}$$

$$\frac{\Delta P_w}{Z} = \left[\frac{4\tau_{wG} S_G + 4\tau_i S_i}{\pi d_h^2 (1-h_{L,d})\sin\theta_c} + \frac{2 f_M \rho_G u_{Gs}^2 N_c L_{eq}}{\left((1-h_{L,d})\varepsilon_p \sin\theta_c\right)^2 d_h}\right] \pm \left[g\rho_G\right] + \left[\frac{\rho_G u_{Gs}^2}{(1-h_{L,d})\varepsilon_p \sin\theta_c} - \frac{\rho_G u_{Gs}^2 h_{L,d}}{(1-h_{L,d})^2 \varepsilon_p \sin\theta_c}\right] \tag{173}$$

where the geometric parameters are: S_G [m] is the perimeter of the single channel crossed by the gas phase in wet condition; S_i [m] is the length of the interfacial chord; d_h [m] is the hydraulic diameter; N_c is the number of bends in a unit height of packing; L_{eq} [m] is the equivalent length of the channel. The N_c parameter can be evaluated in two different conditions: if the column diameter (D) $\leq h_{pe}/\tan\theta_c$ then $N_c = 1/D\tan\theta_c$, while if the $D > h_{pe}/\tan\theta_c$ then $N_c = 1/h_{pe}$. The equivalent length of the channel (L_{eq}) is estimated by the effective height of packing element h_{pe} using θ_c.

The fluid-dynamic parameters are: f_G is the gas friction factor and is a function of two friction constants (B_1 and B_2 reported in **Brunazzi and Paglianti** [196]) and of the Reynolds gas number (Re_G) that can be calculated using the equation proposed by **Brunazzi and Paglianti** [196]; f_M is the friction factor deriving from wall-gas and liquid-gas contact; h_L is the liquid hold-up (**Brunazzi and Paglianti** [135]); $h_{L,d}$ is the dynamic liquid hold-up (it is calculated as ratio between h_L and ε_p); τ_{wG} and τ_i (both expressed as $N \cdot m^{-2}$) are the shear stress at the channel wall relative to the gas phase flowing in the channel and shear stress at the gas-liquid interface, respectively. In particular, τ_i is a function of other two friction constants (B_3 and B_4 proposed by **Brunazzi and Paglianti** [196]), liquid properties, liquid film thickness (δ_f), the Bond number (Bo), the Weber liquid number (We_L) and its exponential parameter (α). The complete formulation for τ_{wG} and τ_i are reported in **Brunazzi and Paglianti** [196]. Conventionally, the gravitational term is negative in counter-current systems, while it is positive in co-current ones.

II.4.1.5. The *Delft* model

Olujić et al. [142] developed a model to calculate pressure drops in wet conditions based on a detailed study on the friction coefficients gas-gas, liquid-gas and wall-gas. This model predicted the pressure drops in the pre-loading (**Eq. (174)**) and loading region (**Eq. (175)**) separately. In particular, an enhancement factor (F_{Load}) is added to **Eq. (174)** when the pressure drops are above the loading point. Therefore, the *Delft* model could not be used as a predictive model because it required the knowledge of the experimental loading point. For this reason, two different calibration factors must be used, for the pre-loading and the loading region.

$$\frac{\Delta P_w}{Z} = C_{p,pl}^{Delft}\left(\zeta_{GL}+\zeta_{GG}+\zeta_{DC}\right)\left(\frac{u_{Gs}}{(\varepsilon_p - h_L)\sin\theta_c}\right)^2 \frac{\rho_G}{2} \tag{174}$$

$$\frac{\Delta P_w}{Z} = \left[C_{P,lp}^{Delft}\left(\zeta_{GL}+\zeta_{GG}+\zeta_{DC}\right)\left(\frac{u_{Gs}}{(\varepsilon_p - h_L)\sin\theta_c}\right)^2 \frac{\rho_G}{2}\right]\cdot\left[C_P^{Delft}\left(\frac{F_G}{F_{G,lp}}\right)^{\frac{2}{\sin\theta_c}}\left(\frac{u_{Ls}^2}{g\varepsilon_p^2 d_{hG}}\right)^{0.13}\right] \tag{175}$$

In these equations: $C_{P,lp}{}^{Delft}$ is the model parameter (for Montz packings its value is 3.80 [142]); $C_P{}^{Delft}$ is the calibration parameter which was put equal to 1 in the original model of **Olujić et al.** [142]; ζ_{GL} is the overall gas-liquid interaction coefficient; ζ_{GG} is the gas-gas interaction coefficient; ζ_{DC} is the interaction coefficient relative to direction change losses; $F_{G,lp}$ is the gas load factor at loading point in $Pa^{0.5}$. Further details about the three interaction coefficients and $F_{G,lp}$ are reported in **Olujić et al.** [142] and **Fair et al.** [140].

II.4.2. Spray towers

Michalski [197]–[199] proposed a model for the prediction of pressure drops in spray towers. The following assumptions were made during the model development:

- droplets are sprayed downward, and they move only vertically;
- the gas has a constant velocity in the whole cross-sectional area of the scrubber;
- the same droplet size distribution is presented in the whole apparatus;
- even with crossing spraying cones from adjacent nozzles, droplet size distribution is the same as that in the single-spray cone.

The last assumption means that an equilibrium of coalescence and break-up rate of droplets persist throughout the scrubber. However, in a more general sense, it can indicate that an equilibrium of coalescence and break-up rates of droplets persists throughout the scrubber. According to this model, the total pressure drops ΔP [Pa] is expressed as:

$$\Delta P = \frac{3}{4}\rho_G \int_0^Z \left[\int_0^1 \frac{u_{Ls}}{D_d} \cdot C_D \frac{\left(u_{Ls} - u_{Gs}\right)\left|u_{Ls}\right|}{u_{Ls}} d\left[\Delta D_d\right] \right] dZ \tag{176}$$

In **Eq. (176)** ΔD_d is the cumulative volumetric droplet size distribution. Accurate pressure drops values for a spray column may be obtained also via CFD analysis.

III. MATERIALS AND METHODS

In this chapter, the experimental facilities adopted for the experimental campaign are presented with the related materials, equipment and analysis instrumentations used. The experimental procedures, the expected results and the methodology for the data analysis will be also described.

In details, the experimental plants used in the three-year doctorate are:

1. A bubble column operating in feed-batch mode installed in the DICMaPI of the University of Naples Federico II (Italy);
2. A packed-bed column equipped with Mellapak 250.X structured packing installed in the DICMaPI of the University of Naples Federico II (Italy);
3. Two pilot spray towers: the first installed in VTS Quarto of Naples (Italy) and named as "VTS spray tower" and the second installed on the Lab-Ship of the Chalmers University of technology at the port of Göteborg (Sweden) and named as "Chalmers spray tower".

III.1. Bubble Column in feed-batch mode

Absorption experiments in the bubble column aimed at assessing SO_2 solubility data in the different absorbing aqueous solutions at 25 °C and 1 atm. The experiments were conducted in feed-batch mode, where the gas containing SO_2 was continuously fed to the column filled with a batch liquid.

III.1.1. Materials

The simulated flue-gas was prepared by mixing SO_2 (2% vol. in N_2) with either N_2 (99.999% vol.) or air (technical grade), supplied by Rivoira Gas Srl in high-pressure cylinders.

Absorption experiments were carried out using different scrubbing solutions:

- an acid water solution (AW) at pH = 3.0, adding HCl solution to distilled water;
- pure distilled water solution (DW) at pH = 6.0, with ionic content less than 0.5 ppm;
- a tap water solution (TW) at pH = 7.55;
- a synthetic seawater solution at pH = 8.2 (in the following referred as seawater, (SW)) obtained by adding 33 $g \cdot L^{-1}$ of NaCl, 4.14 $g \cdot L^{-1}$ of Na_2SO_4, 0.16 $g \cdot L^{-1}$ of $NaHCO_3$ and 0.03 $g \cdot L^{-1}$ of Na_2CO_3 to the tap water;
- a basic aqueous solution at pH = 9.4, adding 200 $mg \cdot L^{-1}$ of NaOH to seawater (SWOH). The NaOH content was chosen so to avoid precipitation, which in the adopted seawater occurs above pH 9.4;
- two chlorite solutions obtained by adding $NaClO_2$ to SW solution. Seawater with 1 $g \cdot L^{-1}$ of $NaClO_2$ (SWC0.1) at pH = 8.33 and seawater with 2 $g \cdot L^{-1}$ of $NaClO_2$ (SWC0.2) at pH = 8.55.

The chemicals used were sodium chloride (99.99% w/w), sodium sulphate (99.99% w/w), sodium bicarbonate (99.99% w/w), sodium carbonate (99.99% w/w), hydrochloric acid aqueous solution (37% w/w), sodium hydroxide in pellets (99.99% w/w) and sodium chlorite (80% w/w) purchased from VWR International Chemicals (Italy) as AR grade.

A chemical characterization of the tap water was performed by ionic chromatography method (Metrohm, AG 883 Basic IC PLUS) and is reported in **Table III.1**.

Table III.1. *Chemical composition of tap water*

Solution	pH -	Cl^- $g \cdot L^{-1}$	SO_4^{2-} $g \cdot L^{-1}$	HCO_3^- $g \cdot L^{-1}$	CO_3^{2-} $mg \cdot L^{-1}$	NO_3^- $mg \cdot L^{-1}$	Na^+ $g \cdot L^{-1}$	Mg^{2+} $mg \cdot L^{-1}$	K^+ $mg \cdot L^{-1}$	Ca^{2+} $g \cdot L^{-1}$
TW	7.6	0.01	0.01	0.53	-	4.21	0.03	26.18	2.34	0.11

III.1.2. Plant description and experimental procedures

The feed-batch bubble column consists in a Pyrex glass vessel (inner diameter: 30 mm; total length: 300 mm) provided with an external jacket (42mm i.d.) with recirculating water for a fine-tuning of the system temperature. The water was heated in a glass container put on the heating plate (ARGO LAB M2-D Pro) and its temperature was controlled by a probe connected to the digital thermometer (PCE, T-390 model). The water was continuously fed to the column with a pump and recirculated to the container and the temperature of the water bath in the external jacket was measured with another probe connected to the digital thermometer.

The bubble column was equipped with a gas distributor using a porous septum P-2 (40 - 100 micron) for small bubbles formation, so to increase the gas-liquid contact surface.

Gas flow rate was measured and controlled with two ASA flowmeters (E5-2600/A/H model) 0 - 120 $L \cdot h^{-1}$ (the first for pure N_2 and the second for the N_2 and SO_2 mixture) and its temperature was kept constant by an electric gas heater (i.d. 50 mm and length 200 mm) having 200 W total power. The gas electric heater was connected to a PID controller (Omron E5CN equipped with two K-type thermocouples) for temperature control. The heating system was externally insulated by a tubular structure made in polycarbonate (*i.e.* 100 mm) with an internal neoprene protection. The desired gas outlet temperature could be reached by setting a set-point temperature (often it must be higher than the desired value, due to heat losses) measured with a probe installed on the heating surface and connected to the PID device. The gas inlet/outlet temperature was measured with a probe connected to a four-channels digital thermometer (PCE Instruments, T-390 model, with accuracy of ± 0.1 °C). Gas pressure was controlled by two manometers 0 - 2 bar (WIKA Instruments, PG23HP-S model) installed on the inlet and outlet gas lines of the bubble column. A third ASA flowmeter up to 240 $L \cdot h^{-}$

[1] allowed controlling the total flow rate at the outlet of the bubble column.

The flowsheet of the experimental device is similar to the set-up used in **Flagiello et al.** [36], [42], and is showed in **Figure III.1**:

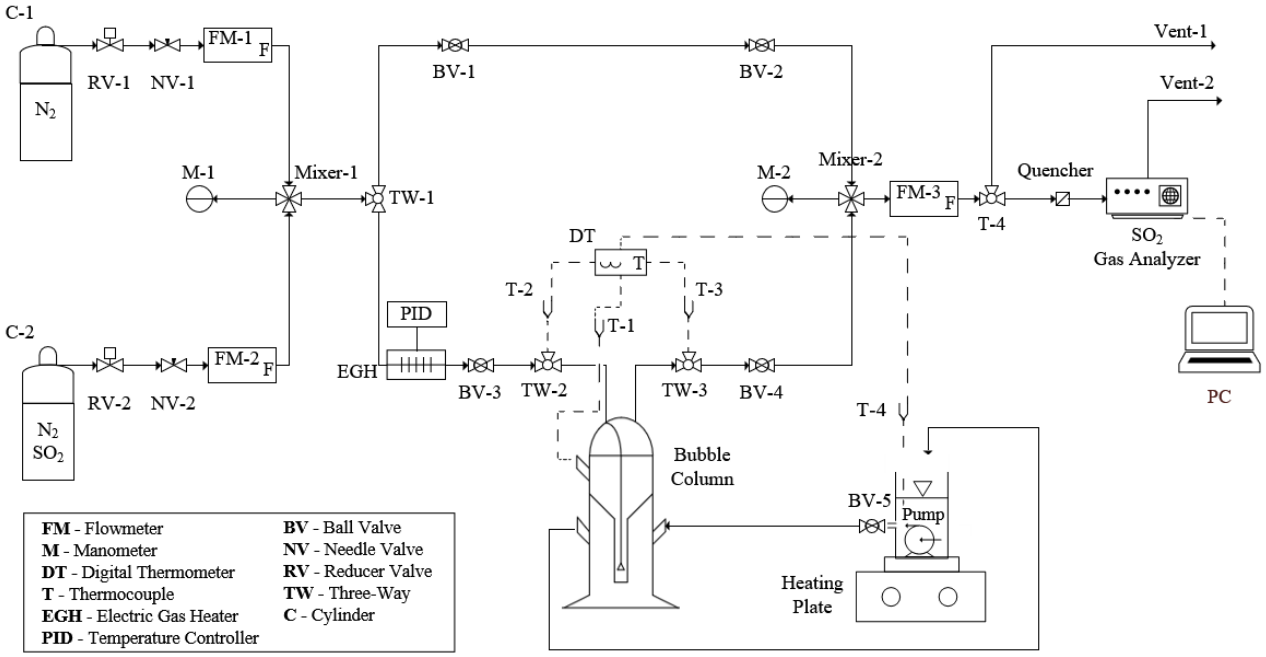

Figure III.1. *P&ID diagram of the experimental set-up of the bubble column in feed-batch mode*

For each test, the absorbing batch solution (M_S, [g]) was charged into the bubble column and a constant volumetric flow rate ($Q_{G,v}$ [$L \cdot h^{-1}$]) of simulated flue-gas with constant SO_2 gas concentration ($C^{\circ}_{SO_2}$, [ppm_v]) was fed until saturation of solution. The saturation of the solution occurs at a certain time of the test (t^*) when the concentration of SO_2 in the gas at the bubble column outlet (C_{SO_2}, [ppm_v]) reaches the initial value adopted in the test ($C_{SO_2} = C^{\circ}_{SO_2}$).

During the tests, it is possible to track the time course of SO_2 concentration in the gas flowing out from the column (with ABB O2020® Advanced optima process gas analyzer, limit of device is up to 5000 ppm_v), obtaining a concentration vs time curve *i.e.* the so-called breakthrough curve. The gas analyzer was equipped with a gas quencher (Bühler Technologies).

Finally, when the test was completed, the pH of the exhaust liquid was measured by HOBO® pH-meter (PCE-228 model, with accuracy of ± 0.01).

III.1.3. Methodology for the data analysis

The solubility of SO_2 in an aqueous solution is obtained starting from an accurate data analysis of the breakthrough curves, mainly consisting in a mass balance on $SO_{2(g)}$ over the bubble column during the test [41]:

$$Q_{G,m}C^{\circ}_{SO_2}dt - Q_{G,m}C_{SO_2}dt = \frac{M_s}{MW_S}x_S(t) \tag{177}$$

Where $Q_{G,m}$ [mol·s^{-1}] is the gas molar flow rate, M_S [g] is the batch solution charged into bubble column, MW_S [g·mol^{-1}] is the molecular weight of the absorbing solution, $C^{\circ}_{SO_2}$ and C_{SO_2} [ppm$_v$] are respectively the SO_2 concentrations before and after the bubble column during the time and $x_S(t)$ is the amount of SO_2 captured per liquid mole unit (μmol·mol^{-1}), expressed as physical solubilization, *i.e.* SO_2 or chemical, *i.e.* HSO_3^-, SO_3^{2-} and SO_4^{2-}.

The integration of **Eq. (177)** from zero to saturation time t^* [s]allows calculating the total amount of SO_2 dissolved in the absorbing solution, including both the solute *A* and the products deriving from the chemical reactions (in the case of chemical absorption):

$$x^*_S = Q_{G,m}\frac{MW_S}{M_s}\int_{t=0}^{t=t^*}\left(C^{\circ}_{SO_2} - C_{SO_2}\right)dt \tag{178}$$

where x_S^* [μmol·mol^{-1} or mol·mol^{-1}] is the mole fraction of gas solute in liquid phase at equilibrium with the corresponding initial concentration of SO_2 in gas phase, $C^{\circ}_{SO_2}$ [ppm$_v$ or mol·mol^{-1}].

Figure III.2 shows a generic concentration vs time curve (breakthrough curve) during the absorption of a gaseous solute in a liquid phase.

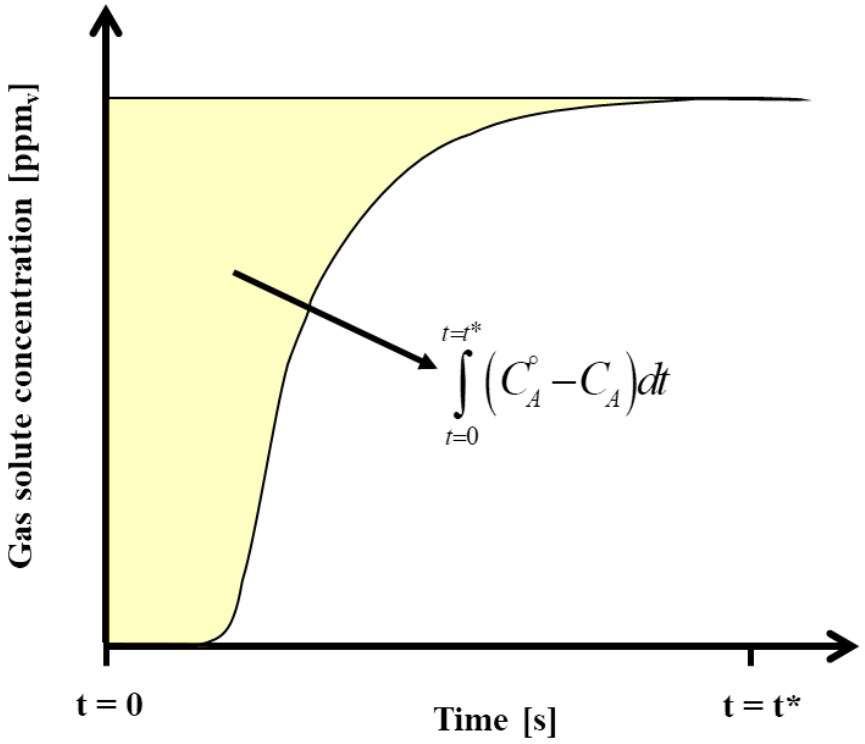

Figure III.2. *Typical breakthrough curve during the absorption of a gaseous solute SO_2 in a liquid phase*

The area marked in yellow above the breakthrough curve represents the integral to be calculated in **Eq. (178)**.

In general, the equilibrium data (y_{eq}, x_{eq}) for the absorption of gas solute *A* in an aqueous phase are obtained from the experimental tests by varying the operating concentration of the gas *A* (C°_{A}), and can be described by **Eq. (179)**.

$$y_{eq,A} = F_{eq} x_{eq,A} \tag{179}$$

where $y_{eq,A}$ is the mole fraction of gas solute *A* in the gas phase $x_{eq,A}$ is the mole fraction of gas solute *A* absorbed in the liquid phase; F_{eq} is an equilibrium function that represents the solubility of the gaseous solute in the liquid phase.

In the case of purely physical absorption, the F_{eq} is a linear function and is also referred as the Henry's constant (K_H) which depends on the concentration of the gas to be absorbed, on pressure and temperature of process, while in the case of absorption with chemical reaction the F_{eq} is not a linear function, and depend on several parameters:

$$F_{eq} = f(y_{eq,A}, P, T, C_{react}, pH) \tag{180}$$

In the **Eq. (180)**, the C_{react} is the concentration of the reagent in liquid phase that interacts with the gaseous solute absorbed by chemical reactions, while *pH* is the pH value of the aqueous solution.

The experimental solubility data obtained during the experimental campaign were also validated by simulations carried out with a commercial software for chemical processes, ASPEN PLUS®. The software provides a simulator block called "Flash block" which simultaneously solves mass, charge and energy balance equations. This block also requires the choice of the thermodynamic property method based on predictive models (already included in the ASPEN PLUS® database) for the calculation of fugacity coefficients for the gas phase and activity coefficients for the liquid phase. In addition, some physical gas-liquid equilibria and the networks of chemical reactions are already included in the ASPEN PLUS® database with the corresponding data on equilibrium constants. Alternatively, the equilibrium data can be implemented in the database by retrieving them from the relevant literature.

III.2. Packed-bed column with Mellapak 250.X

The absorption experiments in the packed column with Mellapak 250.X structured packing (M250.X) aimed to evaluate the efficiency performances on a simulated flue-gas containing SO_2, NO_x or simultaneously both SO_2 and NO_x, using different absorbent aqueous solutions. The column operated at 1 atm and at different gas and liquid temperatures.

III.2.1. Materials, equipment and analytical instruments

The simulated flue-gas was prepared using SO_2 (2% vol. in N_2) and NO (2% vol. in N_2) supplied by Rivoira Gas Srl in high-pressure cylinders and atmospheric air stream provided by a compressor. Absorption experiments were carried out using different scrubbing solutions in the bubble column:

- an acid water solution (AW) at pH = 3.0, adding HCl solution to distilled water;
- pure distilled water solution (DW) at pH = 6.0, with ionic content less than 0.5 ppm;
- a tap water solution (TW) at pH = 7.55;
- a synthetic seawater solution at pH = 8.2 (in the following referred as seawater (SW)) obtained by adding 33 $g \cdot L^{-1}$ of NaCl, 4.14 $g \cdot L^{-1}$ of Na_2SO_4, 0.16 $g \cdot L^{-1}$ of $NaHCO_3$ and 0.03 $g \cdot L^{-1}$ of Na_2CO_3 to the tap water;
- a basic aqueous solution at pH = 9.4, adding 200 $mg \cdot L^{-1}$ of NaOH to seawater (SWOH). The NaOH content was chosen so to avoid precipitation, which in the adopted seawater occurs above pH 9.4;
- six chlorite solutions with different contents of $NaClO_2$ (from 1 to 10 $g \cdot L^{-1}$) added to SW solution. Seawater with 1 $g \cdot L^{-1}$ of $NaClO_2$ (SWC0.1) at pH = 8.33, seawater with 2 $g \cdot L^{-1}$ of $NaClO_2$ (SWC0.2) at pH = 8.55, seawater with 2.5 $g \cdot L^{-1}$ of $NaClO_2$ (SWC0.25) at pH = 8.56, seawater with 5 $g \cdot L^{-1}$ of $NaClO_2$ (SWC0.5) at pH = 8.96, seawater with 7.5 $g \cdot L^{-1}$ of $NaClO_2$ (SWC0.75) at pH = 9.17, seawater with 10 $g \cdot L^{-1}$ of $NaClO_2$ (SWC1.0) at pH = 9.40.

The chemicals used for the tests with the packed-bed column were the same as those reported in **Section III.1.1.**.

III.2.2. Plant description and experimental procedures

Experiments were performed in a Plexiglas column (i.d.: 0.1 m; total column height: 1.6 m) operated at 1 atm. Four modules of a structured packing with a total packing height of 0.892 m (Mellapak 250.X, provided by Sulzer Chemtech) was used as filling material. Mellapak 250.X modules are made in Hastelloy C-22 alloy, which was selected to prevent acid corrosion and oxidation effects during the tests. **Table III.2** shows the values of the physical and geometric characteristic parameters of the Mellapak 250.X packing.

Table III.2. *Physical and geometric characteristics of Mellapak 250.X provided by Sulzer Chemtech and structured packing details with characteristic dimension parameters*

a_e	ρ_{bulk}	ε_p	Ω_p	F_p	δ_p	B_p	S_p	H_p	h_{pe}	Θ_c
$m^2 \cdot m^{-3}$	$kg \cdot m^{-3}$	$m^3 \cdot m^{-3}$	$m^3 \cdot m^{-3}$	$m^2 \cdot m^{-3}$	mm	mm	mm	mm	mm	°

250	200	0.98	0.15	26	1	24.1	17	11.9	223	60

where ρ_{bulk} is the bulk density of packing material; ε_p is the void fraction of the packing; Ω_p is fraction of packing surface area occupied by holes; F_p is the packing factor; δ_p is the packing thickness; B_p is the base width of a packing corrugation; S_p is the slant height of a packing corrugation; H_p is the peak height of a packing corrugation; h_{pe} is the height of a single packing module; θ_c is the corrugation packing angle or inclination angle.

The flow sheet of the experimental plant is similar to the set-up used in **Flagiello et al.** [41]–[43], and is showed in **Figure III.3**.

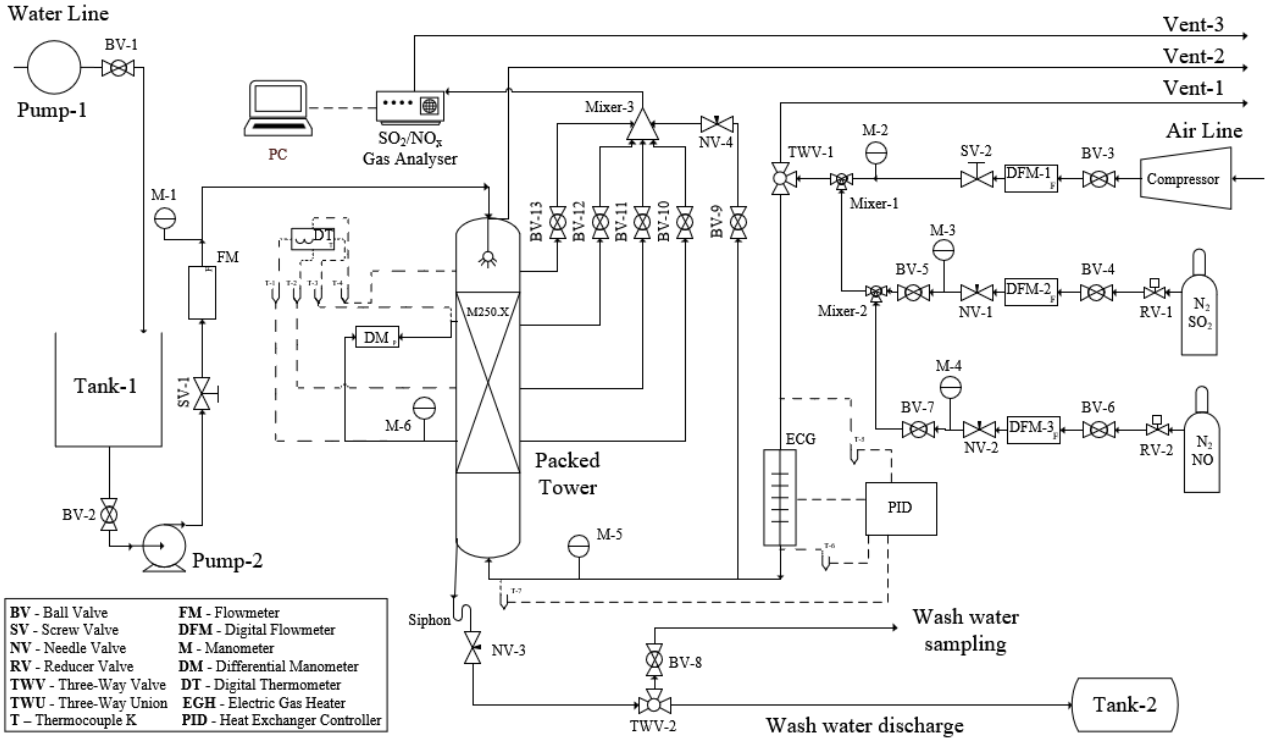

Figure III.3. *P&ID diagram of the experimental set-up of the packed-bed column filled with Mellapak 250.X*

The liquid was fed at the top of the column, in counter-current flow to the gas, by a centrifugal pump (Grundfos Lenntech, CR 3-8 A-A-A-EHQQE model, with total power 0.75 kW) and controlled with a flow meter 20 - 240 $L \cdot h^{-1}$ (Cryotek Engineering, D2 model). The liquid was injected in the column by a PNR® full-cone nozzle (DAM 1212 B31 model, made in stainless steel) with a complete opening of the liquid jet of 45°. The nozzle was positioned at the head of the column, at a distance from the packing (35 mm) so to allow a uniform wetting of the packing surface from the top.

The feeding gas section was managed via three digital flow meters by SMC Corporation (a PFMB7202-F06-F model for air 0 - 500 $L \cdot min^{-1}$ and two PFMB7201S-F02-DWSA model for gas

mixtures in cylinders 0 - 100 $L \cdot min^{-1}$). The simulated flue-gas had an average relative humidity level of 10 - 60% measured by HOBO® onset (UX100-23 model, with accuracy of ± 0.1%) in the operating gas temperature range between 25 - 60 °C. The gas temperature was set using an electric heater (i.d. 110 mm and length 250 mm) supplied by Megaris srl with two electric resistors arranged in series, for a total power of 1 kW. The device was connected to a PID controller (Omron E5CB equipped with two K-type thermocouples) for temperature control. Moreover, it was externally insulated by a tubular structure made in polycarbonate with an internal neoprene protection and two thermostats in contact with aluminum (T_{max} 85 °C).

The gas flow rate was fed up-flow into the column through a Plexiglas gas diffuser, which presents six holes with diameter of 6 mm arranged in a hexagonal mesh. The gas diffuser is placed 40 mm below the gas plastic distribution grid (a square mesh 81 mm^2 with 2 mm thickness) and 110 mm from the packing bottom. The vertical position of the gas diffuser can be changed in order to approach a turbulent plug-flow motion of the gas approaching the packing bottom. Its actual value was set based on the results of dedicated CFD simulations of the column bottom section performed in ANSYS FLUENT®. The simulations showed that, for each of the gas flow rates tested, a fully developed flow was obtained immediately close to the gas diffuser.

A 90 mm height plastic foam demister for the entrained liquid drops was put at 15 mm from the nozzle at the top of the column. The gas pressure at the top and the bottom of the packing was measured by a differential pressure gauge (FLUKE Corporation, Air Flow Meter 922 model with accuracy of ± 0.1 mm_{H_2O}). Three pressure gauge 0 - 600 mbar (WIKA Instruments, 432.50 model) were used for measuring the pressure of the mixing gas, after gas heater and before the column.

A four-channels digital thermometer (PCE Instruments, T-390 model with accuracy of ± 0.1 °C) was used for temperature measure via K-type thermocouples placed at four column levels (at inlet, at 170 mm and 810 mm from the bottom and at the column outlet, after the demister), in order to obtain the temperature profile along the column. Finally, the relative humidity content was measured with a sensor (HOBO® onset) that could be applied to each sampling point along the column.

Absorption tests were carried out by feeding the simulated flue-gas stream to the column at the desired flow rate (G, [$m^3 \cdot h^{-1}$]), temperature (T_G, [°C]) and concentration of SO_2 and NO_x ($C^{\circ}_{SO_2}$ and $C^{\circ}_{NO_x}$ [ppm_v]), which were checked by gas analyzers (ABB O2020® and Eco Physics CLD 62 gas analyzer) before the liquid feeding. The absorbing liquid stream was send in counter-current flow with the gas at the desired flow rate (L, [$L \cdot h^{-1}$]) and temperature (T_L, [°C]); the gas concentration levels of SO_2 and NO_x were monitored and recorded up to a steady state, to reach which a characteristic time dependent on the scrubber fluid-dynamics and its operating conditions was needed.

The ABB O2020® Advanced optima process gas analyzer (limit of device is up to 5000 ppm_v) measured the concentration of SO_2 in the gas stream, while Eco Physics CLD 62 gas analyzer (limit of device is 100 up to 10000 ppm_v) measured the concentration of NO and total NO_x. A gas quencher (Bühler Technologies) was installed before dual analyzer system.

The wash water was collected at the bottom of the column and sent to a sampling point for further analysis: pH value by HOBO® pH-meter (PCE-228 model, with accuracy of ± 0.01); temperature by mini digital thermometer (WINGONEER, with accuracy of ± 0.1); and eventually the ionic composition by ionic chromatography method (Metrohm, AG 883 Basic IC PLUS).

During the tests it was possible to retrieve:

- the gas concentrations of SO_2 and NO_x along the column;
- the gas temperature along the column;
- the relative humidity along the column;
- the gas pressure drops along the column;
- the wash water pH;
- the wash water temperature;
- the content of ionic species in the wash water.

III.2.3. Methodology for the data analysis

The data analysis for the operated packed-bed column were performed starting from the design equations for an absorber. The design equations for absorbers are reported in several textbooks (*e.g.* **Sinnott** [200]**; McCabe et al.** [201]**)**, and allow calculating the height of the column (Z) and the pressure drop ($\Delta P/Z$), from which the column section (S) can be retrieved.

The correlations for determining the effective contact height of the scrubber (Z, [m]) is proposed below:

$$\frac{G_m}{(1-y)}dy = K_{OG}a_e(y-y^*)SdZ \tag{181}$$

The **Eq. (181)** is a standard equation, valid for any type of contact device, where y [mol·mol^{-1}] is the gas mole fraction along the column, y^* [mol·mol^{-1}] is the gas mole fraction at equilibrium with liquid phase, K_{OG} [mol·m^{-2}·s^{1}] is a standard equation, valid for any type of contact device, where y [mol·mol^{-1}] is the gas mole fraction along the column, y^* [mol·mol^{-1}] is the gas mole fraction at equilibrium with liquid phase, K_{OG} [mol·m^{-2}·s^{1}] is the overall mass transfer coefficient referred to gas phase per unit surface, a_e [m^2·m^{-3}] is the effective wet surface area, S [m^2] is the column section and G_m [mol·s^{-1}] is the molar gas flow rate.

When the liquid losses along the column walls are negligible, the parameters in the *RHS* of **Eq. (181)** can be consider as dependent only on *y* and **Eq. (181)** can be integrated by separation of variables obtaining an explicit expression of the effective contact height of the scrubber (*Z*). Moreover, it is possible to simplify the integration by using the average values of the physical properties of the liquid and gas stream along the column, as follows:

$$Z = \left\langle \frac{G_m}{SK_{OG}a_e} \right\rangle \cdot \int_{y_2}^{y_1} \frac{dy}{(1-y)(y-y^*)} \tag{182}$$

where y_1 [mol·mol^{-1}] is the outlet gas mole fraction, y_2 [mol·mol^{-1}] is the inlet gas mole fraction. This formula is largely adopted for packed towers and conveniently indicated that *Z* is the product between a first term, which is the average Height of Transfer Unit, $<HTU_{OG}>$, that account for the actual rate of the process compared to the gas residence time in the scrubber and the integral term, called as Number of Transfer Units (NTU_{OG}), which accounts for the actual separation of the gas solute (from y_1 to y_2) achieved in the column.

The overall mass transfer coefficient englobes all the features of interfacial mass transfer and assumes an equilibrium condition at the gas-liquid interface. Following the two-film theory [124], [125], HTU_{OG} can be calculated as the sum of the resistances to mass transfer in liquid and gas films:

$$HTU_{OG} = HTU_G + \lambda HTU_L = \frac{G_m}{S}\left[\frac{1}{k_y a_e} + \lambda \frac{1}{E_L k_x a_e}\right] \tag{183}$$

$$HTU_G = \frac{G_m}{Sk_y a_e} \tag{184}$$

$$\lambda HTU_L = \left[\left(\left.\frac{\partial y}{\partial x}\right|_i\right)\frac{G_m}{L_m}\right]\frac{L_m}{SE_L k_x a_e} \tag{185}$$

where HTU_G [m] and λHTU_L [m] are the contributions to HTU_{OG} related to the gas and the liquid phases, respectively; λ is the stripping factor, which represents the ratio between the interface and operating conditions; E_L represents the enhancement factor for mass transfer in liquid film (the meaning of the enhancement factor E_L has already been discussed in **Section II.2.**); $(\partial y/\partial x)_i$ is the slope of the equilibrium function (F_{eq}) at the interfacial conditions (x_i,y_i) of each scrubber section, which are defined as those points of the equilibrium curve (x_{eq},y_{eq}) related to each point of the operating curve (*x*,*y*) by the following equation, also called as the transport line:

$$\frac{y_{A,i} - y}{x_{A,i} - x} = -\frac{E_L k_x a_e}{k_y a_e} \cdot (1-y)_{mLn} \tag{186}$$

Where the first term is the equation of a line that correlates the operating conditions to the gas-liquid interface (coordinates y_A,x_A ; $y_{A,i}$,$x_{A,i}$), while the second term is the slope of the transport line.

According to **McCabe et al.** [201], for solute *A* in the gas that is transferred in the liquid phase when the equilibrium function (F_{eq}) and the operating data (L_m/G_m) are known, it is possible to graphically evaluate the slope of the transport line, as depicted in **Figure III.4**:

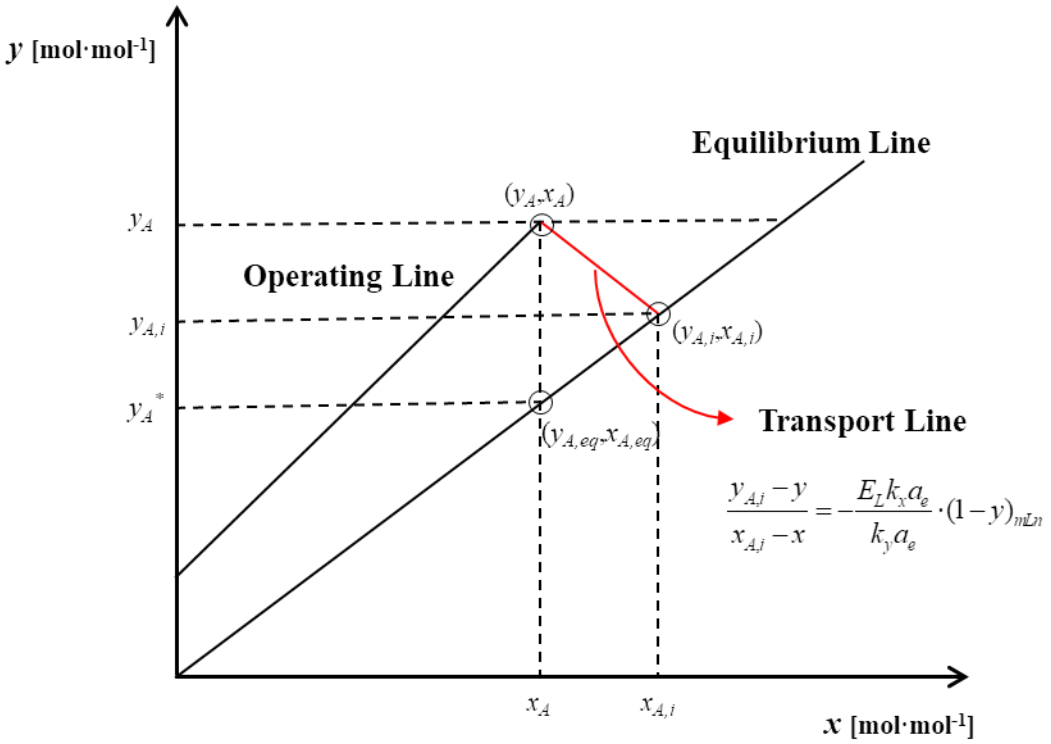

Figure III.4. *Graphic evaluation of the slope of transport line* [201]

In general, the values of HTU_{OG} can be calculated along the column for any kind of contactor, but this value can be successfully averaged from top to bottom, as in **Eq. (183)**, only for packed towers when liquid and gas molar flows varied by less than about 5% [200]**,** [201].

The number of transfer units (NTU_{OG}) is a purely thermodynamic parameter that depends on the driving force, operating conditions and the equilibrium data (y^*) and can be evaluated by solving the integral in **Eq. (187)** [201]**:**

$$NTU_{OG} = \int_{y_2}^{y_1} \frac{dy}{(1-y)(y-y^*)} \tag{187}$$

Referring to the case depicted in **Figure III.4**, y_A^* can be evaluated by correlating the operating conditions (y, x) with the equilibrium data (y_{eq}, x_{eq}) if the equilibrium function F_{eq} is known.

As already stated, Henry's law rules the physical gas-liquid equilibria, and the gas solubility data can be found in the relevant literature. When the absorption is purely physical the mole fraction of the

gas *A* is linearly proportional to the *A* composition in the liquid phase by the Henry's constant (**Eq. (179)**). In the case of an absorption process involving chemical reactions, the function (**Eq. (180)**) is not linear and it is recommended to evaluate the equilibrium data with specific tests (*e.g.* see **Section III.1.3.**).

The general correlation for determining the pressure drop per meter of column ($\Delta P/Z$, [mbar·m^{-1}]) is reported below:

$$\frac{dP}{dZ} = f(F_L, F_G, \Phi, \Upsilon) \tag{188}$$

The gas pressure drop highly depend on the system, and therefore the **Eq. (188)** is written in a general form by simply recalling its main functional dependencies, differently from the predictive models proposed in **Section II.4.1.** and **Section II.4.2.**, such as those on liquid load factor, F_L [m·h^{-1}] and gas load factor, F_G [Pa$^{0.5}$]), physical and transport parameters of liquid and gas (Φ), and finally and the geometric parameters (Υ).

The liquid and gas load factors can be defined as follows:

$$F_L = 3600 u_{L,s} = 10^{-3} \frac{L}{S} \tag{189}$$

$$F_G = \rho_G \sqrt{u_{G,s}} = \rho_G \sqrt{\frac{G}{3600 \cdot S}} \tag{190}$$

in which, L [L·h^{-1}] is the liquid volumetric flow rate, G [m^3·h^{-1}] is the gas volumetric flow rate, u_{Ls} [m·s^{-1}] is the superficial liquid velocity and u_{Gs} [m·s^{-1}] is the superficial gas velocity.

ASPEN PLUS® software was used as a calculation tool, selecting the appropriate predictive models in the software, to perform rigorous calculations to describe the experimental removals and wash water pH data obtained in the packed column with M250.X packing. Indeed, it provide a rigorous model for packed towers design called “Rate-based block”. The proposed block allows to discretize the column following the equations of a plug-flow reactor (PFR) and simultaneously solves mass, charge and energy balance equations. The calculation tool requires the implementation of some predictive models (often are already available in the database), such as:

- a thermodynamic property method based on predictive models for the calculation of the fugacity coefficients for the gas phase and activity coefficients for the liquid phase;
- a flow model;
- a mass transfer model for packed columns;
- a pressure drop model for packed columns;
- a heat transfer model adapted for packed columns;

In addition, it is possible to add networks of physical gas-liquid equilibria and chemical equilibrium reactions (some already included in the ASPEN PLUS® database with the corresponding data on equilibrium constants, selecting Elec-Wizard option) and networks of kinetics of chemical reactions (which are not included in the ASPEN PLUS® database).

The equation to evaluate the absorption efficiency of SO_2 (η_{SO_2}) and NO_x (η_{NO_x}) data in the gas stream is reported below:

$$\eta_{SO_2} = \frac{C^{\circ}_{SO_{2(g)}} - C_{SO_{2(g)}}}{C^{\circ}_{SO_{2(g)}}} \quad (191)$$

$$\eta_{NO_x} = \frac{C^{\circ}_{NO_{x(g)}} - C_{NO_{x(g)}}}{C^{\circ}_{NO_{x(g)}}} \quad (192)$$

where $C^{\circ}_{SO_2(g)}$ and $C^{\circ}_{NO_x(g)}$ are the concentration of SO_2 and NO_x in the gas stream at the column inlet and $C_{SO_2(g)}$ and $C_{NO_x(g)}$ are the concentration of SO_2 and NO_x at the column outlet.

III.3. Pilot spray columns

The absorption experiments carried out in the VTS spray tower aimed to evaluate the removal efficiency of SO_2 from a simulated flue-gas containing SO_2 and compare it with performance obtained in the packed column with M250.X operated at the same experimental conditions. The VTS spray tower operated at 1 atm and 25 °C.

Differently, absorption experiments carried out in Chalmers spray tower aimed to evaluate the removal efficiency of SO_2 on a real flue-gas generated from a diesel engine at different engine load and using seawater solutions with different chemical and physical characteristics as absorbing liquid. The Chalmers spray tower operated at 1 atm and with different gas temperatures.

III.3.1. Materials

III.3.1.1. VTS spray tower

The simulated flue-gas was prepared using SO_2 (10% vol. in N_2) supplied by Rivoira Gas Srl in high-pressure cylinders compressed and filtered air (provided by VTS compressor).

The FGD experiments were carried out using synthetic seawater solution at pH = 8.2 (SW), obtained by adding 33 $g \cdot L^{-1}$ of NaCl, 4.14 $g \cdot L^{-1}$ of Na_2SO_4, 0.16 $g \cdot L^{-1}$ of $NaHCO_3$ and 0.03 $g \cdot L^{-1}$ of Na_2CO_3 to the tap water;

The chemicals used were sodium chloride (food grade), sodium sulphate (99.99% w/w), sodium bicarbonate (99.99% w/w), and sodium carbonate (99.99% w/w) purchased from VWR International Chemicals (Italy) as AR grade.

III.3.1.2. Chalmers spray tower

The flue-gas is generated by a Volvo PENTA 80 kW marine diesel engine, using a marine gas oil (MGO). **Table III.3** reports the engine data collected during the tests fixing the engine load at 10, 25 and 50%.

Table III.3. *Engine data collected for different engine loads (10, 25 and 50%)*

Engine Load	Engine Speed *rpm*	Hydraulic Torque *N·m*	Engine Power *kW*	Fuel Consumption *L/h*	Flue-gas Temperature *°C*
10%	2000	35	8.38	2.7±1	180±6
25%	2000	95	19.90	5.5±1	260±5
50%	2000	190	39.80	10.1±1	318±2

The chemical composition of the MGO fuel used is provided by Saybolt laboratory in Göteborg (Sweden) and is shown in **Table III.4**:

Table III.4. *Chemical composition of the HGO fuel used in the Volvo PENTA 80 kW diesel engine*

Name	Methods	Results
Total aromatics	SS 155116	30.2% vol.
Mono-aromatics	SS 155116	21.3% vol.
Di-aromatics	SS 155116	7.76% vol.
Poly aromatics (Tri+)	SS 155116	1.13% vol.
Sulphur (S)	EN ISO 8754	0.92% w/w
Aluminum (Al)	ASTM D 7111	0.35 $mg \cdot kg^{-1}$
Barium (Ba)	ASTM D 7111	< 0.1 $mg \cdot kg^{-1}$
Calcium (Ca)	ASTM D 7111	< 0.1 $mg \cdot kg^{-1}$
Chromium (Cr)	ASTM D 7111	< 0.1 $mg \cdot kg^{-1}$
Copper (Cu)	ASTM D 7111	< 0.1 $mg \cdot kg^{-1}$
Iron (Fe)	ASTM D 7111	< 0.1 $mg \cdot kg^{-1}$
Lead (Pb)	ASTM D 7111	< 0.1 $mg \cdot kg^{-1}$
Lithium (Li)	ASTM D 7111	< 0.1 $mg \cdot kg^{-1}$
Magnesium (Mg)	ASTM D 7111	< 0.1 $mg \cdot kg^{-1}$
Manganese (Mn)	ASTM D 7111	< 0.1 $mg \cdot kg^{-1}$
Molybdenum (Mo)	ASTM D 7111	< 0.1 $mg \cdot kg^{-1}$
Nickel (Ni)	ASTM D 7111	< 0.1 $mg \cdot kg^{-1}$
Potassium (K)	ASTM D 7111	< 0.1 $mg \cdot kg^{-1}$
Silicon (Si)	ASTM D 7111	< 0.1 $mg \cdot kg^{-1}$
Silver (Ag)	ASTM D 7111	< 0.1 $mg \cdot kg^{-1}$

Sodium (Na)	ASTM D 7111	< 0.1 mg·kg^{-1}
Titanium (Ti)	ASTM D 7111	< 0.1 mg·kg^{-1}
Vanadium (V)	ASTM D 7111	< 0.1 mg·kg^{-1}
Zinc (Zn)	ASTM D 7111	< 0.1 mg·kg^{-1}

The FGD experiments were carried out using two scrubbing solutions:

- a seawater of Kattegat (*SWK*) with a pH = 8.7;
- a basic seawater of Kattegat (*SWKOH*) at pH = 10.5, obtained by adding 100 mg·L^{-1} of NaOH.

The chemicals used was purchased from VWR International Chemicals (Sweden) as AR grade for the synthetic seawater solutions preparation.

The analysis of chemical composition of the Kattegat seawater was performed by ALS Scandinavia AB by ionic chromatography technique. The heavy metals and ionic composition are reported in **Table III.5**, while the organic compounds in **Table III.6**.

Table III.5. *Heavy metals and ionic composition by analysis on Kattegat seawater sample provided by ALS Scandinavia AB (SE)*

Sampling Date:			**KSW**
Heavy metals and ionic composition			**Results**
Ca	Calcium	mg·L^{-1}	19.5
Fe	Iron	mg·L^{-1}	0.0243
K	Potassium	mg·L^{-1}	< 8
Mg	Magnesium	mg·L^{-1}	< 2
Na	Sodium	mg·L^{-1}	13100
Si	Silicon	mg·L^{-1}	1.03
Al	Aluminum	µg·L^{-1}	34.7
Ba	Barium	µg·L^{-1}	10.2
Cd	Cadmium	µg·L^{-1}	< 0.05
Co	Cobalt	µg·L^{-1}	< 0.05
Cr	Chrome	µg·L^{-1}	0.14
Cu	Copper	µg·L^{-1}	12.4
Hg	Mercury	ng·L^{-1}	< 2
Mn	Manganese	µg·L^{-1}	2.85
Mo	Molybdenum	µg·L^{-1}	0.245
Ni	Nickel	µg·L^{-1}	1.38
P	Phosphorus	µg·L^{-1}	< 40
Pb	Lead	µg·L^{-1}	< 0.3
Sr	Strontium	µg·L^{-1}	52.4
Zn	Zinc	µg·L^{-1}	83.1
NO_3^-	Nitrate	mg·L^{-1}	1.32
SO_4^{2-}	Sulphate	mg·L^{-1}	68.9
PO_4^{3-}	Phosphate	mg·L^{-1}	< 0.04
F^-	Fluoride	mg·L^{-1}	< 2
Br^-	Bromide	mg·L^{-1}	< 4
Cl^-	Chloride	mg·L^{-1}	21400
NH_4^+	Ammonium	mg·L^{-1}	< 0.05
HCO_3^-	Bicarbonate	mg·L^{-1}	219

Table III.6. *Organics composition by analysis on Kattegat seawater sample provided by ALS Scandinavia AB (SE)*

Sampling Date: **Organics composition**		**KSW** **Results**
aliphates> C5-C8	$\mu g \cdot L^{-1}$	< 10
aliphates> C8-C10	$\mu g \cdot L^{-1}$	< 10
aliphates> C10-C12	$\mu g \cdot L^{-1}$	< 10
aliphates> C12-C16	$\mu g \cdot L^{-1}$	< 10
aliphates> C5-C16	$\mu g \cdot L^{-1}$	< 20
aliphates> C16-C35	$\mu g \cdot L^{-1}$	< 10
aromatics> C8-C10	$\mu g \cdot L^{-1}$	< 0.30
aromatics> C10-C16	$\mu g \cdot L^{-1}$	< 0.775
metylpyrener/metylfluorantener	$\mu g \cdot L^{-1}$	< 1.0
methylchrysene/dimethylbenz(a)anthracene	$\mu g \cdot L^{-1}$	< 1.0
aromatics C16-C35	$\mu g \cdot L^{-1}$	< 1.0
benzene	$\mu g \cdot L^{-1}$	< 0.20
toluene	$\mu g \cdot L^{-1}$	< 0.20
ethylbenzene	$\mu g \cdot L^{-1}$	< 0.20
m-,p-xylene	$\mu g \cdot L^{-1}$	< 0.20
o-xylene	$\mu g \cdot L^{-1}$	< 0.20
xylenes, sum	$\mu g \cdot L^{-1}$	< 0.20
naphthalene	$\mu g \cdot L^{-1}$	0.038
acenaphthylene	$\mu g \cdot L^{-1}$	< 0.010
acenaften	$\mu g \cdot L^{-1}$	< 0.010
fluorene	$\mu g \cdot L^{-1}$	< 0.010
phenanthrene	$\mu g \cdot L^{-1}$	0.037
anthracene	$\mu g \cdot L^{-1}$	< 0.010
fluoranthene	$\mu g \cdot L^{-1}$	< 0.010
pyrene	$\mu g \cdot L^{-1}$	< 0.010
benzo(a)anthracene	$\mu g \cdot L^{-1}$	< 0.010
chrysene	$\mu g \cdot L^{-1}$	< 0.010
benzo(b)fluoranthene	$\mu g \cdot L^{-1}$	< 0.010
benzo(k)fluoranthene	$\mu g \cdot L^{-1}$	< 0.010
benzo(a)pyrene	$\mu g \cdot L^{-1}$	< 0.010
dibenz(a,h)anthracene	$\mu g \cdot L^{-1}$	< 0.010
benzo(g,h,i)perylene	$\mu g \cdot L^{-1}$	< 0.010
indeno(1,2,3-cd)pyrene	$\mu g \cdot L^{-1}$	< 0.010
PAH, sum 16	$\mu g \cdot L^{-1}$	0.075
PAH, sum carcinogens	$\mu g \cdot L^{-1}$	< 0.035
PAH, sum others	$\mu g \cdot L^{-1}$	0.075
PAH, sum L	$\mu g \cdot L^{-1}$	0.04
PAH, sum M	$\mu g \cdot L^{-1}$	0.04
PAH, sum H	$\mu g \cdot L^{-1}$	< 0.04

III.3.2. Plant description and experimental procedures

III.3.2.1. VTS spray tower

The pilot spray tower (AISI 316 Stainless-steel) used for the experiments has an internal diameter of 0.4 m and length of 4 m, operated at 25 °C and 1 atm. The column was equipped with four same

PNR® full-cone spray nozzles with spray angles of 30°, made in stainless steel. To better study the fluid-dynamics on absorption phenomenon in the spray column, a nozzle (PNR® BRB 2117 B1) characterization was performed using a high-speed camera Phantom model Miro C110. The optical lens was a NIKKOR LENS AF-S 85 mm f1/8G and a macro ring pk11a was added. The light required by the camera was provided by a blue led produced by Thor Lab model LEDD1B. For each test, 4000 frames were recorded with an exposure time of 4 µs. The field of view was a rectangle 1280x1024 mm^2 and the light was placed behind the spray in a way to avoid shadow zone as much as possible. The high-speed camera was focalized with a ruler of 28 mm that was used to calibrate the imagine analysis software (Image J®). Once the droplet diameters were retrieved by Image J, a MATLAB® tool (distribution fitting tool) was used to get the droplets population in **Figure III.5** in terms of *PDF* (**A**) or *CDF* (**B**).

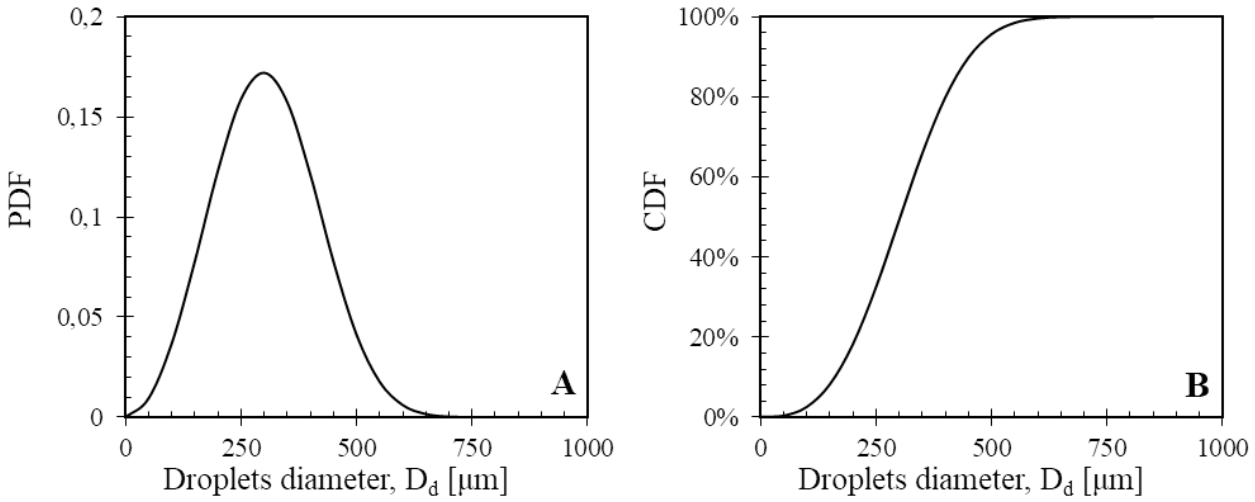

Figure III.5. *Droplets population of PNR® BRB 2117 B1 full-cone nozzle in terms of the Probability Density Function (PDF) and Cumulative Distribution Function (CDF)*

Most of droplets had a diameter in the range 150 - 900 µm and, apart the largest ones, they appeared as spherical and non-oscillating.

The droplets were distributed according to a Rosin-Rammler distribution with an average droplets size of 342 µm and a shape factor of 3; moreover, all droplets rapidly reached their terminal velocity. This pilot unit is part of the experimental set-up previously presented by **Flagiello et al.** [43] and **Di Natale et al.** [202], and its flowsheet is showed in **Figure III.6**:

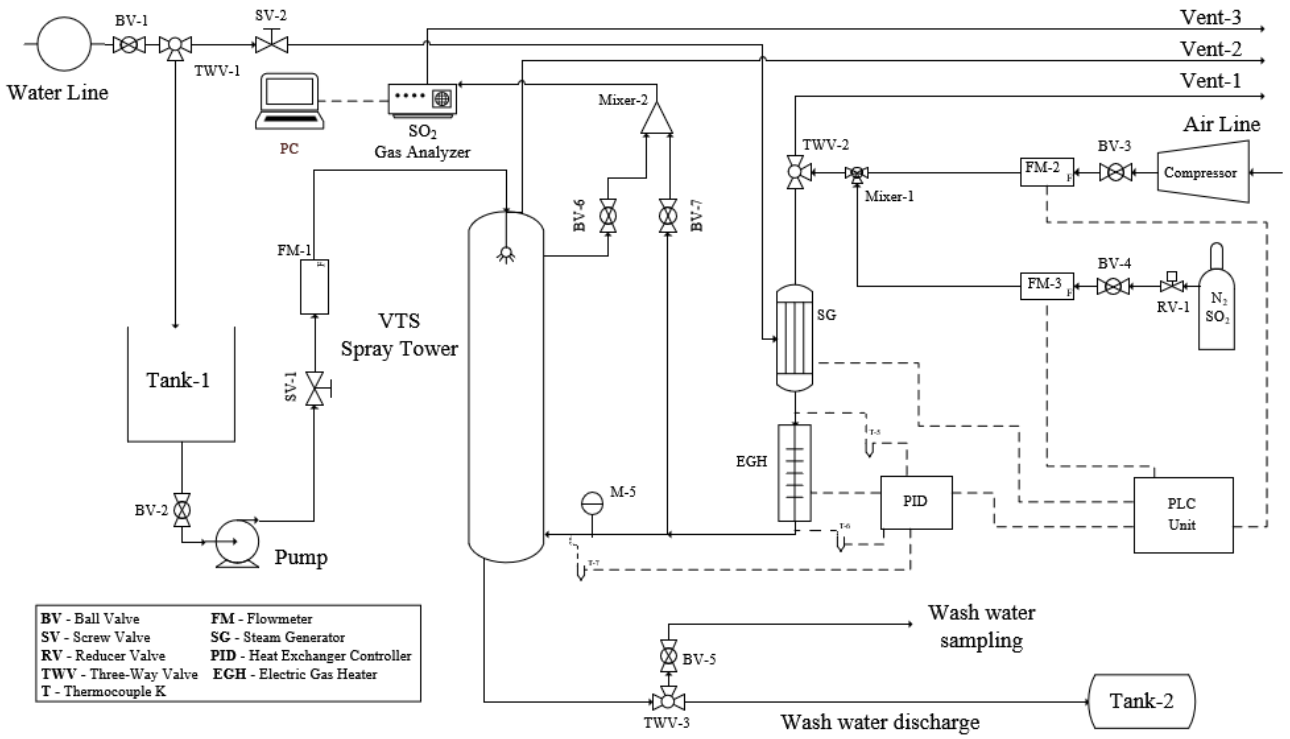

Figure III.6. *P&ID diagram of the experimental set-up of the VTS spray tower*

To assure a good distribution of the sprayed water on the entire column section, four equal nozzles were arranged on the three vertices and in the center of an equilateral triangle (with a total sprays angle equal to 60°). The column was equipped with internal collectors to allow measurements of water flow dispersed on the column walls and of the water composition along the column height. The first was accomplished by using semi-circular accumulation tanks placed at two different column heights (1850 and 3000 mm from the nozzle tip, respectively) and connected with a pipe to an external sampling bottle outside the column. The second task was achieved by a set of five "pockets" connected with external sampling vials, placed at different radial (60° shifting among each other) and height positions (100, 600, 1100, 2350, 2850 mm from the nozzle tip, respectively).

The nozzles were positioned so to have an effective scrubber height of 3.5 m and the water flow rate could be modified by switching off one or more nozzles. The gas velocity was around 20% of the average droplet (342 μm) terminal velocity and corresponded to the terminal velocity of about 75 μm droplets. The droplet size distribution corresponded to an expected loss of droplets by entrainment of about 1%. Above the spray nozzles distribution line, a 150 mm height stainless steel demister is installed for the entrained liquid drops.

The liquid flow was supplied by a centrifugal pump (Lowara CAM 120/35/B, total power 1.5 kW) controlled by a ASA liquid flowmeter up to 120 $m^3 \cdot h^{-1}$ (C/G47_50 Ex d model) and fed at the top of the column in counter-current flow to the gas inlet. Liquid discharges (wash water) were sent to an

accumulation tank, whose content was periodically sampled to measure pH value and SO_3^{2-}/SO_4^{2-} concentrations.

The model gas was compressed and filtered air (ULPA filter), mixed with controlled amounts of SO_2 from a pressurized cylinder, so to achieve the desired column inlet concentration suitably humidified up to water saturation level at the test temperature. The gas feed line was equipped with a ASA gas flowmeter up to 100 $Nm^3 \cdot h^{-1}$ (C47_50 Ex d model) for each gas (air and gas mixture in cylinder), a 6 kW in-line electrical heater (which is able to heat up the gas to 60 °C with a total power of 6 kW) and a water vapor injection provided by a steam generator (5.5 kW power consumption) mounted on the same skid of the scrubber column. The heating device was externally insulated and was connected to a PID controller for temperature control.

The plant was equipped with temperature and pressure sensors along the pipelines at the input and output of the column. All the instrumentation were connected with a dedicated PLC unit that controlled all the input data and registered all the sensor data with a lowest frequency of 1 min^{-1}.

Absorption tests were carried out by feeding the gas stream to the spray column at the desired flow rate (G, [$m^3 \cdot h^{-1}$]), temperature (T_G, [°C]), relative humidity (H_R, [water mass/dry air mass]) and concentration of SO_2 ($C^{\circ}_{SO_2}$, [ppm_v]), which were checked by gas analyzer (ADC-MGA 3000C Multi-Gas Analyzer) before the liquid feeding. The absorbing liquid stream was fed in counter-current to the flow the gas at the desired flow rate (L, [$L \cdot h^{-1}$]) and temperature (T_L, [°C]); the concentration levels of SO_2 were monitored and recorded up to the steady state, to reach which a characteristic time dependent on the scrubber fluid-dynamics and its operating conditions was needed.

The ADC-MGA 3000C Multi-Gas Analyzer with NDIR detectors for $SO_2/CO/CO_2$ and galvanic cell for O_2 measured the concentration of SO_2 in the gaseous stream. The gas analyzer was equipped with a gas quencher (Bühler Technologies). The **Eq. (191)** is used to evaluate the removal efficiency of SO_2 (η_{SO_2}).

The wash water was collected at the bottom of the column and sent to a sampling point for further analysis: pH value and temperature by a pH-meter (Thermo Scientific, ORION Start A111 model); and eventually the ionic composition by ionic chromatography method (Metrohm, AG 883 Basic IC PLUS).

During the tests it was possible to retrieve:

- the concentration for residual SO_2 gas in outlet stream at the column;
- the gas temperature in outlet stream at the column;
- the relative humidity in outlet stream at the column;
- the gas pressure drops along the column;
- the wash water pH;

- the wash water temperature;
- the content of ionic species in the wash water.

III.3.2.2. Chalmers spray tower

The pilot spray tower (i.d.: 400 mm and total length: 500 mm) was made in stainless steel AISI 316L and was positioned horizontally, unlike the common vertical scrubbers. The column operated at atmospheric pressure and different temperatures; the flue-gas derives from a Volvo Penta 80 kW diesel engine. Different engine loads can be tested by varying the engine speed and the hydraulic torque. The load variation influences the fuel consumption, temperature and composition of the flue-gas generated. A PLC unit it allowed to manage the engine rpm, the hydraulic torque, the cooling water and to control the temperatures and pressure of the engine and of the support units.

The flowsheet of the experimental plant is showed in **Figure III.7**:

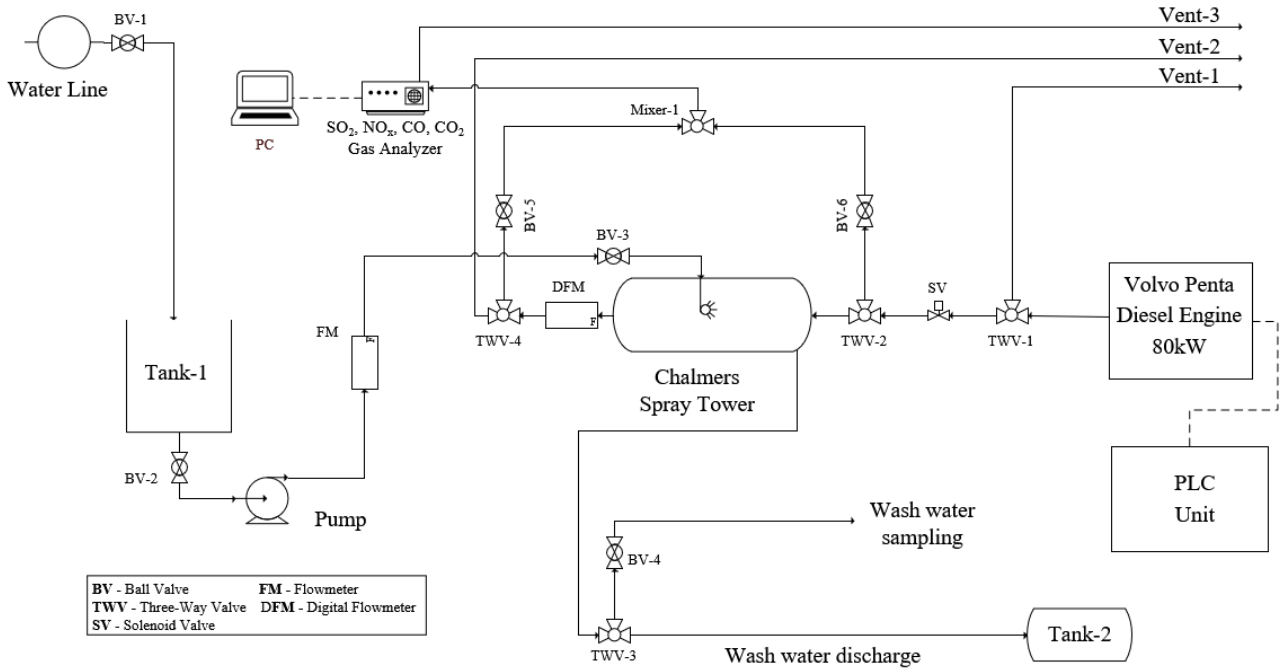

Figure III.7. *P&ID diagram of the experimental set-up of the Chalmers spray tower*

On the outlet line of the Volvo Penta diesel engine exhausts, a solenoid valve allows to split the gas flow rate into two streams: the first was sent to the ship chimney and the second one was sent to the scrubber in order to be treated. A fan installed downstream the entire plant allowed to fix the total gas flow rate and the split ratio of the valve allowed determining the fraction sent to the spray tower. The piping that connected the Volvo Penta to the spray tower was made in Stainless Steel AISI 316L (i.d. 74 mm) and was thermally insulated in order to reduce the heat losses.

The flow rate, temperature and pressure of the flue-gas after the scrubber was measured by the portable analyzer (Testo 480 Multi-function, equipped with a steel probe inserted into the outlet scrubber piping).

The flue-gas was fed in counter-current flow to the water into the scrubber. The liquid flow was fed by a rotative pump (Getriebebau Nord GmbH & Co.KG, D-22941 model, with a total power 1.8 kW) and its pressure was controlled by a pressure gauge 0 - 10 bar (WIKA Instruments, 233.50.63 model). The liquid flow was measured by ROTA Yokogawa liquid rotameter 0 - 10 $L \cdot min^{-1}$ before the scrubber. A BETE® spray nozzle (HA 1.50 - 9020 model, made in stainless steel) was placed at 140 mm of distance from the scrubber inlet. In order to reduce the amount of water dragged by the gas, two honeycomb grid demisters made in stainless steel AISI 316L (i.d.: 400 mm) were put at 140 mm from the scrubber outlet.

The wash water was stored in a steel tank of about 5 m^3 and then disposed. The water samples were collected in sampling bottles at the scrubber outlet for pH and temperature analysis, and they were stored for further qualitative analysis.

Absorption tests were carried out by feeding the gas stream (G, $[m^3 \cdot h^{-1}]$) coming from the diesel engine at fixed engine load to the spray column. The initial concentration of the pollutants was determined by gas analysis system before liquid feeding, while the output concentration levels of pollutants were monitored and recorded up to the steady state, to reach which a characteristic time dependent on the scrubber fluid-dynamics and its operating conditions was needed.

The gas analysis system was a Fuji Electric ZRE type NDIR gas analyzer (SO_2, NO, CO and CO_2) and Ankersmid Sampling (AOX 100 model) NO_x converter. NO_x present as NO_2 into NO. Flue-gas sample was previously cleaned from the soot with hot filter (J.U.M. Engineering, heated sample filter 1128 model) and dehumidified with gas quencher (Ankersmid Sampling gas cooler) at low temperature.

The wash water was collected in a bottle sample for further analysis. The pH value and temperature were measured by Oakton Waterproof pH-meter portable (pH Tester 30 Pocket model with accuracy ±0.1 for pH and temperature value). The ionic, organic and heavy metal composition they could be measured with more specific analysis.

During the tests, it was possible to retrieve:

- the SO_2 NO, NO_x, CO and CO_2 gas residual concentration in the column outlet stream;
- the gas temperature in the column outlet stream;
- the wash water pH;
- the wash water temperature;
- the content of ionic, organics and metals species in the wash water.

III.3.3. Methodology for the data analysis

The data analysis for the spray columns can be performed following the same approach adopted in **Section III.3.2.** for the evaluation of the column height (*Z*) and the pressure drop (or the column section, *S*).

However, regarding the evaluation of the column height (*Z*), the simplification approach proposed in **Eq. (182)** is correct only when the liquid and gas flow rates can be considered as constant, while for spray towers, where liquid losses along the walls must be taken into account, a large variation of HTU_{OG} is expected. Also the calculation approach for NTU_{OG} must be modified because the operating conditions (*e.g.* the *L/G* ratio) vary along the column.

When water losses at the scrubber walls cannot be neglected, as often happens in the spray columns, **Eq. (181)** must be numerically resolved. Hence, for a correct evaluation of the spray column height, the effective liquid flowing along the scrubber $L_m(z)$ [mol·s^{-1}] must be calculated.

The spray tower height (*Z*) can be determined from the integral of the following equation taking into account the overall resistance of liquid-side mass transfer:

$$L_m(z)\,dx = K_{OL}a_e(z)\left(x^* - x\right)S\,dz \tag{193}$$

in which the coordinate *z* is equal to 0 at the nozzle height and equal to *Z* at the bottom of the column; *x* [mol·mol^{-1}] is the mole fraction of the solute in the liquid phase; x^* [mol·mol^{-1}] is the mole fraction of solute in the liquid phase that is in equilibrium with the solute in the gas phase; $K_{OL}a_e(z)$ represents the overall mass transfer coefficient for liquid-side in a differential volume *Sdz* of the column, which is expressed in mol·m^{-3}·s^{-1} as reported below.

$$K_{OL}a_e(z) = \left[\frac{1}{E(z)k_x a_e(z)} + \frac{1}{k_y a_e(z)\cdot\left.\frac{\partial y}{\partial x}\right|_i(z)}\right] \tag{194}$$

The mass transfer coefficients along the column ($k_x a_e(z)$ and $k_y a_e(z)$) were calculated using the predictive models presented in the **Section II.3.2.**, while the conditions at the interface $(\partial y/\partial x)_i$ were evaluated with the same approach described in the **Section III.2.3.** (**Figure III.4**).

It is interesting observing that, by explaining the effective contact height of the scrubber in terms of the liquid properties, it is possible to highlight the direct dependence of the height on the active liquid flow rate, which is a critical aspect of spray towers. The resolution of **Eq. (193)** requires the assessment of the normalized density function distribution $PDF(D_{d,j})$ of droplet size and the velocity of the sprayed droplets (U_j). Moreover, the equilibrium curve for the absorption of a single gaseous

species in the liquid-phase and the mass balance equation over the column (*i.e.* the operating curve) are required. In addition, it is necessary to evaluate the gas and liquid-side mass transfer coefficients for all the droplets as a function of the actual vertical distance *z* from the nozzle, in order to take into account the evolution of droplet size distribution related to evaporation, condensation and coalescence. If these phenomena are neglected, the droplets size distribution can be considered as uniform inside the scrubber and can be determined from spray imaging close to the nozzle (< 50cm). Under this hypothesis, the gas and liquid-side mass transfer coefficients for all the droplets in a differential volume *Sdz* of the column, $k_y a_e(z)$ and $k_x a_e(z)$ can be expressed in mol·m^{-3}·s^{-1} as reported below.

$$k_y a_e(z) = \phi(z)\left[\sum_j k_{y,j} a_{d,j} PDF\left(D_{d,j}\right)\right] \tag{195}$$

$$k_x a_e(z) = \phi(z)\left[\sum_j k_{x,j} a_{d,j} PDF\left(D_{d,j}\right)\right] \tag{196}$$

In **Eqs. (195)** and **(196)** $k_{y,j}$ and $k_{x,j}$ [mol·m^{-2}·s^{-1}] represent the gas-side and liquid-side mass transfer coefficients for a single *j-th* droplet, evaluated as reported in the previous sections (**Section II.3.2.**); $a_{d,j}$ is the droplet surface involved in the mass transfer, previously reported for two different cases in **Eqs. (136)** and **(137)**; $\phi(z)$ is the droplet volume fraction for each axial position *z*.

The droplet volume fraction for each axial position *z* in the scrubber ($\phi(z)$) can be evaluated by **Flagiello et al.** [43] as below:

$$\phi(z) = \frac{L_m(z)\rho_x^{-1}u_{Gs}}{L_m(z)\rho_x^{-1}u_{Gs} + G_m\rho_y^{-1}\left(u_{Ls} - u_{Gs}\right)} \tag{197}$$

The spray column section (*S*) is evaluated using the predictive equations for pressure drop, or can be determined from the droplet terminal velocity (U_j): the gas superficial velocity (u_{Gs}) in the column must be stated so to avoid the entrainment of droplets in the gas phase. Nevertheless, for a generic droplet size distribution, it could result almost impossible to fully avoid it because the finest droplet may be very small and easily entrained. Usually, once a minimum droplet size, $D_{d,cut}$, is defined, the gas velocity is chosen to correspond to 90 - 95% of $D_{d,cut}$ terminal velocity, and the nozzle design and operation are chosen to assure that the droplets smaller or equal to the $D_{d,cut}$ are only a negligible part (usually 1 or 2% at max) of the droplet size distribution.

Following these indications, water loss by gas entrainment is contained below 1%. Once the droplet size distribution and the spray and gas velocities are chosen, the mass transfer coefficient can be determined and the scrubber design is only a function of the ratio between liquid and gas flow rate, which controls the mass balance and, of course, of their chemical and physical properties. One

additional issue is related to the spray fluid dynamic in the confined volume of the scrubber: some of the droplets collide with the scrubber walls and their contribution to scavenging becomes almost negligible. The amount of water that impacts on the scrubber wall is estimated by considering: the nozzle injection velocity (u_j, [m·s^{-1}]) and spray angle (θ_s, [°]), the scrubber diameter (D, [m]) and the droplet size distribution. **Figure III.8** shows the scheme of a spray tower operating in counter-current flow, with the characteristic geometric parameters to be considered in the calculation of the active liquid flow ($L_m(z)$) and its generic trend along the column.

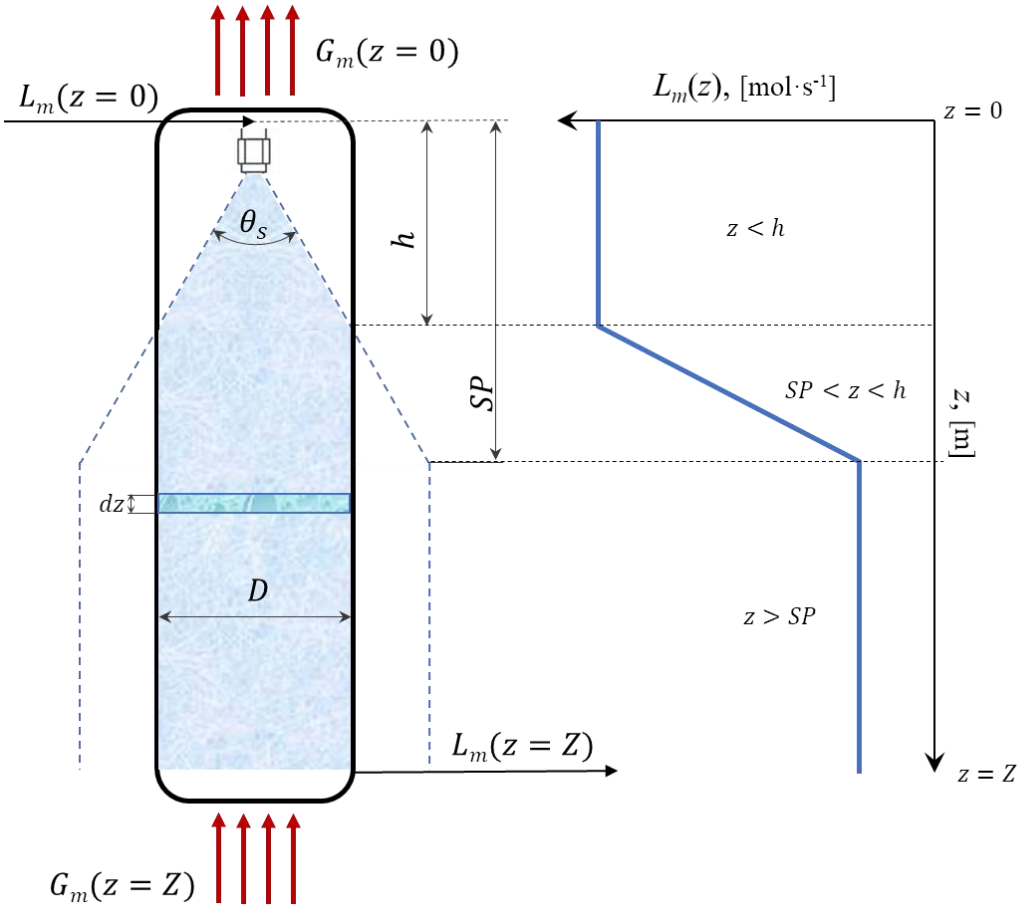

Figure III.8. *Scheme of a spray tower operating in counter-current flow, including the characteristic geometric parameters to be considered in the calculation of the active liquid flow and its generic trend along the scrubber*

Immediately after a droplet is sprayed at high velocity from the nozzle, it decelerated due to the drag force, finally reaching its terminal velocity. This deceleration covers the so-called stop distance (SP, [m]), which is evaluated through the following expression [203]:

$$SP = \frac{u_j m_d \left\{1 + \frac{2\lambda_{air}}{D_d}\left[1.257 + 0.4e^{\left(-\frac{1.1D_d}{2\lambda_{air}}\right)}\right]\right\}}{3\pi\mu_L D_d} \tag{198}$$

In which λ_{air} [m] is the mean free path of air.

For a given droplet size, the stop distance (*SP*) from the nozzle is calculated by classical fluid dynamic of a single sphere: once the droplet reaches its terminal velocity, it is entrained in the gas and follows its streamlines, moving vertically. It is assumed that, for a given spray angle and column diameter, the droplet may touch the scrubber wall only if the stop distance (*SP*) is higher than the impact distance (*h*, [m]), which is given by the following expression:

$$h = \frac{D}{2}\left[\tan\left(\frac{\theta_s}{2}\right)\right]^{-1} \tag{199}$$

Dimiccoli et al. [171] proposed a geometric evaluation of water losses on scrubber walls so to determine the active liquid flow rate along the column $L_m(z)$. By indicating with *z* the axial distance from the nozzle, which varies between 0 and the entire column height (*Z*), for $z > h$ the active liquid flow rate $L_m(z)$ is evaluated using the following equation:

$$L_m(z) = \varphi(z) \cdot L_m \tag{200}$$

in which $\varphi(z)$ represents for each axial position z the ratio between the effective volume occupied by the liquid and the theoretical spray cone volume in open space, which is given by the **Eq. (201)**.

$$\varphi(z) = \frac{\frac{\pi}{3} z \cdot r^2(z) - \left\{\frac{\pi}{3}(z-h)\left[r^2(z) + \frac{D}{2}r(z) + \left(\frac{D}{2}\right)^2\right] - \frac{\pi}{4}D^2(z-h)\right\}}{\frac{\pi}{3} z \cdot r^2(z)} \tag{201}$$

Where $r(z)$ the radius of the spray cone for each axial position *z*, expressed as:

$$r(z) = z\tan\left(\frac{\theta_s}{2}\right) \tag{202}$$

For $z > SP$, $L_m(z)$ is constant and equal to the active molar flow rate evaluated using the **Eqs. (200)-(202)** at the stop distance, $L_m(SP)$.

For the modelling analyses and design of spray systems, commercial software are not available as for packed-bed towers. A calculation tool implemented in MATLAB®, based on the equations previously presented and on mass transfer (**Section II.3.2.**) can allow to evaluate the pollutant concentration at column outlet also taking into account the liquid losses along the scrubber walls, once the effective

spray column height (*Z*) has been set. Therefore, the Z could be indirectly estimated from the experimental removal efficiency values.

Finally, the column section (*S*) can be evaluated by adopting the cut diameter criteria (previously exposed) or using predictive models for pressure drop (**Section II.4.2.**) or via CFD analysis (following the same approach adopted by **Esposito** [204].

IV. RESULTS AND DISCUSSION

This Chapter presents the results of the experimental and modelling investigation carried out during this Ph.D. thesis work. Most of the experiments were published or under submission in several papers on Archival Journals. To help matching between the overall results of the thesis and the attached papers, this chapter is divided in subsections, each of which predominantly referred to one of the papers. In particular, the following sections will be presented:

- FGD process in a packed-bed column with M250.X using seawater-based solutions enhanced with NaOH (**Section IV.1**)
- Mass transfer and pressure drop characterization of M250.X structured packing for absorption columns (**Section IV.2**)
- Seawater desulphurization scrubbing in spray and packed columns for a 4.35 MW Wärtsilä marine Diesel engine (**Section IV.3**)
- FGD process by seawater scrubbing in a pilot spray column for a 80 kW Volvo Penta marine Diesel engine (**Section IV.4**)
- FGD process by wet oxidation scrubbing from model flue-gas using seawater-based solutions enhanced with $NaClO_2$ (**Section IV.5**)
- Wet oxidation scrubbing effect on NO_x emissions using seawater-based solutions enhanced with $NaClO_2$ (**Section IV.6**)
- Simultaneous SO_2 and NO_x removal by wet oxidation scrubbing using seawater-based solutions enhanced with $NaClO_2$ (**Section IV.7**)

IV.1. FGD process in a packed-bed column with M250.X using seawater-based solutions enhanced with NaOH

This section is extracted from a work published on Fuel for the Special Issue devoted to the 8th International Conference on Clean Coal Technologies.

The experiments were performed on a simulated flue-gas (G = 32 $m^3 \cdot h^{-1}$) containing a SO_2 concentration in the range 500 to 2000 ppm_v, treated in a packed column filled with a Mellapak 250.X structured packing (see **Section III.2.2.**) at 1 atm and 25°C, with a liquid-gas ratio (L/G) between 1.25 and 4.06 $L \cdot m^{-3}$ (corresponding to 1.06 and 3.44 $kg \cdot kg^{-1}$).

Three different absorbing solutions were investigated: distilled water (used as a benchmark); a seawater; seawater with NaOH (seawater with 200 $mg \cdot L^{-1}$ of NaOH). Further details on the physical-chemical composition of the liquids used were reported in **Section III.1.1. and III.2.1.**.

In order to analyze the results obtained from packed column tests, SO_2 equilibrium absorption tests at low concentrations (100 - 2000 ppm_v) were carried out in a feed-batch bubble column (see **Section III.1.**) at 1 atm and 25 °C, using the same absorbing solutions tested in the packed column tests.

Finally, the experimental data obtained in the two different experiments were compared with the modeling results retrieved from ASPEN PLUS® simulator using the Flash (see **Section III.1.3.**) and Rate-based (see **Section III.2.3.**) blocks, respectively.

IV.1.1. Operating conditions

Tables IV.1–2 report the experimental conditions adopted in the two different experiments, respectively, for the feed-batch bubble column data and packed column.

Table IV.1. *Operating conditions adopted for the experiments in the feed-batch bubble column*

Absorbing Solutions	$Q_{G,v}$ $L \cdot h^{-1}$	T_G ° C	M_S g	T_L ° C	$C^{\circ}_{SO_2}$ ppm_v
DW	60	25	17	25	67, 278, 560, 813, 1000, 1265, 1545, 1754, 2011
SW	60	25	17	25	110, 202, 425, 617, 799, 1000, 1228, 1502, 1762, 2083
SWOH	60	25	17	25	121, 205, 418, 600, 806, 1000, 1256, 1469, 1753, 2035

Table IV.2. *Operating conditions adopted for the experiments in the packed column*

Scrubbing Solutions	G $m^3 \cdot h^{-1}$	T_G °C	L $L \cdot h^{-1}$	T_L °C	L/G $L \cdot m^{-3}$	$C^{\circ}_{SO_2}$ ppm_v
DW	32	25	40, 50, 60, 70, 80, 90, 100, 110, 120, 130	25	1.25, 1.56, 1.88, 2.19, 2.50, 2.81, 3.13, 3.44, 3.75, 4.06	500, 2000

SW	32	25	40, 50, 60, 70, 80, 90, 100, 110, 120, 130	25	1.25, 1.56, 1.88, 2.19, 2.50, 2.81, 3.13, 3.44, 3.75, 4.06	500, 2000
SWOH	32	25	40, 50, 60, 70, 80, 90, 100, 110, 120, 130	25	1.25, 1.56, 1.88, 2.19, 2.50, 2.81, 3.13, 3.44, 3.75, 4.06	500, 2000

IV.1.2. Results and discussion

IV.1.2.1. SO_2 equilibrium tests

Figure IV.1 presents the experimental results of SO_2 equilibrium tests carried out at 25°C and 1 atm in distilled water, a seawater and a basic solution. The results were expressed in terms of liquid mole fraction (x_S, [µmol·mol^{-1}]) and gas concentration (C_{SO_2}, [ppm$_v$]) in equilibrium conditions (**Figure IV.1A**) and pH of the saturated solution as a function of liquid mole fraction (x_S) (**Figure IV.1B**). **Figure IV.1A** also shows the modeling results obtained with ASPEN PLUS® (Flash block).

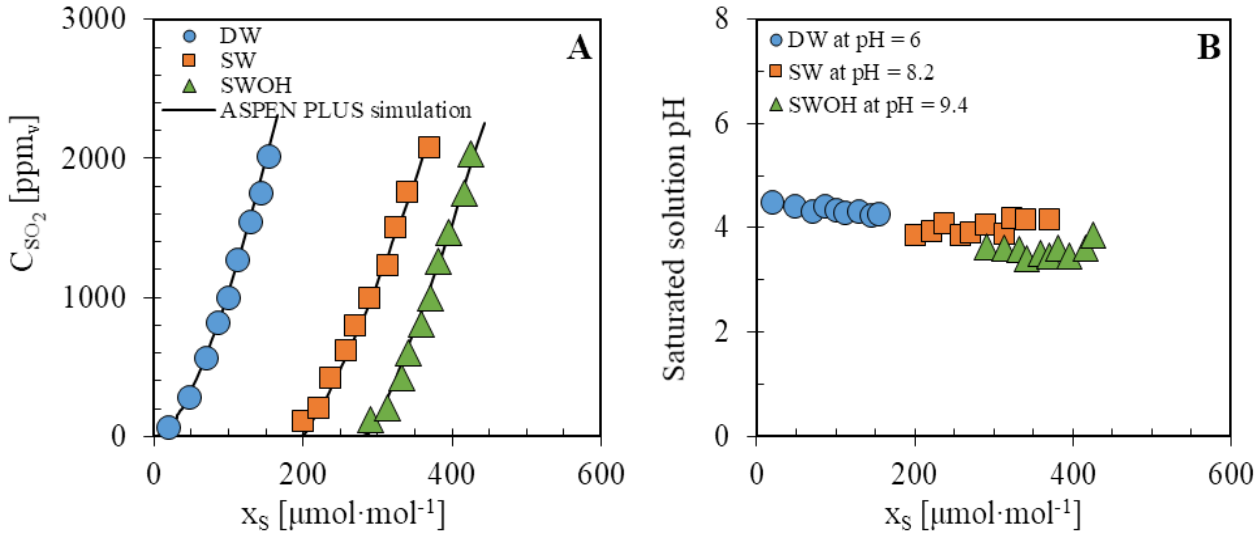

Figure IV.1. *Experimental and modelling SO_2 solubility (A) and experimental pH values of the saturated solution (B) at 25 °C and 1 atm using three different absorbing solution: distilled water at pH = 6.0 (DW); seawater at pH = 8.2 (SW); seawater with NaOH at pH = 9.4 (SWOH)*

As expected, SO_2 solubility was much greater in SW and SWOH than in distilled water, and a significant increase was observed for a slight variation in the solution pH, obtained by adding NaOH to seawater (**Figure IV.1A**). The solubility data of sulphur dioxide in distilled water are consistent with the data reported by different authors [81], [205], [206] .

For SW and SWOH solutions, the experimental data showed the typical trend of absorption phenomena in the presence of chemical interactions with the absorbing solution, and the equilibrium curve is almost a horizontal line by **Eq. (180)** ($F_{eq} \approx 0$) at low gas concentrations. The presence of alkaline species (intrinsic properties of seawater) determined an increase in solubility due to a buffer

effect (**Eqs. (17)-(19)**), which keeps solution pH around neutrality, thus promoting SO_2 absorption. The increase in the solubility with the alkaline content of the absorbing solution results in a right shift of the SO_2 solubility curve (**Figure IV.1A**). This effect was also observed by **Rodriguez-Sevilla et al.** [79] for a solution having a lower alkalinity content than the ones investigated in the present work. The experiments also indicated that for lower the saturation pH (< 4), more sulphur was captured thanks to the buffering effect of the SW and SWOH solutions which allowed a total conversion of the absorbed SO_2 into dissolved HSO_3^- and SO_3^{2-}. On the contrary, when the saturation pH was higher than 4.5, a lower sulphur content was absorbed and the solubility curve becomes the typical power law function of SO_2 absorption in distilled water (as for a pure physical absorption). Intermediate conditions occur for pH between 4.0 and 4.5. This phenomenon clearly indicates how SO_2 absorption is related to the buffering capacity of the solution (**Eqs. (17)-(19)**) and to the fundamental dissociation reactions of SO_2 in water (**Eqs. (10)-(12)**). Indeed, we also observed that chlorides and sulfates improved the equilibrium conditions, by slightly reducing the slope of the solubility curve as compared to that of distilled water. A similar observation was also reported by **Millero et al.** [207].

Figure IV.1A also showed the results of the equilibrium model implemented in ASPEN PLUS®, which provides an excellent description of the experimental data. In the simulation tool, the equations and constants related to the physical gas-liquid and the chemical reaction equilibria involved in the SO_2 absorption (see **Section II.1.**) have been added. The thermodynamic property method selected was the Elec-NRTL [93], already available in the database of the software.

IV.1.2.2. Packed column tests

The experimental results on SO_2 removal efficiency (η_{SO_2}) and wash water pH solutions in packed column tests are shown in **Figure IV.2** as a function of the liquid-gas volumetric ratio (L/G) and parametric with the scrubbing solution used.

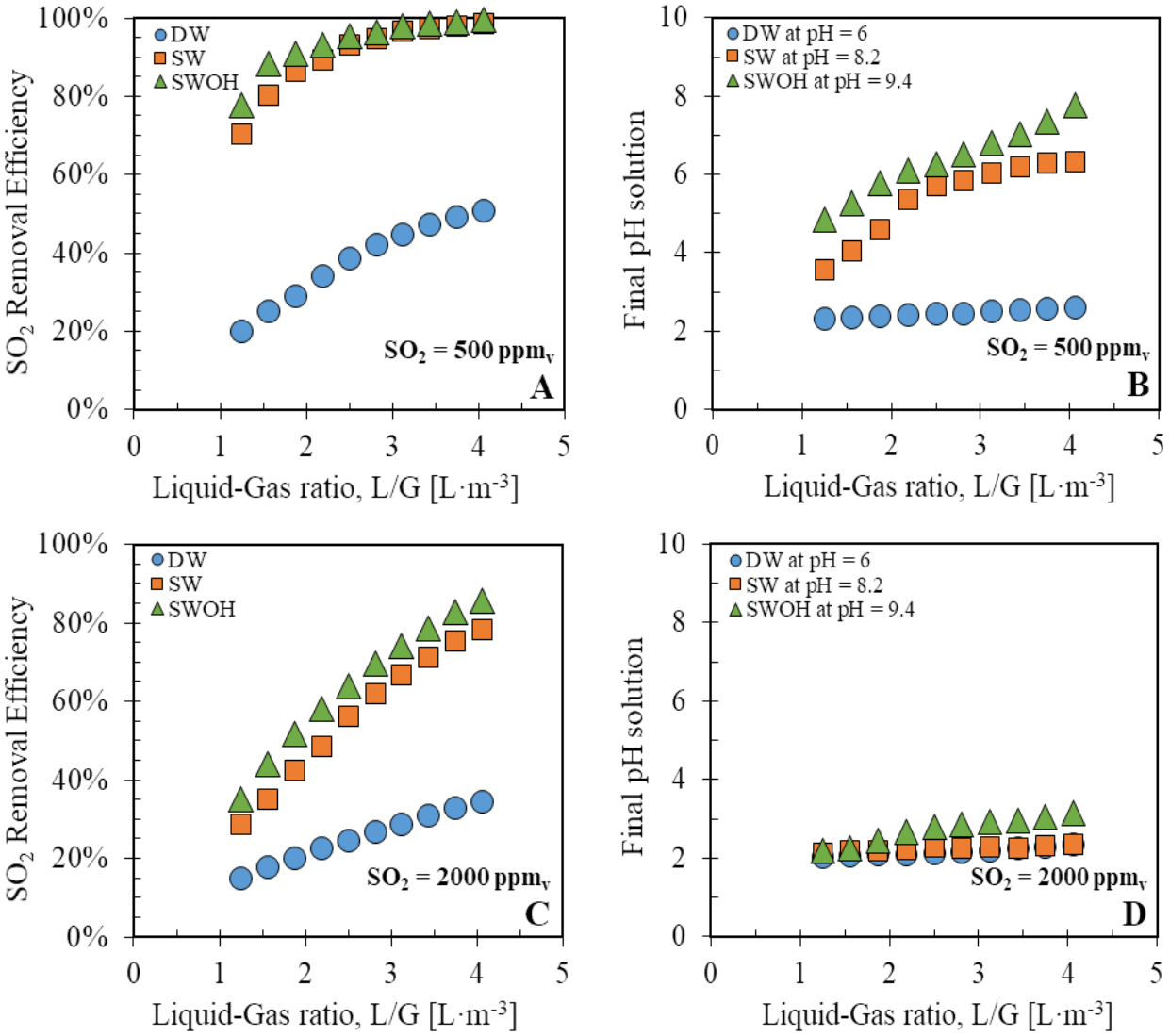

Figure IV.2. *Experimental results of SO_2 removal efficiency (A and C) and wash water pH solutions (B and D)) for a simulated flue-gas (32 $m^3 \cdot h^{-1}$) containing 500, 1000 and 2000 ppm_v of SO_2 at 1 atm and 25 °C, for different liquid-gas ratio (from 1.25 to 4.06 $L \cdot m^{-3}$) and using different scrubbing solutions: distilled water at pH = 6.0 (DW); seawater at pH = 8.2 (SW); seawater with NaOH at pH = 9.4 (SWOH). Figures A and B refer to an initial SO_2 concentration of 500 ppm_v, while Figures C and D refer to an initial SO_2 concentration of 2000 ppm_v*

As expected, the SO_2 absorption efficiency increased with the liquid flow rate, regardless the absorbing solution used, and the removal of sulphur dioxide in distilled water was significantly lower than the value retrieved in the seawater and the basic solution for a same SO_2 initial concentration (**Figure IV.2A**–**C**). The removal efficiency resulted almost similar for the seawater and the basic solution at 500 ppm_v SO_2 initial concentration (**Figure IV.2A**), in particular for high liquid-gas ratio (*L*/*G*). A 98% removal efficiency was obtained with the seawater and the basic solution as long as the liquid flow rate is greater than 110 $L \cdot h^{-1}$ (corresponding to a liquid- gas volumetric ratio about to 3.44

$L \cdot m^{-3}$), while appreciable differences were recorded only for liquid flow rates lower than 70 $L \cdot h^{-1}$ (equivalent to a *L/G* = 2.19 $L \cdot m^{-3}$). For the same SO_2 initial concentration, the final pH of the SW and SWOH solution follows a similar trend (**Figure IV.2B**). This result testifies that the natural alkalinity of seawater is sufficient to buffer the effect on pH related to SO_2 absorption, without any significant effect on the process efficiency. It can be concluded that, in these conditions, the addition of NaOH scarcely improves the scrubber efficiency. On contrary, for DW solution, a constant final pH is observed, which is slightly greater than 2. This confirmed the low alkalinity and buffering capacity of the acidity of distilled water during the SO_2 hydrolysis reaction.

The effect of absorbing liquid composition is more evident for the tests carried out at 2000 ppm_v (**Figure IV.2C**). In fact, the removal efficiency progressively increases reaching values of about 85 and 78% with a liquid feed flow rate of 130 $L \cdot h^{-1}$ (corresponding to a liquid-gas ratio of 4.06 $L \cdot m^{-3}$) for the SWOH and SW, respectively. About a 5% difference between the two solutions is kept for all the investigated liquid flow rates. Correspondingly, the final pH levels were almost 2.5 - 3 for all the investigated conditions (**Figure IV.2D**). In these cases, the final liquid reached concentration levels at the bottom of the column for which the equilibrium curve is in the region controlled by pure physical equilibrium between gaseous SO_2 and aqueous SO_2. These are the dominating phenomena also for tests performed with distilled water, which recorded a slight increase in the efficiency from 15 to 34% and a constant trend of the final pH (approximately equal to 2) for all the investigated conditions.

The experimental results were modelled by *BRF* [134] and *SRP* [144] models (see **Section II.3.1.**), implemented in the simulation tools of ASPEN PLUS®, and using the equilibrium model data provided in **Tables II.1**–**2**. (previously validated in the **Section IV.1.2.1.**).

In addition, to complete the input data required for the simulation, further models for the other operating parameters were selected from the ASPEN PLUS® database:

- Flow model: Counter-current;
- Pressure drop model: **Stichlmair et al.** [195];
- Heat transfer model: **Taylor and Krishna** [208].

The *BRF* modelling predictions of removal efficiency and wash water pH solutions are reported in **Figure IV.3** as parity plots, *i.e.* related to the corresponding experimental values.

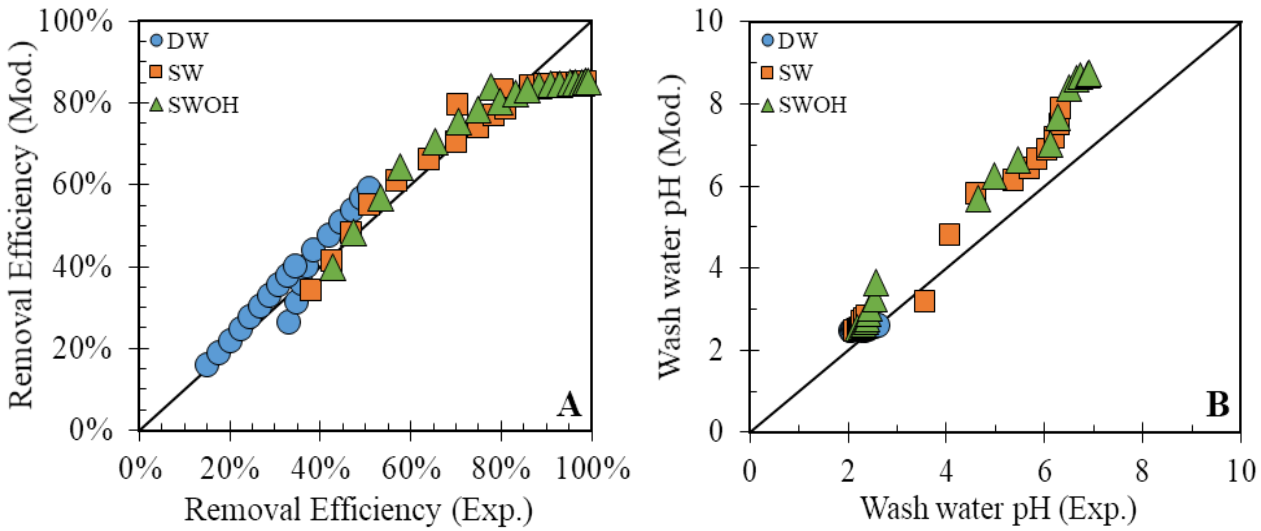

Figure IV.3. *Experimental and modelling results (using BRF model) of SO_2 removal efficiency (A) and wash water pH (B) for a simulated flue-gas (32 $m^3 \cdot h^{-1}$) containing 500 and 2000 ppm_v of SO_2 at 1 atm and 25 °C, for different liquid-gas ratio (from 1.25 to 4.06 $L \cdot m^{-3}$) and using different scrubbing solutions: distilled water at pH = 6.0 (DW); seawater at pH = 8.2 (SW); seawater with NaOH at pH = 9.4 (SWOH). Figures A and B refer to an initial SO_2 concentration in the gas of 500 and 2000 ppm_v*

The model predictions resulted accurate until the 85% of the removal efficiency for all the absorbing solutions, and they resulted slightly better for the seawater and the basic solution, while for very high removal efficiencies the model underestimated the experimental data. Moreover, better results were achieved for higher SO_2 concentration. Coherently, the *BRF* model provided a slight overestimation of the final pH, with better predictions for the tests at 2000 ppm_v.

In regard to the *SRP* model, this was firstly applied assuming C_E = 0.9 and F_{SE} = 0.35 (cf. **Eqs. (118)** and **(120)**), as suggested by the authors for Mellapak 250.Y packing [144], which quite similar to the M250.X used in the present study. The *SRP* (with F_{SE} model parameter for Mellapak 250.Y) modelling predictions of removal efficiency and wash water pH solutions are reported in **Figure IV.4** as parity plots, with the experimental data.

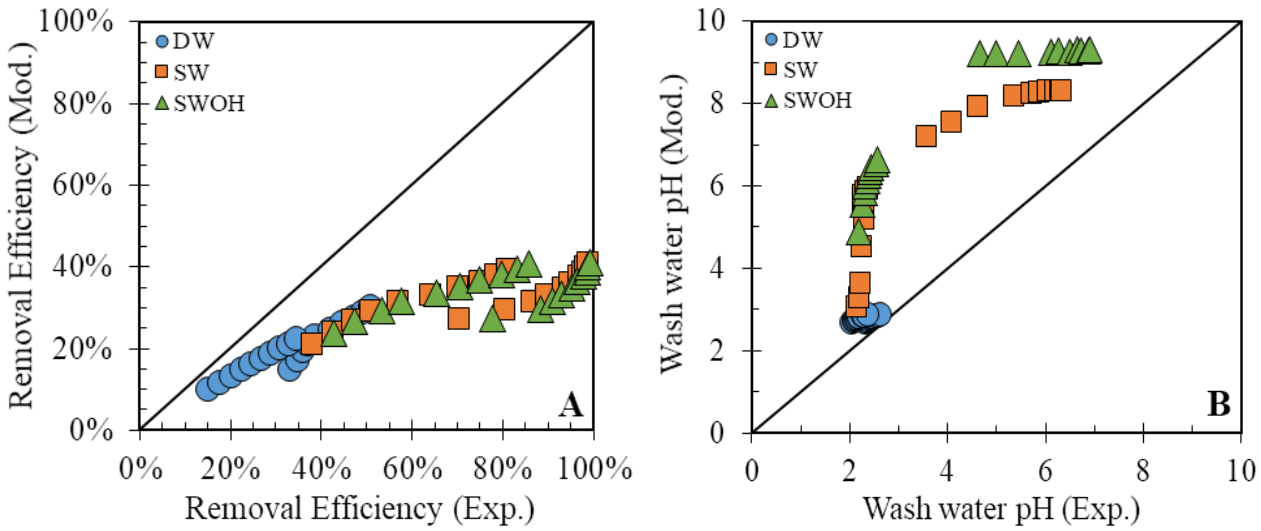

Figure IV.4. *Experimental and modelling results (using SRP model with C_E = 0.9 and F_{SE} = 0.35) of SO_2 removal efficiency (A) and wash water pH (B) for a simulated flue-gas (32 $m^3 \cdot h^{-1}$) containing 500 and 2000 ppm_v of SO_2 at 1 atm and 25 °C, for different liquid-gas ratio (from 1.25 to 4.06 $L \cdot m^{-3}$) and using different scrubbing solutions: distilled water at pH = 6.0 (DW); seawater at pH = 8.2 (SW); seawater with NaOH at pH = 9.4 (SWOH). Figures A and B refer to an initial SO_2 concentration in the gas of 500 and 2000 ppm_v*

However, with these assumptions, the model predictions resulted (**Figure IV.4**) worse than those obtained with *BRF* model, providing a severe underestimation of the experimental results. Hence, in order to improve the *SRP* modelling results also for the Mellapak 250X packing, the value of the *SRP* parameter, *i.e.* the surface enhancement factor (F_{SE}), was maximized and posed equal to 1.0, which is the highest level allowed by the *SRP* model theory [144].

The parity diagram of experimental data and modelling prediction by *SRP* model under the latter assumptions is shown in **Figure IV.5**.

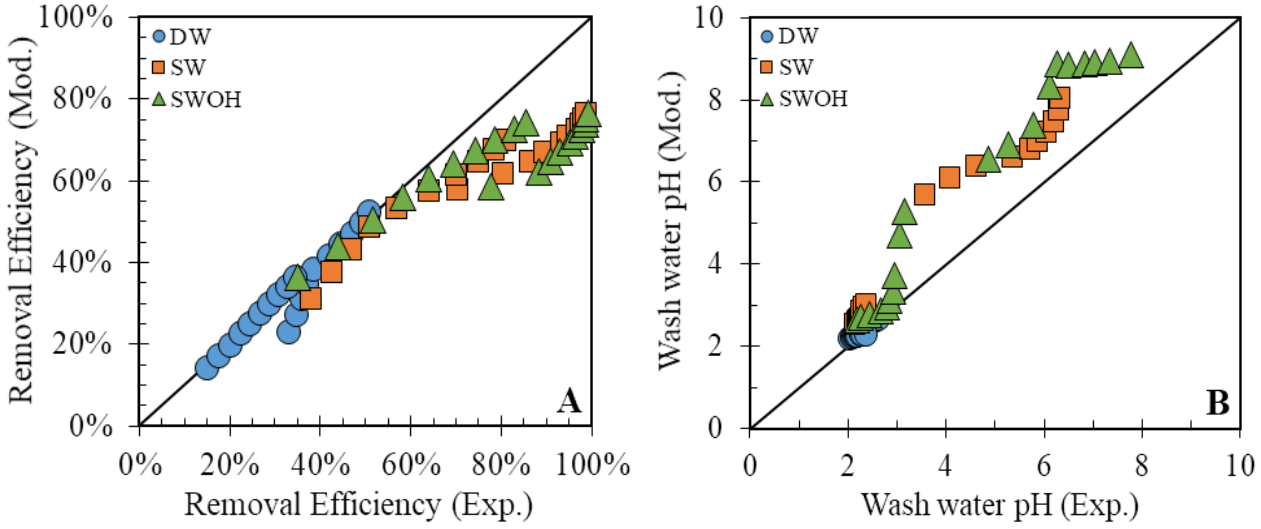

Figure IV.5. *Experimental and modelling results (using SRP model with C_E = 0.9 and F_{SE} = 1) of SO_2 removal efficiency (A) and wash water pH (B) for a simulated flue-gas (32 $m^3 \cdot h^{-1}$) containing 500 and 2000 ppm_v of SO_2 at 1 atm and 25 °C, for different liquid-gas ratio (from 1.25 to 4.06 $L \cdot m^{-3}$) and using different scrubbing solutions: distilled water at pH = 6.0 (DW); seawater at pH = 8.2 (SW); seawater with NaOH at pH = 9.4 (SWOH). Figures A and B refer to an initial SO_2 concentration in the gas of 500 and 2000 ppm_v*

Even with this correction, the model led to a systematic underestimation of the experimental data for removal efficiencies higher than 65% and a corresponding pH overestimation in all the range of the experimental values.

To better understand the results provided by *BRF* and *SRP* models, the following factors might be taken into account. SO_2 absorption kinetics is well recognized as an instantaneous reaction rate process: chemical reactions are faster than mass transfer rates, so that they can be considered in a pseudo-equilibrium condition during the entire process. In this case, the enhancement factor (E_L) that appears in **Eq. (183)** is mostly related to the diffusion of ions at the liquid interface, according to the approach followed by **Schultes** [80]. Besides, as long as there is enough alkalinity and hydroxides in the seawater to assure a complete conversion of $SO_{2(aq)}$ into HSO_3^- and SO_3^-, the mass transfer coefficient is controlled by the gas film resistance, because the equilibrium curve is $F_{eq} \approx 0$. This, together with the value of E_L, makes the contribution of mass transfer in liquid film in **Eq. (185)** as negligible. Consequently, when absorption takes place in these conditions (in our tests, this happened for the test at $C^{\circ}_{SO_2}$ = 500 ppm_v) the gas mass transfer resistance was controlling and the differences between *BRF* and *SRP* in terms of liquid mass transfer coefficient are negligible.

This condition was experimentally verified in former papers. **Darake et al.** [45] presented experiments with a packed column filled with Rashig rings (specific area 150 $m^2 \cdot m^{-3}$ and length 1.86 m) and observed that the SO_2 absorption in a seawater and a basic solution (obtained by adding sodium hydroxide) was limited only by the film gas resistance with increasing liquid-gas ratio and pH of the absorbing solution. The same conclusion was reported by **Schultes** [80] for experiments carried out on a packed column filled with Hiflow® rings (specific area 150 $m^2 \cdot m^{-3}$).

When the alkalinity and the hydroxide contents turn low, the liquid mass transfer rate becomes relevant. This happen in the lower part of the column for the tests at $C^{\circ}_{SO_2}$ = 2000 ppm and lowest *L*/*G* value, for which the pH of the wash-water turned out to be lower than 4.

Therefore, a comparison of two model results can be obtained by determining the model predictions of HTU_{OG}, related to the experimental counterparts for two reference case-studies. A first one, where

the basic reactants and the alkalinity are in excess with respect to SO_2 and a second one where the opposite condition holds true:

- $C^{\circ}_{SO_2}$ = 500 ppm with L/G = 4.06 L·m^{-3} of seawater with NaOH (SWOH);
- $C^{\circ}_{SO_2}$ = 2000 ppm with L/G = 1.25 L·m^{-3} of seawater (SW).

According to the reported theory (cf. **Eq. (183)**), the first case-study is representative of a gas-phase mass transfer resistance regime ($HTU_{OG} \approx HTU_G$) and gives an average HTU_{OG} of about 0.16 m. The HTU_{OG} values predicted by *BRF* and *SRP* (with corrected parameters) are 0.45 m and 0.60 m, respectively. In both the cases, they are far larger than the experimental values and determine a strong underestimation of data (cfr. **Figures IV.3–4)**. A deeper analysis of model equations indicated that the *BRF* model properly considers a negligible contribution of liquid mass transfer resistance (HTU_{OG} = 0.45 m and HTU_{OG} = 0.43 m) but the value of HTU_G is three times higher than the experimental value (0.16 m). On the other hand, the corrected *SRP* model awkwardly provides a very high contribution of the liquid phase mass transfer resistance (HTU_{OG} = 0.6 m, but HTU_G = 0.07 m only). It is also worth noticing that, if the *SRP* model is applied with the parameters recommended by the authors (C_E = 0.9 and F_{SE} = 0.35), the gas phase mass transfer contribution corresponds to HTU_G = 0.155 m, which is very close to the experimental data. However, in this case, the actual value of HTU_{OG} predicted by the *SRP* model is as high as 1.63 m.

These observations indicated that, for the investigated conditions, the *SRP* model with the recommended parameters provides a very good description of the gas phase mass transfer resistance. However, a massive overestimation of the liquid side mass transfer resistance was retrieved, which caused a marked underestimation of data even in those regimes in which liquid gas phase mass transfer resistance is actually negligible. On the contrary, the *BRF* model properly indicates that the gas phase resistance is controlling, but the estimation of HTU_G is far higher than the experimental data.

As regards to the second case-study, the experiments provided an HTU_{OG} of 1.98 m. In this case, in spite of the overestimation of the gas phase resistance, the *BRF* model internal parameters allowed a compensation among HTU_G and HTU_L, and the predicted value of the overall HTU_{OG} is 1.87 m. For the *SRP* model with recommended parameters, the HTU_{OG} is 3.46 m, while with the corrected parameters it is possible to achieve an HTU_{OG} of 1.95 m, very close to the experimental value.

Therefore, the optimal solution should be using the *SRP* model to estimate the gas phase mass transfer resistance, while using a new model for the liquid phase one. With the actual potentialities of the process simulation software adopted here, is not possible to perform a separate tuning of HTU_G and HTU_L. Indeed, *SRP* model can be tuned with the parameter F_{SE}, which should be minor or equal to 1, according to model assumptions [144]. As showed in **Figure IV.5**, the best model predictions can be

achieved by assuming F_{SE} = 1, which provides a good estimation of data as long as the removal efficiency is below 65%.

In conclusion, the models tested provided a poor prediction of SO_2 removal efficiency mainly due to the expressions of the mass transfer coefficients, while the equilibrium model provided an excellent prediction of the equilibrium data. Actually, *BRF* and *SRP* are closed models, which present limited adjustable parameters. In this sense, the development of specific mass transfer models for SO_2 absorption in structured packings of interest is needed for an accurate process design.

IV.1.3. Highlights

In the work published on Fuel Journal, experimental tests on SO_2 solubility in a feed-batch bubble column and SO_2 absorption efficiency in a column filled with a structured packing (M250.X) were carried out. The tested scrubbing solutions were a seawater and a seawater with NaOH addition. Besides, tests with distilled water were performed as benchmark conditions. The main results and conclusion of this work can be summarized as follows:

- The solubility of sulphur dioxide in a seawater was equal to 200 $\mu mol \cdot mol^{-1}$ as long as the partial pressure was lower than 0.01 kPa; The addition of 5000 $\mu mol \cdot L^{-1}$ of NaOH increased the solubility by about 1.5 times;
- An equilibrium model was formulated on the bases of the network of chemical reactions (**Table II.2**) and physical gas-liquid equilibria (**Table II.1**), using the Elec-NRTL model for the activity coefficients [93]. The model provided a very accurate prediction of the experimental results in all the range of the investigated SO_2 equilibrium concentrations.
- For a SO_2 initial concentration equal to 500 ppm_v, a removal efficiency of 98% can be achieved at L/G = 3.13 $L \cdot m^{-3}$ using either seawater or seawater with NaOH addition,
- For a SO_2 initial concentration equal to 2000 ppm_v, the highest removal efficiency registered for the highest value of L/G = 4.06 $L \cdot m^{-3}$, was 78% with seawater and 85% with the NaOH addition.
- A mathematical model for SO_2 absoption in the packed scrubber was developed using ASPEN PLUS® and based on the experimental data of chemical-physical equilibria and testing the predictive mass transfer models of **Bravo et al.** [134] (*BRF*) and **Bravo et al.** [144] (*SRP*). The model results indicated the need for a specific mass transfer model for SO_2 absorption in the Mellapak 250.X structured packing used for the experimental campaign. These experiments are presented in the next section.

IV.2. Mass transfer and pressure drop characterization of M250.X structured packing for absorption columns

This section is part of a paper submitted to the journal "Chemical Engineering Research & Design". The aim of this section is to propose an experimental procedure and a modelling approach to describe and predict the mass transfer coefficients and the pressure drops of a structured packing for absorption column design. The case study of a Hastelloy C-22 Mellapak 250.X (named M250.X in the following) provided by the Sulzer Chemtech is considered, also accounting for the poor prediction values in scrubber modelling adopting the models currently available in the literature, and experienced in the **Section IV.1.2.2.**.

In this section, an investigation on gas absorption using M250.X as packing and SO_2 as probe molecule to assess the mass transfer coefficients was carried out; subsequently, the retrieved results were validated with further desulphurization tests for different operating conditions (similar to the FGD units). In order to support the absorption tests modelling, dedicated experiments to assess the SO_2 equilibrium data in the different absorbing liquids used in packed column runs were made.

Accordingly, the experimental activities were divided into three different set of experiments:

1. a set of experiments (named Set 1) carried out in the feed-batch bubble column (see **Section III.1.**) to evaluate SO_2 equilibrium data at 25 °C and 1 atm, using: an acid water solution; distilled water, a tap water, a seawater; seawater with NaOH (basic solution). Further details on the physical-chemical composition of the liquids used were reported in **Section III.1.1.**. It is worth remembering that absorption tests for equilibrium data were already performed for some of the the solutions (**Section IV.1.2.1.**). These experiments were modelled with ASPEN PLUS® software (see **Section III.2.3.**) following the same approach previously used in the **Section IV.1.2.2.**;
2. a set of experiments (named Set 2) for the determination of the pressure drops in dry and wet conditions were carried out in a packed column filled with M250.X (see **Section III.2**) using an air-water system at 1 atm and 25 °C. Afterwards, experiments for a mass transfer characterization of M250.X referred to the absorption of SO_2 from simulated flue gases in basic and acid water solutions (the same of set 1), operating in the same packed column (see **Section III.2**) at controlled temperature and pressure (25°C, 1 atm) were performed at typical gas and liquid velocity conditions of FGD units.

   The experiments of the Set 2 were analyzed in light of the mass transfer and pressure drops models reported in the literature (see **Section II.3.1.** and **II.3.2.**). If needed, the assessment of a proper calibration of the model parameters for the M250.X was performed;

3. a set of experiments (named Set 3) was required to provide a set of reliable experiments to validate the correctness of the model calibration. Unfortunately, at the best of our knowledge, there are no available data on absorption or distillation processes in Mellapak 250.X column in the pertinent literature. Therefore, a final validation of the obtained modelling results required a new set of experiments. The specific goal of this new tests was to provide a number of reliable data retrieved under experimental conditions typical of FGD processes in packed towers, which were not covered by the Set 2 experiments. To this aim, the experimental campaign included 360 experimental tests, carried out with different absorbing solutions (*i.e.* a distilled water, a tap water, a seawater and a basic solution), a constant gas flow rate but at different SO_2 concentration, temperature and liquid flow rates, providing a reliable benchmark for the model predictions. The calibrated models were implemented in an ASPEN PLUS® simulation tool for SO_2 absorption in a Mellapak 250.X column and the model predictions were compared with the experimental results of the Set 3.

For the Set 2 of experiments, in particular for the determination of the mass transfer coefficients, it is also necessary to specify that the $k_x a_e$ and $k_y a_e$ can be evaluated by means of specific experimental tests for absorption of a diluted solute in which, in turn, one of the resistances is negligible and the equilibrium conditions can be considered as almost constant along the column. In these cases, the stripping factor λ is constant and also HTU_{OG} along the column. The same conditions hold for HTU_G and HTU_L.

A classic example of such methods is the use of absorption/desorption tests carried out alternatively with NH_3 gas and O_2 gas in water, as reported in **McCabe et al.** [201]. Another simple method to assess mass transfer coefficient is the use of SO_2-air (or N_2)/acid aqueous solution and SO_2-air (or N_2)/basic aqueous solution probe systems, as proposed by **Kunze et al.** [209]. In fact, sulphur dioxide is known to be very soluble in high pH aqueous solutions because it reacts very fast with the hydroxyl ions. In this case, the enhancement factor (E_L) is regulated by diffusional mechanisms (E_∞) and can be evaluated by **Eq. (106)**. In high pH solutions, the concentration of hydroxyls is far higher than that of dissolved SO_2, thus $E_L >> 1$ and the gas-side mass transfer coefficient ($k_{y,SO_2} a_e$) can be easier determined, because the liquid side resistance can be considered as negligible. In acid conditions, both mass transfer resistances are significant but E_L is equal to 1. In this case, the liquid-side mass transfer coefficient ($k_{x,SO_2} a_e$) can be determined starting from the experiments and after $k_{y,SO_2} a_e$ has been determined.

In the mass transfer characterization tests, the coefficients ($k_{y,SO_2} a_e$ and $k_{x,SO_2} a_e$) were evaluated under the following assumptions:

- Constant molar flows along the column. In the investigated conditions, the $SO_{2(g)}$ transferred from the gas phase to the liquid phase can be considered as negligible compared to the entire gas flow rate (dilute absorption case), and the amount of water transferred in the gaseous phase (due to evaporation) was very small. In fact, the tests were conducted with a relative humidity level of 10 - 60% and the gas at column outlet had a water content ranging between 40 and 83%. Moreover, the maximum recorded variations of gas and liquid molar flows accounted for approximately 2.0 and 0.7%, respectively;
- Uniform and constant gas and liquid physical properties. These tests were carried out at a constant temperature of 25 °C (for both gas and liquid) and therefore alteration of physical properties along the column can be safely neglected;
- Negligible contribution of the absorption provided by the open spray section on the top of the packing and by the liquid flowing at the bottom, below the packing. These two contributions were neglected on the basis of preliminary calculations performed by taking into account the droplets characteristics and the height of the top (35 mm) and bottom (110 mm) sections (data not shown);
- The increase in surface area for gas-liquid mass transfer due to the liquid-build up along the walls (known problem of columns with small diameter) was assessed. The column surface area available is about 40 $m^2 \cdot m^{-3}$ which corresponds to a value 6 times less than the nominal surface area available on the M250.X packing. However, considering a lower value of 5% of liquid losses along the column (evaluated with the design criteria reported in **Section III.3.3.**) and the presence of several baffles on packing, make the column surface approximately 60 times less than the nominal surface of the M250.X.

The former assumptions allowed to calculate the overall resistance to mass transfer (HTU_{OG}) as an average value along the column and therefore approximately constant. The HTU_{OG} values were obtained from **Eq. (182)** calculating the NTU_{OG} (**Eq. (187)**) and using the appropriate equilibrium and operating data, for acid and basic solutions.

The gas mass transfer coefficient ($k_{y,SO_2}a_e$) was derived from tests with strong SO_2 chemical absorption (*i.e.* using basic solution). In this case, the enhancement factor (E_L) was far larger than 1, and it can be evaluated from **Eq. (106)**, therefore the liquid-film resistance (λHTU_L) can be neglected and the gas-film resistance (HTU_G) almost coincided with the HTU_{OG} (**Eq. (183)**). Hence, $k_{y,SO_2}a_e$ can be evaluated using **Eq. (184)**.

The liquid mass transfer coefficient ($k_{x,SO_2}a_e$) can be obtained by SO_2 physical absorption tests, *i.e.* using the acid solution. In this case, the equilibrium curve can be safely approximated with a straight

line and E_L = 1. Once HTU_{OG} was derived from the experiments, using the gas-film resistance contribution (HTU_G) previously determined, the $k_{x,SO_2}a_e$ coefficient can be estimated from λHTU_L, using **Eqs. (185)** and **(186)**.

IV.2.1. Operating conditions

The operating conditions for the three different experimental sets are resumed in the **Tables IV.3–5**.

Table IV.3. *Operating conditions adopted in the Set 1 of experiments (SO_2 solubility data)*

Absorbing Solutions	$Q_{G,v}$ $L \cdot h^{-1}$	T_G °C	M_S g	T_L °C	$C^{\circ}_{SO_2}$ ppm_v
AW	60	25	17	25	88, 280,682,1000, 1253, 1568, 1734, 2036
TW	60	25	17	25	106, 193, 404, 607, 789, 1000, 1230, 1540, 1740, 2090

Set 1 was completed with experiments aimed at determining the solubility of SO_2 in distilled water, seawater and basic solution (see **Section IV.1.1.**).

Table IV.4. *Operating conditions adopted in the Set 2 of experiments (mass transfer and pressure drop data).* * *the experiments were made with an air/water system and in the absence of SO_2 in the gas*

Experiments	F_G $Pa^{0.5}$	F_L $m \cdot h^{-1}$	$C^{\circ}_{SO_2}$ ppm_v
Determination Pressure drop ($\Delta P/Z$) using a TW solution	1.03, 1.12, 1.22, 1.30, 1.38, 1.50, 1.61, 1.71, 1.80, 1.91, 2.02, 2.16, 2.36, 2.45, 2.58, 2.78, 2.80, 2.85	5.09, 8.92, 12.74, 14.65, 16.56, 19.11, 22.93	0^{*}
Determination Mass Transfer ($k_y a_e$) using SWOH solution	1.08, 1.23, 1.38, 1.54	5.09, 6.37, 7,64, 8.91, 10.20, 11.46, 12.74, 14.01, 15.28, 16.56	447, 455, 470, 493, 500, 505, 548, 555, 570, 585, 626, 650
Determination Mass Transfer ($k_x a_e$) using AW solution	1.08, 1.23, 1.38, 1.54	5.09, 6.37, 7,64, 8.91, 10.20, 11.46, 12.74, 14.01, 15.28, 16.56	513, 523, 530, 562

Table IV.5. *Operating conditions adopted in the Set 3 of experiments (validation model data)*

Scrubbing Solutions	G $m^3 \cdot h^{-1}$	T_G °C	L $L \cdot h^{-1}$	T_L °C	$C^{\circ}_{SO_2}$ ppm_v
DW, TW, SW, SWOH	32	25, 40, 60	40, 50, 60, 70, 80, 90, 100, 110, 120, 130	25	500, 1000, 2000

IV.2.2. Results and discussion

IV.2.2.1. Determination of SO_2 solubility (Set 1)

Figure IV.6 presents the experimental results of SO_2 equilibrium tests carried out at 25°C and 1 atm in an acid solution and a tap water. To complete the thermodynamic analysis proposed in this section, in addition to these results, the equilibrium data obtained in distilled water, a seawater and a basic solution, which have already been reported in **Section IV.1.2.1.** (**Figure IV.1**), must also be considered.

The results were expressed in terms of liquid mole fraction (x_S, [µmol·mol^{-1}]) and gas concentration (C_{SO_2}, [ppm$_v$]) in equilibrium conditions (**Figure IV.6A**) and pH of the saturated solution as a function of liquid mole fraction (x_S) (**Figure IV.6B**). **Figure IV.6A** also shows the modelling results obtained with ASPEN PLUS® (Flash block).

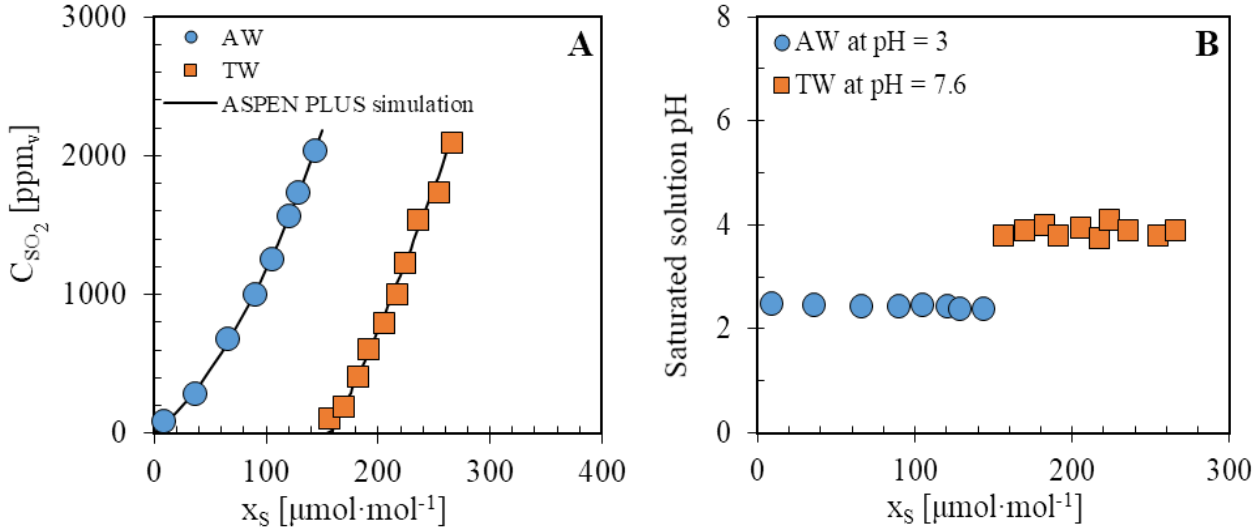

Figure IV.6. *Experimental and modelling SO_2 solubility (A) and experimental pH values of the saturated solution (B) in two different absorbing solution: acid solution at pH = 3.0 (AW); tap water at pH = 7.6 (TW)*

As known, the solubility curve for SO_2 in acidic water rapidly approaches a linear trend whose slope is represented by the Henry constant, K_H (**Figure IV.6A**). The equilibrium pH is very close to the initial one, pH = 3, for all the tests (**Figure IV.6B**). For the tap water solution (**Figure IV.6A**), the equilibrium curve is almost a horizontal line up to a value of $x_S \approx 150$ µmol·mol^{-1}, while at higher concentration, the curve approached an almost straight line very close to the Henry constant for SO_2 absorption in distilled water. This behavior is consistent with a chemical absorption of SO_2 which is completely dissolved as HSO_3^- and SO_3^{2-} ions as long as there is enough alkalinity to complete the reactions. The solution pH for the experimental points (**Figure IV.6B**) are all in the acid range, around

4. The curves in **Figure IV.6A** followed the same trend shown in **Figure IV.1A**, with the curves shifting horizontally according to their total content of OH^- and alkalinity.

The lines in **Figure IV.6A** are the model results retrieved by ASPEN PLUS® simulations adopting the same approach as in the **Section IV.1.2.1.**. Also in this case, the equilibrium model correctly described the experimental data.

IV.2.2.2. Determination of pressure drop for M250.X (Set 2)

Figure IV.7 shows the experimental pressure drops in dry (**A**) and wet (**B**) conditions for the column packed with M250.X, as a function of gas (F_G) and liquid (F_L) load factors.

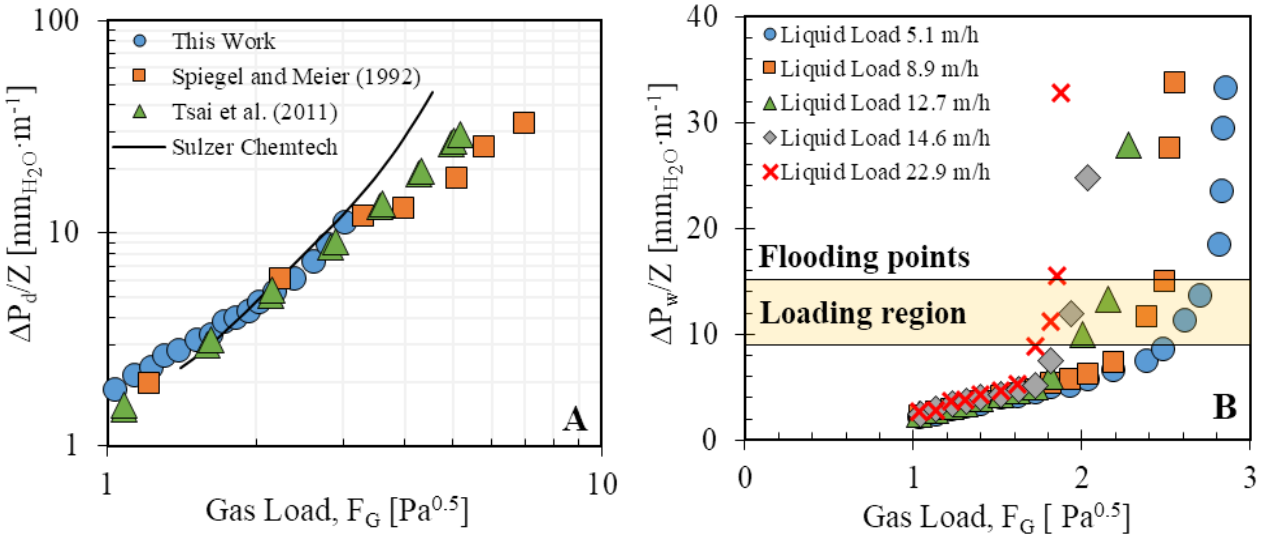

Figure IV.7. *(A) Experimental results of pressure drops in dry conditions for Mellapak 250.X (Hastelloy C-22) using different gas loads (F_G = 1.04 - 3.00 $Pa^{0.5}$ or a gas flow range equal to 27 - 78 $m^3 \cdot h^{-1}$) compared to* ***Spiegel and Meier*** [210] *and* ***Tsai et al.*** [211] *and Sulzer Chemtech data for Mellapak 250.X. (B) Experimental results of pressure drops in wet conditions for Mellapak 250.X (Hastelloy C-22) using different liquid loads (F_L = 5.10 - 22.93 $m \cdot h^{-1}$ or a liquid flow range equal to 40 - 180 $L \cdot h^{-1}$) for each gas flow rate investigated in dry conditions*

The pressure drops occurring in dry conditions (F_L = 0) showed a regular increase with the F_G according to a power-law function with an exponent of about 1.56. Moreover, the experimental data are fully consistent with the experimental data of **Spiegel and Meier** [210] and **Tsai et al.** [211] on M250.X (metal alloy) packing, while they fairly follows the indications provided in the Sulzer Chemtech technical datasheet only for F_G less than 3.0 $Pa^{0.5}$.

The experiments in wet conditions follow the typical trend of wet pressure drops for packed towers observed in **Rocha et al.** [136]; **Brunazzi and Paglianti** [196]; **Olujić et al.** [142]; **Fair et al.** [140]; **Spiegel and Meier** [210].

For a given F_L, the pressure drops were almost proportional to a power function of F_G until a value of about 1.6 $Pa^{0.5}$ was reached and the exponent of the power law curve is almost the same as recorded in dry conditions. For higher F_G, a vertical asymptote appears for a critical pressure drop, called flooding pressure, which in our experiments appeared at about 15 $mm_{H_2O} \cdot m^{-1}$. Between 9 and 15 $mm_{H_2O} \cdot m^{-1}$, the so-called loading region, the pressure drops have an intermediate behavior.

Data on pressure drops in wet conditions for Mellapak 250.X made in Hastelloy C-22 (**Figure IV.7**) have been reworked following the same approach proposed by Eckert's Generalized pressure drop correlation (GPDC), which is used by some textbooks such as **McCabe et al.** [201] and **Sinnott** [200]. **Figure IV.8** reports the gas load factor (F_G) as a function of flow parameter (F_{LG}) and parametric to pressure drop in wet conditions per meter of M250.X (Hastelloy C-22). The flow parameter (F_{LG}) depends on the gas (G_{mass}/S, [$kg \cdot m^{-2} \cdot s^{-1}$]) and liquid ($L_{mass}/S$, [$kg \cdot m^{-2} \cdot s^{-1}$]) mass flow per unit of section of the column and is defined as follows:

$$F_{LG} = \frac{L_{mass}/S}{G_{mass}/S}\sqrt{\frac{\rho_G}{\rho_L}} \tag{203}$$

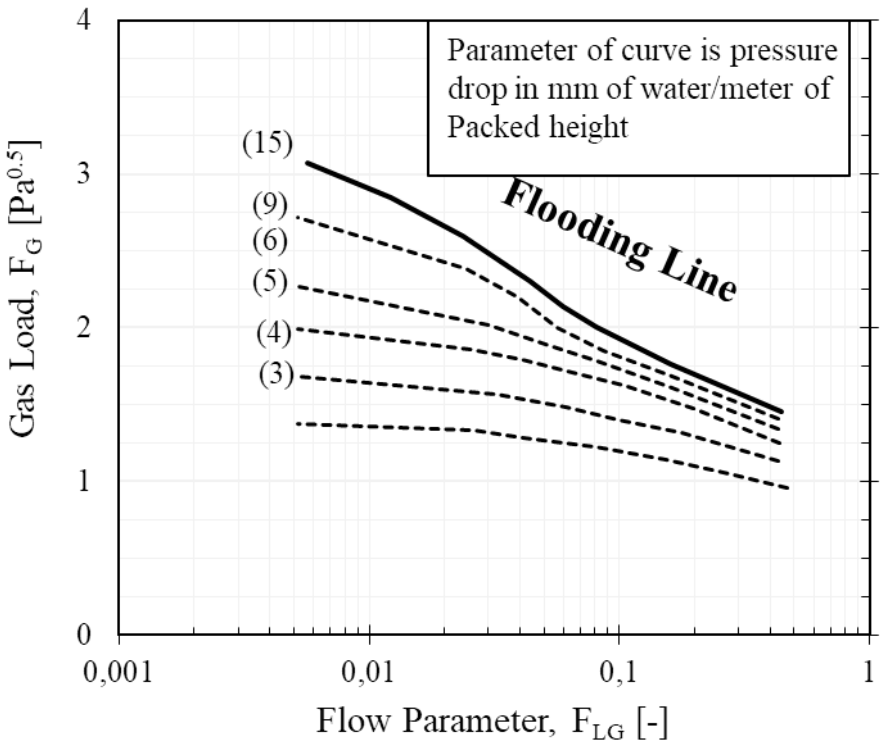

Figure IV.8. *Generalized pressure drop correlation for M250.X mad in Hastelloy C-22, rearranged following the approach proposed by Eckert's* [200]

Figure IV.8 showed that the pressure drop per meter of M250.X were limited up to 15 $mm_{H_2O} \cdot m^{-1}$ which represented the flooding value of the packing. It should be noted that, as the liquid flow rate

increases at a fixed gas load factor, the parametric curves referred to the pressure drop approached each other.

From **Figure IV.8**, a percentage value indicating the distance from the flooding point could be estimated by **Eq. (204)** once the liquid and gas flow rates were fixed, and the gas load factor values referred to the flooding ($F_{G,flood}$) and design ($F_{G,des}$) conditions were evaluated:

$$\%Flood = \sqrt{\frac{F_{G,des}}{F_{G,flood}}} \tag{204}$$

Figure IV.9 shows the comparison between experimental and modelling data in dry **(A)** and wet **(B)** conditions. Only *SBF* and *BP* model (**Section II.4.1**) were used because the authors provided the model parameters suitable for M250.X ($B_1 = 1.78 \cdot 10^{-2}$, $B_2 = 6.20$, $B_3 = 8.71 \cdot 10^{-1}$, $B_4 = 7.0 \cdot 10^{3}$ and $\alpha = 0.6$ for *BP* model, and $C_1 = 27.92$, $C_2 = -3.72$ and $C_3 = 0.39$ for *SBF* model).

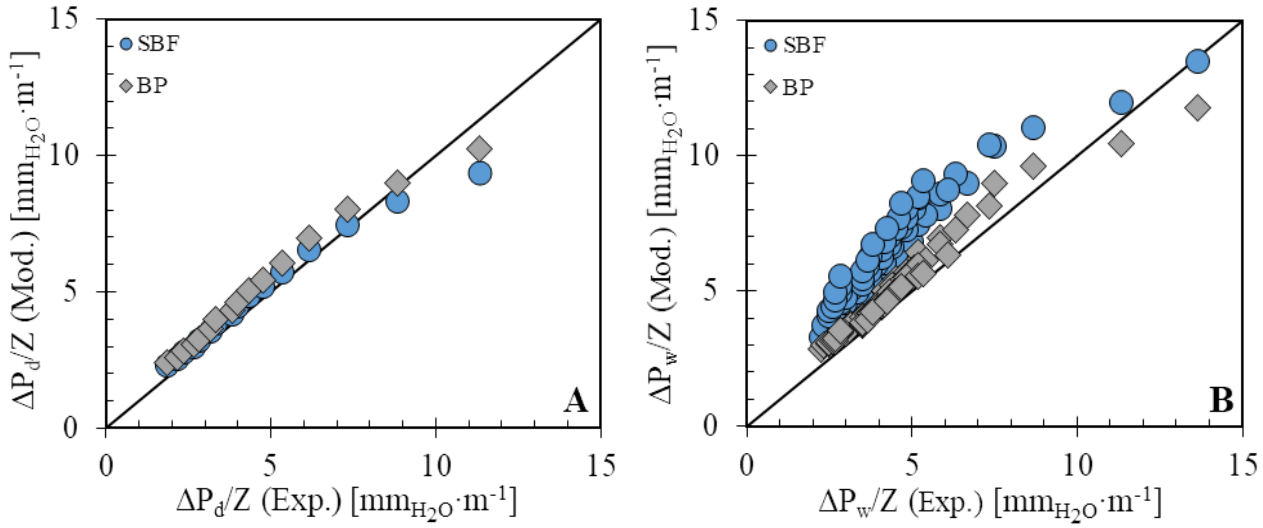

Figure IV.9. *Comparison between experimental and modelling pressure drops data in dry (A) and wet conditions (B) using the SBF and BP models with the M250.X parameters provided by the authors. Data above the flooding point were not reported*

Both the models provided a good estimation of pressure drops in dry conditions (**Figure IV.9A**) with a same R^2 equal to 0.940. In wet conditions (**Figure IV.9B**), the *BP* model showed an excellent fitting for low pressure data and a good estimation in the loading region, with a $R^2 = 0.870$. On the contrary, the *SBF* model overestimated the pressure drop data, and provided a scarce description of data ($R^2 = 0.391$). The authors envisaged that this low prediction capability could be probably attributed to the liquid hold-up assessment [195].

Figure IV.10 reports a comparison between the experimental data of dry (**A**) and wet (**B**) pressure drops and the corresponding calibrated model predictions reported in **Section II.4.1.**. It is worth

remarking that in **Figure IV.10**, the *SBF* and *BP* model in both dry and wet cases were reported in their original forms, so to compare all the models in the literature. The corresponding values of the calibration parameters, as obtained by a best-fitting analysis of the experiments and the corresponding values of the determination coefficient (R^2), are reported in **Table IV.6**.

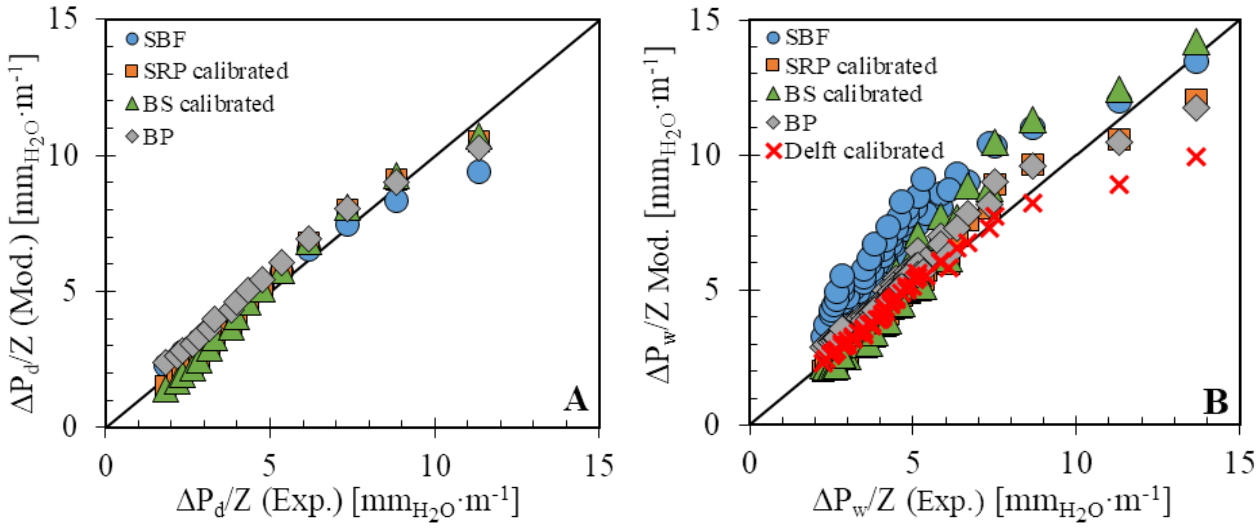

Figure IV.10. *Comparison between experimental and modelling pressure drops data in dry (A) and wet conditions (B) using the models calibrated in this work except for SBF and BP models. Data above the flooding point were not reported*

Table IV.6. *Model calibration parameters and determination coefficients (R^2) for pressure drops data in dry and wet conditions*

Pressure drops, dry equations *($\Delta P_d/Z$)*				**Pressure drops, wet equations *($\Delta P_w/Z$)***				
SBF	***SRP***	***BS***	***BP***	***SBF***	***SRP***	***BS***	***BP***	***Delft***
R^2=0.939	R^2=0.976	R^2=0.971	R^2=0.940	R^2=0.391	R^2=0.948	R^2=0.870	R^2=0.870	R^2=0.963
-	$C_{P,d}$=0.727	C_P=0.080	-	-	$C_{P,w}$=0.840	C_P=0.080	-	$C_{P,lp}$=0.608 $C_{P,l}$=5.120

The modelling results show that, in dry conditions (**Figure IV.10A**), a good estimate of the experimental data can be obtained with all the tested models. The best models were the calibrated *SRP* (R^2 = 0.976) and *BS* (R^2 = 0.971) models (**Table IV.6**) but, the original models of **Stichlmair et al.** [195] and **Brunazzi and Paglianti** [196] are characterized by very good determination coefficients (0.939 and 0.940, respectively).

In wet conditions (**Figure IV.10B**), the pressure drops models can be used only below the flooding point and a good description of the experimental data can be obtained by all the models except by *SBF* model, despite it was applied with the model parameters provided by **Stichlmair et al.** [195].

The best models (**Table IV.6**) resulted to be the calibrated versions of the *Delft* (R^2 = 0.963) and the *SRP* (R^2 = 0.948).

The *BS* calibrated model provided a good estimation of data but overestimated the pressure drops in the experimental range between 7 - 12 $mm_{H_2O} \cdot m^{-1}$ (its determination coefficient was 0.870, see **Table IV.6**). It is worth remembering (**Section II.4.1.**) that the *BS* model explicitly requires a calibration on the specific experimental data set and the parameter C_P^{BS} should be derived from experiments in both dry and wet conditions [148].

The mechanistic model of **Brunazzi and Paglianti** [196] used in its original form provided a good estimation of pressure drops in all the experimental range of pressure drops, using the model parameters retrieved by **Brunazzi and Paglianti** [196] for M250.X. On the contrary, the model of **Stichlmair et al.** [195] is not suitable in wet conditions and it needed a specific calibration for M250.X.

IV.2.2.3. Determination of the mass transfer coefficients for M250.X (Set 2)

Figure IV.11 reports the values of HTU_{OG} as a function of liquid (F_L) and gas load (F_G) factor (calculated as Z/NTU_{OG}) for the two different types of experiments: (**IV.11A**) SO_2 absorption in basic solution (SWOH) and (**IV.11B**) in acid solution (AW).

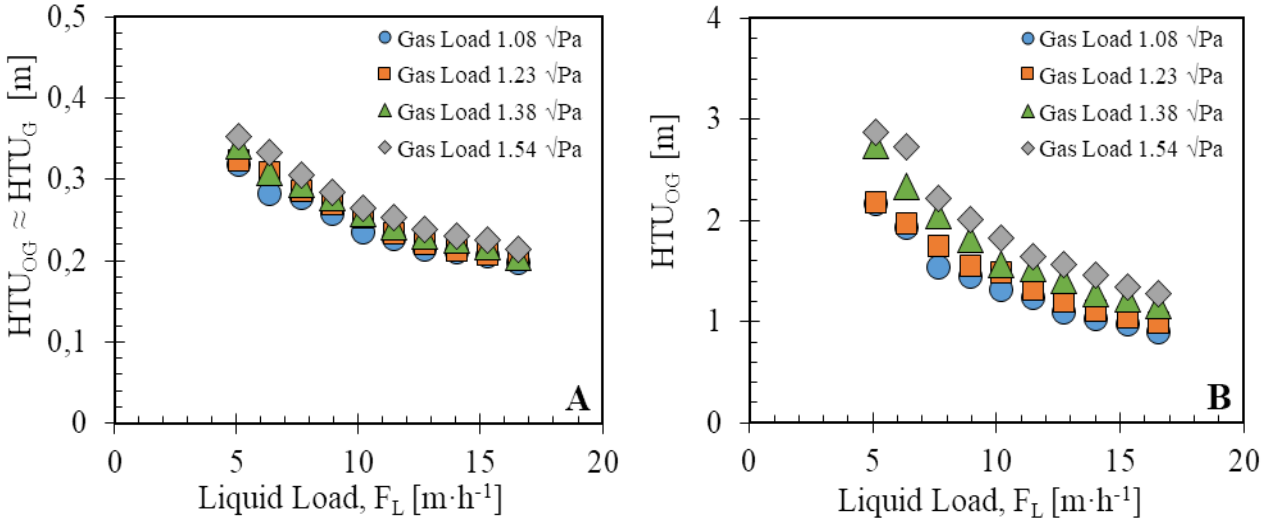

Figure IV.11. *Height of transfer unit (HTU_{OG}) for SO_2 absorption in a packed-bed column filled with Mellapak 250.X in function of liquid load factor 5.10 - 16.56 $m \cdot h^{-1}$ (corresponding to liquid flow rate from 40 to 130 $L \cdot h^{-1}$) and parametric in the gas load factor 1.08 - 1.54 $Pa^{0.5}$ (corresponding to the gas flow rates from 28 to 40 $m^3 \cdot h^{-1}$). Figure (A) refers to seawater with NaOH at pH = 9.4 (SWOH), and Figure (B) refers to distilled water with HCl solution at pH = 3 (AW)*

In the experiments reported in **Figure IV.11A,** SO_2 is mostly captured thanks to the conversion of hydrolyzed SO_2 into SO_3^{2-} and HSO_3^- ions due to the excess of OH^- in solution. In these conditions, the enhancement factor (E) is very high and the slope of the equilibrium curve is close to zero, so that $HTU_{OG} \approx HTU_G$. Therefore, the experiments showed a decrease of gas resistance (HTU_G) with F_L and a slight increase with F_G. A similar, but more pronounced dependence with F_L was shown in **Figure IV.11B** for the case of absorption in acid HCl solution.

Any increase in the liquid load (F_L) determines an increase in liquid velocity and turbulence, thus it affects directly the liquid-film resistance (λHTU_L), but also influences the gas-film resistance because of its effects on the interface velocity and shape. The increase of both the HTUs with F_G simply mirrors the lower gas residence times in the column.

The elaboration of the data reported in **Figure IV.11** using the **Eqs. (184)-(186)** provided the experimental values of $k_{y,SO_2}a_e$ and $k_{x,SO_2}a_e$, shown in **Figure IV.12** as a function of the liquid and gas loads.

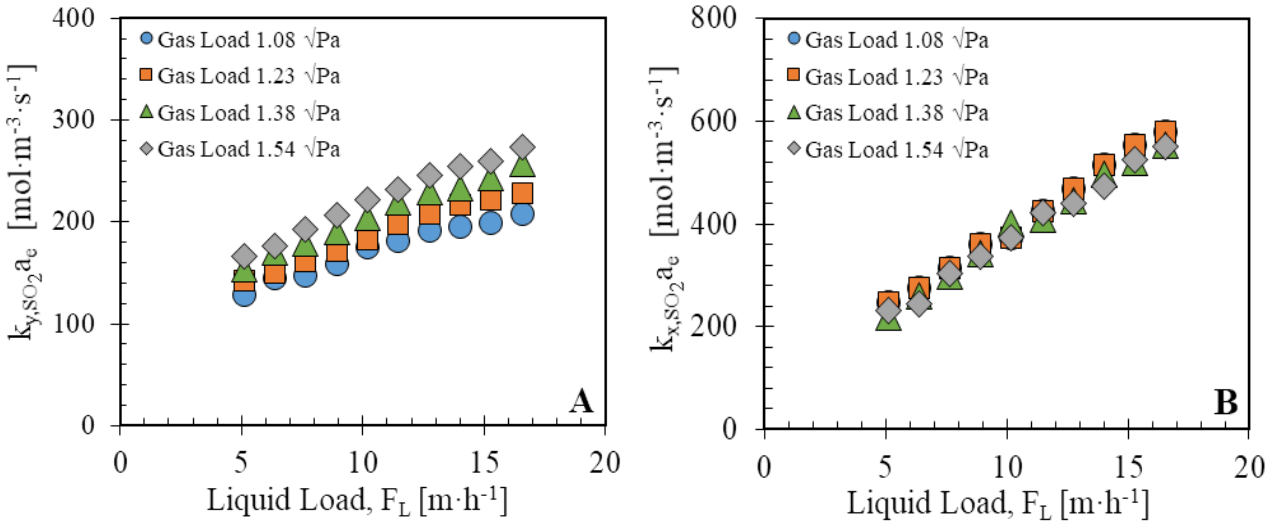

Figure IV.12. *Gas (A) and liquid (B) mass transfer coefficients for SO_2 absorption in a packed-bed column filled with Mellapak 250.X, as a function of the liquid load factor 5.10 - 16.56 m·h^{-1} (corresponding to the liquid flow rate from 40 to 130 L·h^{-1}) and parametric with gas load factor 1.08 - 1.54 Pa$^{0.5}$ (corresponding to gas flow rate from 28 to 40 m^{-3}·h^{-1})*

Figure IV.12A shows that the gas mass transfer coefficient $k_{y,SO_2}a_e$ has an noticeable dependence on both F_G and F_L. On contrary, **Figure IV.12B** shows that the liquid mass transfer coefficient $k_{x,SO_2}a_e$ depends on the liquid flow rate, while a negligible dependency on gas flow rate was observed. Indeed, while in the gas phase both the gas velocity and the interface velocity have an effect on the mass transfer rate, the mass transfer coefficient in the liquid phase is related to its internal mixing, which

is scarcely influenced by the relative gas velocity at the interface. However, both the rates depend on the interfacial area, which is a function of the liquid velocities. These findings are commonly observed in packed systems as shown by the well-known Onda equations for random packing [200].

When the experiments were compared with the results of the models reported in **Section II.3.1.** (*i.e. BRF*, *SRP*, *BS*, *BP*, *Delft*), a poor correlation among them was observed. As an example, **Figure IV.13** shows a comparison between the experimental values of the mass transfer coefficients and the pure predictive values obtained by *BRF* model, which is widely used and commonly implemented in most of the chemical process design software (including ASPEN PLUS®) because no model parameters are required.

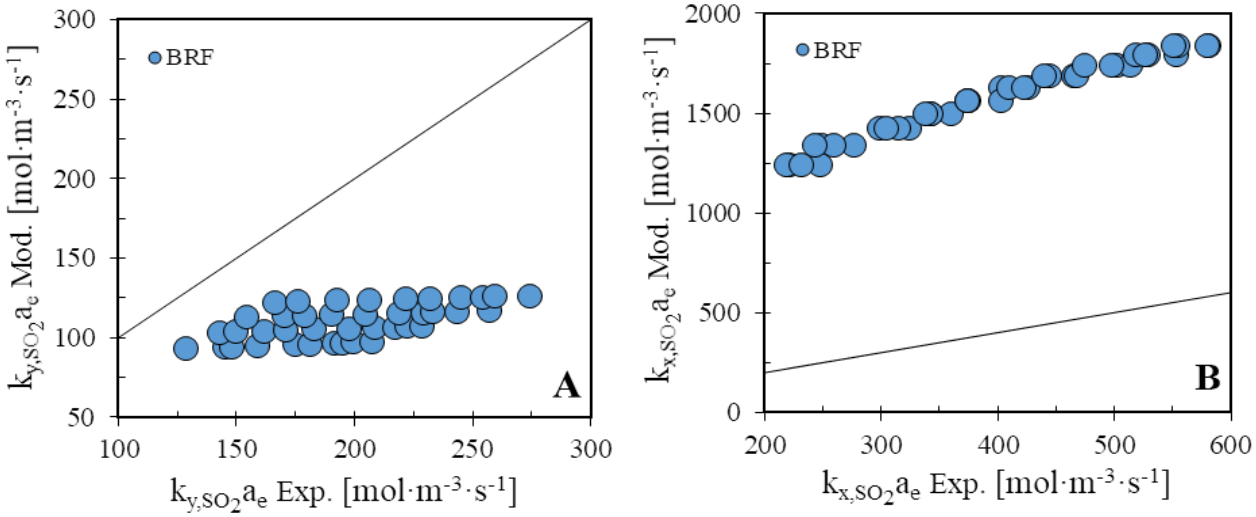

Figure IV.13. *Comparison between experimental and modelling data of mass transfer for $k_{y,SO_2}a_e$ values (A) and $k_{x,SO_2}a_e$ values (B), using the predictive model by* ***Bravo et al.*** [134]

Figure IV.13 shows that the predictive *BRF* model largely fails to predict both the mass transfer coefficients, providing an underestimation from 1.5 to 2.5 times of the gas mass transfer coefficient and an overestimation of the liquid mass transfer coefficient by a factor 5 - 6.

Figure IV.14 shows the comparison between the experimental mass transfer coefficients and all the mass transfer models available in the literature after a suitable calibration of their numerical parameters (See **Section II.3.1.**).

The corresponding values of the calibration parameters as obtained by a best-fitting analysis of the experiments and the values of the determination coefficient (R^2) are reported in **Table IV.7**.

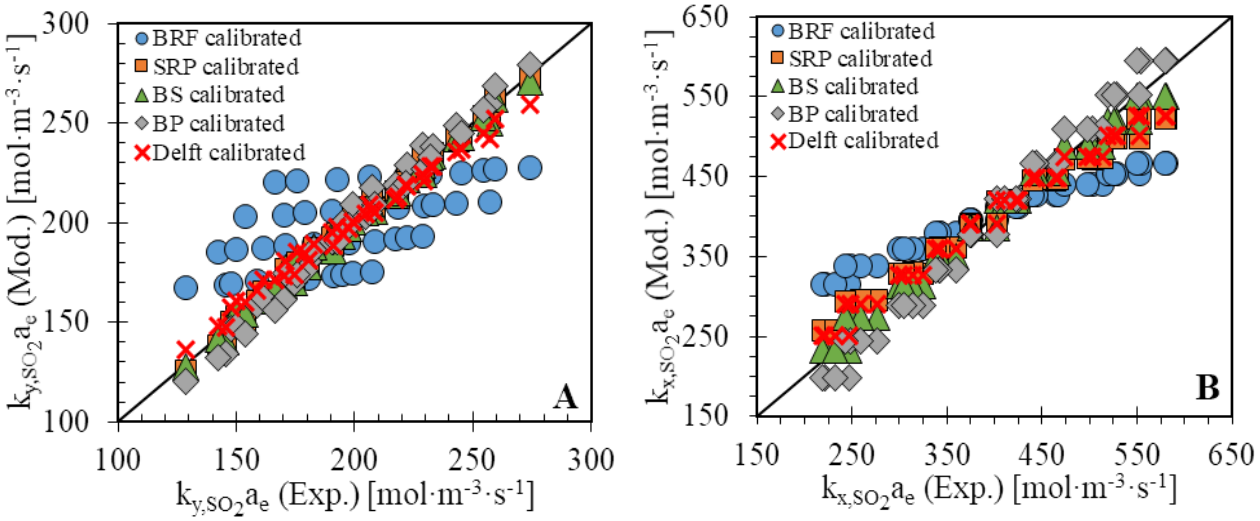

Figure IV.14. *Comparison between experimental data and calibrated model data of mass transfer: $k_{y,SO_2}a_e$ values (A) and $k_{x,SO_2}a_e$ values (B)*

Table IV.7. *Calibration parameters for each tested model and determination coefficients (R^2) of experimental data fitting*

Gas-side mass transfer equations *($k_{y,SO_2}a_e$)*					**Liquid-side mass transfer equations *($k_{x,SO_2}a_e$)***				
BRF	***SRP***	***BS***	***BP***	***Delft***	***BRF***	***SRP***	***BS***	***BP***	***Delft***
R^2=0.384	R^2=0.992	R^2=0.991	R^2=0.976	R^2=0.965	R^2=0.673	R^2=0.934	R^2=0.981	R^2=0.960	R^2=0.944
C_G=0.061	C_G=0.413	C_G=0.564	C_G=0.202	C_G=4.596	C_L=0.506	C_E=0.555	C_L=0.967	c=27.066	C_E=3.880

A comparative analysis indicated that all the calibrated models except the *BRF* provided an accurate description of the experimental data for both $k_{y,SO_2}a_e$ **(Figure IV.14A)** and $k_{x,SO_2}a_e$ **(Figure IV.14B)**. The most accurate fitting of the experimental data was achieved with the *SRP* and *BS* calibrated models (R^2 = 0.992 and 0.991, respectively) for the $k_{y,SO_2}a_e$ (**Table IV.7**) and the *BS* calibrated model (R^2 = 0.981) for the $k_{x,SO_2}a_e$ (**Table IV.7**). The descriptive capacity of the models mirrors their excellent capacities in accounting for the physics of the mass transfer coefficient, so that the calibration parameters are only needed to account for the effects of the specific packing. On the contrary, in spite of the calibration, the *BRF* calibrated model still provides an inadequate estimation of the mass transfer coefficients, with slightly better results for the liquid-film one. This is probably due to the estimation of the effective gas and liquid velocity, which did not take into account for the liquid hold-up (h_L) and the effective wet surface area (a_e). In this model, a_e is equal to a_n and no dependency with liquid flow rate was considered.

IV.2.2.4. Mass transfer model validation (Set 3)

The results of mass transfer modelling analysis were tested with 360 new experimental tests specifically performed to explore SO_2 absorption in wide ranges of experimental conditions, in terms of initial SO_2 concentration, gas inlet temperature and water flow rate, for a constant gas velocity. Further information on the experimental tests were detailed in the **Section IV.2.1.**.

The new experimental data were compared with the corresponding simulation data retrieved with ASPEN PLUS®, and obtained with the **Billet and Schultes** [143] calibrated equations for gas and liquid film mass transfer coefficient (C_L^{BS} = 0.967 and C_G^{BS} = 0.564), chosen among the models reported in **Section II.3.1.** because it allowed to reach a R^2 equal to 0.991 for $k_y a_e$ and 0.981 for $k_x a_e$ during the characterization tests (**Table IV.7**). In addition, a counter-current model flow and a heat transfer model (**Taylor and Krishna** [208]) were selected in the ASPEN PLUS® database, the SO_2 solubility model (validated in the **Section IV.1.2.1.** and **IV.2.2.1.**) was implemented, while the pressure drop data were imported (See **Figure IV.7**) in the ASPEN PLUS® simulations.

A comparison between the experimental data and the corresponding simulation results in terms of SO_2 removal efficiency and wash water pH were reported in **Figure IV.15** as parity diagrams, for different absorbing solutions, gas inlet temperatures and for all the SO_2 concentrations investigated.

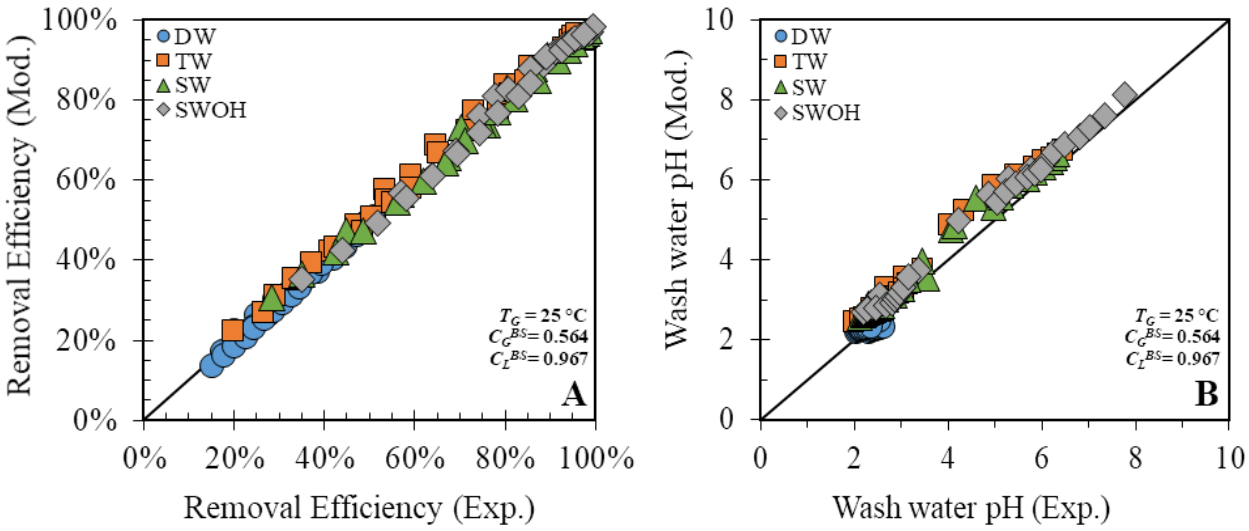

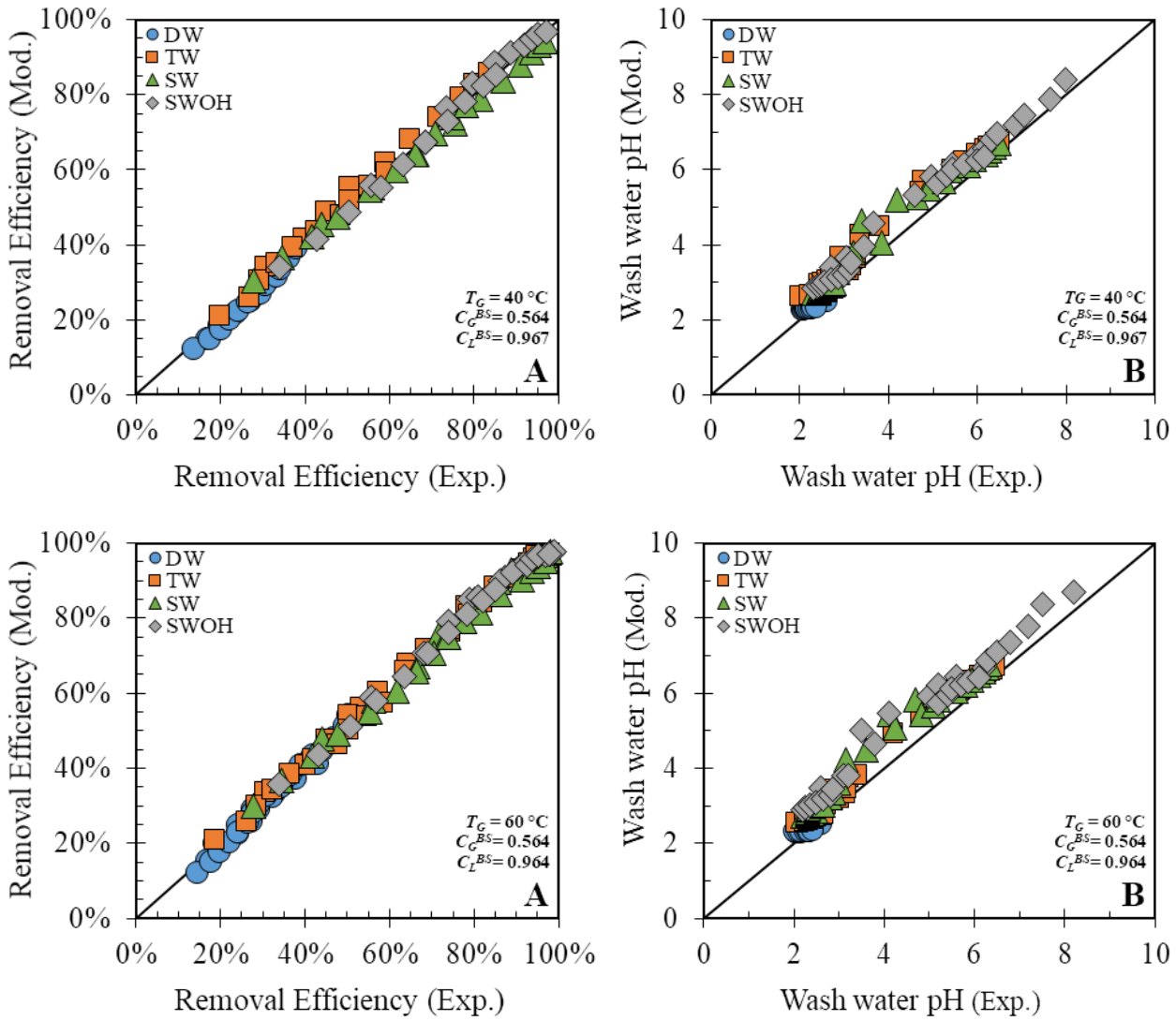

Figure IV.15. *Experimental and simulations results of SO_2 removal efficiency (A) and wash water pH (B) at different SO_2 inlet concentrations (500, 1000 and 2000 ppm_v), with a liquid load factor ranging from 5.10 to 16.56 $m \cdot h^{-1}$ at 25 °C (corresponding to liquid flow rate range 40 - 130 $L \cdot h^{-1}$) and a constant gas load factor 1.23 Pa^{-1} (gas flow rate equal to 32 $m^3 \cdot h^{-1}$) at 1 atm and different gas temperatures (25, 40 and 60 °C). The simulations were performed with* ***Billet and Schultes*** [143] *mass transfer model (the calibrated model parameters: C_L^{BS} = 0.967 and C_G^{BS} = 0.564)*

In all the experimental conditions, in spite of the different equilibrium conditions and gas temperature, the model results provided an excellent estimation of the experimental data: the determination coefficients (R^2) between the experiments and ASPEN PLUS® modelling simulations were as high as 0.998 ± 0.001 for the SO_2 removal efficiencies and 0.982 ± 0.012 for the wash water pH (although for a few conditions, errors in the orders of 20 - 30% were found).

It is observed that the SO_2 removal efficiencies obtained at different gas inlet temperatures (40 and 60 °C) were very similar to those achieved at 25 °C. This result can be ascribed to an almost constant

liquid temperature in the column, regardless the gas inlet temperature. In fact, the highest experimental liquid temperature registered at scrubber outlet resulted to be equal to 28 °C. In turn, this is the result of the low absorption heat of SO_2 and sensible heat transferred from gas to liquid, which are compensated by the small liquid evaporation amount.

IV.2.3. Highlights

The tests reported in this section dealt with an experimental and modelling study for the characterization of structured packings for absorption processes, aimed to calibrate the equations for gas and liquid-film mass transfer coefficients and pressure drops in Mellapak 250.X column. The final goal is to support the analysis of experimental data and to improve our capacity to design structured packing towers. The main findings achieved in this section were:

- The assessment of a robust experimental procedure to measure mass transfer coefficients and pressure drops in controlled hydrodynamics conditions, whose results can be proficiently extended to large-scale columns;
- An in-depth analysis of the most performing and used predictive models for mass transfer and pressure drop retrieved from the reference literature, that were tested and eventually calibrated on the experiments carried with the specific packing;
- *The Delft* and the *SRP* calibrated models for pressure drops provided a very good description of experimental data (with R^2 = 0.963 and 0.948, respectively), but also the mechanistic pressure drop model developed by **Brunazzi and Paglianti** [196] allowed to properly describe the data (R^2 = 0.870) using the model parameters provided by the authors for M250.X
- The *SRP* and *BS* calibrated models (R^2 = 0.991 and 0.992, respectively) for the $k_y a_e$ and the *BS* model (R^2 = 0.981) for the $k_x a_e$.provided an optimal fitting of the data. Also the calibrated model of **Brunazzi and Paglianti** [135] allowed a good description of both mass transfer coefficients (R^2 = 0.976 for $k_y a_e$ and R^2 = 0.960 for $k_x a_e$)
- A mathematical model of the packed scrubber was developed using ASPEN PLUS® on the bases of the experimental data on chemical-physical equilibria and using the calibrated BS model for mass transfer coefficient and the SRP model for pressure drops provide excellent predictions of the experiments (R^2 = 0.998 ± 0.001 for the SO_2 removals, R^2 = 0.982 ± 0.012 for wash water pH) in a wide number of operating conditions accounting for the effect of temperature, concentration and type of absorption liquid.

IV.3. Seawater desulphurization scrubbing in spray and packed columns for a 4.35 MW Wärtsilä marine Diesel engine

In this section, a comparison between two SW-FGD prototypes, a spray column and a packed-bed column (described in **Section III.3** and **III.2**, respectively), was carried out. The devices were tested in the same operating conditions and compared in terms of SO_2 removal efficiency and exhausted liquid (wash water) pH levels. The spray tower was a Stainless-steel column at a pilot-scale, operated in counter-current flow with a model flue-gas and a seawater solution, that was fed by hydraulic full-cone spray nozzles (PNR® BRB 2117 B1 model). The spray characterization in terms of droplet size distribution is reported in the **Section IV.3.1.1.**.

The packed column was the same lab-scale prototype described in the previous section with the same packing (Mellapak 250.X), and it was used to treat a simulated flue-gas in counter-current flow with seawater solution.

Experimental runs were performed in similar conditions in terms of liquid-gas ratio (L/G = 3.84 - 11.53 $L \cdot m^{-3}$), gas velocity (u_{Gs} = 0.29 $m \cdot s^{-1}$), temperature 25 °C and pressure 1 atm, on simulated exhaust flue-gas containing 700 ppm_v of SO_2 (corresponding to an IFO fuel containing about 3.5% w/w of sulphur in marine diesel engine exhausts [24]). The experiments include the determination of mass transfer coefficients, pressure drops of the columns, temperature and pH values of the scrubbers wash water.

The experiments were used to derive suitable models for the mass transfer coefficients in spray and packed towers, starting from a comparison with the models available in the pertinent literature (see **Section II.2.4.1.** and **II.2.3.1.**).

The mass transfer models were used to establish a comparison between packed and spray towers in a reference case-study: the design of a SW-FGD for a Wärtsilä marine diesel engine W-X35-B/(R1)/5cyl (4.35 MW) fueled with a 3% sulphur IFO fuel, which have to comply with the IMO-MARPOL, Annex VI Regulation 14 for SECAs, *i.e.* 0.1% maximum sulphur concentration. The characteristics of the flue-gas deriving from the engine were recovered from **Erto et al.** [212].

Finally, the equipment design and preliminary cost assessment for this case-study were reported and commented.

IV.3.1. Operating conditions

The operating conditions for the experiments in the spray and packed towers with seawater solution (SW) are reported in **Table IV.8**, while the operating conditions for the simulations of the case-study are listed in the **Table IV.9**.

Table IV.8. *Operating conditions adopted in the experiments performed in spray and packed towers*

Experiments	G $m^3 \cdot h^{-1}$	T_G °C	L $L \cdot h^{-1}$	T_L °C	L/G $L \cdot m^{-3}$	$C^{\circ}_{SO_2}$ ppm_v
Spray tower Pilot-scale prototype	130	25	500, 1000, 1500	25	3.84, 9.67, 11.53	700
Packed tower Lab-scale prototype	8.12	25	31.25, 62.50, 93.75	25	3.84, 9.67, 11.53	700

Table IV.9. *Main ship specifications for the seawater scrubbers design (case-study)*

Diesel Engine data		**SWS data**		**Targets**	
Main Engine	Wärtsilä W-X35-B	Flue-gas flow [$m^3 \cdot h^{-1}$]	16350	SO_2 Emission [ppm_v]	20
Power [MW]	4.35	SO_2 emission [ppm_v]	600	Pressure drop [mbar]	< 30
Engine load	70%	Seawater flow [$m^3 \cdot h^{-1}$]	62.79 up to 188.51		
Engine speed [rpm]	165	Flue-gas pressure [mbar]	1030		
Backpressure [mbar]	30	Flue-gas temperature [°C]	70		
Fuel type	IFO	Relative humidity [$w \cdot w^{-1}$]	100%		

IV.3.2. Results and discussion

IV.3.2.1. Comparison between spray and packed towers

Figure IV.16 reports the experimental results of the absorption tests performed with different seawater flow rates (*i.e.* feed liquid-gas ratio, *L/G*) in spray and packed-bed columns with a model flue-gas containing 700 ppm_v of SO_2 at 25°C and 1 atm. Experiments are presented in terms of SO_2 removal efficiency and wash water pH as function of volumetric *L/G* ratio.

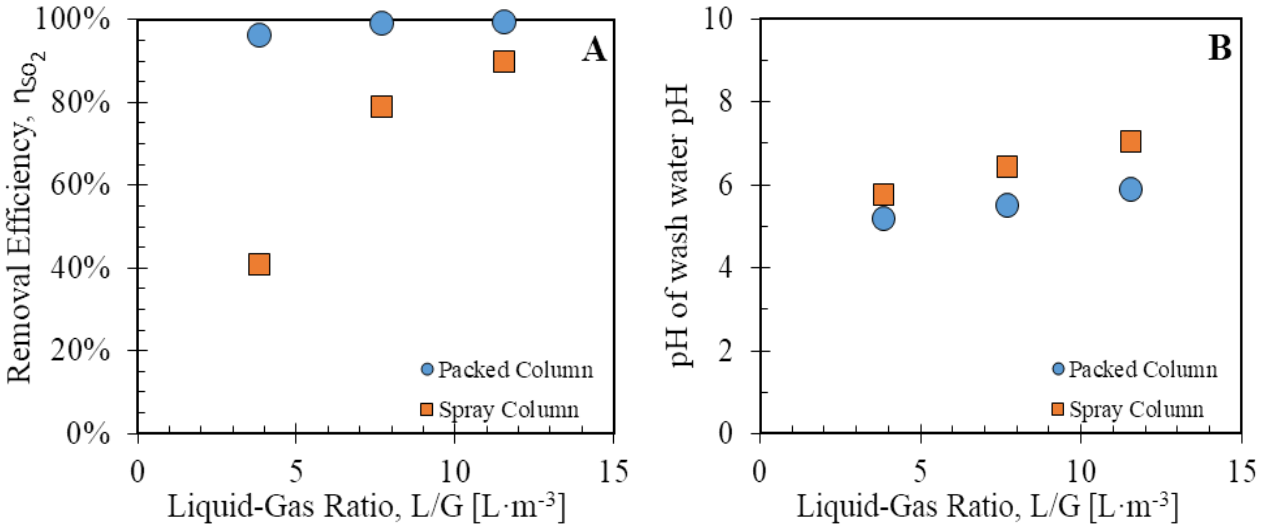

Figure IV.16. *Experimental results in spray and packed-bed (M250.X) columns in terms of SO_2 removal efficiency (A) and wash water pH (B) as a function of the liquid-gas volumetric ratio.*

The experiments in **Figure IV.16** showed that the packed-bed column (filled with M250.X) allows achieving higher SO_2 removal efficiency than the spray system in the entire investigated *L/G* range. In particular, in the packed column, the SO_2 removal efficiencies were very high and equal to 96.1 - 99.6%, hence the seawater flow rate did not exert a significant effect (except for the *L/G* range 3.34 - 7.69 $L \cdot m^{-3}$). Differently, the absorption efficiency in spray column showed a marked increase along with the increase in *L/G* values (41.8 up to 90%), confirming a high dependence on the liquid flow rate.

As a comparison, the packed column provided a 96% removal efficiency with a *L/G* equal to 3.84 $L \cdot m^{-3}$ while a similar efficiency required more than 11.53 $L \cdot m^{-3}$ in the spray tower. The comparison of the two FGD systems also showed that, for a similar efficiency, the packed system provided more than 70% water-savings compared to spray tower. This is likely to be related to a better distribution and utilization of the absorbing liquid in the packed column as well as to a higher effective wet surface of the packing. The wash water pH values reached during the SO_2 capture were slightly acidic (see **Figure IV.16B**), since SO_2 absorption reduces the alkalinity of seawater. As expected, the pH reduction was more severe for lower liquid flow rates and high removal efficiencies. However, pH levels > 5 indicated that seawater alkalinity was not completely consumed. Tests on wash water from packed column indicated that the absorbed SO_2 is almost completely hydrolyzed as SO_3^{2-} while the oxidation to SO_4^{2-} was negligible. The experiments for spray tower also showed that the sulphur capture in the water took place progressively along the column, while the solution pH reduced swiftly to about 6 in the first meter from the nozzle tip, with smaller variation along the remaining part of the column. It is worth to remark that the wash water pH and the sulphite levels indicated that the absorption process did not completely consume the seawater alkalinity. Consequently, the enhancement factor (E_L) is higher than 1 and the mass transfer resistance is concentrated in the gaseous phase ($HTU_G \approx HTU_{OG}$).

Another important result was the low pressure drop recorded in the packed-bed column thanks to the use of structured packings, which were 0.41, 0.43 and 0.45 mm_{H_2O} per meter of packing for the three *L/G* ratios adopted. These values could be compared to those that are generally obtained in spray columns (which are of the order of 1 - 3 mbar).

The modelling results for spray tower were obtained using the equation tool implemented in MATLAB ® (see **Section III.3.3.**), which takes into account both the water losses by dragging and by impact along the walls of the scrubber, and the predictive mass transfer models reported in the

Section II.3.2.. In particular, for these experiments it was observed that under the tested operating conditions, the gas-side mass transfers models that best describe the SO_2 absorption in seawater spray column are probably those based on the steady laminar flow hypothesis for spray columns (see **Section II.3.2.4.**). In general, the mass transfer contribution related to liquid loss along the scrubber walls is negligible, because the mass transfer rate is about two or three orders of magnitude smaller than the one related to droplets [171]. Also, the contribution exerted by the liquid jet formed immediately near the nozzle was negligible [158], [213].

For the packed-bed column with M250.X packing, the modelling results were obtained using the equations tool reported in the **Section III.2.3.** and already used in the previous section. The gas-side mass transfer models used are reported in the **Section II.3.1.** adopting the model parameters calibrated in the previous section (**Section IV.2.2.3.**). In this evaluation, the mass transfer contributions in the column sections above and below the M250.X packing could be neglected as well as the water losses on column walls.

The two calculations for spray and packed columns included the use of the equilibrium model for SO_2 absorption in seawater (validated in the **Section IV.1.2.1.)**.

Figure IV.17 showed the parity diagrams comparing the experimental and modelling SO_2 removal efficiency for the spray (**A**) and packed (**B**) columns.

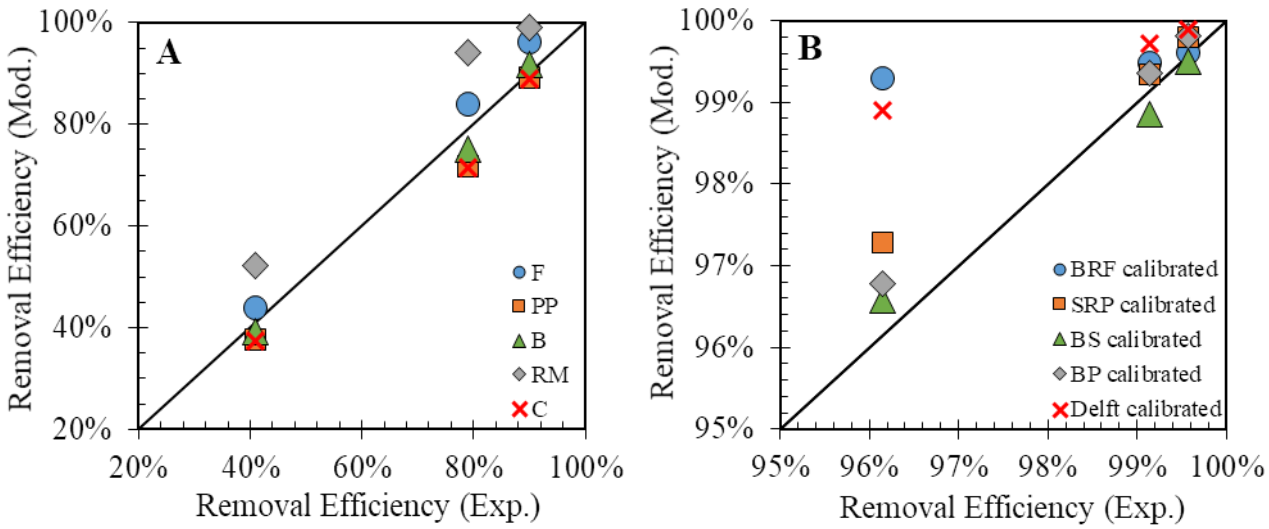

Figure IV.17. *Parity diagram of the experimental and modelling SO_2 removal efficiency for spray tower (A) and packed-bed column filled with Mellapak 250.X (B)*

The modelling results reported in **Figure IV.17** provided a consistent prediction of the removal efficiencies with all the tested models, with a total modelling deviation between 0.04 and 27.17%. In **Figure IV.17A**, the best results are obtained with the **Brauer** [167] model, which showed a deviation

between 2.22 and 4.18%. **Figure IV.17B** showed that all the calibrated models accurately described the experimental data recording a total modelling deviation between 0.04 - 3.28%, thanks to the model parameter calibration performed in the previous **Section IV.2.2.3.**. The best results were obtained with the **Billet and Schultes** [143] model with a model deviation between 0.07 and 0.44%.

IV.3.2.2. Study-case: SWS for a 4.35 MW marine diesel engine

The aim of the seawater scrubber (SWS) to be installed on board ship was to reduce the SO_2 emission until 20 ppm_v (equivalent to 0.1% of sulphur in fuel) in order to comply the emission target fixed by IMO-MARPOL Annex VI Regulation 14 in SECAs.

To define the section of spray column (*S*), the cut diameter criterion was adopted, considering a size droplet distribution as in **Figure III.5** and with a *SDM* = 342 μm, (equal to the experiments performed in **Section IV.3.2.1.**). A cut diameter (D_{dc}) for droplets size distribution was selected at 163 μm, which corresponded to a terminal velocity (*i.e.* gas velocity, u_{Gs}) of 0.64 $m \cdot s^{-1}$. The spray column diameter (*D*) calculated was 3 m and the fraction of water lost by entrainment was less than 10%. The pressure drops ($\Delta P_w/Z$) for spray tower were calculated with a numerical CFD simulator (ANSYS FLUENT®) using the same numerical approach adopted in **Esposito** [204] for the same column operated in co-current flow.

The column diameter (*D*) for packed column was fixed at 2 m using the pressure drops data for Mellapak 250.X (see **Section IV.2.2.2.**). The gas velocity value was set to obtain operating conditions far from the flooding point (15 mm_{H_2O} per meter of packing). The pressure drops ($\Delta P_w/Z$) were fixed at 4.5 - 9.0 mm_{H_2O} per meter of packing for seawater flow rates varied between 62.79 - 188.51 $m^3 \cdot h^{-1}$ and a gas velocity equal to 1.44 $m \cdot s^{-1}$.

To calculate the effective contact height of the scrubbers (*Z*), the same computational approach proposed in **Section IV.3.2.1.** was used for both spray and packed towers. In this case, only the best mass transfer models were tested (**Figure IV.17**). The **Billet and Schultes** [143] calibrated model and **Brauer** [167] model were used to estimate the mass transfer coefficients for the M250.X and spray columns, because provided the best modelling results in **Figure IV.17**.

Both spray and packed scrubbers must be equipped with liquid and gas distribution units (nozzles and gas distributor) and a demister for droplets entrainment removal at the column top. For this reason, a space of 1 m at the column top was considered for the nozzles and demister installations, for both the columns. Additional space is needed at the column bottom to install the gas distributor. For the M250.X column, a 1.5 m were taken into account in order to optimize the gas jetting below the distribution plate, while for the spray tower 0.5 m were considered sufficient. Therefore, Z_c [m] represents the total height of the column.

The same spray distribution of the experiments was adopted to size the spray column for the case-study. A BUB 3110 nozzle in Stainless-steel 316L (provided PNR® Italia Srl) was selected based on the seawater flow rate (142 $L \cdot min^{-1}$) and pressure (5 atm) used to achieve a Sauter mean diameter (*SDM*) close to the one used in the spray tower experiments (342 μm). The estimation of *SDM* was based on the **Lefebvre** [214] equation:

$$SDM = 2.25\sigma_L^{0.25}\mu_L^{0.25}M_L^{0.25}\Delta P_L^{-0.5}\rho_{air}^{-0.25} \quad (205)$$

where σ_L [$N \cdot m^{-1}$] is liquid surface tension; M_L [$kg \cdot s^{-1}$] is mass liquid flow rate; ΔP_L [Pa] is the liquid pressure for atomization; ρ_{air} [$kg \cdot m^{-3}$] is the mass air density.

A Stainless-steel 316L demister (AFP/A/113 model provided by AFP tech Srl) was selected, which is a common type of demister used in the acid gas absorption process with total height of 150 mm. Generally, the technical sheets provided by the vendors were used to estimate pressure drops for gas distributor and demister, which are about 10 - 20 mbar and 1 - 2 mbar, respectively.

Table IV.10 resumes the spray and packed column sizes (diameter *D* and height Z_c) and the pressure drops (including distributor and demister, ΔP_{tot}) derived from calculations, in order to obtain a SO_2 concentration reduction from 600 ppm_v to 20 ppm_v. The simulations were performed at a constant flue-gas flow rate (G = 16350 $m^3 \cdot h^{-1}$) at 70 °C and five different seawater flow rates (Q_L = 62.79 - 188.51 $m^3 \cdot h^{-1}$) at 25 °C.

Table IV.10. *Scrubbers design data for spray and packed (M250.X) columns as a function of seawater flow* rates *(62.79 - 188.51 $m^3 \cdot h^{-1}$) in order to obtain SO_2 concentration reduction from 600 ppm_v to 20 ppm_v*

	SWS with spray			**SWS with M250.X**		
Q_L $m^3 \cdot h^{-1}$	D m	Z_c m	ΔP_{tot} mbar	D m	Z_c m	ΔP_{tot} mbar
62.79	3.0	10.30	17.52	2.0	3.17	16.80
94.26	3.0	7.66	17.21	2.0	3.07	16.78
125.73	3.0	6.54	17.10	2.0	3.01	16.78
157.12	3.0	5.90	17.03	2.0	2.96	16.84
188.51	3.0	5.49	16.98	2.0	2.92	16.88

Table IV.10 showed that M250.X column required a lower height than spray tower. In particular, it was observed that the packing height increased only up to 8% when the seawater flow rate is decreased, mirroring the higher efficiency of mass transfer provided by structured packing.

The height of spray column was influenced by the liquid flow rate, in fact Z_c increased up to 47% by decreasing the seawater flow from 188.51 to 62.79 $m^3 \cdot h^{-1}$. However, a column spray height evaluation for different levels of water losses from 0 to 40% was performed. The results (not included) showed a relevant influence on column height only for water losses above 30%.

The pressure drops were comparable for both the systems (about 16 - 17 mbar). For these values of pressure drops, a fan may be not necessary since they are lower than the nominal allowed backpressure (about 30 mbar) of marine diesel engines [215], [216]. It was observed that, for both the units, the pressure drops are essentially related to the demister and the gas distributor, and for this reason they are almost the same.

An economic comparison of the SWS costs for both the units was performed starting from the model results reported in **Table IV.10**. The economic analysis included the investment costs for the main scrubber equipment: scrubber vessel, Mellapak 250.X packing, nozzles, gas distributor, demister and centrifugal pump. Generally, a wash water treatment unit is always coupled to the FGD plant. The water requalification also involves a flocculation tank for a chemical/physical water treatment to eliminate ash and particulate matter, when the flue-gas comes from a diesel engine or a combustion plant. Furthermore, the heavy metals, organic compounds and oil traces should also be checked prior to water discharge, in order to comply with the emission targets in the wash water. Therefore, an estimation of the wash water treatment costs is not available because the exact sizing of this unit is outside the scope of this experiments.

Table IV.11 shows the cost equations in euros [€] for the scrubber equipment. In particular, cost equations taken from **Peters et al.** [217] were updated to 2018 using the CEPCI index (584.8).

Table IV.11. *Cost equations in euros (€) for scrubber equipment: vessel, M250.X packing, nozzles, gas distribution plate, demister and centrifugal pump*

Scrubber Equipment	Costs Equations [€]		References
Scrubber vessel: D= 2 meters in Stainless-steel (316L)	$C_{€,\text{vessel}} = 37274 + 9051Z_c$	(206)	**Peters et al.** [217]
Scrubber vessel: D= 3 meters in Stainless-steel (316L)	$C_{€,\text{vessel}} = 100147 + 10147Z_c$	(207)	**Peters et al.** [217]
Sulzer Mellapak™ 250.X in Hatelloy (C-22)	$C_{€,\text{M250.X}} = 1972 + 6634V_p$	(208)	Technical sheet extrapolation
Nozzle PNR® BUB 3110 in Stainless-steel (316L)	$C_{€,\text{nozzle}} = 470N_n$	(209)	Technical sheet extrapolation
Gas distribution plate in Stainless-steel (316L)	$C_{€,\text{plate}} = 3413D^{0.95}$	(210)	**Peters et al.** [217]
AFP/A/113 Demister in Stainless-steel (316L)	$C_{€,\text{demister}} = 573e^{0.93D}$	(211)	Technical sheet extrapolation

Centrifugal pump in Stainless-steel (316L)	$C_{€,pump} = 2857 Q_L^{0.34}$	(212)	**Peters et al.** [217]

In **Table IV.11**, V_p [m^3] is the packing volume and N_n is the number of nozzles installed for the different liquid flow rates adopted.

Figure IV.18 shows the equipment costs [k€] and column volume [m^3] for the spray and packed-bed scrubbers referred to case-study (*i.e.* the Wärtsilä marine diesel engine 4.35 MW).

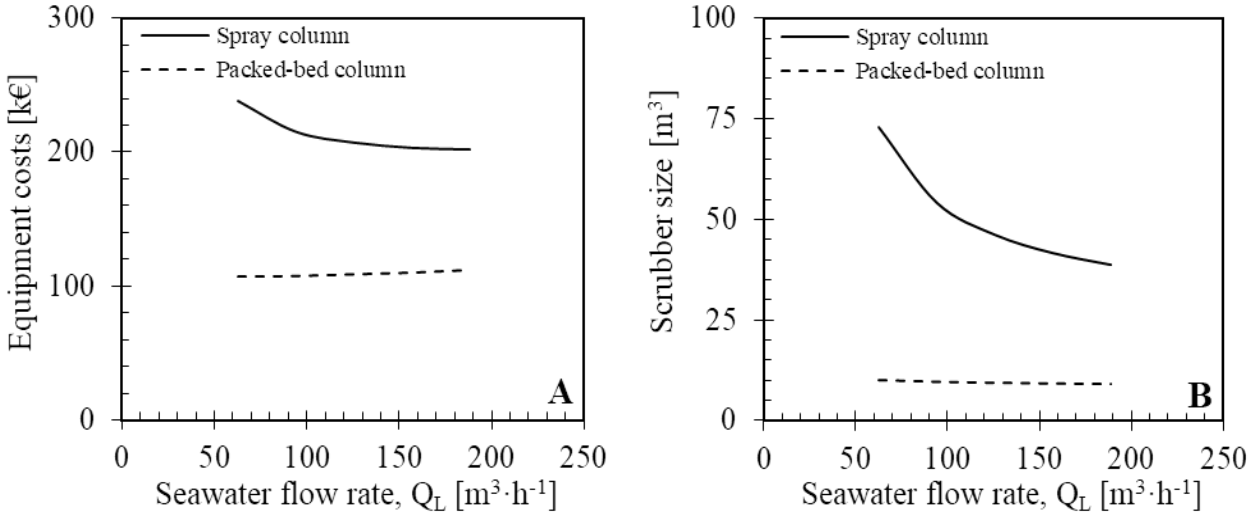

Figure IV.18. *Equipment costs (A) and scrubber size (B) at different seawater flow rates for spray and packed (M250.X) columns*

In **Figure IV.18A,** it can be observed that the packed-bed column filled with M250.X showed a lower capital cost than spray column in all the liquid flow range considered (62.79 to 188.51 $m^3 \cdot h^{-1}$). In particular, a cost-saving from 55 to 44% was obtained, when seawater flow increased, using a packed tower in place of a spray tower. Greater cost-savings were observed despite the structured packing use, which represented an additional cost item, mostly because of the costs of scrubber vessel for the spray tower that overwhelm the packing cost. Indeed, the costs of M250.X packing was 107 - 112 k€ (provided by Sulzer Chemtech) in the considered seawater flow range. It was observed that the equipment costs of M250.X scrubber (**Figure IV.18A**) were about constant. These results confirmed the higher mass transfer performances provided by structured packing with respect to spray system. On the contrary, the equipment costs for spray columns were influenced by seawater flow rates and a cost-saving of 15% was observed when the seawater flow increased from 62.79 to 188.51 $m^3 \cdot h^{-1}$.

Figure IV.18B showed that the M250.X also ensured very lower scrubber volumes compared to the spray tower, as expected. The use of scrubber with M250.X, in place of the spray tower, provided a size reduction from 86 to 76% when the seawater flow is increased from 62.79 to 188.51 $m^3 \cdot h^{-1}$.

Furthermore, it was observed that the packed column size remained almost constant (about 9 - 10 m^3) for each seawater flow used, while the volume of spray tower decreased by 46% when the seawater flow increased from 62.79 to 188.51 $m^3 \cdot h^{-1}$. This evaluation is very important because the space requirements for scrubber installation is a key parameter for naval applications since it implies a parallel loss of financial resources for ship-owners.

An estimation of scrubber total costs (CAPEX) could be achieved using the cost factors provided by **Peters et al.** [217], but since they apply for land-based system and they are estimated as a given fraction of the main equipment costs (equipment installation 47%, instrumentation and controls 37%, electrical systems 11%) we consider them as useless for the comparison. On contrary, it may be worth considering the differences of the piping costs.

The piping costs were not included in this economic assessment but usually are about 60 - 70% of the equipment costs with installation included [217]**.** The costs per meter related to the tubes in Stainless-steel 316L are shown below [217]:

$$C_{€/m,piping} = 3443D^{1.04} \tag{213}$$

The liquid piping costs are related to the seawater consumption in the FGD plant. If a water velocity equal to 2 $m \cdot s^{-1}$ is considered (as suggested by **Peters et al.** [217]**)** for the entire piping lines, a 68% of cost-saving and a 67% of size reduction were expected when the seawater flow rate was set at 62.79 $m^3 \cdot h^{-1}$ compared to the use of 188.51 $m^3 \cdot h^{-1}$.

The operating costs (OPEX) of seawater scrubbers are mostly related to liquid pumping costs. This can be evaluated starting from the energy pump consumption, which depends on liquid flow rates and pumping pressure [217].

$$Power_p = \frac{P_p Q_L F_{eff}}{1000} \tag{214}$$

where $Power_p$ [kW] is the pump power or energy consumption as $kW \cdot h^{-1}$, P_p [Pa] is the pumping pressure and F_{eff} is the efficiency pumping factor.

The energy consumption could be reduced of 67% using the lower seawater flow (62.79 $m^3 \cdot h^{-1}$) in place of 188.51 $m^3 \cdot h^{-1}$. In this case, the scrubber OPEX-saving will be proportional to the energy consumption. Moreover, a different pumping pressure may be considered for the two different scrubber units, because the spray unit requires a higher liquid pressure to assure an optimal atomization and distribution in the column. In this case, a greater OPEX-saving is expected for the M250.X scrubber.

IV.3.3. Highlights

Experimental data retrieved for both packed and spray towers were used to compare the performances of marine FGD scrubbers in order to derive mass transfer models required to design and scale-up these units. To this aim, an extensive library of predictive mass transfer models for packing and spray systems were collected and a simplified model to describe the spray hydrodynamics, also accounting the water losses along the scrubber walls, was developed.

The main findings of this work can be summarized as follows:

- The best mass transfer model to predict spray tower performances was the **Brauer** [167] model, while the **Billet and Schultes** [143] model was the best one for packed tower equipped with Mellapak 250.X.
- The models allowed to design and compare the two units for realistic case-study: the preliminary design of an FGD scrubber for a marine diesel engine (Wärtsilä W-X35-B(R1)/5cyl, having a power of 4.35 MW) fueled with a 3% Sulphur IFO to reduce the SO_2 emission from 600 to 20 ppm_v, in order to comply with the SECA emission target.
- The simulations indicated a significant size reduction for packed tower (76 - 86%) and also in terms of weight saving (27 - 48%). These results are very interesting for naval applications, where space and weight are limited. Furthermore, the packed column also provided cost-savings between 44 - 55% in spite of the use of expensive material for the packing, required to prevent corrosion with warm and acid seawater.
- A 68% cost-saving related to the piping lines was obtained as a consequence of the same reduction of tube size. Also, the pumping costs are strongly influenced by seawater consumption, and in this case, a 67% of OPEX-savings associated to energy pump consumption was achieved.
- In spite of the restriction to the scrubber design deriving from the cost model assumptions, the significant cost-savings and space requirements reduction observed for packed towers make these units as a valuable alternative to spray towers currently used in the naval applications and suggest further efforts to evaluate their realistic application in the marine field.

IV.4. FGD process by seawater scrubbing in a 80 kW pilot spray column for a Volvo Penta marine Diesel engine

This section refers to a work in progress carried out in collaboration with the Chalmers University of Technology of Göteborg (SE). The work refers to an experimental campaign made during March-July 2018 about seawater scrubbing of the flue gases produced by a marine Diesel engine (Volvo Penta, 80 kW) using the spray column prototype shown in **Section III.3.2.2.**. The prototype consists in a Stainless-steel spray column horizontally positioned, operated at 1 atm and in counter-current flow.

The experiments reported in this section were intended to study the effects of FGD on SO_2 emissions and other polluting gases in the gas stream of a marine engine operating with different loads.

The SO_2 emissions in the flue-gas after the scrubbing treatment were compared with the limits set by IMO-MARPOL (Annex VI Regulation 14) for maximum sulphur content in fuel for SECAs and open waters, *i.e.* 0.1% and 0.5%, respectively. In addition, the effect of FGD processes on wash water was evaluated by performing chemical analyses on heavy metals and organic compounds content of three samples collected during the tests at three different engine loads.

Tests were carried out using both real seawater (collected in the Kattegat area) and a basic seawater solution, obtained by adding NaOH to the same seawater. A limited number of experiments were performed using Kattegat seawater in order to exploit the removal of heavy metals and organic pollutants contained in the gas.

Further details on the Diesel engine and the fuel used were reported in **Tables III.3**–**4**, respectively, while **Figure III.5** shows the chemical composition of the Kattegat seawater in terms of the ionic and organic content. The scrubber was tested with two different flue-gas flow rates (G), six liquid flow rates (L) and three fixed engine loads: 10, 25 and 50%. Temperatures and compositions of the flue-gas varied with the engine load and were monitored online.

IV.4.1. References to the IMO Regulations/Guidelines on marine shipping: smokestack pollutants and wash water contaminants

This section contains some brief notes about the changes and improvements in regulations and the guidelines on environmental impact due to the release of pollutants into the air and marine waters.

With the stricter regulations of land-based emissions during the last decades, before the introduction of the IMO regulations [33], ships became responsible of up to 70% of the SO_2 concentration in the air in some regions in the North and Baltic Sea. For example, it was estimated that SO_2 emissions from shipping were around threefold greater than that from all road traffic and aviation combined in

the year 2000 [35]. The 1973/1978/1997 International Convention for the Prevention of Marine Pollution from Ships (MARPOL) is one of the most important sources of environmental regulation of the shipping industry [31]. The IMO's Marine Environment Protection Committee (MEPC) is the main committee for addressing environmental issues falling under the IMO's mandate including vessel source pollution, and is responsible for the adoption and ongoing actualization of the Convention's technical annexes, which address different categories of pollutants: oil and oily water (Annex I), noxious liquid substances in bulk (Annex II), harmful substances in packaged form (Annex III), sewage (Annex IV), garbage (Annex V), and air pollution (Annex VI).

Two levels of regulations apply for SO_x and NO_x emissions according to the IMO MARPOL VI guidelines: a global level valid for al maritime shipping and a stricter level applied in specific areas called "Emission Control Areas" (ECA).

The Article 14 of the MARPOL VI refers to sulphur emission and its application is expected to produce a reduction of the emissions of both SO_2 and particulate matter (PM), related only to sulphate aerosols. However, the possibility to promulgate specific regulations on particulate matter, as for all the other heavy duty engines, is under scrutiny [33]. Other smokestack emissions including organic compounds such as polycyclic aromatic hydrocarbons (PAHs) are not yet regulated by the Annex VI.

The IMO also promulgated specific guidelines on scrubber wash water quality, defining a number of parameters that are currently monitored online on-board all ships installing water based exhaust gas cleaning systems [218]. In particular, the IMO guidelines 2009 (Resolution MEPC 184(59)) specifies limits for key operating parameters in the wash water such as pH, turbidity (as a measure of PMs), nitrates and PAHs [31], which are reported in the **Table IV.12**. These guidelines eventually cope with the NO_x technical code indications included in the Resolution MEPC.177(58)

Table IV.12. *Key operating parameters in the wash water by IMO guidelines 2009 (Resolution MEPC 184(59)),* [20], [31]

Key operating parameters in the wash water by IMO guidelines 2009 (MEPC 184(59))	
Wash water pH	The pH of effluent after EGCS is very acidic (pH ~ 3) when discharged. Large effluent volume discharges could therefore affect the surrounding water pH. This could have adverse health effects on marine life but also potentially affect the ability of the ocean to absorb CO_2. Wash water pH must be sufficiently high to guarantee a pH no lower than 6.5 at 4 m from the discharge point ([20], [31], [219]). The dilution factor to restore the wash water pH to a value not less than 6.5 is generally 2 for open ocean water while it is 1.9 for seawater. Instead, the factor increases up to 7 for fresh water [32].
Particulate Matters (PMs)	Some particulate matters (PMs) present in exhaust gases ends up in scrubber wash water, and they can have adverse health effects. Particulate matters from shipping consist of a complex mixture of soot, sulphate, metals and other organic and inorganic fragments. The quantity and size of particulate matter depends mainly on the type of fuel and its sulphur content, as well as the ship's engine [33]. Turbidity increases with particle matters (PMs) deposition and acidification of the wash water, its value must not exceed 25 Formazin Nephelometric Units (FNU) or 25 Nephelometric Turbidity Units (NTU) above the inlet turbidity.

Nitrates	Nitrates in wash water come from NOx present in the exhaust gases. If nitrate concentration in the ocean water increases too much, eutrophication effects can occur. The MARPOL guidelines for the release of scrubber effluent requires that the scrubber takes up no more than 12% of the NOx in the smokestack gases, which are emitted from fuel combustion processes or beyond 60 $mg \cdot L^{-1}$ normalized for wash water discharge rate of 45 $m^3 \cdot MWh^{-1}$, whichever is greater [33]. This provision is intended to limit the discharge of excess nitrate to surface waters, a particular concern in coastal waters suffering from eutrophication.
Polyaromatic Hydrocarbons (PAHs)	Polyaromatic hydrocarbons (PAHs) are multiple aromatic rings that can have serious health effects on marine life. Both atmospheric deposition and scrubber water discharge can result in the accumulation of particle-bound PAHs in sediments [33]. Studies of PAHs composition in coastal and inland water sediments indicate potentially harmful levels at some sites, but source identification based on PAHs composition is unable to distinguish shipping from other sources using similar fuels [33]. Polycyclic aromatic hydrocarbons (PAH) are the largest known group of carcinogenic substances and include many individual chemical substances containing two or more condensed aromatic rings. A group of 16 PAHs are usually measured and analyzed, but in the IMO wash water criteria, PAH_{phe} or phenanthrene equivalence is used. Phenanthrene is a member of the PAH group and is insoluble in water [219]. In order to control the total quantity of potentially toxic and environmentally harmful PAHs related material that is discharged, a limit of 50 $\mu g \cdot L^{-1}$ as phenanthrene equivalents (PAH_{phe}) above that of wash water system inlet is fixed related to a flow rate of 45 $m^3 \cdot MWh^{-1}$, which is typical for an open seawater Exhaust Gas Cleaning System [219].
Sludge Residues	The sludge are generated from bleed-off of the washwater treatment prior to discharge, used to remove pollutants in a high efficiency treatment plant that combined coagulation and flocculation, dissolved air flotation, oil and sludge skimming, and granular activated carbon adsorption [32]. Pollutants removed from the bleed-off washwater are retained as sludge. Sludge residues generated by the EGCS should be delivered shoreside to adequate reception facilities. Such residues should not be discharged to the sea nor incinerated onboard [32]. The rate of sludge generation is approximately 0.1 to 0.4 $kg \cdot MWh^{-1}$ [32].

When compared with the discharge regulations for land-based units, it clearly appears that several potential pollutants in scrubber effluent are not included. These include: heavy metals, sulfites, ammonia, nitrites, other hydrocarbons (TOCs and PAHs), oil residues, total suspended solids (TSS), dissolved oxygen (DO), chemical oxygen demand (COD), alkalinity residual and conductivity.

The member states of the EU are responsible for assessing water quality and for taking measures to improve the water quality where necessary. In this context, it should be noted that even atmospheric emissions from shipping affect the water quality via deposition of smokestack-derived pollutants. However, such emissions are regulated by IMO and not by the EU or its member states. As discussed above, the current IMO regulations have been developed with the aim of improving air quality, and do not adequately address the question related to water quality. This issue has been brought into focus after by the decision of IMO to allow the use of scrubber technology for to comply with the MARPOL VI regulations on SO_x emissions while burning high-sulphur fuel. Through the discharge of scrubber effluents, this allowance creates the potential for a new source of water pollution that lies outside the control of the EU and its member states.

In 2008, the European Commission launched the Marine Strategy Framework Directive (MSFD), an ambitious plan for efficient protection of the marine environment [33], [34]. The ultimate goal of the MSFD is to reach Good Environmental Status of the marine environment, but this regulation did not

translate into specific limits on water discharge or quality of seawater. Later, the 2016/39/UE regulation (EU Water Framework Directive) provided some specific limits on the quality of natural waters, included coastal areas.

Turner et al. [218] have developed Basin scale modelling projections of the Baltic Sea until 2050 that indicate that shipping will become the major source of strong acid release to surface waters, most particularly if there is widespread use of wet scrubbing systems. The effects on the chemistry of the Baltic Sea are supposed to be transient with a timescale of 15 - 20 years. The authors concluded that the consequences for the alkalinity and pH of the Baltic Sea are small on a basin scale. The acid contribution of shipping was estimated to one order of magnitude less than that of land emissions. **Turner et al.** [218] reports some studies where a strong acidification in three sea areas on an annual basis were predicted, giving decreases of $56 \cdot 10^{-4}$, $1 \cdot 10^{-4}$ and $2.7 \cdot 10^{-4}$ pH units per year for the North Sea, Baltic Sea and South China Sea, respectively.

In addition to decreasing pH in the marine environment, the deposition of combustion by-product and the same scrubber residues may also lead to increase the water turbidity due to particulate matter, as well as the introduction of further pollutants, such as heavy metals, black carbon, PAHs, and other organic compounds [31]. As these compounds may have long lifetimes in atmosphere as well as in seawater, their potential long-term accumulation needs to be considered. The IMO Guidelines, 2015 (Resolution MEPC 259(68)) does not include specific limits for heavy metals in the wash water since these pollutants are mostly included in the particulate matter and thus automatically regulated by the turbidity limits [31]. European directive 2013/39/EC (which amended the 2008/105/EC) on Environmental Quality Standards (EQS) defines thresholds for heavy metals in surface waters including European coastal zones and both North and Baltic Sea ECAs outside the national territorial waters (EU, 2008). The MEPC 2015 Guidelines stated that the environmental criteria for scrubber residues need to be updated and that ship owners and scrubber manufacturers should be requested to additionally monitor pH, PAHs, oil, NO_x, and heavy metals such as cadmium, copper, nickel, lead, zinc, arsenic, chrome, and vanadium in the wash water [31]. Scrubber water contains heavy metals from the fuel and oil as well as other particles from the corrosion of pipes and scrubber vessel.

In this work, we performed measures on the scrubber wash water including pH, heavy metals, organics and PAHs, while the values of total sulphur and nitrogen dissolved could be calculated from mass balance equations. Heavy metals and organics measures were compared with the following regulations:

- (EU-EQS): Europe Environmental Quality Standards, Directive 2013/39/EC, relating to water quality standards in the European Union [2];

- (DE-EQS): Danish Environmental Quality Standards, relating to water quality standards in the Denmark [2];
- (STR-EQS): Stringent Environmental Quality Standards, relating to more stringent criteria for the inland waters and national territorial waters, established by Danish Ministry of Environment [2];
- (EPA-NRWQC): EPA's National Recommended Water Quality Criteria for saltwater organisms [32];
- (IT-DL): Italian Directive for industrial waste water discharge in natural water bodies limits, (D. Lgs 152/06);
- (GE-DL): German Directive for industrial waste water discharge in natural water bodies limits, (Article 2 of 6th Ordinance for Amendment of Waste Water Ordinance Appendix 33 and 37 - industrial scrubber wash water).

IV.4.2. Operating conditions

The operating conditions for the experiments on the Chalmers spray column are reported in **Table IV.13**, while the temperature of the flue-gas and its composition related to three different engine load values were showed in **Table IV.14**.

Table IV.13. *Operating conditions adopted for the experiments in the Chalmers spray column*

Scrubbing Solutions	***Engine Load***	***G*** $m^3 \cdot h^{-1}$	***L*** $L \cdot h^{-1}$
KSW	10, 25, 50%	70, 140	30, 60, 90, 120, 150, 180
KSWOH	10, 25, 50%	70, 140	30, 60, 90, 120, 150, 180

Table IV.14. *Flue-gas composition for different engine loads (10, 25 and 50%)*

Engine Load	**SO_2** *ppm_v*	**NO** *ppm_v*	**NO_x** *ppm_v*	**CO** *ppm_v*	**CO_2** *% vol.*
10%	63±1	160±5	183±6	491±5	3.76±0.04
25%	131±2	318±2	352±2	187±1	5.89±0.01
50%	206±3	673±3	690±5	197±7	8.33±0.04

IV.4.3. Results and discussion

IV.4.3.1. FGD action on gas pollutant emissions

Figure IV.19 shows the SO_2 emissions at the scrubber exit as a function of the liquid-gas mass ratio (*L*/*G*) for Kattegat seawater (KSW) and Kattegat seawater with NaOH addition (KSWOH). The

results are referred to two different flue-gas flow rates, equal to 70 and 140 $m^3 \cdot h^{-1}$ and for three different engine loads: 10, 25 and 50%. The lines denote the maximum allowed SO_2 emissions in SECAs and open sea (GLOBAL). The SECA and GLOBAL targets were assessed starting from the sulphur content in the fuel (0.92% w/w, see **Table III.4**) and the relative SO_2 emissions in the exhaust gas were estimated with the scrubber turned off at different engine loads (10, 25 and 50%).

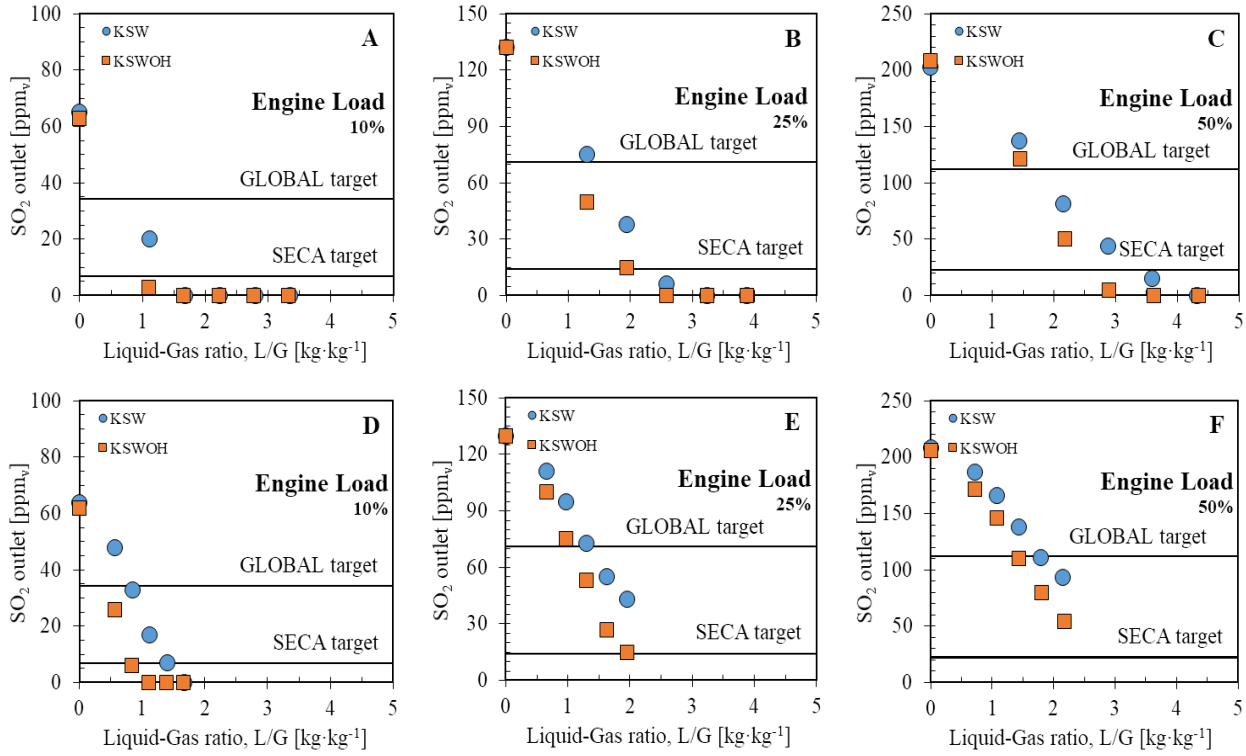

Figure IV.19. *Experimental SO_2 outlet concentrations in FGD pilot unit tests. Outlet concentrations are expressed as a function of the liquid-gas mass ratio and parametric with scrubbing liquid used: Kattegat seawater (KSW) and Kattegat seawater with NaOH addition (KSWOH). The results are referred to different flue-gas flow rate equal to 70 (Figures A, B and C) and 140 $m^3 \cdot h^{-1}$ (Figures D, E and F) and three different engine loads: 10, 25 and 50%*

The results in **Figure IV.19A–C** showed that SO_2 emissions were reduced by an increase in the *L/G* ratio and complied with the SECA and GLOBAL emission target by increasing the liquid flow rate. When the engine load increased, the desulphurization process required a greater increase in the liquid flow rate to meet the emission targets because both the SO_2 level and the gas temperature increased. The KSWOH allowed to reach the targets with lower water flow rates compared with the KSW. In particular, the GLOBAL emissions target was achieved with a water-saving of approximately 50, 33 and 16% for engine loads of 10, 25 and 50%, respectively. The corresponding improvements for SECA emissions target were 33, 30 and 28%.

When the gas flow rate doubles, the desulphurization efficiency lowered due to a reduction in the gas residence time in the scrubber. Besides, the driving force of the process was also reduced due to lower *L/G* ratios and, therefore, a lower amount of SO_2 could be captured. These experimental results are illustrated in **Figure IV.19D**–**F**, which showed that with the KSW the SECA target can be reached only at 10% of the engine load. For KSWOH, at 10% engine load the SECA limit can be achieved with 45% less water and the limit can be complied also at 25% of the engine load. With reference to the GLOBAL emissions target, the use of NaOH allowed savings of 50, 28 and 7% of the fed water for engine loads of 10, 25 and 50% respectively. For the SECA emissions target, only for 10% of load, a water-saving of 45% was observed.

Table IV.15 shows the emissions of other gas pollutants (NO_x, CO and CO_2) at the scrubber outlet as a function of the liquid-gas mass ratio (*L*/*G*) for KSW and KSWOH. The results are referred to the gas flow rates of 70 and 140 $m^3 \cdot h^{-1}$ and for each different engine load: 10, 25 and 50%.

Table IV.15. *Experimental results of NO_x, CO and CO_2 outlet concentrations in FGD pilot unit tests. The outlet concentrations are expressed as a function of the liquid-gas mass ratio and parametric with scrubbing liquid used: Kattegat seawater (KSW) and Kattegat seawater with NaOH addition (KSWOH). The results are referred to different flue-gas flow rate equal to 70 and 140 m3·h-1 and for each different engine load: 10, 25 and 50%*

Scrubbing Solution	Engine Load	G fed	L/G fed	NO_x fed	NO_x out	CO fed	CO out	CO_2 fed	CO_2 out
	-	m^3/h	kg/kg	ppm_v	ppm_v	ppm_v	ppm_v	% vol.	% vol.
KSW	10%	70	1.11	176	176	490	490	3.80	3.80
			1.67	176	178	490	488	3.80	3.80
			2.23	176	175	490	490	3.80	3.81
			2.79	176	176	490	491	3.80	3.80
			3.35	176	175	490	492	3.80	3.80
		140	0.56	177	175	496	494	3.80	3.80
			0.84	177	173	496	493	3.80	3.81
			1.12	177	174	496	495	3.80	3.81
			1.40	177	173	496	493	3.80	3.81
			1.69	177	175	496	493	3.80	3.80
	25%	70	1.30	352	348	188	184	5.90	5.91
			1.94	352	347	188	185	5.90	5.91
			2.59	352	346	188	182	5.90	5.90
			3.23	352	344	188	183	5.90	5.90
			3.88	352	345	188	183	5.90	5.90
		140	0.65	352	347	186	188	5.89	5.90
			0.97	352	347	186	188	5.89	5.91
			1.30	352	346	186	187	5.89	5.91
			1.63	352	351	186	184	5.89	5.90
			1.96	352	347	186	186	5.89	5.90
	50%	70	1.44	686	688	205	205	8.30	8.33
			2.15	686	689	205	204	8.30	8.32
			2.87	686	690	205	201	8.30	8.30
			3.60	686	687	205	201	8.30	8.30
			4.31	686	687	205	201	8.30	8.30
		140	0,72	690	692	202	201	8.32	8.35
			1,07	690	694	202	203	8.32	8.36
			1,43	690	689	202	202	8.32	8.34
			1,80	690	689	202	202	8.32	8.34
			2,15	690	689	202	202	8.32	8.34

KSWOH	10%	70	1.10	176	176	486	487	3.71	3.80
			1.66	176	178	486	488	3.71	3.80
			2.21	176	175	486	488	3.71	3.81
			2.76	176	176	486	486	3.71	3.80
			3.32	176	175	486	487	3.71	3.80
		140	0,56	175	175	492	494	3.74	3.80
			0,84	175	173	492	493	3.74	3.81
			1,11	175	174	492	495	3.74	3.81
			1,39	175	173	492	493	3.74	3.81
			1,66	175	175	492	493	3.74	3.80
	25%	70	1.30	352	348	188	184	5.90	5.91
			1.94	352	347	188	185	5.90	5.91
			2.59	352	346	188	182	5.90	5.90
			3.23	352	344	188	183	5.90	5.90
			3.88	352	345	188	183	5.90	5.90
		140	0.65	352	347	186	188	5.89	5.90
			0.97	352	347	186	188	5.89	5.91
			1.30	352	346	186	187	5.89	5.91
			1.63	352	351	186	184	5.89	5.90
			1.95	352	347	186	186	5.89	5.90
	50%	70	1.44	692	690	204	205	8.35	8.33
			2.17	692	689	204	204	8.35	8.32
			2.90	692	690	204	201	8.35	8.30
			3.61	692	690	204	201	8.35	8.30
			4.34	692	691	204	201	8.35	8.30
		140	0.72	695	692	202	201	8.37	8.35
			1.08	695	694	202	203	8.37	8.36
			1.44	695	689	202	202	8.37	8.34
			1.80	695	689	202	202	8.37	8.34
			2.17	695	692	202	202	8.37	8.34

The results showed that there was no effect of the FGD process on other polluting gases such as NO_x, CO and CO_2 that were practically insoluble in both seawater and seawater with the addition of NaOH, as expected.

Figure IV.20 reported the trends related to the gas temperatures at the scrubber outlet, referred to the tests illustrated in **Figure IV.19**.

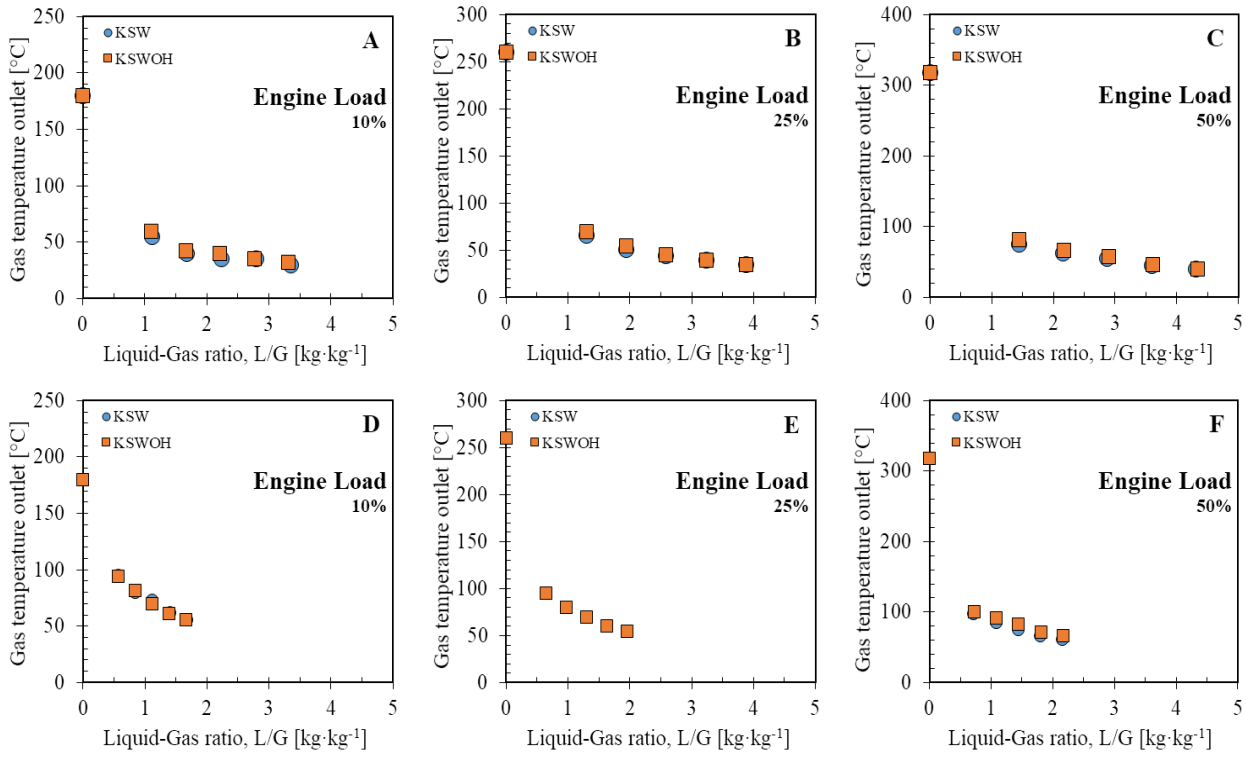

Figure IV.20. *Experimental results of gas temperature outlet from FGD pilot unit tests. Outlet gas temperatures are expressed as a function of the liquid-gas mass ratio and parametric with scrubbing liquid used: Kattegat seawater (KSW) and Kattegat seawater with NaOH addition (KSWOH). The results are referred to different flue-gas flow rate equal to 70 (Figures A, B and C) and 140* $m^3 \cdot h^{-1}$ *(Figures D, E and F) and for each different engine load: 10, 25 and 50%*

The gas temperatures decreased due to the contact with the cold scrubbing liquid, fed at 20 °C and the limited heat of absorption associated with SO_2 solubilization, which was the only gas pollutant absorbed. Despite the initial temperatures were always higher when the load increased, the outlet temperatures were very similar, with a maximum deviation of 10 °C between 10 and 50% loads. In particular, the temperature trends were qualitatively very similar to the results shown for lower gas flow rates (**Figure IV.19**), but with an increase in the gas temperature range of about 20 °C.

IV.4.3.2. FGD effect on wash waters properties

An analysis of the pH and temperatures of the wash water was performed for each FGD test described in the previous section. Further information about other wash water properties such as turbidity and total suspended solids (TSS) were not available. However, experimental observations confirmed that the turbidity of the samples increased with the capture of SO_2 as well as the sulphur smell that was emitted by the liquid. Furthermore, the samples did not appear clear but with the presence of fine suspended black particles, which increased as the engine load increased.

Figures IV.21–**22** show the pH values of the wash water and the temperatures at the scrubber outlet as a function of the liquid-gas mass ratio for KSW and KSWOH. The results are referred to flue-gas flow rates equal to 70 and 140 $m^3 \cdot h^{-1}$ and for three different engine loads: 10, 25 and 50%.

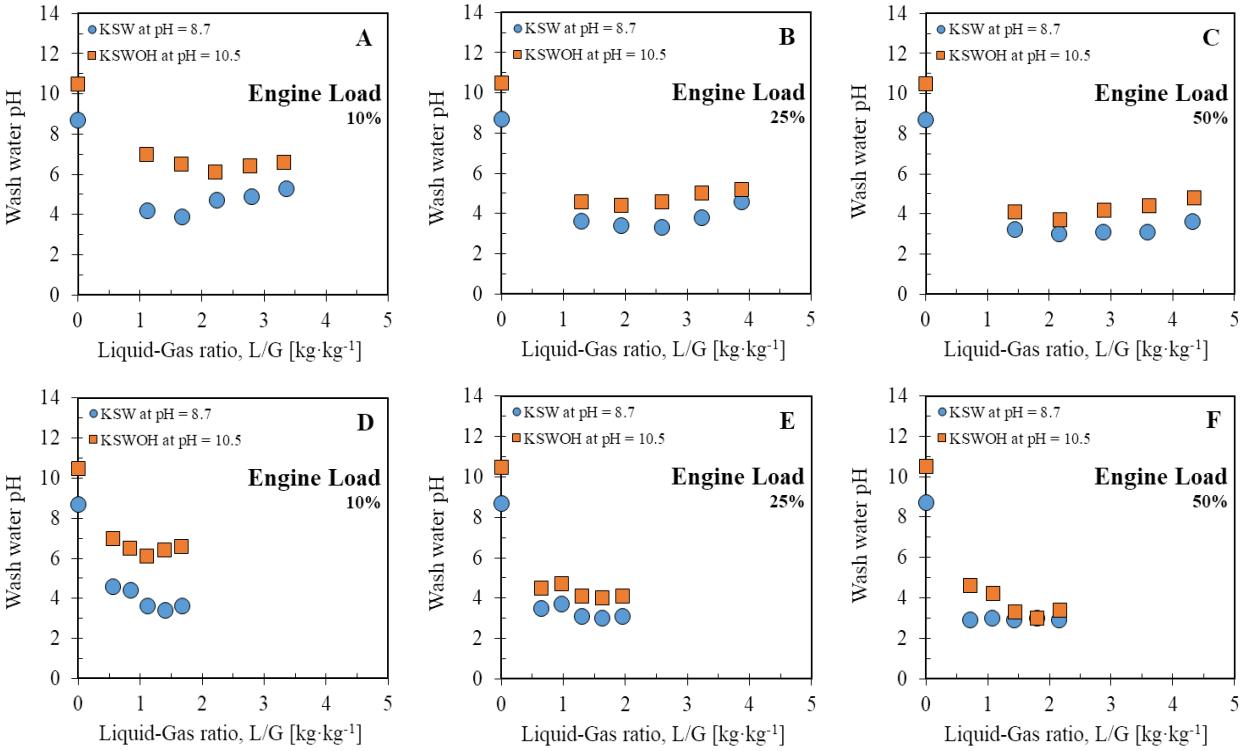

Figure IV.21. *Experimental results of wash water pH value from FGD pilot unit tests. The pH values are expressed as a function of the liquid-gas mass ratio and parametric with scrubbing liquid used: Kattegat seawater (KSW) and Kattegat seawater with NaOH addition (KSWOH). The results are referred to different flue-gas flow rate equal to 70 (Figures A, B and C) and 140 $m^3 \cdot h^{-1}$ (Figures D, E and F) and for three different engine loads: 10, 25 and 50%*

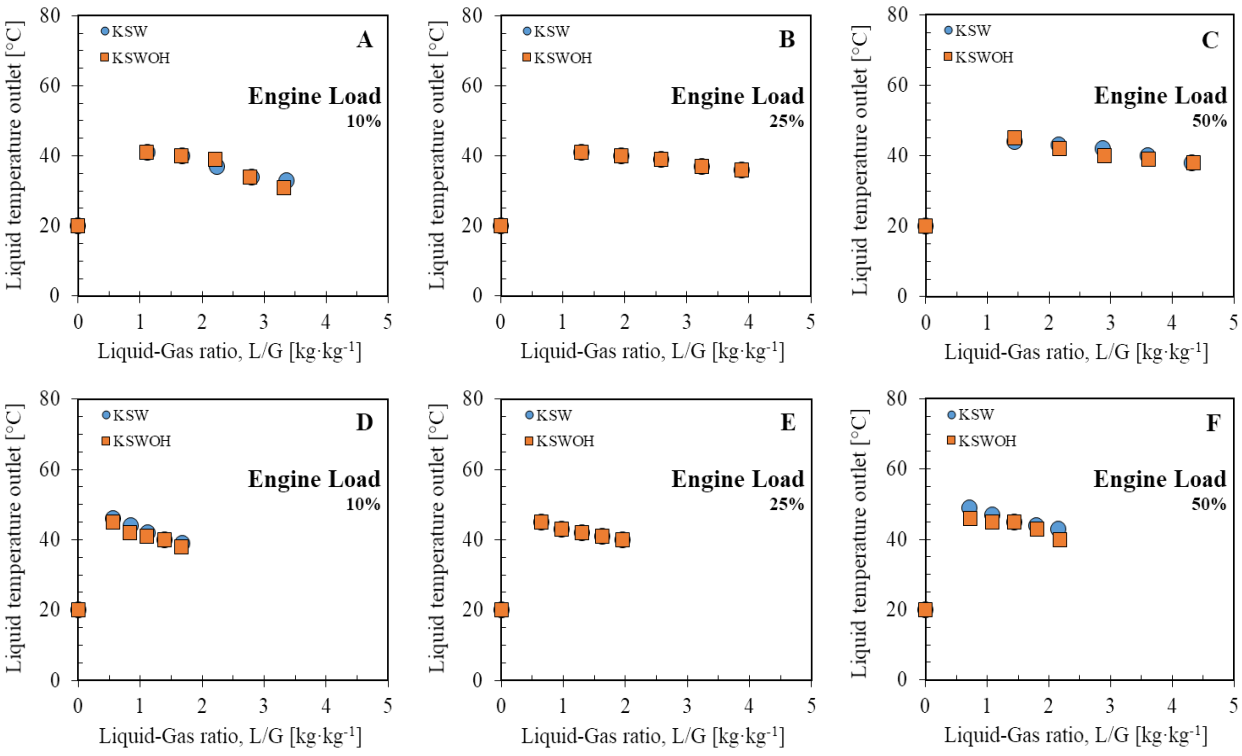

Figure IV.22. *Experimental results of wash water temperatures from FGD pilot unit tests. The liquid temperature values are expressed as a function of the liquid-gas mass ratio and parametric with the scrubbing liquid used: Kattegat seawater (KSW) and Kattegat seawater with NaOH addition (KSWOH). The results are referred to different flue-gas flow rate equal to 70 (Figures A, B and C) and 140 $m^3 \cdot h^{-1}$ (Figures D, E and F) and for three different engine loads: 10, 25 and 50%*

The pH values of the wash water were consistent with the SO_2 emission trends. As the engine load increased, the ranges of pH values in the wash waters lowered because more SO_2 was captured. The use of NaOH in pure seawater increased the final pH values. When the engine load was at 10% the pH was about 7 for each tested *L/G*, while as the load increased the values decreased up to those in pure seawater. The pH values of effluents after the scrubber were in the range 3 - 5, which is considered high enough to guarantee a pH no lower than 6.5 at 4 m from the discharge point, as suggested by IMO guidelines 2009, Resolution MEPC 184(59), ([20], [31], [219]). Generally, the amount of water needed to restore the pH within 4 m is about 1.9 times higher than that used for gas cleaning process, if a seawater is used [32].

The liquid temperature in **Figure IV.22A**–**C** remained almost unvaried with the engine load. This was probably due to the heat losses of the scrubber unit. When del flue-gas flow rate was 140 $m^3 \cdot h^{-1}$ (**Figure IV.22D**–**F**) the exit liquid temperature is almost 5 °C higher than for the case of lower gas flow rate. The temperature values of effluents after the scrubber were generally in the range 30 - 50 °C. Effluent discharges with temperatures above 40 °C can cause eutrophication effects, as suggested by IMO guidelines 2009 (Resolution MEPC 184(59)). The mixing operation with fresh seawater, made to restore the pH [32], is also useful to cool down the scrubber effluents.

IV.4.3.3. FGD effect on heavy metals and organics emissions in wash waters

To evaluate the effect of the FGD process on heavy metals and organics emissions in the scrubber wash waters, further chemical analysis on water samples collected at the scrubber outlet were made, under three different conditions:

- SAMPLE 1: engine load = 10%; G = 70 $m^3 \cdot h^{-1}$; L = 60 $L \cdot h^{-1}$;
- SAMPLE 2: engine load = 25%; G = 70 $m^3 \cdot h^{-1}$; L = 120 $L \cdot h^{-1}$; L/h;
- SAMPLE 3: engine load = 50%; G = 70 $m^3 \cdot h^{-1}$; L = 150 $L \cdot h^{-1}$; L/h.

The sample analyses were performed by ALS Scandinavia AB and the results (including those for KSW from **Tables III.4**–**5**) are reported in **Table IV.16** for heavy metals content and **in Table IV.17**

for organics content. These analyzes were performed with filtering (0.45 µm) only for wash water samples.

Table IV.16. *Heavy metals concentration values in the KSW and for the three wash water samples*

Sampling Date:		**KSW**	**SAMPLE**	**SAMPLE**	**SAMPLE**
Heavy metals composition		**INLET**	**1**	**2**	**3**
Ca	$mg \cdot L^{-1}$	19.5	21.15	20.30	20.58
Fe	$mg \cdot L^{-1}$	0.0243	0.29	1.02	2.59
K	$mg \cdot L^{-1}$	< 8	8.40	8.40	9.29
Mg	$mg \cdot L^{-1}$	< 2	2.17	3.24	6.35
Na	$mg \cdot L^{-1}$	13100	13102	13122	13181
Si	$mg \cdot L^{-1}$	1.03	1.09	1.06	1.07
Al	$\mu g \cdot L^{-1}$	34.7	57.1	173.70	363.70
Ba	$\mu g \cdot L^{-1}$	10.2	11.4	10.68	10.70
Cd	$\mu g \cdot L^{-1}$	< 0.05	0.10	0.10	0.12
Co	$\mu g \cdot L^{-1}$	< 0.05	2.16	6.65	14.45
Cr	$\mu g \cdot L^{-1}$	0.14	32.54	243.14	630.14
Cu	$\mu g \cdot L^{-1}$	12.4	22.8	38.30	62.80
Hg	$ng \cdot L^{-1}$	< 2	4	4	4
Mn	$\mu g \cdot L^{-1}$	2.85	17.6	64.85	150.85
Mo	$\mu g \cdot L^{-1}$	0.245	7.12	10.095	19.64
Ni	$\mu g \cdot L^{-1}$	1.38	132.38	409.38	947.38
P	$\mu g \cdot L^{-1}$	< 40	80	80	80
Pb	$\mu g \cdot L^{-1}$	< 0.3	6.77	5.25	9.47
Sr	$\mu g \cdot L^{-1}$	52.4	55.75	64.5	73.30
Zn	$\mu g \cdot L^{-1}$	83.1	190.10	347.10	707.10

Table IV.17. *Organics concentration values in the KSW and for the three wash water samples*

Sampling Date:		**KSW**	**SAMPLE**	**SAMPLE**	**SAMPLE**
Organics composition		**INLET**	**1**	**2**	**3**
aliphates> C5-C8	$\mu g \cdot L^{-1}$	< 10	< 10	< 10	< 10
aliphates> C8-C10	$\mu g \cdot L^{-1}$	< 10	< 10	< 10	< 10
aliphates> C10-C12	$\mu g \cdot L^{-1}$	< 10	32	25	23
aliphates> C12-C16	$\mu g \cdot L^{-1}$	< 10	36	26	21
aliphates> C5-C16	$\mu g \cdot L^{-1}$	< 20	68	51	44
aliphates> C16-C35	$\mu g \cdot L^{-1}$	< 10	75	102	125
aromatics> C8-C10	$\mu g \cdot L^{-1}$	< 0.30	14.5	< 0.57	1,64
aromatics> C10-C16	$\mu g \cdot L^{-1}$	< 0.775	< 1.49	< 1.49	< 1.49
metylpyrener/metylfluorantener	$\mu g \cdot L^{-1}$	< 1.0	< 1.0	< 1.0	< 1.0
methylchrysene/dimethylbenz(a)anthracene	$\mu g \cdot L^{-1}$	< 1.0	< 1.0	< 1.0	< 1.0
aromatics C16-C35	$\mu g \cdot L^{-1}$	< 1.0	< 1.0	< 1.0	< 1.0
benzene	$\mu g \cdot L^{-1}$	< 0.20	0.23	< 0.20	< 0.20
toluene	$\mu g \cdot L^{-1}$	< 0.20	< 0.20	< 0.20	< 0.20
ethylbenzene	$\mu g \cdot L^{-1}$	< 0.20	< 0.20	< 0.20	< 0.20
m-,p-xylene	$\mu g \cdot L^{-1}$	< 0.20	< 0.20	< 0.20	< 0.20
o-xylene	$\mu g \cdot L^{-1}$	< 0.20	< 0.20	< 0.20	< 0.20
xylenes, sum	$\mu g \cdot L^{-1}$	< 0.20	< 0.20	< 0.20	< 0.20
naphthalene	$\mu g \cdot L^{-1}$	0.038	0.179	< 0.048	< 0.048
acenaphthylene	$\mu g \cdot L^{-1}$	< 0.010	< 0.048	< 0.048	< 0.048

acenaften	µg·L^{-1}	< 0.010	< 0.048	< 0.048	< 0.048
fluorene	µg·L^{-1}	< 0.010	< 0.048	< 0.048	< 0.048
phenanthrene	µg·L^{-1}	0.037	0.098	<0.048	<0.048
anthracene	µg·L^{-1}	< 0.010	< 0.048	< 0.048	< 0.048
fluoranthene	µg·L^{-1}	< 0.010	< 0.048	< 0.048	< 0.048
pyrene	µg·L^{-1}	< 0.010	< 0.048	< 0.048	< 0.048
benzo(a)anthracene	µg·L^{-1}	< 0.010	< 0.048	< 0.048	< 0.048
chrysene	µg·L^{-1}	< 0.010	< 0.048	< 0.048	< 0.048
benzo(b)fluoranthene	µg·L^{-1}	< 0.010	< 0.048	< 0.048	< 0.048
benzo(k)fluoranthene	µg·L^{-1}	< 0.010	< 0.048	< 0.048	< 0.048
benzo(a)pyrene	µg·L^{-1}	< 0.010	< 0.048	< 0.048	< 0.048
dibenz(a,h)anthracene	µg·L^{-1}	< 0.010	< 0.048	< 0.048	< 0.048
benzo(g,h,i)perylene	µg·L^{-1}	< 0.010	< 0.048	< 0.048	< 0.048
indeno(1,2,3-cd)pyrene	µg·L^{-1}	< 0.010	< 0.048	< 0.048	< 0.048
PAH, sum 16	µg·L^{-1}	0.075	0.28	< 0.38	< 0.38
PAH, sum carcinogens	µg·L^{-1}	< 0.035	< 0.17	< 0.17	< 0.17
PAH, sum others	µg·L^{-1}	0.075	0.28	< 0.22	< 0.22
PAH, sum L	µg·L^{-1}	0.04	0.22	0.11	0.11
PAH, sum M	µg·L^{-1}	0.04	0.13	0.16	0.16
PAH, sum H	µg·L^{-1}	< 0.04	0.23	0.23	0.23

The analyses indicated that the FGD caused an increase in the metals concentrations together with an increase in the engine load and liquid flow rate. In particular, some metals such as Fe, Al, Co, Cu, Cr, Mn, Mo, Ni, Pb and Zn significantly increased their content in the wash water. As regards the organics, an increase in the order between 2 and 5 times of their concentration compared with the raw seawater was generally observed. The PAH levels are below detection limits. The only exceptions were the Aliphatics and some aromatics species whose variation with the engine load and water flow rate did not have a specific trend as for metals.

Figure IV.23 resumes the trends of the wash water concentration of those pollutants that had a most relevant increase, as a function of the load engine. The experiments were presented as the ratio between the concentration of pollutant in the wash water sample and that of the Kattegat seawater (C_{SAMPLE}/C_{KSW}) from **Tables IV.16–17**.

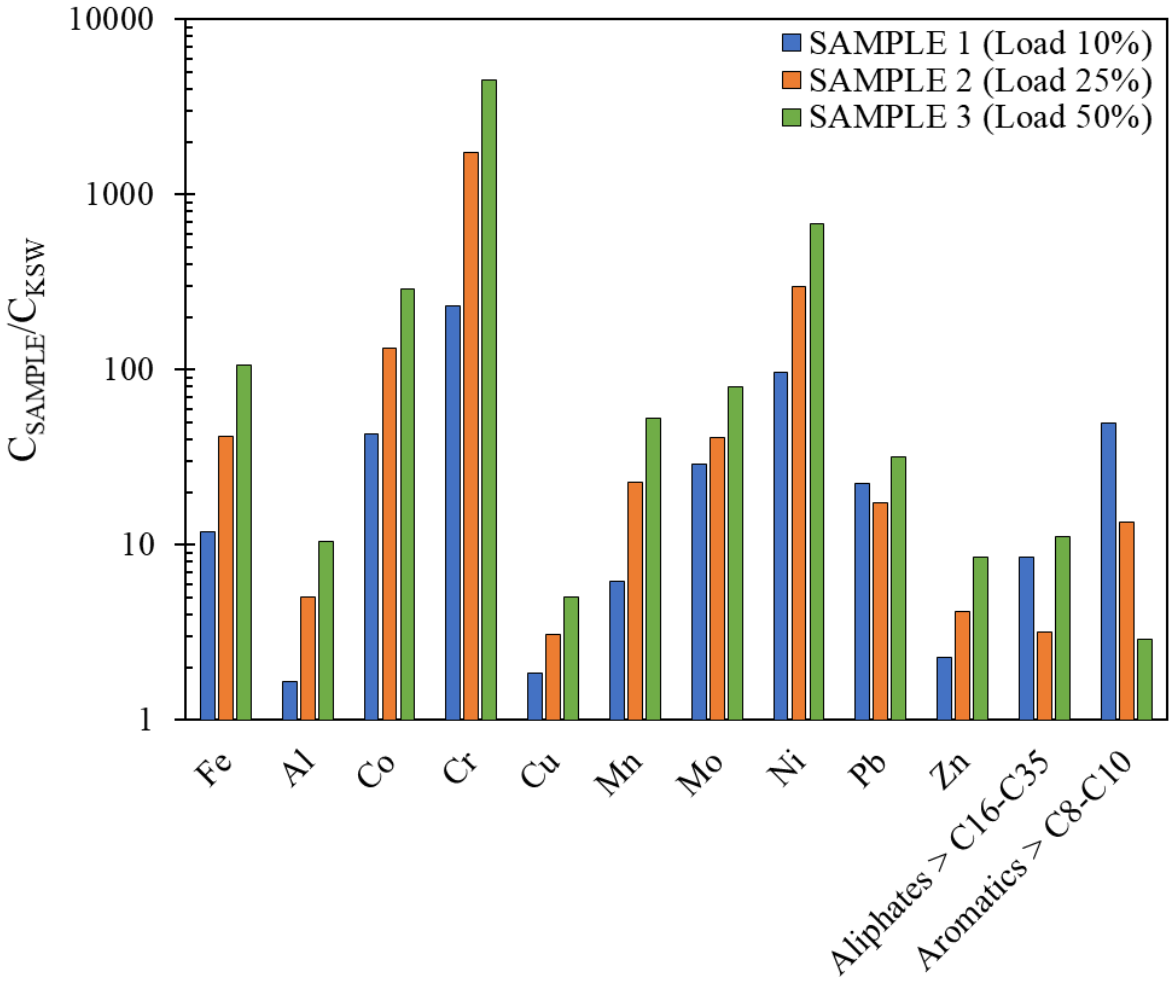

Figure IV.23. *Comparison between the concentrations of the heavy metals and organic species that varied more than 5 times respect to the Kattegat seawater in the Samples 1,2 and 3*

Figure IV.23 shows that zinc, copper and aluminum concentration in the wash water increased with the engine load and up to a value between 5 and 10 times that of fresh KSW, while iron, cobalt, manganese, molybdenum and lead increased up to 30 - 100 times. On contrary, a significant increase was observed for chromium which reached a maximum value of almost 4500 times than fresh KSW, while for nickel it was 650, for the load at 50%. The only two organic species that were higher than KSW were aliphatics > C16-C35, up to 10 times, and aromatics > C8-C10, between 3 and 50 times. These experiments can be compared with some experimental results reported in the pertinent literature. **Kjølholt et al.** [2] report results of the chemical analyses of metals, THCs, PAHs and other parameters, conducted on the wash water samples from a seawater scrubber operating in open-loop mode on the Ficaria Seaways. The results are listed in **Table IV.18**, for two different types of fuel and engine loads.

Table IV.18. *Chemical analyzes on wash water samples from a seawater scrubber operating in open-loop mode on the Ficaria Seaways using two fuels with different content of Sulphur (HFO, 2.2% S and HFO, 1.0% S) at two different engine load (high = 85 - 90% and low = 40 - 45%). The seawater flow rate was set as constant at 1000 $m^3 \cdot h^{-1}$(**Kjølholt et al.*** [2]*)*

Parameters		**SW**	**Wash water from SW scrubber open-loop**			
			2.2% S High load	**2.2% S Low load**	**1.0% S High load**	**1.0% S Low load**
Fuel Consumption	$kg \cdot h^{-1}$	-	3510	1850	3360	3360
pH	-	7.8	3.7	5.2	5.5	5.8
Suspended solids (SS)	$mg \cdot L^{-1}$	14	14	10	15	12
COD	$mg \cdot L^{-1}$	44	52	56	48	46
Sulphur (tot-S)	$mg \cdot L^{-1}$	865	900	900	890	870
Nitrogen (tot-N)	$mg \cdot L^{-1}$	0.12	0.56	0.34	0.36	0.22
Arsenic	$\mu g \cdot L^{-1}$	1.5	< 1.0	1.80	< 1.0	< 1.0
Lead	$\mu g \cdot L^{-1}$	< 0.20	21	3.60	5.80	3.80
Cadmium	$\mu g \cdot L^{-1}$	< 0.20	< 0.20	< 0.20	< 0.20	< 0.20
Copper	$\mu g \cdot L^{-1}$	5.0	260	150	110	150
Mercury	$\mu g \cdot L^{-1}$	0.12	0.086	0.092	0.099	0.064
Nickel	$\mu g \cdot L^{-1}$	8.90	43	20	19	9.10
Vanadium	$\mu g \cdot L^{-1}$	1.8	180	81	49	25
Zinc	$\mu g \cdot L^{-1}$	< 0.20	450	150	110	98
Sum, benzene - C35	$\mu g \cdot L^{-1}$	N/A	110	140	330	200
PAH (16EPA)	$\mu g \cdot L^{-1}$	N/A	0.96	1.1	1.8	1.6
Naphthalene	$\mu g \cdot L^{-1}$	N/A	0.48	0.51	0.52	0.57
PAH, filtered sample	$\mu g \cdot L^{-1}$	N/A	0.62	0.65	0.78	0.86

The **Table IV.18** shows the main parameters of the wash water investigated by **Kjølholt et al.** [2], and it was evident that for most of the metals, the concentration levels increased with increasing both engine load (as noted in **Table IV.16**) and sulphur content. Note that the concentration values of benzene - C35 content were particularly high in all four cases but it reached its maximum in correspondence of the lower sulphur content. Besides, vanadium, zinc and copper content increased significantly as compared to their concentration values in the seawater (as noted in **Table IV.16**). The authors verified that this was due to the effects of high temperature and acid corrosion of pipes and scrubber. **Kjølholt et al.** [2] also reported an interesting comparison between the wash water discharges of a seawater scrubber in open-loop (Ficaria Seaways) and a scrubber operated with fresh water and NaOH, in a closed-loop after only 2 hours of recirculation (Ficaria Seaways). As expected, the results of the chemical analysis on the waste water flowing out from the closed-loop scrubber confirmed that the concentration levels of heavy metals, organic and PAHs were of the order of about 100 times higher than the corresponding values from the open-loop scrubber.

Turner et al. [33] collected the chemical analyses on discharge water deriving from open-loop scrubbers from several works and found that both copper and zinc concentrations were well above the suggested by risk assessments of environmental impact on water in the EU (2.6 and 7.8 $\mu g \cdot L^{-1}$, respectively). The highest total copper and zinc concentrations reported in discharge water are 260 and 537 $\mu g \cdot L^{-1}$, respectively, based on the monitoring of some ships, *i.e.* Pride of Kent (RoRo), Ficaria (RoRo), Magnolia (RoRo), Fjordshell (tanker) and Zaandam (passenger).

While for copper our measurements were significantly 4 to 10 times smaller than the data collected by **Turner et al.** [33], it was observed that the zinc values were about 1.3 higher than **Turner et al.** [33] data at the maximum engine load. It is interesting to note that the zinc measurements increase significantly with the engine load and with the liquid flow rate: in fact from 10% to 50%, the zinc captured increased from 190.1 to 707.1 $\mu g \cdot L^{-1}$ despite the seawater flow rate increased and diluted the sample. This result could confirm that the Zn particles were mostly due to high temperature and acid corrosion of the pipes and scrubber vessel.

Turner et al. [33] reports that the main metal sources include combustion of fuel and lubricants and a potential copper sources include the use of impressed current cathodic protection systems in the sea chest, which operate by releasing copper ions that are carried through the cooling system. Another source of release of copper could be represented by the antifouling paints and by the corrosion scrubber itself [34]. This could also explain the low copper concentration detected with respect to the values reported in **Turner et al.** [33]. However, iron is the main metal that can have a significant impact on oceanic ecosystems. The seawater solubility of particulate iron produced from oil combustion is significantly higher than that related to other iron-containing aerosols and shipping emissions could contribute for 30 - 60% of the soluble iron deposition in the North Atlantic and North Pacific oceans by the year 2100 [33]. In fact, **Table IV.16** shows a significant increase in the iron particles captured by the seawater, increasing by about 11 up to 100 times than KSW when the load increased from 10 to 50%.

Ytreberg et al. [34] carried out scrubbing tests using the same experimental apparatus of this Ph.D. thesis, an MGO fuel at 1% sulphur, with engine load at 25% and water collected from the research station Askö, Baltic Sea. Wash water analysis showed much lower metal contents than those reported in the **Table IV.16**. This was probably due to the adopted exhaust gas flow rate which was approximately 80 times lower than that used in the present work thesis. However, an increase in the concentrations of Al, Cr, Cu, Ni and Zn were observed higher in the scrubbed wash water, almost 3 to 19 times as compared to the fresh inlet water. This further suggests that these pollutants originated mostly from the corrosion of the scrubber walls and pipelines, rather than from the fuel itself.

Starting from the analysis of fuel samples and their consumption during tests and assuming that all the metals in the fuel are transferred to the water, it is possible to calculate the maximum concentration for each heavy metal ($C_{M,max}$) that can be found in the water samples as:

$$C_{M,\max} = \frac{FC\rho_F C_M}{L}\left(\frac{G}{G_{eng}}\right) \tag{215}$$

where C_M [mg·kg^{-1}] indicates the mass concentration of metals in the fuel, FC [L·h^{-1}] is fuel consumption for each engine load (see **Table III.3**), $\rho_F = 0.84$ kg·L^{-1} is the MGO fuel density, L [L·h^{-1}] is the seawater flow rate fed to the scrubber, G [m^3·h^{-1}] is the flue-gas flow rate fed to the scrubber, G_{eng} [m^3·h^{-1}] is the total exhaust gas flow rate produced by the engine (estimated as 144 Nm^3·h^{-1}, on the bases of the engine speed and size).

The ratios between $C_{M,max}$ (maximum possible metal content deriving from the fuel) and the metals content observed in the wash water samples, $C_{M,obs}$ (obtained as the difference between the metals content in the samples and the Kattegat seawater metals content from **Table IV.16**) are reported in **Table IV.19**.

Table IV.19. *Ratios between maximum possible metal content deriving from the fuel and the metals content observed in the wash water samples (purged the starting content in the KSW)*

Heavy metals		$C_{M,max}/C_{M,obs}$ **SAMPLE 1**	$C_{M,max}/C_{M,obs}$ **SAMPLE 2**	$C_{M,max}/C_{M,obs}$ **SAMPLE 3**
Ca	Calcium	1784	824	843
Fe	Iron	237	1026	2003
K	Potassium	357	412	1007
Mg	Magnesium	151	1278	3396
Na	Sodium	1785	22680	63240
Si	Silicon	53	31	31
Al	Aluminum	6	41	73
Ba	Barium	1	0.5	0.4
Cd	Cadmium	N/A	N/A	N/A
Co	Cobalt	N/A	N/A	N/A
Cr	Chrome	29	250	492
Cu	Copper	9	27	39
Hg	Mercury	N/A	N/A	N/A
Mn	Manganese	N/A	N/A	N/A
Mo	Molybdenum	6	10	15
Ni	Nickel	117	420	739
P	Phosphorus	N/A	N/A	N/A
Pb	Lead	6	5	7
Sr	Strontium	N/A	N/A	N/A
Zn	Zinc	95	272	487

Table IV.19 shows that almost all the metals in the scrubber wash water do not derive from the capture of particles deriving from the fuels but rather on corrosion processes. In particular, for metals

such as Fe, Al, Cr, Cu, Mn, Co, Ni, Pb, Zn their abundant presence, compared to the maximum values expected from the metal content in the fuel, is closely related to the corrosion of the scrubber's steel and pipe line. On the other hand, the high values found also for other metals such as Ca, K, Mg, Na and Si, which are not generally deriving from the construction material of the scrubber and equipment, could probably be ascribed to problems of scale residues build-up in the scrubber chamber due to its vertical positioning and which were then washed away during the tests.

Tables IV.20–**21** shows the concentration limits of some heavy metals and organics in the discharge wash water according to the regulations listed above (**Section IV.4.1**.).

Table IV.20. *Discharge limits in the wash water of heavy metals according to currently available regulations and guidelines*

Heavy Metals		**EU EQS**	**DE EQS**	**STR EQS**	**EPA NRWQC**	**IT DL**	**GE DL**
Lead	$\mu g \cdot L^{-1}$	14	2.8	0.34	8.1	200	500
Mercury	$\mu g \cdot L^{-1}$	0.07	0.07	0.05	N/A	5	50
Nickel	$\mu g \cdot L^{-1}$	34	6.8	0.23	8.2	2000	1000
Copper	$\mu g \cdot L^{-1}$	N/A	2	1	3.1	100	500
Vanadium	$\mu g \cdot L^{-1}$	N/A	57.8	4.1	N/A	N/A	N/A
Zinc	$\mu g \cdot L^{-1}$	N/A	8.4	7.8	N/A	N/A	N/A
Arsenic	$\mu g \cdot L^{-1}$	N/A	1.1	0.11	36	N/A	N/A
Chromium	$\mu g \cdot L^{-1}$	N/A	N/A	N/A	74	2000	500
Selenium	$\mu g \cdot L^{-1}$	N/A	N/A	N/A	71	N/A	N/A
Cadmium	$\mu g \cdot L^{-1}$	0.45	1.5	0.2	N/A	20	100
Iron	$\mu g \cdot L^{-1}$	N/A	N/A	N/A	N/A	2000	N/A
Alluminium	$\mu g \cdot L^{-1}$	N/A	N/A	N/A	N/A	1000	N/A
Barium	$\mu g \cdot L^{-1}$	N/A	N/A	N/A	N/A	500	N/A

Table IV.21. *Discharge limits in the wash water of organics and PAHs according to currently available regulations and guidelines*

Organics and PAHs		**EU EQS**	**DE EQS**	**STR EQS**	**EPA NRWQC**	**IT DL**	**GE DL**
Benz[*a*]anthracene	$ng \cdot L^{-1}$	N/A	N/A	N/A	18	N/A	N/A
Benzo[*a*]pyrene	$ng \cdot L^{-1}$	50	N/A	N/A	18	N/A	N/A
Benzo[*b*+*k*]fluoranthene	$ng \cdot L^{-1}$	34	N/A	N/A	18	N/A	N/A
Chrysene	$ng \cdot L^{-1}$	N/A	N/A	N/A	18	N/A	N/A
Dibenz[*a*,*h*]anthracene	$ng \cdot L^{-1}$	N/A	N/A	N/A	18	N/A	N/A
Fluorene	$mg \cdot L^{-1}$	N/A	N/A	N/A	5.3	N/A	N/A
Indeno[1,2,3-*cd*]pyrene	$ng \cdot L^{-1}$	2	N/A	N/A	18	N/A	N/A
Phenanthrene	$\mu g \cdot L^{-1}$	N/A	N/A	N/A	50	N/A	N/A
Pyrene	$mg \cdot L^{-1}$	N/A	N/A	N/A	4	N/A	N/A
Benzene	$\mu g \cdot L^{-1}$	8	N/A	N/A	50	N/A	N/A
Naphthalene	$\mu g \cdot L^{-1}$	1.2	N/A	N/A	N/A	N/A	N/A
Antracen	$\mu g \cdot L^{-1}$	0.1	N/A	N/A	N/A	N/A	N/A
Fluoranthene	$\mu g \cdot L^{-1}$	1.12	N/A	N/A	N/A	N/A	N/A

Benzo(*g,h,i*)perylene	ng·L^{-1}	8.2	N/A	N/A	N/A	N/A	N/A

Figures IV.24–25 compare the discharge concentrations of the heavy metals and organics in the three wash water samples (**Tables IV.16–17**) with the regulations in **Tables IV.20–21**: EU-EQS; DE-EQS; STR-EQS; EPA-NRWQC; IT-DL; GE-DL.

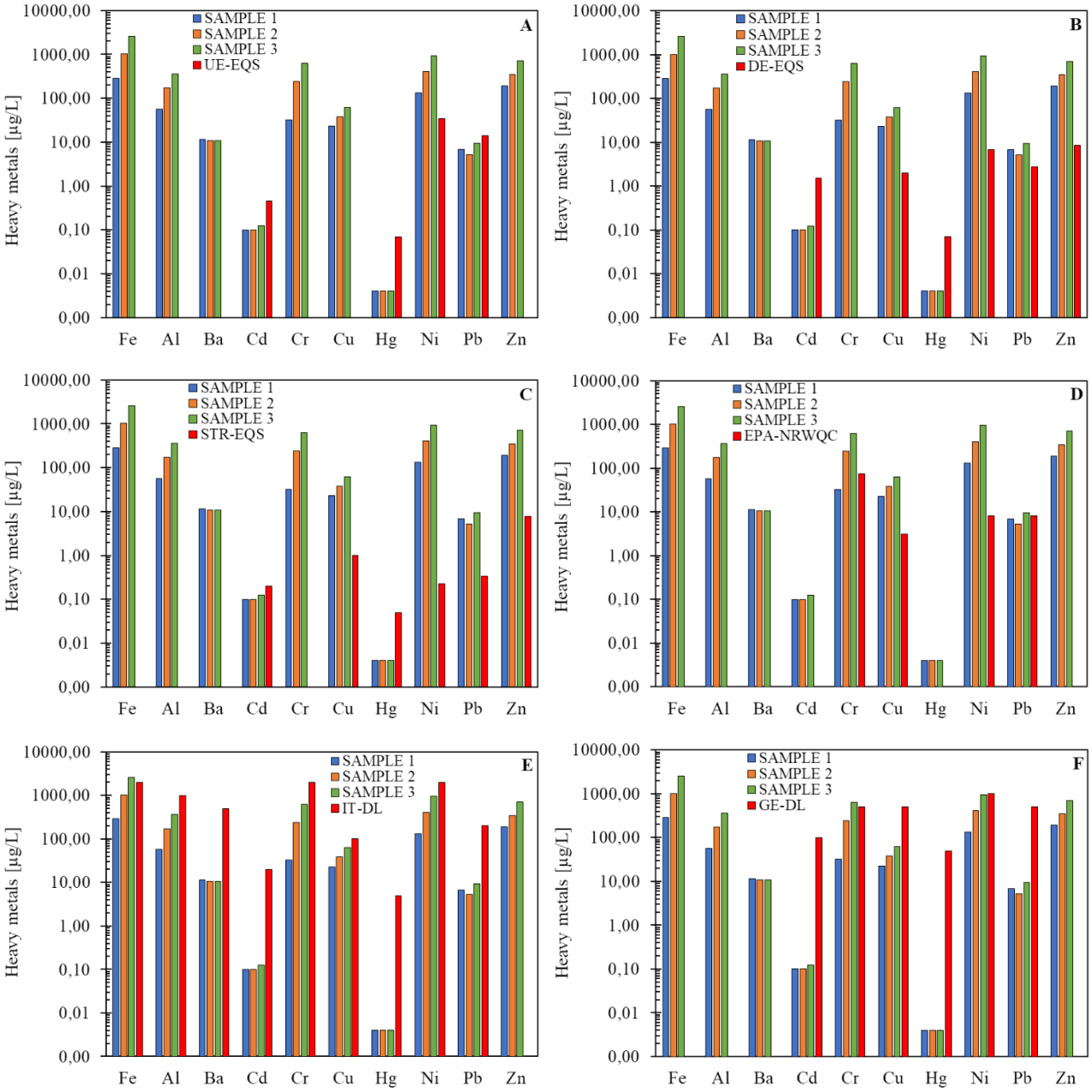

Figure IV.24. *Comparison between the concentrations of the heavy metals in the three wash water samples with the available regulations: EU-EQS; DE-EQS; STR-EQS; EPA-NRWQC; IT-DL; GE-DL*

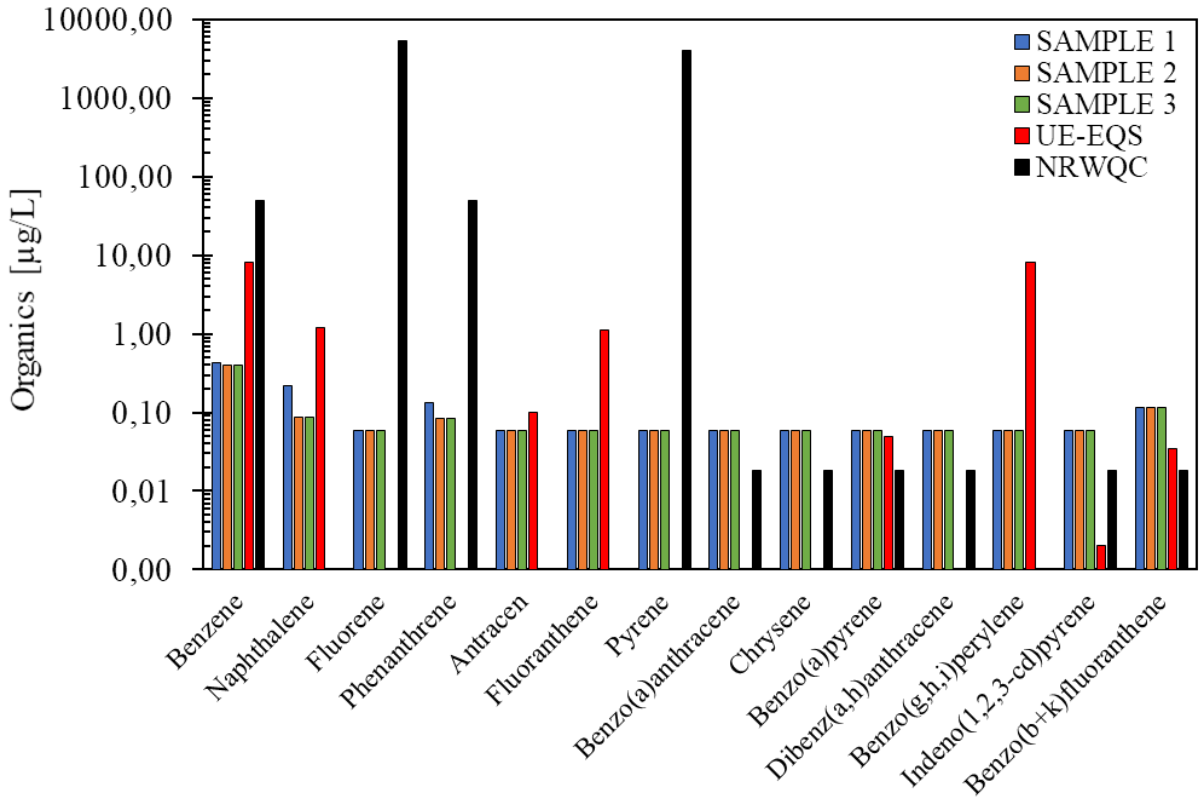

Figure IV.25. *Comparison between the concentrations of the organics and PAHs in the three wash water samples with the available regulations: EU-EQS; EPA-NRWQC*

Figure IV.24 showed that most of the heavy metals, *e.g.* Cd, Cr, Cu, Hg, Ni, Pb and Zn, have quite high concentrations, and failed to complied with the all EQS and NRWQC Regulations for wash water discharge, except for cadmium and mercury. As previously mentioned, the concentrations of some metals were higher than those expected and fail to meet the more stringent regulations *i.e.* the water quality standard (EQS). It is worth noticing that the comparison with Regulations for natural waters is not really pertinent, and if applied straightforwardly, as done by some researcher, it would led to the conclusion that none of the existing human activity would be allowed, neither the land based nor the maritime one. However, if the metal measurements are compared with the IT-DL and DE-DL Regulations, which refer directly to the discharge of wash water from industrial activities or scrubbers, it can be observed that the limits are almost all complied. In this case, only Fe and Cr exceed the limits by a factor higher than 1.3 times. A similar reduction coefficient can be easily achieved by dilution, as shown by the studies referred to pH previously reported [32]. In this case, a smaller amount of seawater is required than the dilution required to restore the wash water pH.

Figure IV.25 showed that most of the organics and PAHs levels met the UE-EQS limits, except for Indeno(1,2,3-*cd*)pyrene which was much higher than the limit by a factor of about 30. The levels of

Benzo(*b+k*)fluoranthene and Benzo(*a*)pyrene were slightly above the allowed limit. Although, the organics and PAHs levels appeared very low, most micro-pollutants: Benzo(*a*)anthracene, Chrysene, Benzo(*a*)pyrene, Dibenz(*a,h*)anthracene, Indeno(1,2,3-*cd*)pyrene, Benzo(*b+k*)fluoranthene were above the EPA-NRWQC targets, by a factor of about 3 - 6 times. However, it is worth noting that most of the organics shown in **Figure IV.25** were below the detection limit of the analytic instrument and would probably be closer to the EPA-NRWQC targets.

IV.4.4. Highlights

This activity was aimed to evaluate the performance of a pilot spray FGD column used to clean the gases deriving from a marine Diesel engine (Volvo Penta 80 kW) operated at different loads. The tested scrubbing liquid was Kattegat seawater, either as raw or doped with NaOH. The SO_2 emissions at the scrubber exit were compared with the limits set by IMO-MARPOL (Annex VI - Regulation 14) for the SECA and GLOBAL targets. The effect of the FGD process on other gas pollutants (NO_x, CO and CO_2) and on micro pollutants in wash waters (heavy metals and organics) was also tested. The main findings of this activity can be summarized as follows:

- For 70 $m^3 \cdot h^{-1}$ of flue-gas, the SECA target was respected with L/G = 1.5 $kg \cdot kg^{-1}$ for 10% of engine load, 2.4 $kg \cdot kg^{-1}$ for 25% of engine load and 3.5 $kg \cdot kg^{-1}$ for 50% of engine load. The addition of NaOH to the seawater allowed to meet the SECA target with a water-savings of 50, 21 and 23%, respectively.
- For 140 $m^3 \cdot h^{-1}$ of flue-gas, the SECA target was respected only with L/G = 1.40 $kg \cdot kg^{-1}$ for 10% of engine load, with a water-saving around 40% associated with the use of NaOH. The seawater doped with NaOH could reach the SECA limit even at 25% of the engine load using an L/G = 1.95 $kg \cdot kg^{-1}$.
- No effect on other gas pollutants was observed during FGD tests: NO_x, CO and CO_2 were actually insoluble both in the raw and the NaOH doped Kattegat seawater.
- Capture of heavy metals and organic pollutants deriving from the hydrodynamic scavenging of oils and particulate matter in the gas were compliant with the wash water discharge Guidelines for scrubbers and for land-based activities, and sometimes slightly higher than the discharge limits for natural water bodies. The worst case appeared for iron and chrome, which are 1.3 times larger than the limit imposed by IT-DL and DE-DL regulations. This limit can be easily achieved with a dilution factor of about 1.3 for wash water discharge, which is easily achieved close within 4 m from ships hull in movement. Interestingly in this case study, the dilution factor required for reducing the excess of metals was very similar to that for restoring wash water pH, which is

approximately 1.9 for seawater use. The limits for organic and PAHs were generally respected, only for the EPA-NRWQC Regulation, and some species exceeded the targets by about 3 or 6 times. However, it should be noted that most of the measurements were below the detection limit of the analytic instrument and could probably be below the regulatory limits too.

IV.5. FGD process by wet oxidation scrubbing from model flue-gas using seawater-based solutions enhanced with $NaClO_2$

This section is extracted from two works. The first was presented at the 42th Meeting of the Italian Section of the Combustion Institute, and included tests to evaluate the SO_2 solubility in seawater-based with sodium chlorite aqueous solutions. The second is a work under review for the Special Issue of Fuel for the 14th International Conference on Energy for a Clean Environment, and included experimental and modelling calculation of solubilities in the feed-batch bubble column, and the SO_2 removal efficiencies from desulphurization tests carried out in the packed tower, using seawater solutions containing sodium chlorite.

The experiments refer to innovative flue-gas desulphurization process based on the wet oxidation scrubbing (WOS), using sodium chlorite ($NaClO_2$), which offers strong oxidizing power even in acid conditions, generally unfavorable for the absorption of acid gases such as SO_2. Sodium chlorite is one of the most promising additives thanks to its oxidizing nature both in alkaline and acidic conditions. Under acid conditions, $NaClO_2$ has an even greater oxidative potential due to the formation of further oxidants, such as $ClO_{2(aq)}$ and $Cl_{2(aq)}$.

These experiments aim to test the performance of sodium chlorite seawater solutions by measuring the removal efficiencies of SO_2 in packed column (see **Section III.2.2**) at 1 atm and at different initial pH of the scrubbing solution. The results were compared with the performances of the seawater performances presented and discussed in the **Section IV.1.2**.

Preliminary tests in the bubble column feed-batch (see **Section III.1.2**) were performed at 1 atm, 25 °C and different initial pH of the absorbing solution to evaluate the solubility of SO_2 in sodium chlorite seawater-based aqueous solutions and to support the analysis of the packed column experiments. Further details on the physical-chemical composition of the liquids used are reported in **Section III.1.1** and **III.2.1**.

Finally, the experimental data obtained in the two different experiments were compared with the modelling results obtained from ASPEN PLUS® simulator using the Flash (see **Section III.1.3**) and Rate-based (see **Section III.2.3.**) blocks, respectively.

IV.5.1. Operating conditions

Tables IV.22–23 report the experimental conditions adopted in the two different set of experiments for the feed-batch bubble column data and the packed column, respectively.

Table IV.22. *Operating conditions adopted for the experiments in the feed-batch bubble column*

Absorbing Solutions	$Q_{G,v}$ $L \cdot h^{-1}$	T_G °C	M_S g	T_L °C	**pH** -	$C^{\circ}_{SO_2}$ ppm_v
SW	60	25	17	25	8.20	110, 202, 425, 617, 799, 1000, 1228, 1502, 1762, 2083
					6	66, 278, 560, 813, 1000, 1265, 1545, 1754, 2011
					3	88, 279, 681, 1000, 1253, 1568, 1734, 2036
SWC0.1	60	25	17	25	8.33	109, 223, 435, 614, 817, 1000, 1218, 1514, 1746, 2113
					6	111, 258, 439, 616, 824, 1000, 1258, 1594,1776, 2173
					3	124, 265, 449, 618, 829, 1000. 1348, 1554, 1886, 2113
SWC0.2	60	25	17	25	8.55	113, 195, 397, 590, 775, 1000, 1223, 1524, 1756, 2033
					6	118, 191, 394, 599, 782, 1000, 1293, 1634, 1796, 2083
					3	107, 205, 388, 605, 785, 1000, 1303, 1564, 1806, 2105

Table IV.23. *Operating conditions adopted for the experiments in the packed column*

Scrubbing Solutions	G $m^3 \cdot h^{-1}$	T_G °C	L $L \cdot h^{-1}$	T_L °C	L/G $L \cdot m^{-3}$	**pH** -	$C^{\circ}_{SO_2}$ ppm_v
SW	32	60	40, 70, 100, 130	25	1.25, 2.19, 3.13, 4.06	8.20,6,3	500, 1000 2000
SWC0.1	32	60	40, 70, 100, 130	25	1.25, 2.19, 3.13, 4.06	8.33,6,3	500, 1000 2000
SWC0.2	32	60	40, 70, 100, 130	25	1.25, 2.19, 3.13, 4.06	8.55,6,3	500, 1000 2000

The operating conditions of the experiments with seawater, performed both in the bubble column and packed column, are reported in the **Sections IV.1.1.**.

IV.5.2. Results and discussion

IV.5.2.1. SO_2 equilibrium tests

Figure IV.26 shows the SO_2 solubility curves (**A-C**) and the corresponding pH values of the saturated solutions (**D**–**F**) as a function of total sulphur absorbed (x_S), obtained for SW and SWC0.1 and SWC0.2, each tested at the three different initial pH. **Figure IV.26A**–**C** also reports the equilibrium curves as predicted by the Flash block model of ASPEN PLUS® that will be commented later in this paragraph.

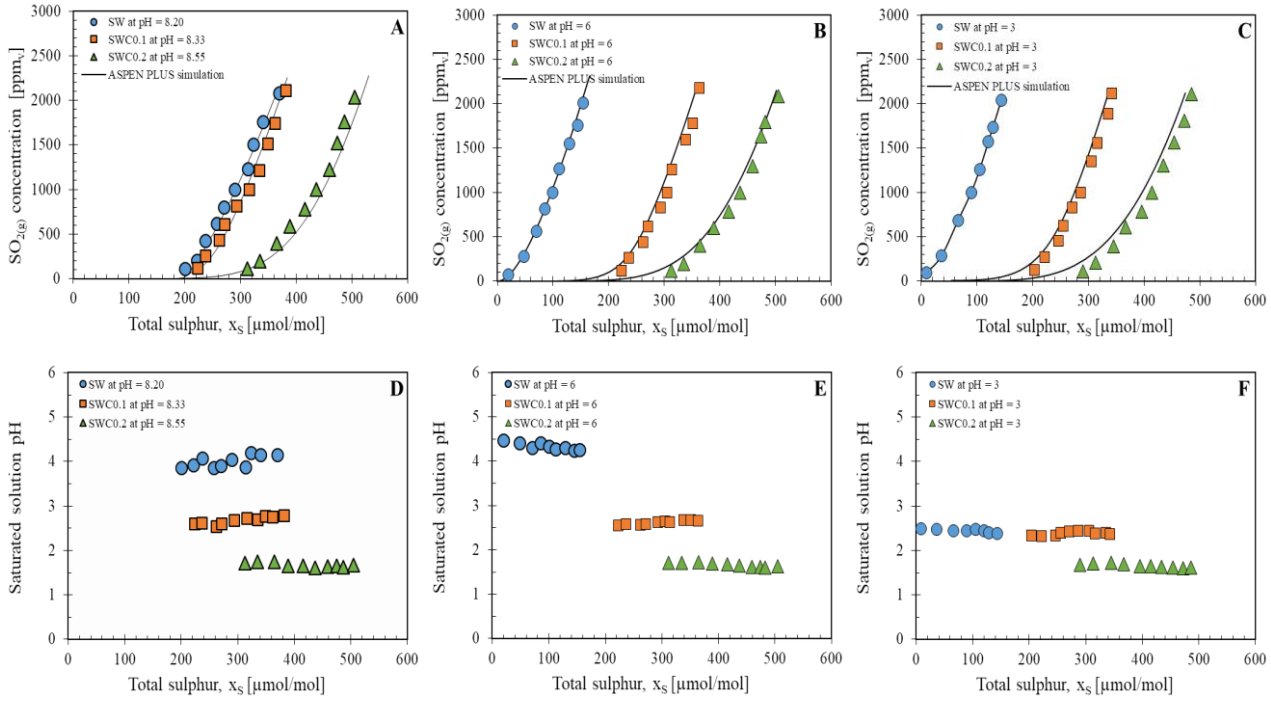

Figure IV.26. *Experimental and modelling SO_2 solubility (A-C) and experimental pH values of the saturated solution (D-F) as a function of total sulphur absorbed (x_S) obtained in three different scrubbing solutions, each at different initial pH. Figures A and D refer to the natural solution pH = 8.20 - 8.55; Figures B and E refers to solutions acidified at pH 6; Figures C and F refers to solutions acidified at pH 3*

Experimental results (**Figure IV.26A**–**C**) showed the typical flat, zeroed value form of chemical absorption with complete conversion of the SO_2 in water, similar to those observed for NaOH solutions (*e.g.* [42], [45], [46], [78]–[80], [220]). When the chemical reactions are almost completed, the solubility curve approached an almost linear trend similar to Henry's law for a purely physical absorption in distilled water. The visual observation of the experiments performed with SWC0.1 and SWC0.2 solutions allows retrieving an interesting result: a fast establishment of acidic conditions in the feed-batch bubble column occurs, since both the chlorite solutions rapidly became greenish (after about 10 - 20 seconds from the beginning of the test) and in the final part of the test they turned almost transparent, when the system reached the saturation and all the chlorite is consumed. These observations clearly confirmed that the SO_2 oxidation mechanism in $NaClO_2$ solutions mainly occurred under acidic conditions, in which the solution assume the greenish color.

Figure IV.26A and **Figure IV.26D** shows that the SO_2 solubility in SW and SW0.1 is almost similar for a basic pH, hence it is scarcely altered by the chlorite content of SWC0.1 (199 $\mu mol \cdot mol^{-1}$). The alkalinity content of the two solutions is the same (for SW is 193 $\mu mol \cdot mol^{-1}$), therefore it is likely to drive the process. In fact, the effect of chlorite is just the oxidation of the already solubilized $S_{(IV)}$

ions, formed by SO_2 hydrolysis (**Eqs. (10)-(12),(17)-(19)**), to $S_{(VI)}$ ions. The slight differences between the two curves could be likely ascribed to the slight difference between chlorite content and alkalinity, which is the real supplemental contribution to SO_2 absorption offered by chlorite presence. In any case, according to the reactions occurring (**Eqs. (83)-(84)**), a difference between the two series of data exists as the SWC0.1 solution became more acidic, as testified by the equilibrium pH reported in **Figure IV.26D**. When the chlorite content is doubled (398 $\mu mol \cdot mol^{-1}$) as in SWC0.2, the solubility curve shifts rightward indicating a significant increase in SO_2 solubility. In this case, the difference between alkalinity (always constant) and chlorite content is far higher, and it determines the significant supplemental SO_2 absorption. As expected, the equilibrium solution of SWC0.2 became more acidic due to the higher amount of absorbed sulphur. For both the SWC solutions, when the alkalinity content was consumed and the solution pH became lower than 6, *i.e.* almost immediately after the beginning of the tests, the *Acidic Oxidation Mechanism* (AOM) started to be active allowing further absorption of SO_2 and the formation of $S_{(VI)}$ ions in solution. The slope of the linear part of the solubility curve is similar for all the tests and very close to the typical values of the Henry's law constant for distilled water determined in a low gas concentration range ($K_H \sim 12$ atm).
When the initial solution pH was lowered (**Figures IV.26B**–**C**), the solubility of pure seawater dropped down due to the loss of alkalinity by the reactions reported in **Eqs. (17)-(19)** and for the parallel leftward shift of reactions **Eqs. (10)-(12)**. On the contrary, the solubility curves for chlorite solutions remained almost unchanged (**Figures IV.26B-C**) with respect to the corresponding values obtained with non-altered pH (**Figure IV.26A**). This result suggested that the oxidation reactions **Eqs. (83)-(84)** allowed the complete and fast depletion of the small amount of $S_{(IV)}$ ions produced by reactions **Eqs. (10)-(12)** so that the series of physical absorption and oxidation reactions (mainly AOM) remained unaltered and determines the same final results in term of SO_2 solubility. As expected, the solution pH lowered in these cases (**Figure IV.26E**–**F**).
The experimental results were further analyzed in light of an equilibrium model, in order to improve the comprehension of the observed phenomena. The Flash block of software ASPEN PLUS®, which allows the calculation of the equilibrium between liquid (either SW, SWC0.1 or SWC0.2) and the gas, was adopted for the definition of the theoretical equilibrium curves. The block solves the mass, charge and energy balances; moreover, it requires a set of equilibrium equations and a suitable model for activity/fugacity coefficient determination. In this work, we used the ELEC-NRTL [93] model for electrolyte solutions. The set of equilibrium reactions and liquid-gas phase equilibria required to describe the process includes the **Eqs. (10)-(12),(17)-(19),(79)-(80),(83)-(84)** and other reactions related to other ions in seawater, as shown in **Flagiello et al.** [42] and resumed in the **Tables II.1**–**2** and **Tables II.4**–**5**. However, some concerns arose in the use of **Eqs. (79)-(80)**, whose equilibrium

constants are extremely high, corresponding to ΔG° values very similar to those calculated by **Park et al.** [72]. If these values were adopted to predict the pH of the solution deriving from the addition of chlorite to seawater, the theoretical result would be far greater than the experimental value. In fact, those constants would determine a complete conversion of chlorite into chlorine dioxide **Eq. (79)** and chlorine **Eq. (80)** and a strong basification of the solution, regardless the initial solution pH, that did not occur in the practice. In order to describe SWC0.1 and SWC0.2 solution pH, the following procedure was followed. First, we merged **Eqs. (79)-(80)** obtaining:

$$6ClO_2^- + 8H_3O^+ + 2Cl^- \rightleftharpoons 4ClO_{2(aq)} + 2Cl_{2(aq)} + 12H_2O \quad (216)$$

Then, the equilibrium constant of **Eq. (216)** was taken as fitting parameter of the equation set forming the equilibrium model, applied to the experimental data retrieved for SWC solutions. The fitting value of the equilibrium constant of **Eq. (216)** resulted to be $K_{eq(216)} = e^{67.5\pm3}$ $(mol \cdot mol^{-1})^{-10}$.

A similar mismatch between experimental data and theoretical indications arose when considering the reactions **Eqs. (83)-(84)**, whose equilibrium constants imply a greater oxidation of SO_2 than the observed values. These mismatch between experimental and theoretical findings probably indicated that some further side-reactions, which were not accounted for, reduced the actual conversion of chlorite. Following a similar procedure as above, the reactions expressed by **Eqs. (83)-(84)** were merged as:

$$6HSO_3^- + 6SO_3^{2-} + 4ClO_{2(aq)}2Cl_{2(aq)} + 18H_2O \rightleftharpoons 12SO_4^{2-} + 8Cl^- + 14H_3O^+ \quad (217)$$

and its equilibrium constant was used to fit the solubility experiments in the feed-batch reactor carried out with SWC solutions. The best fitting of experimental results provided a value of $K_{eq(217)} = e^{2\pm0.1}$ $(mol \cdot mol^{-1})$[16]. The results of data fitting are reported in **Figure IV.26A–C**.

Figure IV.27 reports the model profiles (symbols with lines) of the solution pH as a function of total absorbed sulphur (x_S) in SW, SWC0.1 and SWC0.2, as calculated by ASPEN PLUS® with the Flash block. The Flash block allows the calculation of the equilibrium between the absorbing liquid and the gas and, for each SO_2 absorbed amount, indicates which is the equilibrium pH.

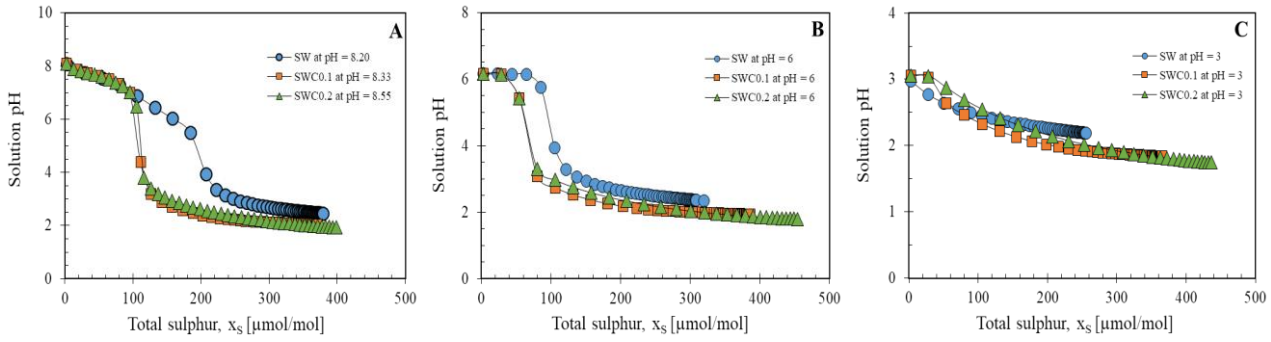

Figure IV.27. *Modelling profile of the solution pH as a function of total absorbed sulphur for SW,*

SWC0.1 and SWC0.2, as calculated by ASPEN PLUS® in the Flash block. Figure A is related to non-altered initial pH of scrubbing solutions; Figure B is related to initial pH value of scrubbing solutions equal to 6; Figure C is related to initial pH value of scrubbing solutions equal to 3

The descriptive model reported in **Figure IV.27** provided an interesting result: the SW solution pH evolved following the typical trend derived from the buffering capacity given by the alkalinity content. For SWC0.1 and SWC0.2 solutions, the pH follows the trend imposed by the alkaline buffer, followed by the rapid oxidation, until pH is > 6 (**Figure IV.27A**). When pH starts to decrease and gets lower than 6, the AOM oxidation starts to take place giving rise to a relevant improvement of SO_2 absorption followed by an intense acidification of the solution. This result is consistent with the observed greenish color of the absorbing solution from the very beginning of the absorption tests. The same behavior was also observed in **Figure IV.27B** starting from a solution pH equal to 6, but in this case the absorption capacities of SW decreased while those of the two SWC solutions remained high. Experimental pH measurements, aimed at confirming the rapid evolution of the solution pH during the tests carried out with sodium chlorite addition in the feed-batch column, were not possible. However, the simulations allowed to overcome this lack by providing a behavior consistent with the one experimentally observed. **Figure IV.27C** showed the absence of the buffer effect of alkalinity and a low sulphur absorption in SW at pH = 3, while a considerable amount of sulphur could be absorbed with SWC solutions even at very acidic pH. The trends of the solution pH suggested that the absorption with the chlorite solutions evolved independently on the alkaline content (see **Figure IV.27**). Thanks to the onset of AOM phenomena, the solubility of SO_2 in SWC0.1 and SWC0.2 was almost independent on the initial solution pH.

IV.5.2.2. Packed column tests

The experimental results on SO_2 removal efficiency (η_{SO_2}) and the wash water pH value obtained in the packed tower tests are shown in **Table IV.24** as a function of the liquid-gas volumetric ratio (L/G) and parametric with the scrubbing solution used and with the concentration of SO_2 in the gas fed to the column.

Table IV.24. *Experimental results of SO_2 removal efficiency and wash water pH solution for a simulated flue-gas (32 $m^3 \cdot h^{-1}$) contained 500, 1000 and 2000 ppm_v of SO_2 at 1 atm and 60 °C, for different liquid-gas ratio (from 1.25 to 4.06 $L \cdot m^{-3}$) and using three different scrubbing solutions (SW, SWC0.1 and SWC0.2) at 25 °C with their natural initial pH and after acidification until 6 and 3*

	Solution pH non-altered value	***Solution pH 6***	***Solution pH 3***

Solution	G fed	C_{SO_2} fed	L/G fed	η_{SO_2}	Final pH	η_{SO_2}	Final pH	η_{SO_2}	Final pH
	m^3/h	ppm_v	L/m^3	-	-	-	-	-	-
SW	32	500	1.25	71.6%	3.64	18.6%	2.42	12.4%	2.20
			2.19	88.8%	5.62	32.8%	2.45	22.6%	2.15
			3.12	95.8%	6.15	44.2%	2.51	31.6%	2.18
			4.06	98.2%	6.35	50.2%	2.63	38.1%	2.22
		1000	1.25	44.1%	2.64	16.7%	2.22	9.1%	2.01
			2.19	73.8%	2.92	27.3%	2.32	19.5%	2.05
			3.12	91.5%	4.25	34.6%	2.35	21.2%	2.10
			4.06	96.5%	5.20	41.7%	2.65	28.8%	2.05
		2000	1.25	27.7%	2.22	14.5%	2.15	6.5%	1.95
			2.19	47.8%	2.45	22.1%	2.20	8.9%	1.99
			3.12	66.3%	2.38	27.5%	2.24	11.1%	2.03
			4.06	77.7%	2.65	34.2%	2.45	18.1%	1.95
SWC0.1	32	500	1.25	87.1%	2.45	85.6%	2.45	79.8%	2.35
			2.19	99.9%	3.68	99.1%	2.21	97.2%	2.15
			3.12	99.9%	4.92	99.9%	2.95	99.9%	2.22
			4.06	99.9%	5.95	99.9%	4.15	99.9%	2.25
		1000	1.25	55.1%	2.62	53.6%	2.45	51.7%	2.05
			2.19	78.5%	2.36	77.4%	2.48	75.2%	1.99
			3.12	97.5%	2.14	96.6%	2.25	93.8%	2.05
			4.06	99.9%	2.22	99.9%	2.32	99.9%	2.02
		2000	1.25	32.1%	1.87	31.1%	1.96	30.2%	1.68
			2.19	54.5%	1.82	51.7%	1.85	50.4%	1.75
			3.12	73.1%	1.84	70.4%	1.85	68.9%	1.75
			4.06	84.5%	1.92	82.6%	1.94	82.9%	1.74
SWC0.2	32	500	1.25	97.1%	4.32	94.4%	2.55	91.8%	2.05
			2.19	99.9%	4.75	96.2%	2.65	99.9%	2.15
			3.12	99.9%	5.26	98.9%	2.95	99.9%	2.2
			4.06	99.9%	6.05	99.9%	4.12	99.9%	2.05
		1000	1.25	74.5%	2.13	71.1%	2.05	67.2%	1.72
			2.19	98.1%	2.04	96.2%	2.45	94.1%	1.65
			3.12	99.3%	2.65	98.9%	1.95	97.8%	1.75
			4.06	99.9%	4.45	99.9%	2.25	99.9%	1.75
		2000	1.25	41.1%	1.54	39.9%	1.55	38.6%	1.31
			2.19	69.9%	1.55	68.4%	1.45	66.8%	1.35
			3.12	89.2%	1.45	87.9%	1.43	86.1%	1.36
			4.06	98.8%	1.78	98.2%	1.48	96.8%	1.25

Table IV.24 shows that, for SWC0.1 solution at non-altered pH, an almost complete SO_2 removal was achieved with a *L/G* = 2.19 $L \cdot m^{-3}$ at 500 ppm_v and a *L/G* = 3.12 $L \cdot m^{-3}$ for 1000 ppm_v. Differently, for 2000 ppm_v, the highest removal efficiency recorded was 84% achieved with 4.06 $L \cdot m^{-3}$. It is worth noting that the SO_2 capture of SWC0.1 solution (pH = 8.33) resulted slightly higher than that of SW (pH = 8.20), showing that absorption is fastened by the $S_{(IV)}$ ions oxidation determined by the chlorite. The removal efficiencies obtained for SWC0.2 (pH = 8.55) were far higher in each test, and a complete removal of sulphur dioxide was achieved with a water saving greater than 70% at 500 ppm_v and 50% at 1000 ppm_v if compared to SW. For 2000 ppm_v tests, it was possible to reach a 98.8% SO_2 capture with the maximum value of *L/G* (4.06 $L \cdot m^{-3}$). These results confirmed that SO_2 absorption was enhanced by an increase in sodium chlorite dosage.

The water-savings obtained with SWC0.2 solution could be associated also with a cost-saving in equipment, *i.e.* pumps, nozzles and pipe-lines, and a further energy saving related to pumping costs could be also considered (cost assessments and equations are reported in **Flagiello et al.** [43]). This result would also allow to sustain the costs related to the consumption of the oxidizing reagent compared to the use of a traditional seawater scrubber.

The results of the tests carried out with acidified SWC solutions at initial pH 6 and 3 in **Table IV.24** showed a partial reduction in the efficiencies that were still high though, while for SW solutions they collapsed dramatically due to the effect of the initial acidification that consumed the alkalinity responsible of absorption. As for the results of the equilibrium tests, also the absorption efficiency using SWC solutions in the packed tower resulted scarcely dependent on the actual content of alkalinity and initial solution pH.

During the dynamic tests with SWC solutions at non-altered pH, it was observed that the scrubbing solution rapidly became yellowish and then greenish flowing along the column, as a consequence of the rapid absorption occurring and of the parallel acidification of the solution itself. A similar result was observed in former works available in the literature ([65], [72], [106], [108], [111]). In all the experiments, the color shift of the liquid occurred between 0.1 - 0.4 meters from the top of the column.

The experimental results in packed tower can be reported also in terms of SO_2 removal efficiency as a function of the ratio between the mole of HCO_3^- and $SO_{2(g)}$ fed in the column ($d_{b/s}$) for SW (**IV.28A**), and moles of ClO_2^- on $SO_{2(g)}$ ($d_{c/s}$) for the SWC0.1 and SWC0.2 scrubbing solutions (**IV.28B**), as shown in **Figure IV.28**. The results are shown parametrically with the initial pH of the scrubbing solutions.

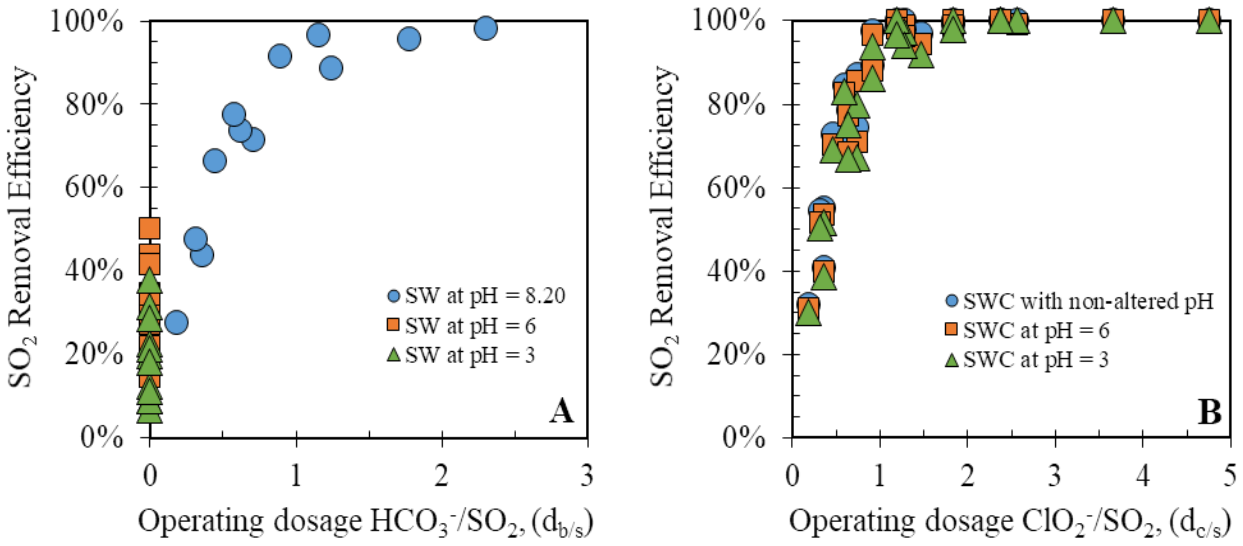

Figure IV.28. *Experimental results of SO_2 removal efficiency for a simulated flue-gas (32 $m^3 \cdot h^{-1}$) contained 500, 1000 and 2000 ppm_v of SO_2 at 1 atm and 60 °C, for different liquid-gas ratio (from 1.25 to 4.06 $L \cdot m^{-3}$) and using three different scrubbing solutions (SW, SWC0.1 and SWC0.2) at 25 °C*

with their natural initial pH and after acidification until 6 and 3. The removal efficiencies were a function of the ratio between the total dosage of the alkalinity in SW solution expressed as HCO_3^- moles and the SO_2 moles in the feed gas (A) or the ratio between the dosage of ClO_2^- moles in both SWC solutions and the SO_2 moles in the feed gas (B)

Figure IV.28 clearly indicated that, in order to achieve a removal efficiency higher than 95%, the total dosage of alkalinity and chlorite in solution should be higher than 1.3 and 1.1 times the moles of SO_2 fed in the column, respectively, regardless the initial solution pH. The only exception is for for SW solution, where the preliminary acidification at pH equal to 6 and 3 dampened the buffering effect of HCO_3^- until it was negligible and reduced its ability to capture SO_2. In light of these results and also considering the equilibrium data, chlorite and bicarbonates did not give rise to additive absorption capacity, but they rather operate in a series/parallel network of reactions as those reported in **Eqs. (10)-(12),(17)-(19),(79)-(80),(83)-(84)**.

Before proceeding with the analysis of data, it is worth remembering that the absorption efficiency of a packed column can be correlated to the resolution of the following equation for absorber design (182). For sulphur dioxide absorption in alkaline water, *i.e.* seawater, the enhancement factor (E_L.) is regulated by diffusional mechanisms (E_∞) and can be calculated by **Eq. (106)**, as suggested in **Flagiello et al.** [43].

The comparison between SW and SWC0.1 with non-altered pH showed a very similar solubility curve (**Figure IV.26A**–**B**); therefore, in order to have a similar efficiency with the same column height, a similar value of $K_{OG}a_e$ is needed. This means that also the enhancement factor should be similar for both the reacting systems. Therefore, the experiments suggested that the oxidation reactions are at least as fast as the SO_2 hydrolysis reactions, so that the enhancement factor is still controlled by the interfacial diffusion, similar to the case of hydrolysis in alkaline solutions. The comparable values of seawater alkalinity (equivalent to 193 $\mu mol \cdot mol^{-1}$) and chlorite concentration in SWC0.1 (199 $\mu mol \cdot mol^{-1}$) allowed explaining the similarity of the observed results. Of course, when the chlorite content is higher, the higher solubility and the higher enhancement factors (E_L) led to an increase in the absorption efficiency.

The experimental data were compared with the simulations performed with ASPEN PLUS® using the equilibrium model described before. To complete the input data, the following models specifications were selected from the ASPEN PLUS® database:

- Counter-current flow model;
- **Billet and Schultes** [143] mass transfer model with calibrated model parameters [221] adapted for M250.X packing (C_G = 0.564 and C_L = 0.967);

- Pressure drop data for M250.X packing were imported (See **Figure IV.7**);
- **Taylor and Krishna** [208] heat transfer model.

The SO_2 removal efficiency and wash water pH obtained from ASPEN PLUS® simulations are reported in **Figure IV.29** as parity plots, corresponding to all the experimental data collected at different SO_2 concentrations, *L/G* ratios and type of scrubbing solutions with their initial pH.

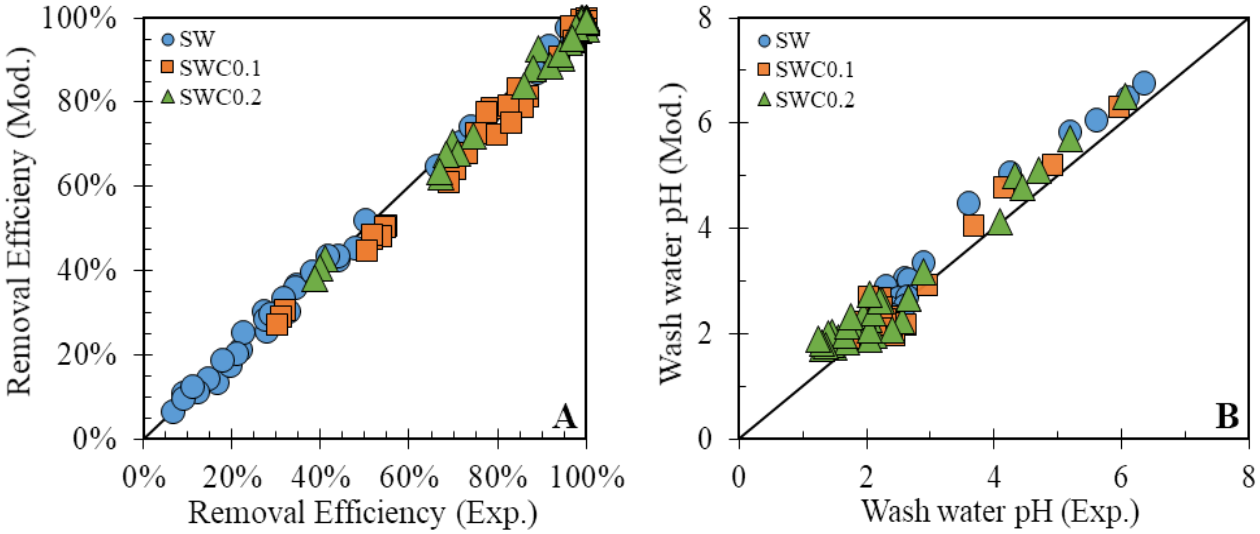

Figure IV.29. *Experimental and modelling results of SO_2 removal efficiency (A) and wash water pH solutions (B) for a simulated flue-gas (32 $m^3 \cdot h^{-1}$) contained 500, 1000 and 2000 ppm_v of SO_2 at 1 atm and 60 °C, for different liquid-gas ratio (from 1.25 to 4.06 $L \cdot m^{-3}$) and using three different scrubbing solutions (SW, SWC0.1 and SWC0.2) at 25 °C with their natural initial pH and after acidification until 6 and 3*

The model results satisfactorily predicted the experimental data for all the investigated conditions, confirming that the integration of appropriate mass transfer and equilibrium models allows an accurate prediction of oxidative scrubbing phenomena with ASPEN PLUS®.

Figure IV.30 shows the modelling profiles of SO_2 mole fraction in the gas stream and of the main species responsible for hydrolysis and oxidation, such as bicarbonates and chlorites, in the liquid stream from the top to the bottom, together with the pH trend, for the two SWC solutions at pH = 8.33 and 8.55. Two case studies that can best represent the oxidative process with the two different SWC solutions were selected and simulated in the Rate-based block of ASPEN PLUS®.

1. Operating dosage, $d_{c/s} < 1.1$:

   (A) SWC0.1; G= 32 $m^3 \cdot h^{-1}$ (60 °C); L= 100 $L \cdot h^{-1}$ (25 °C); $C_{SO_{2(g)}}$= 2000 ppm_v;

   (B) SWC0.2; G= 32 $m^3 \cdot h^{-1}$ (60 °C); L= 40 $L \cdot h^{-1}$ (25 °C); $C_{SO_{2(g)}}$= 1000 ppm_v.

2. Operating dosage, $d_{c/s} > 1.1$:

(C) SWC0.1; G= 32 $m^3 \cdot h^{-1}$ (60 °C); L= 70 $L \cdot h^{-1}$ (25 °C); $C_{SO_{2(g)}}$= 500 ppm_v;

(D) SWC0.2; G= 32 $m^3 \cdot h^{-1}$ (60 °C); L= 100 $L \cdot h^{-1}$ (60 °C); $C_{SO_{2(g)}}$= 1000 ppm_v.

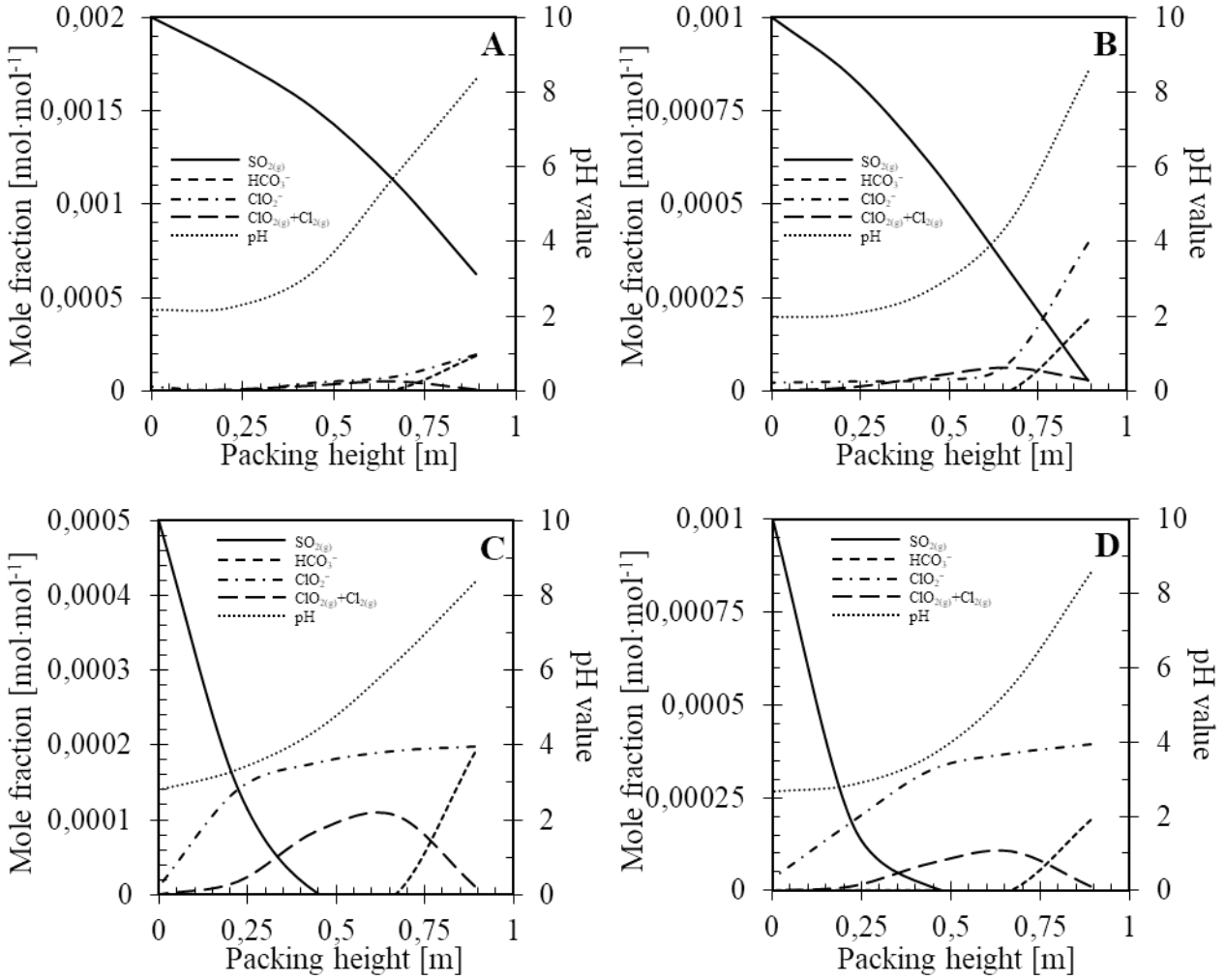

Figure IV.30. *ASPEN PLUS® modelling profiles of SO_2 mole fraction in the gas stream from the bottom (0 m) to the top of the column (0.892 m) and bicarbonates, chlorites and pH trend in the liquid stream from the top to the bottom, for the two SWC solutions at non-altered pH (8.33 and 8.55). Simulation data for four case studies (A-D) were reported above*

The simulations in **Figure IV.30** show a decreasing trend of $SO_{2(g)}$ along the column together with the ClO_2^-, which reacts in the liquid phase, as expected. Furthermore, a rapid acidification between pH = 3 - 5 was observed starting from the top of the column in the height range 0.680 - 0.892 m, which was consistent with the experimental observations about the rapid coloring of the liquid to yellowish and then greenish mentioned above. The simulation data also validated the hypothesis that, under acid conditions, the process is controlled by the oxidative mechanisms and that $SO_{2(aq)}$ is oxidized to $S_{(VI)}$ by reactions with $ClO_{2(aq)}$ and $Cl_{2(aq)}$ (**Eqs. (79)-(80),(89)-(90),(83)-(84)**). The

simulations also correctly predicted the trend of the solution alkalinity represented as HCO_3^- in the two different cases reported:

- When $d_{c/s}$ was less than 1.1 (**Figure IV.30A**–**B**), the consumption of HCO_3^- can be related to the $SO_{2(g)}$ hydrolysis products **Eqs. (10)-(12),(17)-(19)** at the top of the column, where the pH > 6;

- When $d_{c/s}$ was greater than 1.1 (**Figure IV.30C**–**D**), at the top of the column, $SO_{2(g)}$ was already completely captured but a rapid consumption of HCO_3^- was observed, which in this case can be attributed to the reactions with the $Cl_{2(aq)}$ and $ClO_{2(aq)}$ species in aqueous phase. These species first desorb from the acid liquid stream at pH < 6 (after dismutation reactions in **Eqs. (79)-(80),(93)-(94)**) at the bottom of the column and afterwards absorb in the liquid again at the top of the column by **Eqs. (93)-(94)** and react in water according to **Eqs. (89)-(90)** at pH > 6.

IV.5.3. Highlights

In this activity, a study on SO_2 solubilities in two different seawater solutions doped with $NaClO_2$ performed in the feed-batch bubble column and the evaluation of the performance of SO_2 removal in the packed column using the wet oxidation process (with the same two $NaClO_2$ solutions previously tested) was carried out. This work also contains an absorption data modelling section performed in ASPEN PLUS®. The main findings of this work can be summarized as follows:

- The seawater solution doped with 0.2% w/w of $NaClO_2$ was able to absorb as much as 290 $\mu mol \cdot mol^{-1}$ SO_2 for a partial pressure in the gas phase as small as 0.01 kPa. For the 0.1% w/w doped solution, this value was 220 $\mu mol \cdot mol^{-1}$, resulting very similar to the pure seawater. It was interesting to note that the alkaline and chlorite contents in SWC0.1 were practically equal (193 $\mu mol \cdot mol^{-1}$ and 199 $\mu mol \cdot mol^{-1}$, respectively) and the effect of chlorite was just the oxidation of the already solubilized $S_{(IV)}$ ions, formed by SO_2 hydrolysis (**Eqs. (10)-(12),(17)-(19)**), to $S_{(VI)}$ ions.
- The SO_2 absorption process with $NaClO_2$ was controlled by an *Acidic Oxidation Mechanism* (AOM). This was confirmed by the marked change of the color of the solution during the tests: the solution is initially yellowish, as soon as an acid pH is established (after 10 - 20 seconds testing), ClO_2 and Cl_2 are formed and the solution became greenish. Finally, the solution progressively yellowed and then became transparent when ClO_2 and Cl_2 are consumed. Furthermore, the wash water pH for the $NaClO_2$ solutions were almost constant and equal to about 1.5 - 2.5.

- The ASPEN PLUS® simulations in the Flash block aimed to describe all the solubility data and provided a good description of experiments using the AOM described by the **Eqs. (10)-(12),(17)-(19),(79)-(80),(83)-(84)**.
- When the SO_2 was 500 ppm_v, a 98% of removal efficiency in packed tower was achieved with pure seawater at 4.06 $L \cdot m^{-3}$, a water-saving > 48% was reached with SWC0.1, and this saving became > 70% SWC0.2.

  For 1000 ppm_v SO_2 concentration, a 97% of removal efficiency in packed tower was achieved with pure seawater at 4.06 $L \cdot m^{-3}$, a water-saving of 23% was reached with SWC0.1, and this saving became > 70% with SWC0.2.

  For 2000 ppm_v SO_2 concentration, only with SWC0.2 it was possible to reach a complete removal in packed tower at 4.06 $L \cdot m^{-3}$, while for SWC0.1 and SW solutions, the maximum removal efficiencies were 84 and 78%, respectively.

  SWC solutions were able to provide an effective absorption also at acid pH, when the hydrolysis effects became negligible, thanks to the onset of *Acidic Oxidation Mechanisms* (AOM) and, in very acidic conditions, also for the establishment of a *Gaseous Oxidation Mechanisms* (GOM), while for SW solutions the absorption performance dropped down dramatically at low pH. The oxidation was as fast as the hydrolysis reactions, providing to achieve removal efficiencies at a rate similar to those observed for seawater also at low pH: this suggested a diffusional control behavior for the chemical absorption at the liquid gas interface.
- In conclusion, the absorption efficiency using SWC solutions in the packed tower resulted scarcely dependent on the actual content of alkalinity and initial solution pH and molar dosage of sodium chlorite as about 1.1 times higher than SO_2 moles in the gas fed was and it was sufficient to obtain a complete removal in the investigated conditions.
- The ASPEN PLUS® simulations adopting the Rate-based block, once properly integrated with the appropriate equilibrium and mass transfer models, is able to provide a very excellent prediction of experimental results with a determination coefficient (R^2) equal to 0.99 for removal efficiencies prediction and 0.91 for wash water pH prediction. Furthermore, the model allows a prediction of the trends of the main species, both in gas and liquid streams, along the column and also the solution pH. Therefore, the simulations could allow to effectively design a wet oxidation unit for large scale applications.

IV.6. Wet oxidation scrubbing effect on NO_x emissions using seawater-based solutions enhanced with $NaClO_2$

This section reports the data of the tests carried out in the packed column aimed at evaluating the performance of the oxidative scrubbing with chlorite solutions on the removal of NO_x.

After the successful tests on SO_2 removal, the wet oxidation scrubbing was also tested for a gas stream polluted with NO_x, which are scarcely soluble in water or alkaline solutions. The theory of oxidative absorption reported in **Section II.2.** indicated that the capture of NO_x increased with the addition of sodium chlorite. The scope of this activity is to verify if an effective oxidative scrubbing can be used in typical conditions for gas cleaning processes.

The experiments were performed at 1 atm on a simulated flue-gas fed in the packed column described in the **Section III.2.2.**, using a constant gas flow rate, four liquid flow rates and five different scrubbing liquids: four sodium chlorite seawater solutions from 0.25 to 1% w/w and pure seawater, used as a benchmark. The effect of the gas temperature and the initial pH of the liquid on the NO_x removal efficiency were investigated as well.

IV.6.1. Operating conditions

Table IV.25 reports the operating conditions adopted in this set of experiments.

Table IV.25. *Operating conditions adopted for the experiments of NO_x removal in the packed column*

Scrubbing Solutions	***G*** $m^3 \cdot h^{-1}$	T_G *°C*	***L*** $L \cdot h^{-1}$	T_L *°C*	***pH*** -	$C^{\circ}_{NO_x}$ ppm_v
SW	32	25, 40, 60	40, 70, 100, 130	25	8.20	1030
SWC0.25	32	25, 40, 60	40, 70, 100, 130	25	8.56	1030
SWC0.5	32	25, 40, 60	40, 70, 100, 130	25	8.96	1030
SWC0.75	32	25, 40, 60	40, 70, 100, 130	25	9.17	1030
SWC1.0	32	25, 40, 60	40, 70, 100, 130	25	9.40, 6, 3	1030

Further details on the physical-chemical composition of the liquids used are reported in **Section III.1.1.** and **III.2.1.**.

IV.6.2. Results and discussion

Figure IV.31 shown the experimental removal efficiencies of total NO_x (**A**) and the final wash water pH (**B**) for a simulated flue-gas containing 1030 ppm_v of NO_x at 25 °C and using sodium chlorite

solutions at different weight fractions at 25 °C. The results are shown parametrically with the liquid-gas volumetric ratios, varied between 1.25 and 4.06 $L \cdot m^{-3}$.

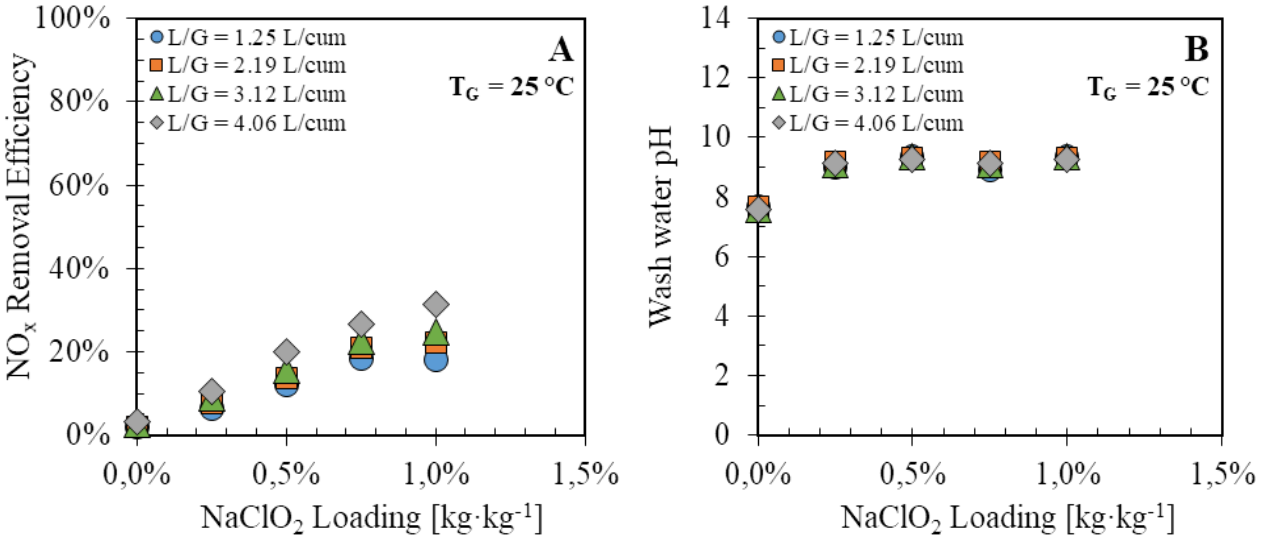

Figure IV.31. *Experimental results of total NO_x removal efficiency (A) and wash water pH solutions (B) for a simulated flue-gas (32 $m^3 \cdot h^{-1}$) containing 1030 ppm_v of NO_x at 1 atm and 25 °C, for different liquid-gas ratio (from 1.25 to 4.06 $L \cdot m^{-3}$) and using five different scrubbing solutions at 25 °C: seawater at pH 8.2 (SW); four seawater solutions containing from 0.25 to 1% w/w of $NaClO_2$ at pH from 8.56 to 9.4*

Figures IV.31A shows that the NO_x removal efficiency in pure seawater is very low (about 1 - 3%), consistently with the theory reported in the **Section II.1.** and with the experiments reported in the previous **Section IV.4.3.1.**. This was due to the low solubility of NO and NO_2 in water and to the very slow hydrolysis reactions (see **Section II.1.**). On the contrary, the total NO_x removal efficiency increased up to 31% by increasing the $NaClO_2$ content A slight influence of the liquid flow rate (or *L/G* ratios) was observed under these operating conditions, with effects more pronounced for *L/G* = 4.06 $L \cdot m^{-3}$.

Figure IV.31B showed that the final pH in the wash water solutions were negligibly affected by the *L/G* ratio. Besides, both the seawater and the chlorite solutions exploited a final pH very close to the initial values. While for the seawater no absorption take place and, thus, the preservation of pH is expected, for chlorite solutions, this observation confirms that the reaction between chlorite and NO and NO_2 in the aqueous phase occurred without altering the solution pH, according to the *Basic Oxidation Mechanism*, BOM, (**Eqs. (74)-(76)**).

Further tests were performed under the same operating conditions but varying the gas temperature alternatively at 40 and 60 °C, and the results in terms of NO_x removal efficiency and wash water pH solutions are shown in **Figure IV.32**.

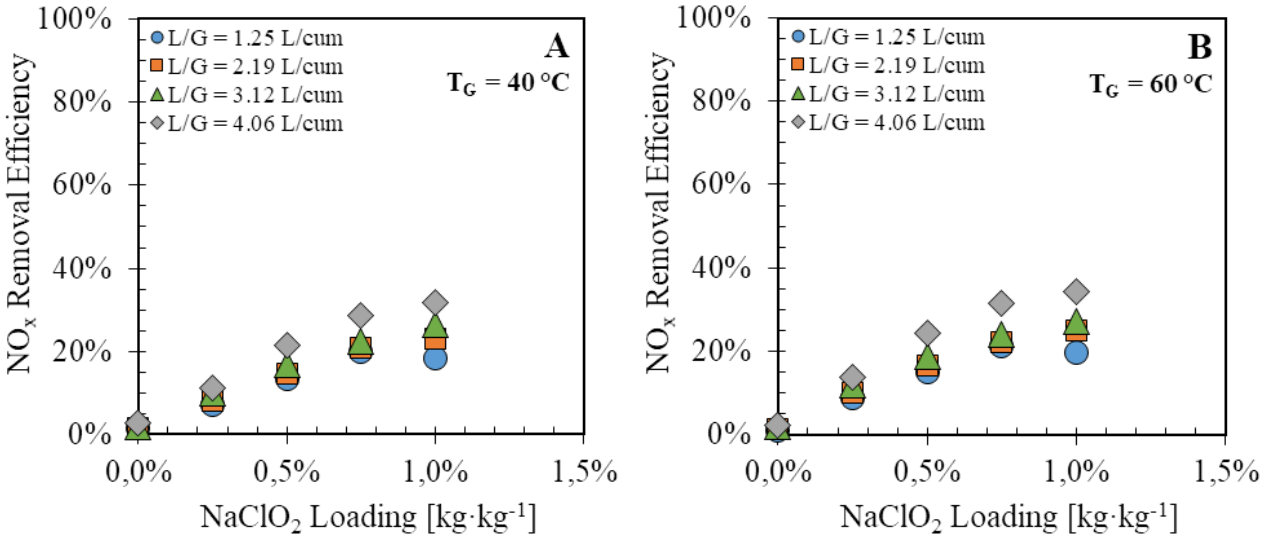

Figure IV.32. *Experimental results of total NO_x removal efficiency at 40 °C (A) and 60 °C (B) for a simulated flue-gas (32 $m^3 \cdot h^{-1}$) containing 1030 ppm_v of NO_x at 1 atm, for different liquid-gas ratio (from 1.25 to 4.06 $L \cdot m^{-3}$) and using five different scrubbing solutions at 25 °C: seawater at pH 8.2 (SW); four seawater solutions containing from 0.25 to 1% w/w of $NaClO_2$ at pH from 8.56 to 9.4*

In the investigated conditions, the removal efficiencies were very similar for all the tested temperatures, as shown in **Figure IV.31A** and **Figures IV.32A**–**B**. Similarly to the findings described in **Section IV.5.**, this result can be ascribed to the low alteration of liquid (and thus interface) temperature, which reached a maximum of 28°C due to the adopted *L/G* ratio and for the low heat of absorption of NO_x species.

The **Figure IV.33** shows the experimental correlation between NO_x removal efficiency and the ratio between moles of ClO_2^- and $NO_{x(g)}$ fed in the column ($d_{c/n}$). The results are shown parametrically with the temperature of the gas and contains all data with different $NaClO_2$ contents.

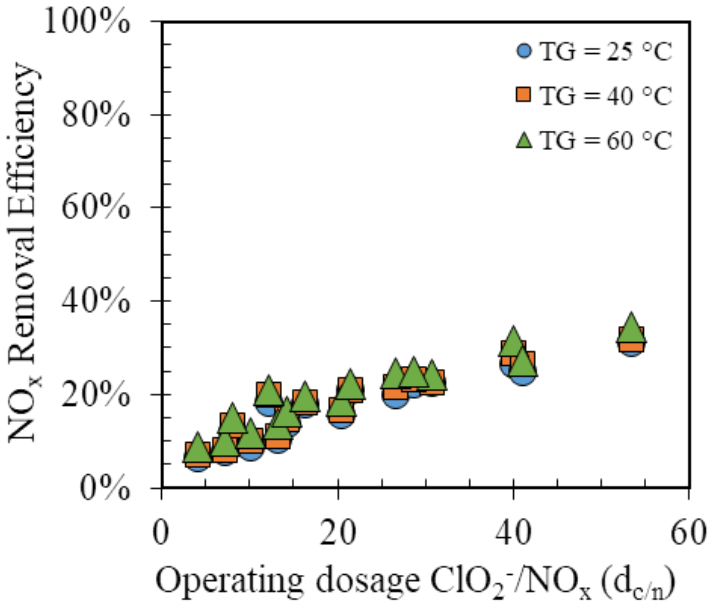

Figure IV.33. *Experimental results of NO_x removal efficiency for a simulated flue-gas (32 $m^3 \cdot h^{-1}$) containing 1030 ppm_v of NO_x at 1 atm, for different liquid-gas ratio (from 1.25 to 4.06 $L \cdot m^{-3}$) and using four different scrubbing solutions (SWC0.25, SCWC0.5,SWC0.75 and SWC1.0) at 25 °C with their non-altered initial pH. The removal efficiencies were a function of the ratio between the dosage of ClO_2^- moles in the SWC solutions and the NO_x moles in the feed gas. The results were shown parametrically with the temperature of gas fed (25, 40 and 60 °C)*

Figure IV.33 shows that, although the addition of sodium chlorite improved the NO_x removal efficiency, a larger sodium chlorite concentration is needed to reach high removal efficiency. Indeed, the maximum removal achieved (34%) required a quantity of sodium chlorite about 53 times greater than the NO_x molar fed. This value was far higher than the dosage needed for desulphurization (**Section IV.5.**) and confirmed that the NO_x oxidation reactions were much slower.

Further experiments were performed at different initial pH of the scrubbing solutions. In this new set of experiments, $NaClO_2$ concentration was kept at 1% w/w. To this aim, **Figure IV.34** shows the experimental removal efficiencies of total NO_x (**A**) and final wash water pH solutions (**B**) for a simulated flue-gas containing 1030 ppm_v of NO_x at gas and liquid inlet temperature of 25 °C. The results were parametric with the liquid flow rates, *i.e.* with liquid-gas volumetric ratios (1.25 - 4.06 $L \cdot m^{-3}$).

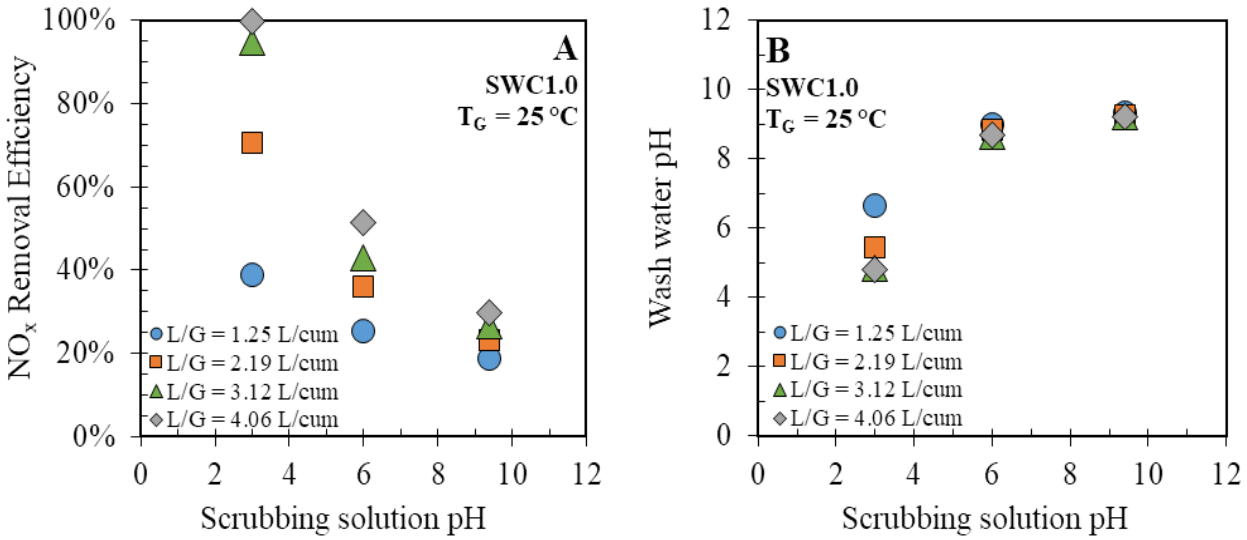

Figure IV.34. *Experimental results of total NO_x removal efficiency (A) and wash water pH solutions (B) for a simulated flue-gas (32 $m^3 \cdot h^{-1}$) containing 1030 ppm_v of NO_x at 1 atm, for different liquid-gas ratio (from 1.25 to 4.06 $L \cdot m^{-3}$) and using the seawater solution with $NaClO_2$ at 1% w/w (SWC1.0) at 25 °C and different initial pH: 9.4, 6 and 3*

The results in **Figure IV.34A** indicated a marked increase in total NO_x removal efficiency when the starting pH of the solution was decreased to 6 and, more, to 3. This result confirms that the acid oxidation mechanism was more effective than the neutral or basic ones (see **Figures IV.31**–**32**). Under acidic conditions, the formation of $ClO_{2(aq)}$ and $Cl_{2(aq)}$ (**Eqs. (79)-(80)**) and the activation of the *Acidic Oxidation Mechanism* (AOM) occurred (**Eqs. (79)-(80),(85)-(88)**). The presence of chlorine dioxide and chlorine were also confirmed by a greenish color of the solution when the pH was modified at 6 and 3, and a pungent odor arose. In this case, it is believed that the AOM mechanism could already act from the top of the column when the SWC1.0 solution was acidified.

The increase in NO_x removal was strongly influenced by the liquid-gas ratio (*L/G*) and a complete removal of NO_x could be achieved with a *L/G* = 4.06 $L \cdot m^{-3}$ when the scrubbing liquid pH was decreased to 3. Even at *L/G* = 1.25 $L \cdot m^{-3}$ a removal efficiency of about 40% (around 25% greater than the tests with non-acidified solutions) was observed.

Figure IV.34B showed a decrease of wash water pH down to 5 - 7 with the decrease of the initial pH of the $NaClO_2$ solution. It is worth noticing that the final pH values are higher than the initial values and this could be ascribed to the H_3O^+ consumption required to catalyze the chlorite decomposition into $ClO_{2(aq)}$ and $Cl_{2(aq)}$ (**Eqs. (79)-(80)**). In addition, for the solutions at initial pH = 9.4 and 6 it must be considered that, unlike the absorption of SO_2 where the hydrolysis reactions acidify the liquid to trigger the *Acidic Oxidation Mechanism*, the residual alkalinity was not consumed by the NO_x hydrolysis and the pH remained almost unvaried.

The effect of gas temperature was considered with tests carried out under the same conditions shown above (**Figure IV.34**) but with different gas temperatures (40 to 60 °C), and the results are reported in **Figure IV.35**.

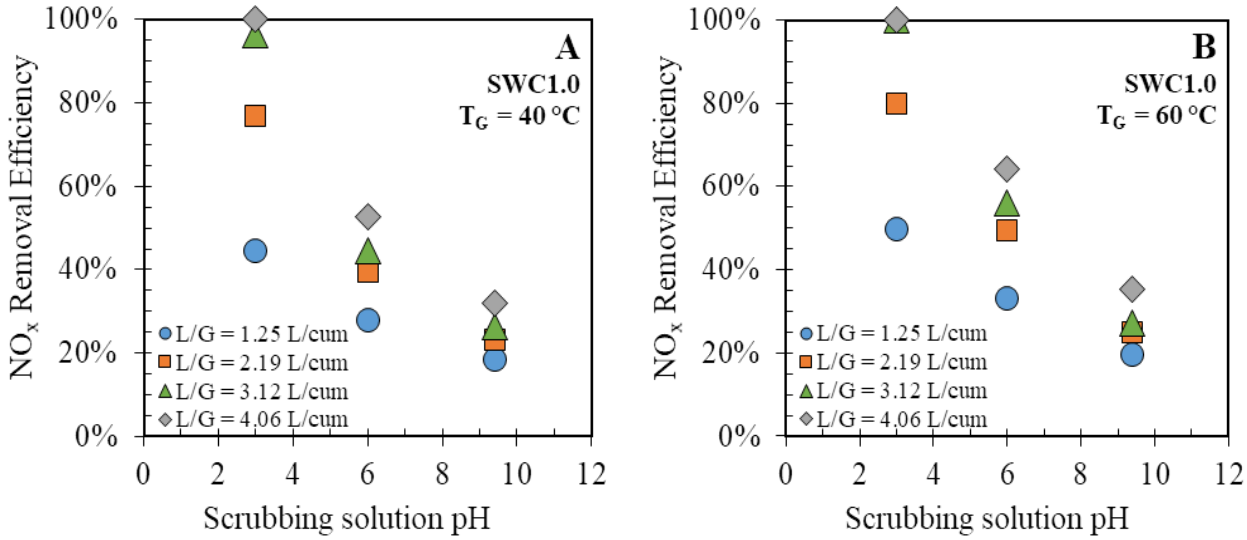

Figure IV.35. *Experimental results of total NO_x removal efficiency at 40 °C (A) and 60 °C (B) for a simulated flue-gas (32 $m^3 \cdot h^{-1}$) containing 1030 ppm_v of NO_x at 1 atm, for different liquid-gas ratio (from 1.25 to 4.06 $L \cdot m^{-3}$) and using the seawater solution with $NaClO_2$ at 1% w/w (SWC1.0) at 25°C and different initial pH: 9.4, 6 and 3*

Figure IV.35 showed that the increase in gas temperature provided an improvement in the NO_x capture efficiency and this effect was more pronounced at 60 °C. The beneficial effect of the temperature probably indicated a kinetic control mechanisms (GOM) in the oxidative scrubbing of NO_x, that probably occurred in the gas phase involving NO_x and Cl_2 and ClO_2 desorbed from the liquid surface (**Eqs. (93)-(100)**) as suggest by **Park et al.** [72] and **Hao et al.** [111]

The **Figure IV.36** shows a new correlation between NO_x removal efficiency and the ratio between the moles of ClO_2^- and $NO_{x(g)}$ fed in the column ($d_{c/n}$). The results are shown parametrically with initial pH of SWC1.0 (9.4, 6 and 3) and they are shown only for a gas temperature of 60 °C, which had a more pronounced effect on the removal efficiencies compared to 25 and 40 °C.

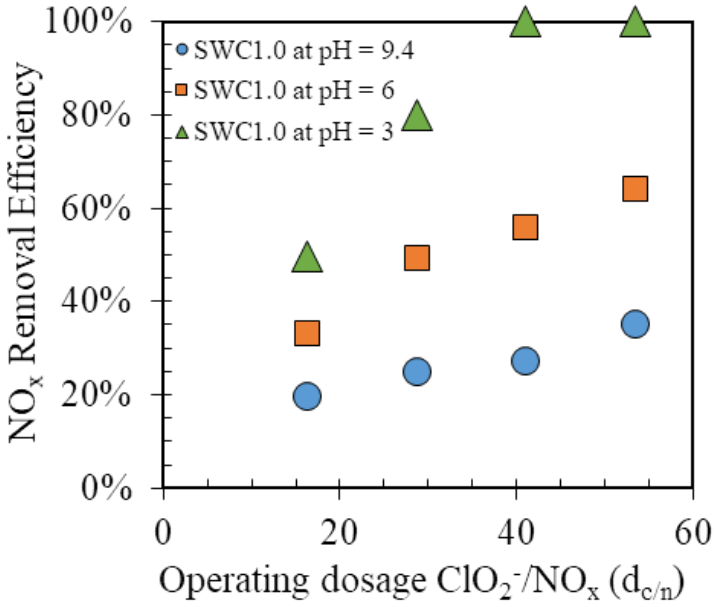

Figure IV.36. *Experimental results of NO_x removal efficiency for a simulated flue-gas (32 $m^3 \cdot h^{-1}$) containing 1030 ppm_v of NO_x at 1 atm and 60 °C, for different liquid-gas ratio (from 1.25 to 4.06 $L \cdot m^{-3}$) and using seawater solution with 1% w/w of $NaClO_2$ (SWC1.0) at 25 °C with their natural initial pH and after acidification until 6 and 3. The removal efficiencies were a function of the ratio between the dosage of ClO_2^- moles in the SWC1.0 solution and the NO_x moles in the feed gas. The results were shown parametrically with the initial pH of SWC1.0 solution (9.4, 6 and 3)*

The results suggested that the molar dosage of ClO_2^- required for a complete removal was approximately 40 times greater than the moles of NO_x fed when SWC solutions are acidified up to the pH value = 3. Differently, only 55% efficiency was achieved for the same chlorite dosage but at pH = 6. In general, an improvement of about 60 - 72% in capture performances was observed when the pH decreased from 9.4 to 3.

Although the chlorite dosage was always much greater than that required in the case of desulphurization, in which $d_{c/s} \sim 1.1$ (**Section IV.5**), in this case, the amount of oxidant allowed a complete removal of NO_x and also a saving of about 20% compared to the results reported in **Figure IV.33**.

IV.6.3. Highlights

This work aimed to evaluate the oxidative abilities of sodium chlorite on NO_x which are generally not very soluble in water using the packed column with a model flue-gas containing 1030 ppm_v of NO_x. The $NaClO_2$ was added to a seawater, with a dosage from 0 to 1% w/w (SW and SWC solutions). The main findings of this work can be summarized as follows:

- The use of $NaClO_2$ allowed to reach up to a complete removal of 1030 ppmv of NO_x, compared to the use of a pure seawater, for which the removal efficiencies were very low.
- The maximum NO_x capture was 31% using SWC1.0 at pH = 9.4 and 4.06 $L \cdot m^{-3}$, with a gas temperature equal to 25 °C. Only a slight improvement was observed by increasing the gas temperature, which allowed a maximum removal of 34%. In general, no improvement could be attributed to gas temperature increase. When the wash water pH was greater than 7, it was confirmed that only reactions under basic conditions, BOM (**Eqs. (74)-(76)**), occurred
- When the SWC1.0 was acidified to 3, the total oxidation performance improved until the complete NOx removal. These results confirmed the activation of a further oxidation mechanism that occurs only under acidic conditions (AOM) with the formation of additional oxidants, such as Cl_2 and ClO_2 (**Eqs. (79)-(80),(85)-(88)**). Probably, another oxidation mechanism, GOM (**Eqs. (93)-(100)**) in gas phase also occurred.
- For SWC1.0 at pH = 3 and for a gas temperature of 60° C, a molar dosage of ClO_2^- about 40 times higher than NO_x moles was needed. The operating dosage ($d_{c/n}$), *i.e.* the ratio between ClO_2^- and $NO_{x(g)}$ fed, was approximately 90 times the stoichiometric ratio (ClO_2^-/NO_x) evaluated by the reactions in AOM and GOM (**Eqs. (79)-(80),(85)-(88),(93)-(100)**). Interestingly, this ratio value indicated a large excess of chlorite for acid mechanism reactions, whereas for the desulphurization (**Section IV.5**) only a slight excess of chlorite was required for a complete removal of SO_2. These evaluations suggested that the NO_x oxidation reactions were much slower than those SO_2.

IV.7. Simultaneous SO_2 and NO_x removal by wet oxidation scrubbing using seawater-based solutions enhanced with $NaClO_2$

In light of the results of **Section IV.5.** and **Section IV.6.**, a new set of experiment was performed to analyze the simultaneous capture of SO_2 and NO_x from a model flue-gas. Indeed, experiments in the **Section IV.6** suggested that SO_2 might help producing a natural acidification of the liquid, thus activating further oxidative mechanisms and improving the NO_x capture performance. However, a competitive oxidation effect must be considered. The results presented in this section are only part of a more extensive activity, which allowed to apply for a patent still under evaluation.

The experiments were performed in the packed column setup (see **Section III.2.2.**) under the same operating conditions as of **Section IV.6.1.** (reported in detail below) but with the addition of 500 ppm_v of SO_2 in the model flue-gas. The pH of the scrubbing solutions and the gas temperature were varied in order to compare the results with those reported in the **Section IV.6.2.**.

IV.7.1. Operating conditions

Table IV.26 reports the experimental conditions adopted in this set of experiments.

Table IV.26. *Operating conditions adopted for the experiments of SO_2 and NO_x removal in the packed column*

Scrubbing Solutions	***G*** $m^3 \cdot h^{-1}$	***T_G*** *°C*	***L*** $L \cdot h^{-1}$	***T_L*** *°C*	***pH*** -	***$C^\circ_{SO_2}$*** ppm_v	***$C^\circ_{NO_x}$*** ppm_v
SW	32	25, 40, 60	40, 70, 100, 130	25	8.20	500	1030
SWC0.25	32	25, 40, 60	40, 70, 100, 130	25	8.56	500	1030
SWC0.5	32	25, 40, 60	40, 70, 100, 130	25	8.96	500	1030
SWC0.75	32	25, 40, 60	40, 70, 100, 130	25	9.17	500	1030
SWC1.0	32	25, 40, 60	40, 70, 100, 130	25	9.40, 6, 3	500	1030

Further details on the physical-chemical composition of the liquids used are reported in **Section III.1.1. and III.2.1.**.

IV.7.2. Results and discussion

Figure IV.37 shown the experimental removal efficiencies of SO_2 (**A**) and the final wash water pH (**B**) in a simulated flue-gas containing SO_2 = 500 ppm_v and NO_x = 1030 ppm_v at 25 °C and 1 atm, using different dosages of sodium chlorite in seawater (from 0 to 1% w/w) at 25 °C. The results were expressed as parametric with the liquid flow rates, *i.e.* with the liquid-gas ratios, varied between 1.25 and 4.06 $L \cdot m^{-3}$.

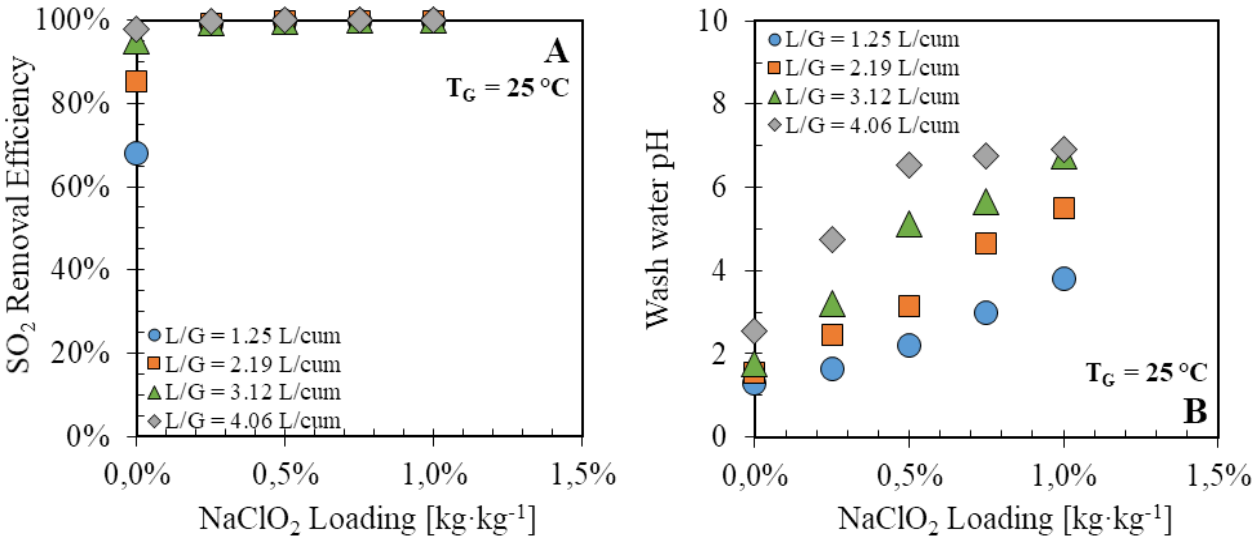

Figure IV.37. *Experimental results of SO_2 removal efficiency (A) and wash water pH solutions (B) in a simulated flue-gas (32 $m^3 \cdot h^{-1}$) containing SO_2 = 500 ppm_v and NO_x = 1030 ppm_v at 1 atm and 25 °C, for different liquid-gas ratio (from 1.25 to 4.06 $L \cdot m^{-3}$) and using five different scrubbing solutions at 25 °C: seawater at pH 8.2 (SW); four seawater solutions containing from 0.25 to 1% w/w of $NaClO_2$ at pH from 8.56 to 9.4*

The results in **Figure IV.37A** showed that with the lowest tested sodium chlorite concentration was possible to achieve a complete removal of sulphur dioxide.

The pH values of the wash water (**Figure IV.37B**) followed a trend consistent with the removal data. In fact, any further increase of *L/G* above the value at which SO_2 was completely captured led to a liquid dilution, which determined a progressive lower reduction of the wash water pH solution. Most of the final pH data was below 6 and confirmed the activation of the acidic SO_2 oxidation mechanism (AOM), described in the **Section II.2** (**Eqs. (79)-(80),(83)-(84)**).

The NO_x results for simultaneous absorption under the same operating conditions as in **Figure IV.37** are shown in **Figure IV.38** and compared with the data obtained for NO_x absorption as single-compound (already reported and discussed in **Figure IV.31**).

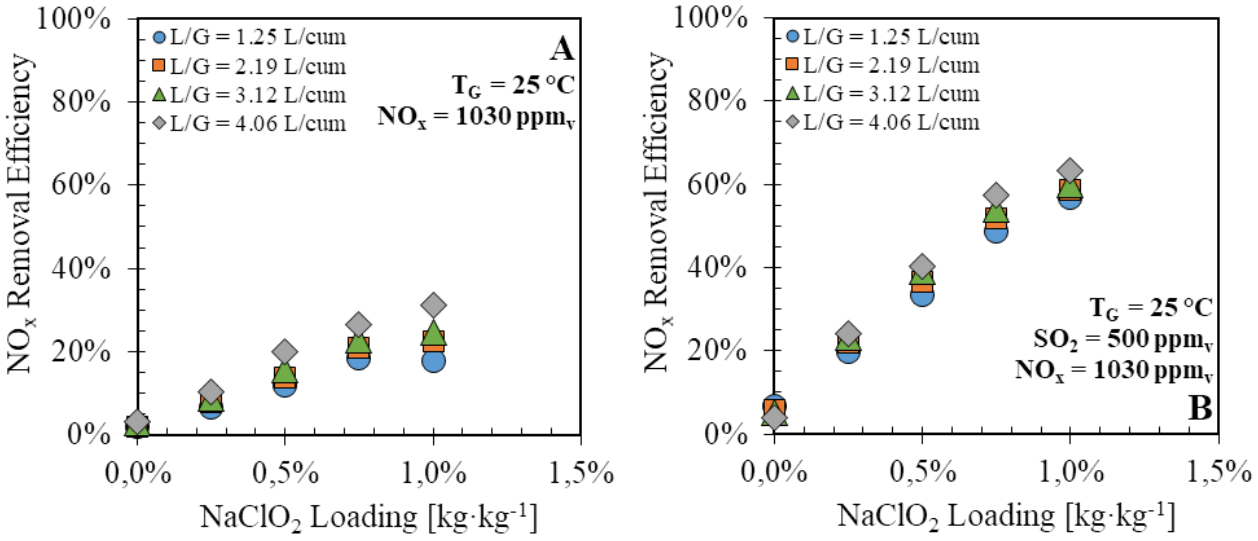

Figure IV.38. *Experimental results of total NO_x removal in a simulated flue-gas (32 $m^3 \cdot h^{-1}$) containing only 1030 ppm_v of NO_x (A) and total NO_x removal in a simulated flue-gas (32 $m^3 \cdot h^{-1}$) containing SO_2 = 500 ppm_v and NO_x = 1030 ppm_v (B). The experiments were performed at 1 atm and 25 °C, for different liquid-gas ratio (from 1.25 to 4.06 $L \cdot m^{-3}$) and using five different scrubbing solutions at 25 °C: seawater at pH 8.2 (SW); four seawater solutions containing from 0.25 to 1% w/w of $NaClO_2$ at pH from 8.56 to 9.4*

The presence of SO_2 significantly improved the capture of NO_x, which reached a maximum value of approximately 63% (**Figure IV.38B**), equal to twice the value reached without SO_2 (**Figure IV.38A**). The removal efficiencies increased with the added $NaClO_2$ content and only a slight dependence on the liquid-gas ratio was observed.

As observed in **Section IV.6**, the increase in NO_x capture can be related to the activation of a further oxidation mechanism that occurs only in acidic conditions (AOM). Indeed, a slight effect of L/G was observed, as the low liquid flow rate was compensated by the increasing acidity (see **Figure IV.37B**). This was also confirmed by the scrubbing liquid color observed during the tests, which quickly changed to greenish with a pungent odor as further oxidizer, such as chlorine and chlorine dioxide, were likely developed (**Eqs. (79)-(80),(85)-(88)**).

Further absorption experiments for SO_2 and NO_x simultaneous removal were performed to investigate the effect of gas temperature (at 40 and 60 °C) on the performance of the oxidative process. The operating conditions were the same as in **Figure IV.38B** and the results were reported in **Figure IV.39**.

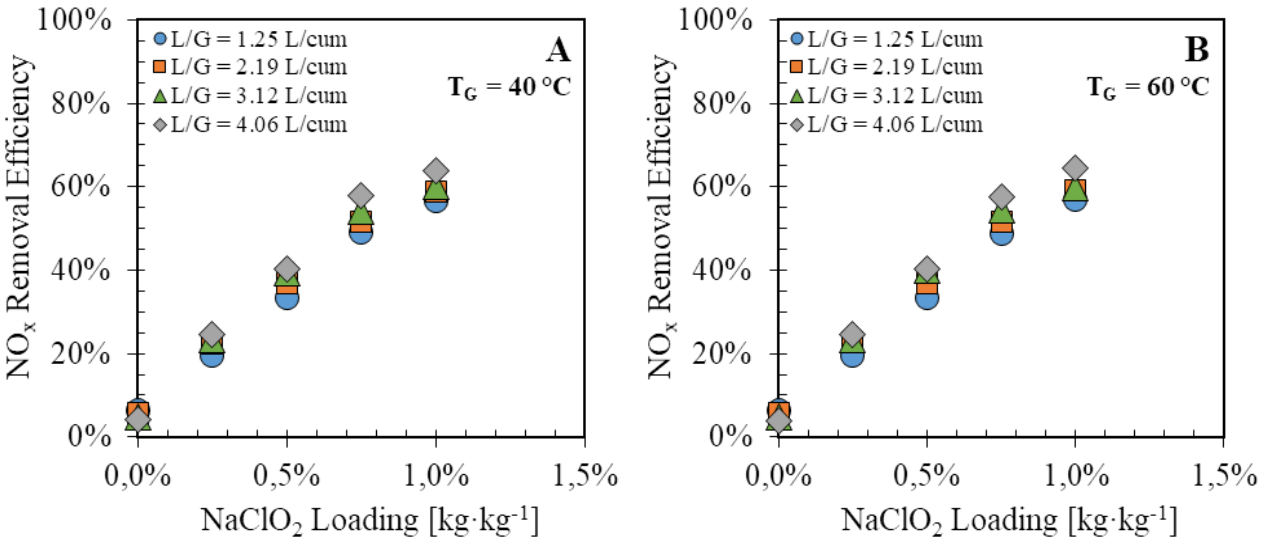

Figure IV.39. *Experimental results of total NO_x removal in a simultaneous absorption at 40 °C (A) and total NO_x removal in in a simultaneous absorption at 60 °C (B). The experiments were performed with a simulated flue-gas (32 m^3/h) containing SO_2 = 500 ppm_v and NO_x = 1030 ppm_v at 1 atm, for different liquid-gas ratio (from 1.25 to 4.06 $L \cdot m^{-3}$) and using five different scrubbing solutions at 25 °C: seawater at pH 8.2 (SW); four seawater solutions containing from 0.25 to 1% w/w of $NaClO_2$ at pH from 8.56 to 9.4*

Any significant effects of gas temperature on NO_x removal efficiencies were observed in **Figure IV.39**. Again, this result can be likely ascribed to the liquid temperature, which in all the experiments reached at most a value of 27 - 28 °C, only 3°C higher than the inlet value. For the same tests, the

removals of SO_2 were complete for each $NaClO_2$ concentration tested (data not reported) and showed a complete independence from gas temperature.

Other experiments on simultaneous absorption were performed with a constant concentration of $NaClO_2$ equal to 1% w/w (SWC1.0) and modifying the initial solution pH to 6 and 3, using HCl solution. **Figure IV.40** shows the experimental removal efficiencies of total NO_x (**A**) and final wash water pH (**B**) in a simulated flue-gas containing SO_2 = 500 ppm_v and NO_x = 1030 ppm_v at 25 °C and 1 atm, using sodium chlorite seawater solutions at 1% w/w and at different initial pH: 9.4, 6 and 3. The results were reported as parametric with the liquid-gas volumetric ratios (1.25 - 4.06 $L \cdot m^{-3}$).

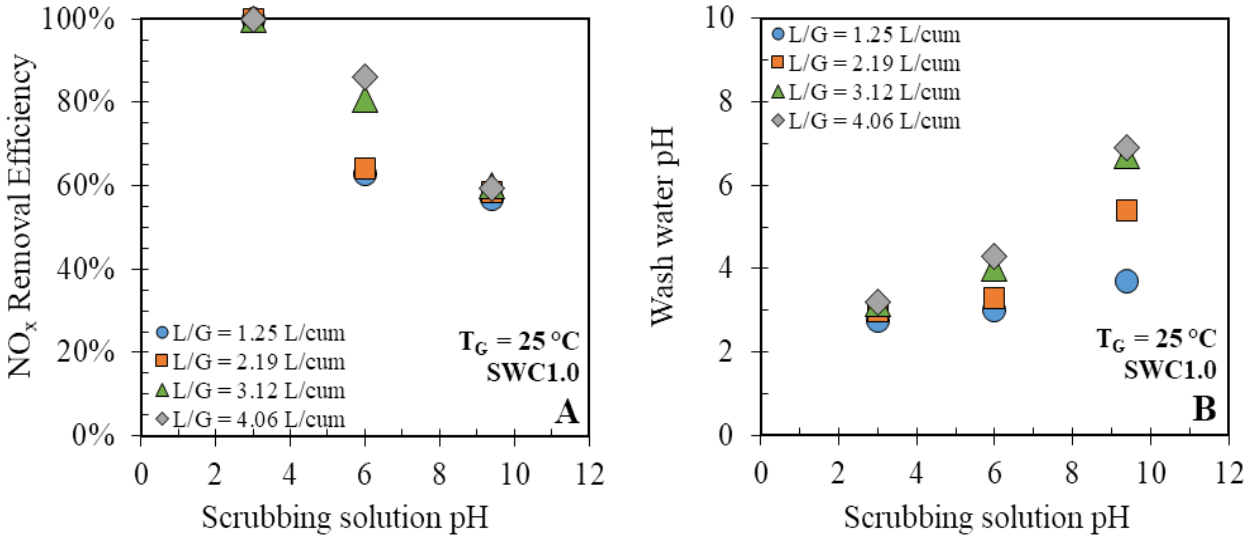

Figure IV.40. *Experimental results of total NO_x removal efficiency (A) and wash water pH solutions (B) in a simulated flue-gas (32 $m^3 \cdot h^{-1}$) containing SO_2 = 500 ppm_v and NO_x = 1030 ppm_v at 1 atm and 25 °C, for different liquid-gas ratio (from 1.25 to 4.06 $L \cdot m^{-3}$) and using seawater solution with $NaClO_2$ at 1% w/w (SWC1.0) at 25 °C and different initial pH: 9.4, 6 and 3*

Figure IV.40A shows that the simultaneous presence of SO_2 determined an acidified scrubbing solution, which led to a significant increase in the NO_x removal efficiency that reached a complete removal for initial pH = 3 at all the investigated *L/G* ratios. In addition, at pH = 6, a marked influence of *L/G* was observed, with a 80 and 87% removal efficiency obtained for the *L/G* ratios higher than 2.19 $L \cdot m^{-3}$. Differently, no effect of initial pH of the scrubbing liquid on SO_2 removals (data not shown) was observed.

The pH of the wash water increased by increasing the initial solution pH and by increasing the *L/G* ratio (**Figure IV.40B**). The pH values were consistent with the removal data and confirmed the activation of the *Acidic Oxidation Mechanism*, AOM (**Eqs. (79)-(80),(85)-(88)**) which improved the oxidation performance thanks to the formation of the oxidizing Cl_2 and ClO_2.

Further experiments were performed to investigate the effect of gas temperature on the performance of the oxidative process in a simultaneous SO_2 and NOx absorption. The gas temperature was set at 40 and 60 °C using the same operating conditions as in **Figure IV.40A** and the results were compared in **Figure IV.41**.

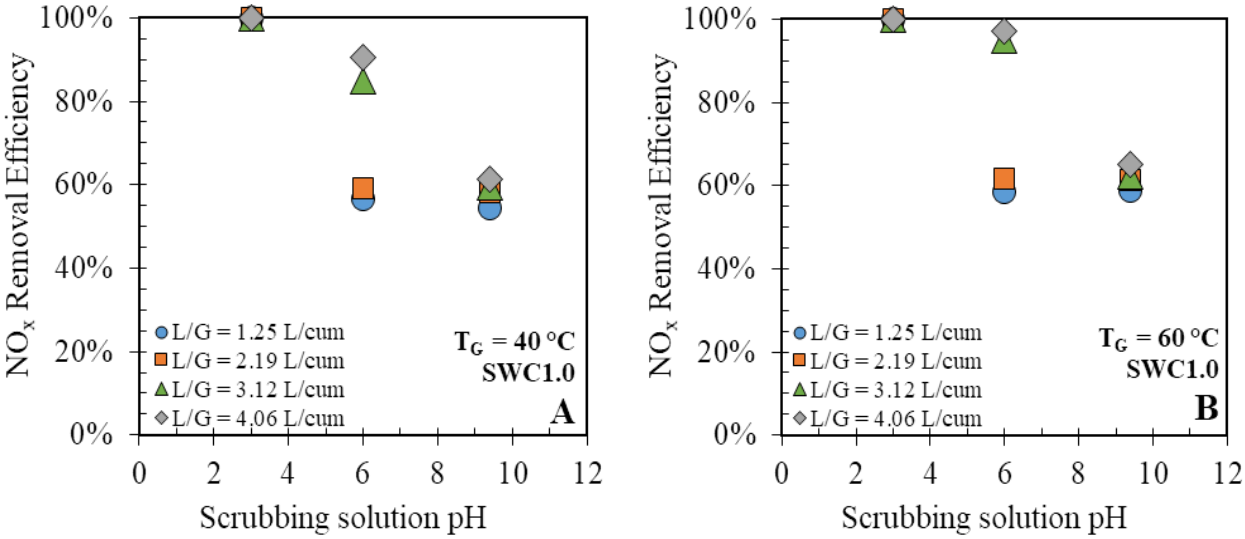

Figure IV.41. *Experimental results of total NO_x removal in a simultaneous absorption at 40 °C (A) and total NO_x removal in in a simultaneous absorption at 60 °C (B). The experiments were performed with a simulated flue-gas (32 m^3/h) containing SO_2 = 500 ppm_v and NO_x = 1030 ppm_v 1 atm, for different liquid-gas ratio (from 1.25 to 4.06 $L \cdot m^{-3}$) and using seawater solution with $NaClO_2$ at 1% w/w (SWC1.0) at 25 °C and different initial pH: 9.4, 6 and 3*

An appreciable effect of gas temperature was observed only at pH = 6 for *L/G* = 3.12 and 4.06 $L \cdot m^{-3}$ where NO_x removals progressively increased of about 5 % from 25 to 40 °C and of about 15% from 25 to 60 °C. This improvement could be due to a further oxidation mechanism that occurs in the gas phase (GOM) due to the interaction of NO_x with Cl_2 and ClO_2 desorbed by the liquid (**Eqs. (93)-(100)**), confirmed by the studies of **Park et al.** [72] and **Hao et al.** [111]. Any measurable effect of temperature on SO_2 removals was observed (data not shown).

The experimental campaign showed that the presence of SO_2 had no competitive effects with NO_x to consume chlorite ions and no decrease in total performance on oxidation process was observed. On the contrary, the presence of SO_2 indirectly induced a synergistic effect on NO_x removals. In fact, a complete capture of NO_x was reached with a scrubbing solution at pH = 3 and a molar chlorite dosage 16 times higher than NO_x moles fed. Only 58% efficiency was achieved for the same chlorite dosage when the pH of SWC solution was 6 and 9.4. This result allowed to reduce the molar consumption of sodium chlorite by 60% using acidic SWC solution at pH = 3 compared to the absorption without SO_2.

IV.7.3. Highlights

This activity aimed to evaluate the capacity of sodium chlorite solutions to simultaneously remove NO_x and SO_2 from a flue-gas. Absorption tests were performed in the packed column with a model flue-gas containing 1030 ppm_v of NO_x and 500 ppm_v of SO_2 to simulate typical conditions of marine Diesel engines. The $NaClO_2$ was added to a seawater-based solution from 0 to 1% w/w

- The experiments on SO_2 showed that a complete removal was already achieved by adding 0.25% w/w of sodium chlorite. Only for pure seawater the efficiencies were influenced by the *L/G* ratio in the investigated conditions.
- A maximum NO_x removal of about 63% was achieved in the simultaneous absorption tests with 4.06 $L \cdot m^{-3}$ of SWC1.0 solutions;
- In absence of SO_2, the NO_x removal efficiency was only around 31%. This indicated that NO_x removal was improved by the presence of SO_2 probably thanks to the induction of *Acidic Oxidation Mechanism* (AOM) This is also confirmed by the pH values of the wash water and by the progressive greening of the solutions along the column, also accompanied by a pungent chlorine odor (whose odor threshold is very low).
- Significant improvements of NO_x removal efficiency were associated with an artificial acidification of SWC1.0 solutions combined with the presence of SO_2. This allowed to achieve a complete NO_x removal at lower *L/G* ratio as 1.25 $L \cdot m^{-3}$.
- Increasing the gas temperature to 40 and 60 °C combined with the artificial acidification of the SWC1.0 solutions allowed to increase the removal efficiency by a percentage between 5 and 15%. This confirmed the presence of oxidation mechanism taking place in the gas phase (GOM) and favored by the gas temperature.
- A complete capture of NO_x was reached with SWC1.0 solutions at pH = 3 and a gas temperature of 60 °C, using a sodium chlorite molar dosage of ClO_2^- 16 times higher than NO_x moles fed. The operating dosage ($d_{c/n}$) was approximately 36 times the stoichiometric ratio (ClO_2^-/NO_x) evaluated by the reactions occurring in AOM and GOM (**Eqs. (79)-(80),(85)-(88),(93)-(100)**). This allowed to reduce the consumption of sodium chlorite by 60% using SWC solutions at pH = 3 compared to the absorption without SO_2. The presence of SO_2 played a synergistic role on total performance of NO_x capture.

V. FINAL REMARKS

This Ph.D. Research Program aimed to advance the development of seawater-based flue gas desulphurization units enhanced by the use of chemical additives such as NaOH and $NaClO_2$ to reduce water consumption and scrubber size. The work included both experimental runs at laboratory and pilot scale plants and modelling analyses. Experimental and modelling results are summarized in the following.

- Solubility data for SO_2 absorption in seawater-based solutions:

  The experiments were performed in a feed-batch bubble column and allowed evaluating the solubility of SO_2 in seawater-based solutions. Solubility data covered a wide range of investigated SO_2 concentrations from about 100 to 2000 ppm_v at atmospheric pressure and temperature. The SO_2 solubility was investigated in several aqueous solutions as:

  - seawater;
  - seawater doped with NaOH;
  - seawater doped with $NaClO_2$;
  - HCl solutions in distilled water;
  - distilled water;
  - tap water.

  The last three solutions were used as benchmark experiments and to calibrate the equilibrium and mass transfer models. The sulphur dioxide solubility in seawater and seawater with NaOH showed the typical pathways of a "chemical absorption": as long as the alkalinity and the OH^- ions were enough to convert all the SO_2 absorbed in SO_3^{2-}, the solubility curve was very close to the ideal condition of zero gas concentration ($C_{SO_{2(g)}} \approx 0$). When the chemicals are consumed, the solubility curve followed an almost linear trend with a slope similar to the Henry constant value for distilled water.

  Different results were observed for sodium chlorite solutions. In this case, the SO_2 absorption experiments showed a rapid acidification of the solution, which gave a change in the liquid color from yellowish to greenish. The liquid became transparent when the reaction completed and the chlorite consumed. Sodium chlorite had a greater oxidizing power under acidic conditions rather than under basic or neutral ones, due to the formation of further strong oxidants such as chlorine and chlorine dioxide. This phenomenon was called *Acidic Oxidation Mechanism* (AOM).

Experiments proved that the natural acidification of the solution following the SO_2 hydrolysis is sufficient to activate the AOM. An equilibrium model was developed in ASPEN PLUS® using the Flash block, which includes: the Elec-NRTL thermodynamic property method; the physical gas-liquid equilibria data; the chemical reaction equilibria data. The model provided an accurate description of the experimental data for each scrubbing solution tested.

- Characterization of the mass transfer coefficient and pressure drop in Structured packings and spray towers:

  Dedicated tests were performed to assess mass transfer coefficients and pressure drops in a packed column filled with M250.X packing, under typical conditions of FGD units. These results were compared with the most consolidated models for mass transfer and pressure drop for structured packings available in the reference literature.

  The calibrated mass transfer and pressure drop models were tested against a large number of FGD tests carried out in a wide and different range of operating conditions, by varying gas temperature, SO_2 concentration, liquid-gas ratio and using different scrubbing solutions. The column was modelled in ASPEN PLUS® using the aforementioned equilibrium model and the calibrated mass transfer and pressure drop models. The simulations showed an accurate description of the experimental data both in terms of removal efficiencies and wash water pH values. The same characterization procedure was used with the VTS spray column and the data were validated with a dedicated calculation tool developed in MATLAB®.

  The development of predictive models for FGD with absorption columns allowed to design spray and packed towers for seawater scrubbing process applied to a real case-study: the treatment of exhaust gases produced by a Wärtsilä marine Diesel engine (4.35 MW) in order to reach the SECA emission target starting from a 3% sulphur IFO fuel. The results of the simulations showed that a reduction in size (76 - 86%) and in weight (27 - 48%) was achieved with the use of packed tower with Mellapak 250.X. While these results can be largely predicted, we also noticed a remarkable reduction (around 44 - 55%) in the capital costs for packed columns compared with spray towers, in spite of the use of a very expensive packing material. A reduction in operating costs could also be achieved.

- Experimental data on real FGD systems efficiency using seawater-based solutions:

  Experimental tests on the lab-scale column equipped with M250.X and on the pilot scale spray column allowed estimating the FGD performance using both the traditional seawater process or using seawater doped with either NaOH or $NaClO_2$. The experiments showed that the use of

sodium chlorite allowed higher efficiencies with respect to pure seawater and with seawater doped with NaOH. For instance, a water-saving up to 50% could be reached with a seawater doped with 0.2% of sodium chlorite as compared with pure seawater. For a complete desulphurization, an optimal molar chlorite dosage equal to 1.1 times the SO_2 moles fed with the gas was estimated. Interestingly, this operative dosage ($d_{c/s}$) was very close to the theoretical stoichiometric ratio ($d_{stech} = 1$) of the reactions occurring in the *Acidic Oxidation Mechanism* (AOM).

FGD tests were also performed on a pilot spray column in collaboration with the Chalmers University of Technology using the treat a portion of the exhaust gases produced by a marine Diesel engine (Volvo Penta, 80kW) using seawater from the Kattegat area. The experiments showed that the addition of 100 $mg \cdot L^{-1}$ NaOH in seawater allowed complying with the IMO targets with a water-saving of about 28 - 33%, as compared with pure seawater. The reduction in water consumption may be associated with a size and cost reduction in scrubber equipment. These results are very interesting in light of the high space and weight requirement for the installation of FGD systems on-board the ship.

- <u>Effect of the FGD processes on the absorption of other gas pollutants and the capture of aerosol pollutants:</u>

  The effects of the FGD process on wash waters composition and other pollutants was investigated for the exhaust gases produced by the Chalmers Volvo Penta Engine. Analysis on scrubber wash waters samples associated to different engine loads, confirmed that the heavy metal contents mostly derived from sources different than the flue gas scrubbing, probably related to corrosion of scrubber and piping materials. Now standing this, their concentrations mostly complied with the Regulations concerning wash water discharge for land-based activity and scrubbers. A full compliance with the standards could easily be achieved with a dilution factor of 1.3 using a fresh seawater.

  The organic pollutants were mostly in line with the current regulation on water quality standards, but some species were within 3 - 6 times to maximum concentration allowed in natural water body. This dilution can be easily reached a few tens of meters from the ship hull, giving result very similar to those associated with atmospheric deposition of these pollutants. Furthermore, most of the measurements were below the detection limit of the analysis instrument, for this reason it is possible to consider these concentrations much close to the standards.

  The tests confirmed that no effect of the FGD process was observed on other gas pollutants such as NO_x, CO and CO_2 due to their low solubility in the tested seawater. The same result was observed with seawater doped with NaOH.

Differently, tests with $NaClO_2$ added to seawater in the lab scale packed column showed that a NO_x removal up to 31% can be achieved on a model flue gas containing only NO_x. The experiments showed that acidification of a 1% $NaClO_2$ solution allowed to reach a complete NO_x removal operating the scrubber with a liquid-gas ratio of 4.06 $L \cdot m^{-3}$. The experiments also suggested that at acid pH, both gas and liquid side oxidation reactions took place (GOM and AOM), thanks to the formation of additional oxidants such as, $ClO_{2(g)}$ and $Cl_{2(g)}$.

Further tests were performed with the addition of SO_2 in the model flue gas. On the one hand, sulphur dioxide promotes the acidification, thus improving the de-NO_x process; on the other hand, a competitive effect could take place during the oxidative process. Experiments revealed that the simultaneous absorption process favored NO_x removal by more than two times the case when SO_2 was not present in the model flue-gas. A complete removal of NO_x in the presence of SO_2 was observed when the 1% w/w $NaClO_2$ seawater solution (SWC1.0) was acidified at pH = 3 for a liquid-gas ratio as low as 1.25 $L \cdot m^{-3}$. The experiments also indicated that the optimal molar chlorite dosage required to completely remove NO_x in the presence of SO_2 was about 16 times higher than the NO_x fed moles. In this case, the operative dosage ($d_{c/n}$) was quite larger to the theoretical stoichiometric ratio (d_{stech} = 0.44) of the reactions occurring in the AOM and GOM. Moreover, the molar chlorite dosage for the de-NO_x process was still higher than that of desulphurization. It is interesting to note that the presence of SO_2 in the simulated flue-gas allowed a reduction of the molar dosage of chlorite from 40 to 16 with a consequent 60% in oxidant-saving.

- <u>ASPEN PLUS® model to describe the experimental data:</u>

  Simulations with ASPEN PLUS® proved to be effective tool to design absorbed, if the mass transfer coefficients and the equilibrium data were suitably addressed. Thanks to the adopted set of experiments, it was possible to calibrate the equilibrium and mass transfer models in such a way to provide a very good description of all the investigated conditions, providing accurate estimation of the physical chemical characteristics of gases and liquid streams leaving the absorber.

- <u>Environmental impact on air and water quality due to the use of sodium chlorite solutions in the Exhaust Gas Cleaning System (EGCS)</u>

  Although the use of the scrubbers fed with seawater enhanced with sodium chlorite allows an effective cleaning of the exhausted gases from SO_2 and NO_x, a risk assessment on the environmental impact on air and water for contamination by chlorine-based species must be

accounted. The details of this analysis and the methods adopted to prevent this risk are addressed in a patent application, also including specifications on exhaust gas treatment process.

REFERENCES

[1] S. J. Biondo and J. C. Marten, "A history of flue gas desulfurization systems since 1850: Research, development and demonstration," *J. Air Pollut. Control Assoc.*, vol. 27, no. 10, pp. 948–961, 1977.

[2] J. Kjølholt, S. Aakre, C. Jürgensen, and J. Lauridsen, "Assessment of Possible Impacts of Scrubber Water Discharges on the Marine Environment," 2012.

[3] A. Poullikkas, "Review of Design, Operating, and Financial Considerations in Flue Gas Desulfurization Systems," *Energy Technol. Policy*, vol. 2, no. 1, pp. 92–103, 2015.

[4] P. S. Nolan, "Flue Gas Desulfurization Technologies for Coal-Fired Power Plants," in *Coal-Tech 2000 International Conference*, 2000, pp. 1–13.

[5] A. Lancia, D. Musmarra, and F. Pepe, "Aspetti chimico-ingegneristici dei principali processi di desolforazione ad umido dei fumi di combustione," *Termotec. Milano*, vol. 45, no. 5, pp. 65–73, 1991.

[6] J. Kjärstad and F. Johnsson, "The European power plant infrastructure-Presentation of the Chalmers energy infrastructure database with applications," *Energy Policy*, vol. 35, no. 7, pp. 3643–3664, 2007.

[7] S. J. Smith, J. Van Aardenne, Z. Klimont, R. J. Andres, A. Volke, and S. Delgado Arias, "Anthropogenic sulfur dioxide emissions: 1850-2005," *Atmos. Chem. Phys.*, vol. 11, no. 3, pp. 1101–1116, 2011.

[8] Y. Ohtsuka, "Desulfurization of Coal," in *COAL, OIL SHALE, NATURAL BITUMEN, HEAVY OIL AND PEAT-Encyclopedia of Life Support Systems (EOLSS)*, vol. I, 2009.

[9] D. W. Green and R. H. Perry, *Perry's Chemical Engineers' Handbook*. New York: McGraw-Hill Education, 1984.

[10] J. A. Kent, *Riegel's Handbook of Industrial Chemistry*. 1983.

[11] X. Zhang, "Emission standards and control of PM2.5 from coal-fired power plants," *Air Waste Manag. Assoc. - Power Plant Pollut. Control "MEGA" Symp. MEGA 2016*, no. July, pp. 653–664, 2016.

[12] G. Wynn and P. Coghe, "Europe's Coal-Fired Power Plants: Rough Times Ahead Analysis of the Impact of a New Round of Pollution Controls," 2017.

[13] S. K. Paliwal, "Environmental Regulations for Coal based Thermal Power Plant," in *Clean Air Asia*, 2017.

[14] R. Gaigward, W. L. Boward, and W. DePriest, "Wet Flue Gas Desulfurization Technology Evaluation (PROJECT NUMBER 11311-000)," 2003.

[15] L. K. Wang, C. Williford, and W. Y. Chen, "Desulfurization and Emissions Control," *Adv. Air Noise Pollut. Control*, vol. 2, pp. 35–95, 2007.

[16] I. M. Bernhardsen, "Removal of SO2 from Flue Gas-Study of the Regenerable Labsorb Process," Norwegian University of Science and Technology, 2015.

[17] H. F. Johnstone and P. W. Leppla, "The Solubility of Sulfur Dioxide at Low Partial Pressures. The Ionization Constant and Heat of Ionization of Sulfurous Acid1," *J. Am. Chem. Soc.*, vol.

56, no. 11, pp. 2233–2238, Nov. 1934.

[18] B. Behrends and G. Liebezeit, “Reducing SO2 and NOx Emissions from Ships by a Seawater Scrubber,” 2003.

[19] U. Neumann, “Sulphur Dioxide and Nitrogen The Wellman Lord Process. In: van Velzen D. (eds) Sulphur Dioxide and Nitrogen Oxides in Industrial Waste Gases: Emission, Legislation and Abatement.,” *EurocoursesChemical Environ. Sci.*, 1991.

[20] IMO (International Maritime Organization) MEPC 74/INF.10, “Pollution Prevention and Response: Scrubber Environmental Impact Literature Review,” 2019.

[21] L. Čampara, N. Hasanspahić, and S. Vujičić, “Overview of MARPOL ANNEX VI regulations for prevention of air pollution from marine diesel engines,” in *SHS Web of Conferences*, 2018, vol. 58, no. 2018, p. 01004.

[22] Y. Gu and S. W. Wallace, “Scrubber: A potentially overestimated compliance method for the Emission Control Areas: The importance of involving a ship’s sailing pattern in the evaluation,” *Transp. Res. Part D Transp. Environ.*, vol. 55, no. 2017, pp. 51–66, 2017.

[23] L. Johansson, J. P. Jalkanen, J. Kalli, and J. Kukkonen, “The evolution of shipping emissions and the costs of regulation changes in the northern EU area,” *Atmos. Chem. Phys.*, vol. 13, no. 22, pp. 11375–11389, 2013.

[24] F. Di Natale and C. Carotenuto, “Particulate matter in marine diesel engines exhausts: Emissions and control strategies,” *Transp. Res. Part D Transp. Environ.*, vol. 40, pp. 166–191, 2015.

[25] T. Henriksson, “SOx scrubbing of marine exhaust gases,” *Wärtsilä Tech. J.*, vol. 2, 2007.

[26] T. Notteboom, “The impact of low sulphur fuel requirements in shipping on the competitiveness of roro shipping in Northern Europe,” *WMU J. Marit. Aff.*, vol. 10, no. 1, pp. 63–95, 2011.

[27] E. den Boer and M. Hoen, “Scrubbers – An economic and ecological assessment,” 2015.

[28] M. & C. Arnauld Filancia Director, “Reducing Emissions from Shipping Wärtsilä’s Solutions,” *Wärtsilä Corp.*, 2011.

[29] K. Lee *et al.*, “Global relationships of total alkalinity with salinity and temperature in surface waters of the world’s oceans,” *Geophys. Res. Lett.*, vol. 33, no. 19, 2006.

[30] C. Pahl-Wostl, E. Mostert, and J. D. Tàbara, “The Growing Importance of Social Learning in Water Resources Management and Sustainability Science,” *Ecol. Soc.*, vol. 13, no. 1, Jan. 2008.

[31] S. Endres *et al.*, “A new perspective at the ship-air-sea-interface: The environmental impacts of exhaust gas scrubber discharge,” *Front. Mar. Sci.*, vol. 5, pp. 1–13, 2018.

[32] United States Environmental Protection Agency, “Exhaust Gas Scrubber Washwater Effluent,” 2011.

[33] D. R. Turner, I. M. Hassellöv, E. Ytreberg, and A. Rutgersson, “Shipping and the environment: Smokestack emissions, scrubbers and unregulated oceanic consequences,” *Elementa*, vol. 5, 2017.

[34] E. Ytreberg, I. M. Hassellöv, A. T. Nylund, M. Hedblom, A. Y. Al-Handal, and A. Wulff, “Effects of scrubber washwater discharge on microplankton in the Baltic Sea,” *Mar. Pollut.*

Bull., vol. 145, pp. 316–324, 2019.

[35] V. Eyring, H. W. Köhler, A. Lauer, and B. Lemper, "Emissions from international shipping: 2. Impact of future technologies on scenarios until 2050," *J. Geophys. Res. D Atmos.*, vol. 110, no. 17, pp. 183–200, 2005.

[36] D. Flagiello, A. Lancia, A. Erto, and F. Di Natale, "Desulphurization of combustion flue-gases by Wet Oxidation Scrubbing Desulphurization of combustion flue-gases by Wet Oxidation Scrubbing (WOS)," in *Proceedings of the 42th ASICI, Ravenna, Italy*, 2019, no. September, pp. 5–10.

[37] F. Di Natale, C. Carotenuto, and A. Lancia, "Enhanced SO2 removal by using charged water droplets," *Chem. Eng. Trans.*, vol. 52, pp. 505–510, 2016.

[38] L. Manna, F. Di Natale, C. Carotenuto, and A. Lancia, "Electrified Water Sprays Generation for Gas Pollutants Emission Control," *Chem. Eng. Trans.*, vol. 52, Oct. 2016.

[39] F. Di Natale, C. Carotenuto, L. Manna, and A. Lancia, "Chemi-electro-hydrodynamic of sulphur dioxide absorption by electrified water sprays," *Chem. Eng. Trans.*, vol. 69, pp. 685–690, 2018.

[40] F. Di Natale, C. Carotenuto, S. Caserta, M. Troiano, L. Manna, and A. Lancia, "Experimental evidences on the chemi-electro-hydrodynamic absorption of sulphur dioxide in electrified water sprays," *Chem. Eng. Res. Des.*, vol. 146, pp. 249–262, 2019.

[41] D. Flagiello, F. Di Natale, A. Erto, and A. Lancia, "Marine diesel engine flue gas desulphurization by seawater scrubbing in a structured packing absorption column," in *Proceedings of the 40th ASICI, Rome, Italy*, 2017.

[42] D. Flagiello, A. Erto, A. Lancia, and F. Di Natale, "Experimental and modelling analysis of seawater scrubbers for sulphur dioxide removal from flue-gas," *Fuel*, vol. 214, pp. 254–263, 2018.

[43] D. Flagiello, A. Parisi, A. Lancia, C. Carotenuto, A. Erto, and F. Di Natale, "Seawater desulphurization scrubbing in spray and packed columns for a 4.35 MW marine diesel engine," *Chem. Eng. Res. Des.*, vol. 148, pp. 56–67, 2019.

[44] M. Schultes, J. Brauer, P. Chen, and S. Doong, "Marinization of mass transfer columns for FLNG applications," *Chem. Eng. Trans.*, vol. 69, pp. 301–306, 2018.

[45] S. Darake, A. Rahimi, M. S. Hatamipour, and P. Hamzeloui, "SO2 Removal by Seawater in a Packed-Bed Tower: Experimental Study and Mathematical Modeling," *Sep. Sci. Technol.*, vol. 49, no. 7, pp. 988–998, 2014.

[46] I. Iliuta and M. C. Iliuta, "Modeling of SO2 seawater scrubbing in countercurrent packed-bed columns with high performance packings," *Sep. Purif. Technol.*, vol. 226, no. March, pp. 162–180, 2019.

[47] J. M. Kasper, C. A. Clausen III, and C. D. Cooper, "Control of Nitrogen Oxide Emissions by Hydrogen Peroxide-Enhanced Gas-Phase Oxidation Of Nitric Oxide," *J. Air Waste Manag. Assoc.*, vol. 46, no. 2, pp. 127–133, 1996.

[48] J. L. de Paiva and G. C. Kachan, "Modeling and Simulation of a Packed Column for NOx Absorption with Hydrogen Peroxide," *Ind. Eng. Chem. Res.*, vol. 37, no. 2, pp. 609–614, 1998.

[49] I. Liémans, B. Alban, J. P. Tranier, and D. Thomas, "SOx and NOx absorption based removal into acidic conditions for the flue gas treatment in oxy-fuel combustion," *Energy Procedia*,

vol. 4, pp. 2847–2854, 2011.

[50] Y. Liu, J. Zhang, and C. Sheng, "Kinetic model of NO removal from SO2-containing simulated flue gas by wet UV/H2O2 advanced oxidation process," *Chem. Eng. J.*, vol. 168, no. 1, pp. 183–189, 2011.

[51] R. T. Guo *et al.*, "Removal of NO by using Fenton reagent solution in a lab-scale bubbling reactor," *Fuel*, vol. 90, no. 11, pp. 3295–3298, 2011.

[52] I. Liémans and D. Thomas, "Simultaneous NOx and SOx reduction from oxyfuel exhaust gases using acidic solutions containing hydrogen peroxide," *Energy Procedia*, vol. 37, no. x, pp. 1348–1356, 2013.

[53] Y. Liu, J. Pan, A. Tang, and Q. Wang, "A study on mass transfer-reaction kinetics of NO absorption by using UV/H2O2 /NaOH process," *Fuel*, vol. 108, no. x, pp. 254–260, 2013.

[54] Y. Liu, Q. Wang, Y. Yin, J. Pan, and J. Zhang, "Advanced oxidation removal of NO and SO2 from flue gas by using ultraviolet/H2O2 /NaOH process," *Chem. Eng. Res. Des.*, vol. 92, no. 10, pp. 1907–1914, 2014.

[55] Y. Zhao, R. Hao, P. Zhang, and S. Zhou, "An integrative process for Hg0 removal using vaporized H2O2/Na2S2O8," *Fuel*, vol. 136, pp. 113–121, 2014.

[56] Z. Wang and Z. Wang, "Mass Transfer-Reaction Kinetics Study on Absorption of NO with Dual Oxidants (H2O2/S2O82-)," *Ind. Eng. Chem. Res.*, vol. 54, no. 41, pp. 9905–9912, 2015.

[57] Y. Zhao, R. Hao, B. Yuan, and J. Jiang, "Simultaneous removal of SO2, NO and Hg0 through an integrative process utilizing a cost-effective complex oxidant," *J. Hazard. Mater.*, vol. 301, pp. 74–83, 2016.

[58] L. Wang, W. Zhao, and Z. Wu, "Simultaneous absorption of NO and SO2 by Fe(II)-EDTA combined with Na2SO3 solution," *Chem. Eng. J.*, vol. 132, no. 1–3, pp. 227–232, 2007.

[59] H. S. Zhu, Y. P. Mao, X. J. Yang, Y. Chen, X. L. Long, and W. K. Yuan, "Simultaneous absorption of NO and SO2 into FeII-EDTA solution coupled with the FeII-EDTA regeneration catalyzed by activated carbon," *Sep. Purif. Technol.*, vol. 74, no. 1, pp. 1–6, 2010.

[60] X. J. Yang, L. Yang, L. Dong, X. L. Long, and W. K. Yuan, "Kinetics of the [Fe(III)-EDTA]-reduction by sulfite under the catalysis of activated carbon," *Energy and Fuels*, vol. 25, no. 10, pp. 4248–4255, 2011.

[61] Y. G. Adewuyi and M. A. Khan, "Nitric oxide removal from flue gas by combined persulfate and ferrous–EDTA solutions: Effects of persulfate and EDTA concentrations, temperature, pH and SO2," *Chem. Eng. J.*, vol. 304, pp. 793–807, 2016.

[62] E. Sada, H. Kumazawa, I. Kudo, and T. Kondo, "Absorption of NO in aqueous mixed solutions of NaClO2 and NaOH," *Chem. Eng. Sci.*, vol. 33, no. 3, pp. 315–318, 1978.

[63] H. W. Hsu, C. J. Lee, and K. S. Chou, "Absorption of NO by NaClO2 solution: Performance characteristics," *Chem. Eng. Commun.*, vol. 170, no. January 2015, pp. 67–81, 1998.

[64] H. Chu, T. W. Chien, and B. W. Twu, "The absorption kinetics of NO in NaClO2/NaOH solutions," *J. Hazard. Mater.*, vol. 84, no. 2–3, pp. 241–252, 2001.

[65] T. W. Chien, H. Chu, and H. T. Hsueh, "Kinetic study on absorption of SO2 and NOx with acidic NaClO2 solutions using the spraying column," *J. Environ. Eng.*, vol. 129, no. 11, pp. 967–974, 2003.

[66] H. K. Lee, B. R. Deshwal, and K. S. Yoo, “Simultaneous removal of SO2 and NO by sodium chlorite solution in wetted-wall column,” *Korean J. Chem. Eng.*, vol. 22, no. 2, pp. 208–213, 2005.

[67] D. S. Jin, B. R. Deshwal, Y. S. Park, and H. K. Lee, “Simultaneous removal of SO2 and NO by wet scrubbing using aqueous chlorine dioxide solution,” *J. Hazard. Mater.*, vol. 135, no. 1–3, pp. 412–417, 2006.

[68] N. D. Hutson, R. Krzyzyńska, and R. K. Srivastava, “Simultaneous removal of SO2, NOx, and Hg from coal flue gas using a NaClO2-enhanced wet scrubber,” *Ind. Eng. Chem. Res.*, vol. 47, no. 16, pp. 5825–5831, 2008.

[69] B. R. Deshwal, S. H. Lee, J. H. Jung, B. H. Shon, and H. K. Lee, “Study on the removal of NOx from simulated flue gas using acidic NaClO2 solution,” *J. Environ. Sci.*, vol. 20, no. 1, pp. 33–38, 2008.

[70] B. R. Deshwal and H. K. Lee, “Mass transfer in the absorption of SO2 and NOx using aqueous euchlorine scrubbing solution,” *J. Environ. Sci.*, vol. 21, no. 2, pp. 155–161, 2009.

[71] Y. Zhao, F. Liu, T. Guo, and Y. Zhao, “Experiments and reaction characteristics of liquid phase simultaneous removal of SO2 and NO,” *Sci. China, Ser. E Technol. Sci.*, vol. 52, no. 6, pp. 1768–1775, 2009.

[72] H. W. Park, S. Choi, and D. W. Park, “Simultaneous treatment of NO and SO2 with aqueous NaClO2 solution in a wet scrubber combined with a plasma electrostatic precipitator,” *J. Hazard. Mater.*, vol. 285, no. x, pp. 117–126, 2015.

[73] Z. Han, S. Yang, D. Zhao, B. Liu, X. Pan, and Z. Yan, “An investigation of mass transfer-reaction kinetics of NO absorption by wet scrubbing using an electrolyzed seawater solution,” *RSC Adv.*, vol. 7, no. 31, pp. 18821–18829, 2017.

[74] R. Hao *et al.*, “Reactivity of NaClO2 and HA-Na in air pollutants removal: Active species identification and cooperative effect revelation,” *Chem. Eng. J.*, vol. 330, pp. 1279–1288, 2017.

[75] N. E. Khan and Y. G. Adewuyi, “Absorption and oxidation of nitric oxide (NO) by aqueous solutions of sodium persulfate in a bubble column reactor,” *Ind. Eng. Chem. Res.*, vol. 49, no. 18, pp. 8749–8760, 2010.

[76] V. K. Sharma, “Potassium ferrate(VI): An environmentally friendly oxidant,” *Adv. Environ. Res.*, vol. 6, no. 2, pp. 143–156, 2002.

[77] Y. Zhao, Y. Han, T. Guo, and T. Ma, “Simultaneous removal of SO2, NO and Hg0 from flue gas by ferrate (VI) solution,” *Energy*, vol. 67, pp. 652–658, 2014.

[78] A. Andreasen and S. Mayer, “Use of Seawater Scrubbing for SO2 Removal from Marine Engine Exhaust,” *Energy & Fuels*, vol. 21, no. 5, pp. 3274–3279, 2007.

[79] J. Rodríguez-Sevilla, M. Álvarez, M. C. Díaz, and M. C. Marrero, “Absorption equilibria of dilute SO2 in seawater,” *J. Chem. Eng. Data*, vol. 49, no. 6, pp. 1710–1716, 2004.

[80] M. Schultes, “Absorption of Sulphur Dioxide with Sodium Hydroxide Solution in Packed Columns,” *Chemical Engineering and Technology*, vol. 21, no. 2. pp. 201–209, 1998.

[81] R. N. Goldberg and V. B. Parker, “Thermodynamics of solution of SO2(g) in water and of aqueous sulfur dioxide solutions,” *J. Res. Natl. Bur. Stand. (United States)*, vol. 90, no. 5, pp. 341–358, 1985.

[82] P. J. Hoftyzer and F. J. G. Kwanten, “Absorption of nitrous gases, Gas Purification Processes for Air Pollution Control,” in *G. Nonhebel*, 1972, pp. 164–187.

[83] K. R. Jethani, N. J. Suchak, and J. B. Joshi, “Modeling and Simulation of a Spray Column for NOx Absorption,” *Comput. Chem. Eng.*, vol. 16, no. 1, pp. 11–25, 1992.

[84] R. Sander, “Compilation of Henry’s law constants (version 4.0) for water as solvent,” *Atmos. Chem. Phys.*, vol. 15, no. 8, pp. 4399–4981, 2015.

[85] P. W. Atkins, *Physical Chemistry. 3rd Edition*. Oxford University Press, 1986.

[86] E. Wilhelm, R. Battino, and R. J. Wilcock, “Low-pressure solubility of gases in liquid water,” *Chem. Rev.*, vol. 77, no. 2, pp. 219–262, Apr. 1977.

[87] M. Luckas, K. Lucas, and H. Roth, “Computation of phase and chemical equilibria in flue-gas/water systems,” *AIChE J.*, vol. 40, no. 11, pp. 1892–1900, 1994.

[88] W. Henry, “Experiments on the Quantity of Gases Absorbed by Water, at Different Temperatures and under Different Pressures,” *Philos. Trans. R. Soc. London*, vol. 93, pp. 29–42, 1803.

[89] M. Spoor, “Modeling and stochastic simulation of the reactions and absorption of NOx in water,” TUDelft, 1992.

[90] D. D. Schmidt, “Simulating Aerosol Formation and Efefcts in NOx Absorption in Oxy-fired Boiler Gas Processing Units Using ASPEN Plus,” Kansas State University, 2013.

[91] H. Komiyama and H. Inoue, “Reaction and transport of nitrogen oxides in nitrous acid solutions,” *J. Chem. Eng. Japan*, vol. 11, no. 1, pp. 25–32, 1978.

[92] K. Fredenhagen and M. Wellmann, “Ätzwirkungen des Fluorwasserstoffs und Gegenmittel,” *Angew. Chemie*, vol. 45, no. 33, pp. 537–538, 1932.

[93] C. C. Chen and L. B. Evans, “A local composition model for the excess Gibbs energy of aqueous electrolyte systems,” *AIChE J.*, vol. 32, no. 3, pp. 444–454, 1986.

[94] K. S. Pitzer, “Thermodynamics of electrolytes. I. Theoretical basis and general equations,” *J. Phys. Chem.*, vol. 77, no. 2, pp. 268–277, Jan. 1973.

[95] L. A. Bromley, “Thermodynamic properties of strong electrolytes in aqueous solutions,” *AIChE J.*, vol. 19, no. 2, pp. 313–320, 1973.

[96] D. N. Miller, “Mass transfer in nitric acid absorption,” *AIChE J.*, vol. 33, no. 8, pp. 1351–1358, 1987.

[97] F. Ullmann, *Ullmann’s Encyclopedia of Industrial Chemistry: Sixth, Completely Revised Edition.* American Chemical Society, 2003.

[98] C. Brogren and H. T. Karlsson, “Modeling the absorption of SO2 in a spray scrubber using the penetration theory,” *Chem. Eng. Sci.*, vol. 52, no. 18, pp. 3085–3099, 1997.

[99] H. Tsukahara, T. Ishida, and M. Mayumi, “Gas-phase oxidation of nitric oxide: Chemical kinetics and rate constant,” *Nitric Oxide - Biol. Chem.*, vol. 3, no. 3, pp. 191–198, 1999.

[100] D. Kühnemuth, F. Normann, F. Johnsson, and K. Andersson, “Evaluation of concepts for secondary SO2 and NOx removal from the oxy-fuel process,” in *Power Generation & Challenges in Capture , Transportation and Storage Recommendation*, 2008, no. X, p. 2008.

[101] C. England and W. H. Corcoran, “Kinetics and mechanisms of the gas phase reaction of water

vapor and nitrogen dioxide," *Ind. Eng. Chem. Fundam.*, vol. 13, no. 4, pp. 373–384, 1974.

[102] M. A. Siddiqi, J. Petersen, and K. Lucas, "Influence of nitrogen monoxide on the complex phase and chemical equilibria in wet flue gas cleaning processes," *Ind. Eng. Chem. Res.*, vol. 42, no. 7, pp. 1406–1413, 2003.

[103] Y. N. Lee and S. E. Schwartz, "Reaction kinetics of nitrogen dioxide with liquid water at low partial pressure," *J. Phys. Chem.*, vol. 85, no. 7, pp. 840–848, 1981.

[104] C. E. Corriveau, "The absorption of N2O3 into water," University of California, Berkeley, 1971.

[105] M. M. Wendel and R. L. Pigford, "Kinetics of nitrogen tetroxide absorption in water," *AIChE J.*, vol. 4, no. 3, pp. 249–256, 1958.

[106] B. R. Deshwal and H. K. Lee, "Kinetics and mechanism of chloride based chlorine dioxide generation process from acidic sodium chlorate," *J. Hazard. Mater.*, vol. 108, no. 3, pp. 173–182, 2004.

[107] H. W. Park and D. W. Park, "Removal kinetics for gaseous NO and SO2 by an aqueous NaClO2 solution mist in a wet electrostatic precipitator," *Environ. Technol.*, vol. 38, no. 7, pp. 835–843, Apr. 2017.

[108] R. Krzyzyńska and N. D. Hutson, "Effect of solution pH on SO2, NOx, and Hg removal from simulated coal combustion flue gas in an oxidant-enhanced wet scrubber," *J. Air Waste Manage. Assoc.*, vol. 62, no. 2, pp. 212–220, Feb. 2012.

[109] J. Kaczur, "Oxidation Chemistry of Chloric Acid in NOx/SO2 and Air Toxic Metal Removal from Gas Streams," *Environ. Prog.*, vol. 15, pp. 245–254, Dec. 1996.

[110] C. Brogren, H. T. Karlsson, and I. Bjerle, "Absorption of NO in an Aqueous Solution of NaClO2," *Chem. Eng. Technol.*, vol. 21, no. 1, pp. 61–70, 1998.

[111] R. Hao, S. Yang, B. Yuan, and Y. Zhao, "Simultaneous desulfurization and denitrification through an integrative process utilizing NaClO2/Na2S2O8," *Fuel Process. Technol.*, vol. 159, pp. 145–152, 2017.

[112] C. H. Zheng *et al.*, "Simultaneous absorption of NOx and SO2 in oxidant-enhanced limestone slurry," *Environ. Prog. Sustain. Energy*, vol. 33, no. 4, pp. 1171–1179, 2014.

[113] Y. G. Adewuyi, X. He, H. Shaw, and W. Lolertpihop, "Simultaneous absorption and oxidation of NO and SO2 by aqueous solutions of sodium chlorite," *Chem. Eng. Commun.*, vol. 174, no. 1, pp. 21–51, 1999.

[114] B. R. Deshwal, H. D. Jo, and H. K. Lee, "Reaction Kinetics of Decomposition of Acidic Sodium Chlorite," *Can. J. Chem. Eng.*, vol. 82, no. 3, pp. 619–623, 2008.

[115] Z. Han, S. Yang, D. Zheng, X. Pan, and Z. Yan, "An investigation on NO removal by wet scrubbing using NaClO2 seawater solution," *Springerplus*, vol. 5, no. 1, p. 751, Jun. 2016.

[116] Caffaro Brescia S.p.A., "Il biossido di cloro," 2014.

[117] C. L. Yang and H. Shaw, "Aqueous absorption of nitric oxide induced by sodium chlorite oxidation in the presence of sulfur dioxide," *Environ. Prog.*, vol. 17, no. 2, pp. 80–85, 1998.

[118] Z. Mo, S. Hu, and D. Hu, "Kinetics of the preparation of chlorine dioxide by sodium chlorite and hydrochloric acid at low concentration," *Chem. Eng. Trans.*, vol. 46, no. 2004, pp. 49–54, 2015.

[119] Z. J. Tang, P. Fang, J. H. Huang, and P. Y. Zhong, “Emission characteristics of Cl2 and ClO2 during simultaneous removal of SO2 and NO using NaClO2 solution,” *IOP Conf. Ser. Earth Environ. Sci.*, vol. 113, no. 1, 2018.

[120] M. Teramoto, S. I. Hiramine, Y. Shimada, Y. Sugimoto, and H. Teranishi, “Absorption of dilute nitric monoxide in aqueous solutions of Fe(II)-EDTA and mixed solutions of Fe(II)-EDTA and Na2SO3,” *J. Chem. Eng. Japan*, vol. 11, no. 6, pp. 450–457, 1978.

[121] E. Sada, H. Kumazawa, Y. Yamanaka, I. Kudo, and T. Kondo, “And nitric oxide in aqueous mixed solutions of sodium chlorite and sodium hydroxide,” *J. Chem. Eng. Japan*, vol. 11, no. 4, pp. 276–282, 1978.

[122] E. Sada, H. Kumazawa, I. Kudo, and T. Kondo, “Absorption of Lean NOx in Aqueous Solutions of NaClO2 and NaOH,” *Ind. Eng. Chem. Process Des. Dev.*, vol. 18, no. 2, pp. 275–278, Apr. 1979.

[123] P. V. Danckwerts and A. Lannus, *Gas-liquid reactions.*, vol. 117(10). 1970.

[124] W. G. Whitman, “The two film theory of gas absorption,” *Int. J. Heat Mass Transf.*, vol. 5, no. 5, pp. 429–433, 1962.

[125] R. Zarzycki, A. Chacuk, and J. M. Coulson, *Absorption: Fundamentals and Applications*. Oxford, UK, 1993.

[126] O. Levenspiel, *Chemical reaction engineering*. 1962.

[127] A. Lancia, D. Musmarra, and F. Pepe, “Modeling of SO2 Absorption into Limestone Suspensions,” *Ind. Eng. Chem. Res.*, vol. 36, no. 1, pp. 197–203, 1997.

[128] Z. Yi, H. Peng, H. Yinghui, and Z. Bingjian, “Removal of 1,2,4-TCB from flue gas by aqueous chlorine-dioxide scrubbing solution in a lab-scale bubbling reactor,” in *2009 International Conference on Environmental Science and Information Application Technology, ESIAT 2009*, 2009, vol. 3, pp. 748–751.

[129] M. C. Taylor, J. F. Whitte, G. P. Vincent, and G. I. Cunnigham, “Sodium chlorite properties and reactions,” *Ind. Eng. Chem.*, vol. 32, no. 7, pp. 899–903, Jul. 1940.

[130] J. F. White, M. C. Taylor, and G. P. Vincent, “Chemistry of Chlorites,” *Ind. Eng. Chem.*, vol. 34, no. 7, pp. 782–792, 1942.

[131] Z. Li, R. D. Wuebbles, and N. J. Pylawka, “Rate constant measurement for the reaction of OC1O with NO at 220-367 K,” *Chem. Phys. Lett.*, vol. 354, no. 5–6, pp. 491–497, 2002.

[132] M. T. Leu and W. B. DeMore, “Rate constant for the reaction chlorine oxide + nitric oxide to atomic chlorine + nitrogen dioxide,” *J. Phys. Chem.*, vol. 82, no. 19, pp. 2049–2052, Sep. 1978.

[133] J. Haunstetter and N. Weinhart, “Evaluation of a Novel Concept for Combined NO x and SO x Removal Master’s thesis in Master Programme Sustainable Energy Systems,” Chalmers University of Technology, 2015.

[134] J. L. Bravo, J. R. Fair, and J. A. Rocha, “Mass transfer in Gauze Packings,” *Hydrocarb. Process.*, vol. 64, pp. 91–95, 1985.

[135] E. Brunazzi and A. Paglianti, “Liquid-Film Mass-Transfer Coefficient in a Column Equipped with Structured Packings,” *Ind. Eng. Chem. Res.*, vol. 36, no. 9, pp. 3792–3799, 1997.

[136] J. A. Rocha, J. L. Bravo, and J. R. Fair, “Distillation columns containing structured packings: a comprehensive model for their performance. 1. Hydraulic models,” *Ind. Eng. Chem. Res.*,

vol. 32, no. 4, pp. 641–651, Apr. 1993.

[137] Ž. Olujić, A. F. Seibert, and J. R. Fair, “Influence of corrugation geometry on the performance of structured packings: An experimental study,” *Chem. Eng. Process. Process Intensif.*, vol. 39, no. 4, pp. 335–342, 2000.

[138] Ž. Olujić, “Effect of column diameter on pressure drop of a corrugated sheet structured packing,” *Chem. Eng. Res. Des.*, vol. 77, no. 6, pp. 505–510, 1999.

[139] E. Brunazzi, G. Nardini, A. Paglianti, and L. Petarca, “Interfacial Area of Mellapak Packing: Absorption of 1,1,1,-Trichloroethane by Genosorb 300,” *Chem. Eng. Technol.*, vol. 18, pp. 248–255, 1995.

[140] J. R. Fair, A. F. Seibert, M. Behrens, P. P. Saraber, and Ž. Olujić, “Structured packing performance - Experimental evaluation of two predictive models,” *Ind. Eng. Chem. Res.*, vol. 39, no. 6, pp. 1788–1796, 2000.

[141] E. M. A. Nicolaiewsky, F. W. Tavares, K. Rajagopal, and J. R. Fair, “Liquid film flow and area generation in structured packed columns,” *Powder Technol.*, vol. 104, no. 1, pp. 84–94, 1999.

[142] Ž. Olujić, M. Behrens, L. Colli, and A. Paglianti, “Predicting the efficiency of corrugated sheet structured packings with large specific surface area,” *Chem. Biochem. Eng. Q.*, vol. 18, no. 2, pp. 89–96, 2004.

[143] R. Billet and M. Schultes, “Predicting mass transfer in packed columns,” *Chem. Eng. Technol.*, vol. 16, no. 1, pp. 1–9, 1993.

[144] J. L. Bravo, J. A. Rocha, and J. R. Fair, “A comprehensive model for the performance of columns containing structured packings,” *Inst. Chem. Eng. Symp. Ser.*, vol. 128, pp. A489–A507, 1992.

[145] M. Shi and A. Mersmann, “Effective Interfacial Area in Packed Columns,” *Ger. Chem. Eng.*, vol. 8, pp. 87–96, 1985.

[146] J. A. Rocha, J. L. Bravo, and J. R. Fair, “Distillation columns containing structured packings: A comprehensive model for their performance. 2. Mass-transfer model,” *Ind. Eng. Chem. Res.*, vol. 35, no. 5, pp. 1660–1667, 1996.

[147] C. Murrieta, “Liquid phase mass transfer in structured packing-Separation research program report,” 1991.

[148] R. Billet and M. Schultes, “Prediction of mass transfer columns with dumped and arranged packings: Updated summary of the calculation method of Billet and Schultes,” *Chem. Eng. Res. Des.*, vol. 77, no. 6, pp. 498–504, 1999.

[149] P. Suess and L. Spiegel, “Hold-up of mellapak structured packings,” *Chem. Eng. Process.*, vol. 31, pp. 119–124, 1992.

[150] G. Nardini, A. Paglianti, L. Petarca, and E. Viviani, “Sulzer BX gauze: Fluid dynamics and absorption of acid gases,” *Chem. Eng. Technol.*, vol. 19, no. 1, pp. 20–27, 1996.

[151] C. F. Colebrook and C. M. White, “Experiments with fluid friction in roughened pipes,” *Proc. R. Soc. London. Ser. A - Math. Phys. Sci.*, vol. 161, no. 906, pp. 367–381, 1937.

[152] K. Onda, H. Takeuchi, and Y. Okumoto, “Mass transfer coefficients between gas and liquid phases in packed columns,” *J. Chem. Eng. Japan*, vol. 1, no. 1, pp. 56–62, 1968.

[153] R. Clift, J. R. Grace, and M. E. Weber, *Bubbles, Drops, and Particles*. 1978.

[154] J. R. Grace, "Shapes and Velocities of single drops," *Trans. Inst. Chem. Eng.*, vol. 54, no. 3, pp. 167–173, 1976.

[155] D. Bhaga and M. E. Weber, "Bubbles in viscous liquids: Shapes, wakes and velocities," *J. Fluid Mech.*, vol. 105, pp. 61–85, 1981.

[156] E. Michaelides, C. T. Crowe, and J. Schwarzkopf ohn D, *Multiphase Flow Handbook 2nd Edition*. 2016.

[157] K. H. Javed and J. F. Attiyah, "Experimental measurement of drop phase mass transfer coefficients for the carbon tetracloride-acetic acid-water system," *Eng. J. Qatar Univ.*, vol. 4, no. 1931, pp. 15–23, 1991.

[158] N. K. Yeh and G. T. Rochelle, "Liquid-phase mass transfer in spray contactors," *AIChE J.*, vol. 49, no. 9, pp. 2363–2373, 2003.

[159] M. Wegener, N. Paul, and M. Kraume, "Fluid dynamics and mass transfer at single droplets in liquid/liquid systems," *Int. J. Heat Mass Transf.*, vol. 71, pp. 475–495, 2014.

[160] A. J. Klee and R. E. Treybal, "Rate of rise or fall of liquid drops," *AIChE J.*, vol. 2, no. 4, pp. 444–447, 1956.

[161] A. H. P. Skelland and R. M. Wellek, "Resistance to mass transfer inside droplets," *AIChE J.*, vol. 10, no. 4, pp. 491–496, 1964.

[162] A. Kumar and S. Hartland, "Correlations for prediction of mass transfer coefficients in single drop systems and liquid-liquid extraction columns," *Chem. Eng. Res. Des.*, vol. 77, no. 5, pp. 372–384, 1999.

[163] S. K. Friedlander, "A note on transport to spheres in stokes flow," *AIChE J.*, vol. 7, no. 2, pp. 347–348, 1961.

[164] J. T. Davies, *Turbulence Phenomena*, vol. 18, no. 1. Elsevier Inc., 1972.

[165] I. Proudman and J. R. A. Pearson, "Expansions at small Reynolds numbers for the flow past a sphere and a circular cylinder," *J. Fluid Mech.*, vol. 2, no. 3, pp. 237–262, 1957.

[166] B. Dou, W. Pan, Q. Jin, W. Wang, and Y. Li, "Prediction of SO2 removal efficiency for wet Flue Gas Desulfurization," *Energy Convers. Manag.*, vol. 50, no. 10, pp. 2547–2553, 2009.

[167] H. Brauer and D. Mewes, *Stoffaustausch einschliesslich chemischer Reaktionen.* Aarau; Frankfurt a.M.: Sauerlnder, 1971.

[168] W. Ranz and W. R. Marshall, "Evaporation from drops. Part I," *Chem. Eng. Prog.*, vol. 48, no. 3, pp. 141–146, 1952.

[169] S. T. Hoh, M. M. Farid, and J. J. J. Chen, "Mass transfer to droplets formed by the controlled breakup of a cylindrical jet - physical absorption," *Chem. Eng. Sci.*, vol. 73, pp. 329–333, 2012.

[170] A. C. Lochiel and P. H. Calderbank, "Mass transfer in the continuous phase around axisymmetric bodies of revolution," *Chem. Eng. Sci.*, vol. 19, no. 7, pp. 471–484, 1964.

[171] A. Dimiccoli, M. Di Serio, and E. Santacesaria, "Mass transfer and kinetics in spray-tower-loop absorbers and reactors," *Ind. Eng. Chem. Res.*, vol. 39, no. 11, pp. 4082–4093, 2000.

[172] F. H. Garner and M. Tayeban, "The Importance of the Wake in Mass Transfer from both Continuous and Dispersed Phase Systems," *An. la Real Soc. Española Química*, vol. 56, 1960.

[173] A. E. Handlos and T. Baron, “Mass and heat transfer from drops in liquid-liquid extraction,” *AIChE J.*, vol. 3, no. 1, pp. 127–136, 1957.

[174] R. M. Griffith, “Mass transfer from drops and bubbles,” *Chem. Eng. Sci.*, vol. 12, no. 3, pp. 198–213, 1960.

[175] G. S. Laddha and T. E. Degaleesan, *Transport phenomena in liquid extraction*. New York: McGraw-Hill, 1976.

[176] E. Ruckenstein, “Mass transfer between a single drop and a continuous phase,” *Int. J. Heat Mass Transf.*, vol. 10, no. 12, pp. 1785–1792, 1967.

[177] G. A. Hughmark, “Liquid-liquid spray column drop size, holdup, and continuous phase mass transfer,” *Ind. Eng. Chem. Fundam.*, vol. 6, no. 3, pp. 408–413, 1967.

[178] A. Saboni and S. Alexandrova, “Sulfur dioxide absorption and desorption by water drops,” *Chem. Eng. J.*, vol. 84, no. 3, pp. 577–580, 2001.

[179] P. M. Rose and R. C. Kintner, “Mass transfer from large oscillating drops,” *AIChE J.*, vol. 12, no. 3, pp. 530–534, 1966.

[180] R. J. Brunson and R. M. Wellek, “Mass transfer within oscillating liquid droplets,” *Can. J. Chem. Eng.*, vol. 48, no. 3, pp. 267–274, 1970.

[181] M. Yamaguchi, T. Fujimoto, and T. Katayama, “Experimental studies of mass transfer rate in the dispersed phase and moving behavior for single oscillating drops in liquid-liquid systems,” *J. Chem. Eng. Japan*, vol. 8, no. 5, pp. 361–366, 1975.

[182] R. Higbie, “The rate of absorption of a pure gas into a still liquid during short periods of exposure,” *Trans. Am. Inst. Chem. Eng.*, vol. 31, pp. 365–389, 1935.

[183] C. J. Walcek and H. R. Pruppacher, “On the scavenging of SO2 by cloud and raindrops: I. A theoretical study of SO2 absorption and desorption for water drops in air,” *J. Atmos. Chem.*, vol. 1, no. 3, pp. 269–289, 1983.

[184] V. Srinivasan and R. C. Aiken, “Mass transfer to droplets formed by the controlled breakup of a cylindrical jet—physical absorption,” *Chem. Eng. Sci.*, vol. 43, pp. 3141–3150, Dec. 1988.

[185] G. Astarita, *Mass transfer with chemical reaction*. Elsevier Science Ltd, 1967.

[186] J. S. Hadamard and W. Rybczynski, “Creeping flow past a liquid sphere,” *Comptes rendus l’ académie des Sci.*, vol. 152, p. 1735, 1911.

[187] H. Amokrane and B. Caussade, “Gas absorption into a moving spheroidal water drop,” *J. Atmos. Sci.*, vol. 56, no. 12, pp. 1808–1829, 1999.

[188] W. H. Piarah, A. Paschedag, and M. Kraume, “Numerical simulation of mass transfer between a single drop and an ambient flow,” *AIChE J.*, vol. 47, no. 7, pp. 1701–1704, 2001.

[189] A. E. Hamielec and A. I. Johnson, “Viscous flow around fluid spheres at intermediate reynolds numbers,” *Can. J. Chem. Eng.*, vol. 40, no. 2, pp. 41–45, 1962.

[190] E. Berry and M. R. Pranger, “Equations for calculating the terminal velocities of water drops,” *J. Appl. Meteorol.*, vol. 13, pp. 108–113, 1973.

[191] H. Lamb, *Hydrodynamics*. 1945.

[192] R. R. Hughes and E. R. Gilliland, “The mechanics of drops.,” *Chem. Eng. Prog.*, vol. 48, no. 10, pp. 497–504, 1945.

[193] F. Mashayek and N. Ashgriz, “Nonlinear oscillations of drops with internal circulation,” *Phys. Fluids*, vol. 10, no. 5, pp. 1071–1082, 1998.

[194] R. R. Schroeder and R. C. Kintner, “Oscillations of drops falling in a liquid field,” *AIChE J.*, vol. 11, no. 1, pp. 5–8, 1965.

[195] J. Stichlmair, J. L. Bravo, and J. R. Fair, “General model for prediction of pressure drop and capacity of countercurrent gas/liquid packed columns,” *Gas Sep. Purif.*, vol. 3, no. 1, pp. 19–28, 1989.

[196] E. Brunazzi and A. Paglianti, “Mechanistic pressure drop model for columns containing structured packings,” *AIChE J.*, vol. 43, no. 2, pp. 317–327, 1997.

[197] J. A. Michalski, “Aerodynamic characteristics of FGD spray towers,” *Chem. Eng. Technol.*, vol. 20, no. 2, pp. 108–117, 1997.

[198] J. A. Michalski, “The influence of spraying angle on aerodynamic characteristics of FGD spray towers,” *Chem. Eng. Commun.*, vol. 165, no. March, pp. 17–40, 1998.

[199] J. A. Michalski, “Aerodynamic characteristics of flue gas desulfurization spray towers - Polydispersity consideration,” *Ind. Eng. Chem. Res.*, vol. 39, no. 9, pp. 3314–3324, 2000.

[200] R. K. Sinnott, *Coulson & Richardson’s Chemical Engineering, Chemical Engineering Design*, vol. 6. 1999.

[201] W. L. McCabe, J. C. Smith, and P. Harriott, *Unit Operations of Chemical Engineering*. 1996.

[202] F. Di Natale *et al.*, “Capture of fine and ultrafine particles in a wet electrostatic scrubber,” *J. Environ. Chem. Eng.*, vol. 3, no. 1, pp. 349–356, 2015.

[203] J. H. Seinfeld and S. N. Pandis, *Atmospheric Chemistry and Physics: From Air Pollution to Climate Change, 3rd Edition*. 2016.

[204] M. Esposito, “PhD thesis dissertation: Electyrostatic scrubbing of submicron particles:experimental and modeling,” 2018.

[205] J. Krissmann, M. Aslam Siddiqi, and K. Lucas, “Thermodynamics of SO2 absorption in aqueous solutions,” *Chem. Eng. Technol.*, vol. 21, no. 8, pp. 641–644, 1998.

[206] M. A. Siddiqi, J. Krissmann, P. Peters-Gerth, M. Luckas, and K. Lucas, “Spectrophotometric measurement of the vapour-liquid equilibria of (sulphur dioxide + water),” *J. Chem. Thermodyn.*, vol. 28, no. 7, pp. 685–700, 1996.

[207] F. J. Millero, J. B. Hershey, G. Johnson, and J. Z. Zhang, “The solubility of SO2 and the dissociation of H2SO3 in NaCl solutions,” *J. Atmos. Chem.*, vol. 8, no. 4, pp. 377–389, 1989.

[208] R. Taylor and R. Krishna, *Multicomponent mass transfer (Vol. 2)*. New York, USA, 1992.

[209] A. K. Kunze *et al.*, “Mass transfer measurements in absorption and desorption: Determination of mass transfer parameters,” *Chem. Eng. Res. Des.*, vol. 104, no. 0, pp. 440–452, 2015.

[210] L. Spiegel and W. Meier, “A generalized pressure drop model for structured packings.,” *IChemE*, pp. 85–94, 1992.

[211] R. E. Tsai, A. F. Seibert, R. B. Eldridge, and G. T. Rochelle, “A dimensionless model for predicting the mass-transfer area of structured packing,” *AIChE J.*, vol. 57, no. 5, pp. 1173–1184, 2011.

[212] A. Erto, M. Balsamo, L. Paduano, A. Lancia, and F. Di Natale, “Utilization of alumina-

supported K2CO3 as CO2-selective sorbent: A promising strategy to mitigate the carbon footprint of the maritime sector," *J. CO2 Util.*, vol. 24, pp. 139–148, Mar. 2018.

[213] C. A. Hall and P. K. Agrawal, "Separation of kinetics and mass-transfer in a batch alkoxylation reaction," *Can. J. Chem. Eng.*, vol. 68, no. 1, pp. 104–112, 1990.

[214] A. H. Lefebvre and V. G. McDonell, *Atomization and Sprays-2nd Edition*. CRC Press-Taylor & Francis Group, 1989.

[215] H. Sapra, M. Godjevac, K. Visser, D. Stapersma, and C. Dijkstra, "Experimental and simulation-based investigations of marine diesel engine performance against static back pressure," *Appl. Energy*, vol. 204, pp. 78–92, 2017.

[216] A. Mayer, *Number based emission limits, VERT-DPF-verification procedure and experience with 8000 retrofits*. Switzerland: VERT, 2004.

[217] M. S. Peters, K. D. Timmerhaus, and R. E. West, *Plant design and economics for chemical engineers-Fifth edition*. Boston: McGraw-Hill, 2003.

[218] D. R. Turner *et al.*, "The potential future contribution of shipping to acidification of the Baltic Sea," *Ambio*, vol. 47, no. 3, pp. 368–378, 2018.

[219] D. Gregory and N. Confuorto, *A practical guide to exhaust gas cleaning systems for the maritime industry*. 2012.

[220] S. Darake, M. S. Hatamipour, A. Rahimi, and P. Hamzeloui, "SO2 removal by seawater in a spray tower: Experimental study and mathematical modeling," *Chem. Eng. Res. Des.*, vol. 109, pp. 180–189, 2016.

[221] D. Flagiello, F. Di Natale, A. Lancia, and A. Erto, "Characterization of mass transfer coefficients and pressure drops for packed towers with Mellapak 250.X," *Under Rev. Chem. Eng. Res. Des.*, 2020.